RETURN TO THE IDAHO LIBRARY

-7850

ANL-7850

CHEMICAL ENGINEERING DIVISION RESEARCH HIGHLIGHTS

January—December 1971

U of C-AUA-USAEC

ARGONNE NATIONAL LABORATORY, ARGONNE, ILLINOIS

Prepared for the U.S. ATOMIC ENERGY COMMISSION
under contract W-31-109-Eng-38

The facilities of Argonne National Laboratory are owned by the United States Government. Under the terms of a contract (W-31-109-Eng-38) between the U. S. Atomic Energy Commission, Argonne Universities Association and The University of Chicago, the University employs the staff and operates the Laboratory in accordance with policies and programs formulated, approved and reviewed by the Association.

MEMBERS OF ARGONNE UNIVERSITIES ASSOCIATION

The University of Arizona
Carnegie-Mellon University
Case Western Reserve University
The University of Chicago
University of Cincinnati
Illinois Institute of Technology
University of Illinois
Indiana University
Iowa State University
The University of Iowa
Kansas State University
The University of Kansas
Loyola University
Marquette University
Michigan State University
The University of Michigan
University of Minnesota
University of Missouri
Northwestern University
University of Notre Dame
The Ohio State University
Ohio University
The Pennsylvania State University
Purdue University
Saint Louis University
Southern Illinois University
The University of Texas at Austin
Washington University
Wayne State University
The University of Wisconsin

NOTICE

This report was prepared as an account of work sponsored by the United States Government. Neither the United States nor the United States Atomic Energy Commission, nor any of their employees, nor any of their contractors, subcontractors, or their employees, makes any warranty, express or implied, or assumes any legal liability or responsibility for the accuracy, completeness or usefulness of any information, apparatus, product or process disclosed, or represents that its use would not infringe privately-owned rights.

Printed in the United States of America
Available from
National Technical Information Service
U.S. Department of Commerce
5285 Port Royal Road
Springfield, Virginia 22151
Price: Printed Copy $3.00; Microfiche $0.95

ANL-7850
General, Miscellaneous
and Progress Reports

ARGONNE NATIONAL LABORATORY
9700 South Cass Avenue
Argonne, Illinois 60439

CHEMICAL ENGINEERING DIVISION RESEARCH HIGHLIGHTS

January-December 1971

R. C. Vogel, Division Director
L. Burris, Associate Division Director
A. D. Tevebaugh, Associate Division Director
D. S. Webster, Associate Division Director
E. R. Proud, Assistant Division Director
J. Royal

TABLE OF CONTENTS

	Page
ABSTRACT	7
I. FUEL-CYCLE TECHNOLOGY	8
A. Liquid-Metal Decladding of Reactor Fuels	8
1. Proposed Flowsheet for LMFBR Fuel Decladding	9
2. Engineering Development	11
3. Process Demonstration Experiments	13
4. Zinc Decladding for Long-Cooled LMFBR Fuel	14
5. Melt Decladding	15
B. Continuous Conversion of U/Pu Nitrates to Oxides	18
1. Laboratory Investigations	18
2. Engineering Program	22
C. In-Line Analysis in Fuel Fabrication	24
1. Plutonium/Uranium Ratio in Fuel	24
D. Adaptation of Centrifugal Contactors in LMFBR Fuel Processing	28
E. Electrolytic Reduction of Plutonium in Purex Processes	33
II. SODIUM TECHNOLOGY	39
A. On-Line Monitoring of Impurities in Sodium	39
1. Oxygen Meter	39
2. Hydrogen Meter	41
3. Carbon Meters	43
4. Meter Modules for FFTF	45
5. Detectors for Leaks in Steam Generators	49
6. Characterization of Impurity Meters and Meter Response to Impurity Species	50
B. Analytical Standards Program	51
1. Administrative Activities	51
2. Laboratory Activities	53
C. Sodium Chemistry	56
1. The Na-Na_2O-$NaOH$-NaH System	57
2. Vacuum Distillation as an Analytical Method for Impurities in Sodium	60
3. Solubility of Krypton in Liquid Sodium	62

TABLE OF CONTENTS

Page

D. Fission-Product and Cover-Gas Technology. 64

1. Proposed System for Fuel-Failure Detection and Characterization on FFTF 65
2. Analysis of Cover Gas 66
3. Analysis of Sodium by Sparging 68

III. MATERIALS CHEMISTRY AND THERMODYNAMICS 71

A. High-Temperature Thermodynamic Phase and Kinetic Studies 71

1. The Effect of Fuel Burnup on Oxygen Potentials 71
2. Phase and Reaction Studies of U-O-Na and U-Pu-O-Na Systems 72
3. Partial Relative Ion Cross Sections of U and U-O Molecules and Partial Pressures over the U-Pu-O System 78

B. Chemistry of Irradiated Fast-Reactor Fuels and Materials. 82

1. Ion Microprobe Analysis of Stainless Steel 82
2. Oxygen Potential Gradients in Irradiated Mixed Oxide Fuels 84

C. Reactor Safety and Physical Property Studies. 90

1. Enthalpies and Heat Capacities by Drop Calorimetry. . . 91
2. Speed of Sound in Molten Reactor Materials. 92
3. Matrix-Isolation Spectroscopy. 93
4. Theoretical Extrapolation of Measured Physical-Property Data to Higher Temperatures. 94
5. Thermal Diffusivity of Reactor Materials 95
6. Reactor Materials-Fuel Phase Studies at High Temperatures 95

D. Calorimetry 96

1. Na_3UO_4 96
2. Na_2O. 97
3. $CsHC_2$. 97
4. ThS 98
5. N≡SF 98
6. XeF_6, XeF_4, and XeF_2 98
7. BrO_3F. 99
8. Quantum-Chemical Investigations 99

TABLE OF CONTENTS

Page

IV. ANALYTICAL AND REACTOR CHEMISTRY 100

A. Dosimetry 100

1. Development of Dosimetry 100
2. Service Dosimetry 101

B. Fast-Reactor Cross-Section Measurements 102

1. Spectrum-Averaged Measurements 102
2. Fast-Neutron Fission Yields of Tritium 103

C. Determination of Fast-Neutron Fission Yields 108

V. PHYSICAL INORGANIC CHEMISTRY 112

A. Thermodynamics of Lithium-Chalcogen Systems. 112

1. Phase-Equilibrium Studies of Binary Lithium-Chalcogen Systems 112
2. Thermodynamics of the Pseudo-Ternary Lithium Selenide-Selenium-Alkali Halide System by Emf Methods 114
3. Phase Diagram of the Pseudo-Ternary Lithium Selenide-Selenium-Alkali Halide System 116

B. Lithium-Hydrogen-Metal Systems of Importance to Fusion Reactors 117

1. Thermodynamics of Lithium-Hydrogen Systems 117
2. Some Estimates of the Consequences of Tritium Permeation in the Core of a D-T Fusion Reactor 120

C. Structure Investigations by Spectroscopic Methods 122

1. Studies of Divalent Metal Halide Melts 122
2. Reactions of Iodine-Containing Species with Molten Nitrates 125
3. Cation Effects on the Structure of the Iodate Ion in Molten Nitrates 126

D. Nucleation Studies 127

1. Measurements of the Limit of Superheat of Liquids. . . . 127
2. Theory for Homogeneous Nucleation Involving Nonideal Gases. 130

E. Theoretical Studies in Thermodynamics 131

1. Gas Solubility in Liquid Metals 131

TABLE OF CONTENTS

Page

VI. ENERGY CONVERSION 135

A. Lithium/Sulfur Cells for Electric Vehicle Propulsion . . . 135

1. Cell Studies 135
2. Supporting Laboratory Studies. 144
3. Materials and Components 151
4. Electric Automobile Performance Calculations 153

B. Lithium/Chalcogen Cells for Hybrid-Vehicle Propulsion . 155

1. Cell Studies 155

C. Lithium/Selenium Batteries for Implantation 159

1. Cell Lifetime Studies. 160
2. Studies of Full-Sized Cells 162

VII. FLUIDIZED-BED COMBUSTION OF FOSSIL FUELS. 164

A. Bench-Scale Combustion Experiments. 164

1. Results of Single-Stage Combustion Runs 165
2. Results of Two-Stage Combustion Runs. 165

B. Mechanism of Lime Sulfation Reaction 168

C. Regeneration of Calcium Sulfate with Carbon Monoxide/ Carbon Dioxide Mixtures 169

D. Modelling Studies 170

VIII. NUCLEAR SAFEGUARDS STUDY 174

IX. ADDENDUM 175

ABSTRACT

During 1971, Argonne's Chemical Engineering Division continued its investigations in fuel-cycle technology, sodium technology, fast-reactor materials properties, liquid-metal and molten-salt chemistry, reactor safety, thermochemistry, electrochemical energy conversion, fluidized-bed combustion of fossil fuels, and nuclear safeguards. Fuel-cycle studies were directed toward the development of a pyrochemical process for decladding LMFBR fuel, a centrifugal contactor for the plutonium isolation steps in aqueous fuel reprocessing, a process for converting U/Pu nitrates to oxide powders suitable for fuel fabrication, analytical procedures adaptable to in-line use in the fabrication of LMFBR fuel, and a method for the electrolytic reduction of plutonium in Purex processes. In the sodium technology program, research was directed toward the development of on-line monitoring devices for impurities in sodium, the detection and characterization of fuel-element failures, and sodium chemistry relevant to LMFBRs. Administrative and laboratory work was carried out on the national analytical standards program for coolant sodium. Materials studies included the determination of the effect of fuel burnup on oxygen potentials, the phase, reaction, and thermodynamic studies of the U-O-Na and U-Pu-O-Na systems, and mass-spectrometric studies of the U-Mo-O and U-Cs-O systems. Electron microprobe analysis was used to estimate oxygen-potential gradients in irradiated mixed-oxide fuels using the Mo-MoO_2 system as a redox indicator. High-temperature physical-property data needed for fast-reactor safety analysis were obtained. These included the determination of the enthalpies and heat capacities of Na_3UO_4 and $U_{0.8}Pu_{0.2}O_{1.97}$, the speed of sound in liquid sodium, thermodynamic properties of $UO_{2\pm x}$ by matrix-isolation spectroscopy, and the distribution of fission products between molten iron and molten UO_2. Calorimetric studies included the determination of the enthalpies of formation of Na_3UO_4, Na_2O, $CsHC_2$, ThS, NSF, XeF_2, XeF_4, XeF_6 and BrO_3F. Quantum-chemical investigations were made on the N-F, Si-F, N-S, and N-O systems. A dosimetry program was established, and data were obtained on the integral capture-to-fission ratios of the major fissile and fertile isotopes in EBR-II. Fast-neutron fission yields of tritium from ^{235}U and of short-lived, gamma-active nuclides from ^{235}U, ^{238}U, and ^{239}Pu were determined. Phase-equilibrium studies were made on several lithium-chalcogen systems. In work related to fusion reactors, a thermodynamic analysis of existing data on the Li-LiH system was made, and the consequences of tritium permeation in the core of a deuterium-tritium-fueled reactor were estimated. Raman spectroscopic studies of divalent metal halide melts were continued. Infrared spectroscopy was used in the study of reactions of iodine-containing species with molten nitrates. Experimental and theoretical studies of the homogeneous nucleation of vapor bubbles in superheated liquids were initiated. Work was continued on the development of a mathematical model for the solubility of noble gases in liquid metals. The energy conversion program was directed toward

improving the performance of lithium/chalcogen cells for use in electric vehicles and as an implantable power source for an artificial heart or as a heart-assist device. Cell studies included research on cathode design, materials, and sealing methods, the effect on cell performance of additives to the cathode reactants, the use of paste and liquid electrolytes, and the scale-up of cells to larger sizes. Work on the fluidized-bed combustion of fossil fuels as a means of controlling the emission of atmospheric pollutants included single-stage and two-stage bench-scale experiments. Also, the mechanism of the lime sulfation reaction and the regeneration of calcium sulfate were explored, and mathematical models were derived for the prediction of SO_2 removal by lime in a fluidized bed. The establishment of safeguards-related criteria for special nuclear material was continued.

I. FUEL-CYCLE TECHNOLOGY

A. Liquid-Metal Decladding of Reactor Fuels

The reference fuel recovery process for future liquid-metal-cooled fast breeder reactors (LMFBRs) is a modified shear-leach process followed by solvent extraction to purify and recover uranium and plutonium. Shear-leach includes sodium removal, partial disassembly of the fuel subassembly, shearing of the fuel pins, and oxidation of the UO_2 to U_3O_8 to remove iodine and fission-product gases contained in the oxide matrix. The shear-leach procedure is used for reprocessing stainless steel-clad and Zircaloy-clad oxide fuels from the present thermal reactors. Early LMFBR fuels will consist of UO_2-PuO_2 jacketed in stainless steel tubes. Because of the nature of fuel discharged from LMFBRs (the higher burnups, higher burnup rates, shorter cooling times, residual sodium, and higher plutonium contents), operations to prepare the fuel for introduction into the acid dissolver are expected to be difficult and costly steps.

Liquid-metal decladding processes are under development at Argonne as alternatives to the reference head-end process for LMFBR fuel. The major steps of one head-end process, which utilizes liquid zinc, are as follows: (1) After the stainless steel portions of the subassembly below the core and blanket regions have been removed mechanically, the stainless steel cladding and structural members in the fuel-containing region are dissolved in liquid zinc at 800°C. The zinc readily dissolves the stainless steel but does not react with uranium oxide or plutonium oxide. (2) The zinc-steel phase is removed from the vessel containing the fuel oxides, and the fuel oxides are reduced to metal by stirring the oxides in a molten salt-metal reduction system such as $CaCl_2$/Zn-Mg-Ca. (3) The resulting liquid-metal solution is transferred from the reaction vessel to a second vessel where the solvent metal is separated from the uranium and plutonium by distillation. The uranium and plutonium may then be dissolved in acid in preparation for solvent extraction.

This procedure has the following potential advantages over a shear-leach head-end operation:

1. Mechanical disassembly of the subassembly is avoided.

2. Shearing of the fuel pins is avoided.

3. Fission-product decay heat is dissipated easily.

4. Residual sodium is disposed of without separate sodium-removal steps.

5. Xenon and krypton are collected in high concentration in an inert cover-gas mixture of small enough volume to allow storage in gas cylinders.

6. Other fission products including iodine are collected as solid wastes having good heat-transfer properties.

Another high-temperature decladding operation, melt decladding, has been investigated briefly. In this process, the fuel subassembly is heated above the melting point of stainless steel to melt the cladding and structural members of the subassembly and thus separate the fuel oxide from the steel sufficiently to expose the oxide for acid dissolution. This type of process avoids mechanical disassembly and shearing of the fuel, but has the disadvantage that volatile fission products (chiefly xenon, krypton, and iodine) contained in the oxide matrix are not completely removed and collected before acid dissolution.

1. Proposed Flowsheet for LMFBR Fuel Decladding

One of several versions of the process flowsheet for zinc decladding of stainless steel-clad UO_2-PuO_2 fuel subassemblies is shown in Fig. I-1. All process steps except the evaporation steps are performed sequentially in a single tungsten crucible. In Step I, the core and blanket

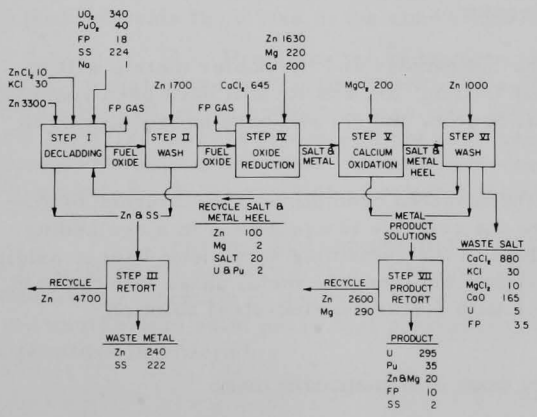

Fig. I-1

Liquid-Zinc Head-End Process. High-zinc reduction alloy. (Basis: 3 A.I core subassemblies; quantities in kilograms.)

regions of three subassemblies from a conceptual 1000-MWe LMFBR[1] are immersed in molten zinc at 800°C in the tungsten crucible. The stainless steel (SS) cladding is dissolved in the zinc, which has a liquid $ZnCl_2$-KCl cover layer to prevent excessive zinc vaporization. The bulk of the zinc-stainless steel solution is then transferred out of the tungsten crucible. The oxide fuel particles remain in the crucible. In Step II, the fuel oxide heel is washed with fresh zinc to reduce the stainless steel content to an acceptable level. The zinc-stainless steel streams from Steps I and II are combined and retorted in Step III to recover the bulk of the zinc for recycle and to reduce the volume of zinc that must be stored with the active stainless steel.

For the reduction of fuel oxide in Step IV, liquid Zn-Mg-Ca and liquid $CaCl_2$ are added to the tungsten crucible containing the fuel oxide, and the crucible contents are stirred at 860°C. As the uranium and plutonium are reduced to metal, they dissolve in the reduction alloy. To ensure that all the uranium and plutonium are in solution, $MgCl_2$ is added in Step V to oxidize the residual calcium at 860°C and remove it from the metal phase. (The solubility of uranium and plutonium in the metal is substantially increased by the removal of calcium.) Then the metal solution containing the uranium and plutonium is transferred to the product retort. In Step VI, the salt-metal heel in the tungsten crucible is washed with fresh zinc to remove most of the uranium and plutonium that had remained in the metal phase after the first transfer of product. This zinc wash solution is combined with the product solution from Step V. The bulk of the salt is then removed from the tungsten crucible and becomes a process waste.

It is also possible that the bulk of the salt may be treated and recycled. In Step VII, the combined metal solutions from Steps V and VI are retorted to isolate the uranium and plutonium fuel alloy and to recover zinc and magnesium for recycle to the process. The fuel alloy is cast into shapes suitable for acid dissolution.

Nearly all of the lanthanides and the nobler metals will be present in the fuel alloy, but tritium, Xe, and Kr will have been removed as gases, and I, Cs, Rb, Ba, Sr, Sm, and Eu will have been removed in the waste salt.

After Step VI, the tungsten crucible will be returned to Step I, the decladding step. Before the crucible is again used in a decladding operation, $ZnCl_2$ will be added to the remaining salt-metal heel to oxidize uranium, plutonium, and magnesium from the metal phase into the salt phase and prevent their loss with discarded zinc-steel solution.

[1] Atomics International Follow-On Study, USAEC report AI-AEC-12791 (1969).

2. Engineering Development

a. Reduction of UO_2 Pellets

Two liquid metal-salt systems for reducing the fuel oxides to metals have been proposed; the first employs a high zinc-low magnesium alloy in which both plutonium and uranium are soluble; the second employs a low zinc-high magnesium reduction alloy in which plutonium dissolves but uranium precipitates as the solid metal. Both alloys contain about 6 at. % calcium, which is the reductant. The flowsheet shown in Fig. I-1 is for the process using the first metal-salt system. In the second scheme, transfer of the plutonium-bearing solution out of the reaction vessel is followed by dissolution of the uranium in a second metal alloy.

Reduction runs were made to determine the effects of alloy composition on completeness of reduction for pressed and sintered UO_2 pellets. Complete reductions were achieved in less than 6 hr at temperatures between 800 and 840°C with either reduction alloy in the presence of a salt phase that was primarily $CaCl_2$. Up to 600 g of UO_2 pellets (0.21 in. diameter, 0.25 in. long) were reduced in a 5 1/2-in.-ID, baffled tungsten crucible with a 3-in.-dia agitator rotating at 900 rpm.

In both the decladding and the reduction steps of the head-end process, the liquid salt phase serves several necessary functions. The salt phase:

1. Removes iodine from fission gases released from the oxide matrix. (The iodine dissolves in the salt phase as zinc iodide in the decladding step or as calcium iodide in the reduction step.)

2. Decreases the amount of zinc volatilized from the melt.

3. Wets and collects fine oxide particles during decladding, and thus prevents their loss in the zinc-stainless steel solution.

4. Promotes the reduction reaction by dissolving calcium from the metal phase, contacting it with the solid oxide phase, and dissolving the CaO formed by the reduction reaction. (Good contacting of the solid oxide particles with the liquid-salt phase is essential for rapid and complete reduction because under most circumstances the step limiting the reduction rate appears to be the reaction of calcium metal with the solid oxide phase.)

Various salt compositions have been studied to determine their effect on the reduction rate. The composition of the salt phase will influence the retention of iodine by the salt and will affect the composition of the equilibrium solid phase that precipitates as CaO is added or as the temperature is lowered.

Experiments described in the preceding report in this series (ANL-7750, pp. 11-14) showed that gaseous iodine released by fuel during decladding at 800°C was converted to ZnI_2. With a cover layer of molten KCl-LiCl on the metal, the iodide was prevented from volatilizing; the decontamination factor for iodine was greater than 10^5. It has since been concluded that potassium ions are necessary in the salt phase during decladding to complex ZnI_2 and thereby prevent its volatilization. Also, the addition of a large fraction of KCl to the reduction salt would result in an advantageous lowering of the solidus temperature of the salt. Consequently, the use of a $CaCl_2$-KCl cover salt was considered for the decladding step of the zinc-head-end process. Initial experiments were with a $CaCl_2$-25 mol % KCl salt phase and either a high-zinc or a low-zinc alloy. However, reductions were appreciably slower than in comparable runs with no KCl in the salt phase, possibly because of the lower solubility of CaO in salt that contains KCl. Apparently, the amount of KCl in the reduction salt should be restricted to the small amount carried over from the decladding operation. In the flowsheet shown in Fig. I-1, if the decladding salt contains 66 mol % KCl, the reduction salt will contain only 6 mol % KCl.

The volume of salt removed from the process as waste must be minimized, and no salt should accompany the uranium and plutonium fed to the nitric acid dissolver since halide ions cause corrosion of the aqueous processing equipment. A possible source of salt is reduction salt entrained with the product alloy fed to the zinc-magnesium evaporation step. In the latter step, any small amounts of $CaCl_2$ and KCl present would be volatilized, but CaF_2 (another proposed constituent of the reduction salt) is not sufficiently volatile to be removed and would enter the acid dissolver. This suggested the use of $CaCl_2$ alone as the reduction salt.

In additional reduction experiments, it was found that the use of $CaCl_2$ as the salt phase places a lower limit on either the quantity of salt or the reduction temperature because $CaCl_2$ forms a partially soluble compound with the CaO produced by reduction. For the $CaCl_2$-CaO system, the equilibrium solid phase is CaO at temperatures above 835°C, but is an undesirable voluminous compound, $CaO \cdot 2CaCl_2$, below 835°C. These data indicate that for the salt phase to be liquid in reductions below 835°C, the mole ratio of $CaCl_2$ to UO_2 must be greater than 4. In practice, it was found that this ratio must be 5 or greater to achieve satisfactory reductions. With the addition of at least 25 mol % CaF_2 to $CaCl_2$, the equilibrium phase when CaO is added in excess of its solubility is CaO and no $CaO \cdot 2CaCl_2$ precipitates at any temperature. When excess CaO is added to a salt with a composition of $CaCl_2$-20 mol % CaF_2, the equilibrium solid phase at temperatures above 720°C is CaO. However, when as much as 20 mol % CaF_2 is present in the salt phase, experiments have shown that reduction is not rapid and complete at salt-to-UO_2 ratios below ~4. Because the inclusion of large amounts of CaF_2 in the reduction salt does not reduce

the total amount of salt required and because any CaF_2 carried with the product alloy cannot be removed by retorting, CaF_2 will not be used in the reduction salt.

b. Retorting of Zinc

The need to reduce the volume of wastes may provide the incentive to recover and recycle the zinc from the zinc-stainless steel decladding solution. Retorting appears to be the most favorable method for zinc recovery. Because it would be difficult to remove the steel-rich residue remaining in the retort vessel, the use of inexpensive retort crucibles that could be used as storage vessels for the steel waste has been investigated. Crucibles fabricated from stainless steel are not suitable for this application because they are subject to corrosion by nickel leaching in zinc. Nickel-free iron alloys would not be seriously attacked by the zinc alloy because the zinc-steel alloy is saturated with iron. A crucible fabricated of mild steel has been evaluated.

An experiment was performed in which three successive melts, each consisting of 380 g of stainless steel dissolved in 3.42 kg of zinc, were poured at 800°C into an unheated mild steel crucible. After each charging, the crucible was placed in a vacuum retort and the bulk of the zinc was vaporized at 850°C. About 83% of the total quantity of zinc poured into the crucible was evaporated in the three steps. The percentage of zinc removed from the steel could be increased easily by using an optimized retort, but removal of 85 to 95% of the zinc should be adequate. The only visible corrosion of the steel crucible used in this experiment was near the top and was probably due to refluxing of the zinc vapors. The vessel can be modified to prevent refluxing by reducing the heat loss from the upper portion of the vessel.

3. Process Demonstration Experiments

Experimental apparatus has been installed in the shielded hot cell facilities of this Division for experiments to demonstrate the principal steps of the pyrochemical decladding process with highly irradiated fuel. The experimental apparatus, which is sized for processing 100-g quantities of fuel, has been installed and tested in shakedown experiments with simulated fuel pins containing unirradiated UO_2 and UO_2-20 wt % PuO_2 and with an irradiated stainless steel rod. A demonstration experiment with an irradiated fuel pin has also been completed.

In an experiment, a fuel pin is placed in a perforated tantalum basket that is lowered vertically into liquid zinc. As the stainless steel is dissolved by the zinc, the oxide fuel pellets fall into the basket. When the cladding has been completely removed, the basket is raised out of the melt.

A magnesium plug is then forced into the top of the basket, and the basket is inverted and partially immersed in a 90 mol % $CaCl_2$-10 mol % CaF_2/Zn-2.5 at. % Mg-5 at. % Ca melt contained in a second vessel. (The decision to use CaF_2-containing salts in the demonstration experiments was made before the efficacy of CaF_2-free salts was proven in laboratory experiments described above.) When the plug melts, the fuel pellets drop into the melt. The melt is stirred, and the uranium and plutonium oxides are reduced to metal.

In one of the shakedown experiments, an irradiated, Type 304 stainless steel rod (0.41 in. OD, 10.5 in. long) was dissolved at 800°C in 6000 g of zinc covered by 420 g of $CaCl_2$-10 mol % CaF_2. This rod had been irradiated in EBR-II to a peak fluence of 7×10^{22} n/cm^2, and had cooled about two years. The only significant activities in the rod were ^{60}Co and ^{54}Mn. The iron and cobalt remained completely in the zinc phase, but about 30% of the manganese was in the salt phase and between 0.1 and 1% was volatilized from the melt, presumably as $MnCl_2$. If the decladding melt is made oxidizing by the addition of $ZnCl_2$ (as indicated in the flowsheet in Fig. I-1), some manganese will be carried with the salt phase to the reduction step and will then be removed with the uranium and plutonium product. This amount of manganese in the product (less than 1 kg in 295 kg of uranium and 35 kg of plutonium) will cause no problems in the aqueous processing steps.

Two irradiated fuel pins have been obtained, one for each of two successive demonstration experiments. Before irradiation, the fuel pin used in the first experiment contained 79.9 g of UO_2-20% PuO_2 and 36.5 g of normal UO_2 clad with 0.252-in.-OD, 15-mil-thick, Type 316L stainless steel tubing. The two pins were irradiated in EBR-II at peak linear powers ranging from 8.7 to 13.8 kW/ft. They reached a burnup of 3.6 at. % and were removed from the reactor in August, 1968. Information from the nondestructive testing of these two pins and from the destructive testing of similar pins from the same irradiation capsule is available to characterize the fuel used in the experiments. As stated above, a demonstration experiment with one of the irradiated pins was completed. Preliminary analytical results indicate that the operations were performed successfully.

4. Zinc Decladding for Long-Cooled LMFBR Fuel

With the objective of gaining practical experience with a pyrochemical head-end operation, a simplified zinc decladding process has been developed and tested on a small scale. This process is intended for long-cooled fuel that will be discharged from the first large LMFBRs (e.g., FFTF and the demonstration reactors). The techniques used are those applicable to treating the core section of an FFTF fuel assembly containing about 40 kg of UO_2-PuO_2 and about 20 kg of stainless steel cladding and shroud

material. Because of the long cooling, no provisions need be made for a high fission-product heat output or a high ^{131}I content.

This proposed decladding process, like the zinc decladding process that includes a reduction step, is designed to replace a number of difficult or costly steps usually associated with a chop-leach head-end procedure (sodium removal, partial disassembly, shearing, and oxidation). Reliability, simplicity, and economy are emphasized.

In this head-end process, the stainless steel cladding is dissolved in zinc in a graphite crucible held within a tilt-pour furnace. The concentration of stainless steel in the zinc is about 8 wt % at about 850°C. After 2 hr at temperature, the melt is agitated for 30 min to ensure uniform distribution of the stainless steel slurry. Evaporation of zinc from the crucible is reduced to an acceptable level by operating under an argon atmosphere of 15 psig.

The bulk of the zinc-stainless steel slurry is poured into a side-arm receiver by tilting the furnace body about 90° (or 1 or 2° beyond horizontal). A small amount of fuel oxide tends to pour out of the crucible with the melt but is trapped on a mild steel screen placed on top of the receiving vessel. Since the melt is saturated with iron, it does not attack the screen. The oxide and the screen are recycled to the following decladding run.

When the furnace has cooled, the receiver for the zinc-steel slurry is removed, and a steel vessel for fuel oxide transport is installed in the side arm. The furnace is then tilted an additional 45° beyond horizontal to pour the fuel oxide into the steel vessel. Since the oxide is not wet by the residual zinc-stainless steel and since no salt is present, more than 90% of the oxide can be poured into the receiver and subsequently charged to a fuel dissolver. The oxide heel in the crucible is recycled to the next decladding run.

5. Melt Decladding

Melt decladding designates head-end processes in which the steel cladding and structural members of the reactor subassembly are melted to expose the fuel oxide. The feasibility of the procedure depends upon sufficient draining of stainless steel so that the exposed oxide can be completely separated in the following step, which will be either acid dissolution or voloxidation. Several methods of partially separating the stainless steel from the oxide fuel were investigated in small-scale experiments with simulated fuel assemblies.

In one type of experiment, a bundle of stainless steel tubes containing UO_2 pellets was melted while resting on the interior side of

a magnesia or alumina crucible inclined at an angle of 10 to 20° from the horizontal. Temperatures of 1490 to 1650°C were maintained for 1 hr and the furnace atmosphere was either argon or argon-4 vol % H_2 at a total pressure of about 600 Torr. In every run, most of the steel flowed away from the pellets, which remained in a loose pile near their original position in the crucible. The amount of steel remaining with the pellets was greatly influenced by the degree of wetting between the oxide and the metal. The factors that influence wetting have not yet been determined. In every case, however, enough surface of the oxide pellets was exposed so that the oxide could be further oxidized or would be accessible to acid.

In another melt decladding concept, a vertically suspended subassembly is lowered into a heated zone to melt the steel and to release the oxide fuel pellets. The pellets and molten metal fall onto a cold surface or into a relatively cool liquid such as liquid nitrate salts where the metal solidifies. After separation of the larger pieces of steel from the cooled particles by screening, the mixture of oxide and steel is fed to an acid dissolver or an oxidation operation. Preliminary work on a small scale gave promising results. Experiments are planned to evaluate melt decladding with full-scale mock fuel assemblies.

Two experiments were performed to study a tilt-pour concept in which stainless steel, UO_2 pellets (~600 g), and UO_2 fines (~50 g) were heated to 1550°C in a magnesia crucible (2 1/2 in. diameter, 8 in. long). After the steel had melted, the crucible was tilted 15° beyond horizontal to pour the steel. In both runs, about 85% of the steel was poured out. In one experiment, only 0.04% of the UO_2 was poured out of the crucible with the steel; in the other experiment about 6% poured out. Only about 5% of the UO_2 was bonded to the steel remaining in the crucible.

A conceptual design for melt decladding 1 metric ton of fuel per 8-hr day was prepared, based on the use of the tilt-pour melt decladding concept for separating oxide from molten steel. The furnace design for this operation is shown in Fig. I-2. Two subassemblies will be suspended in a magnesia crucible and melted at temperatures between 1500 and 1600°C. After the steel has been melted, the crucible will be tilted (to the right in Fig. I-2) 10° past the horizontal to pour the molten steel into the mold. Next, the crucible will be tilted to the left 45° past the horizontal to dump the oxide fuel pellets and the residual steel into a transport vessel from which the cooled mixture will be fed to the acid dissolution step.

An advantage of melt decladding as a potential head-end step is its basic simplicity; however, development work must be done to make the technique feasible.

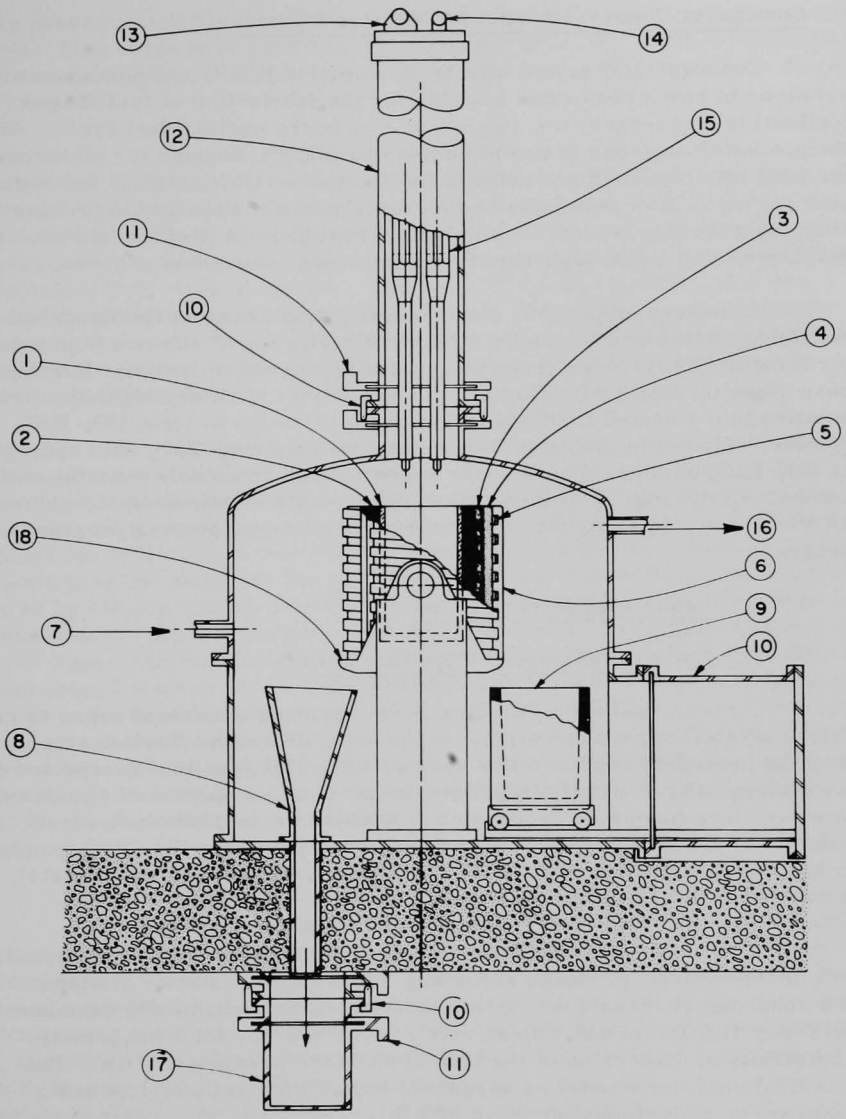

Fig. I-2. Tilt-Pour Melt Decladding Furnace. 1. MgO liner of crucible, 2. graphite crucible, 3. SiC insulation, 4. zirconia insulation, 5. induction coils, 6. coil support, 7. argon supply, 8. UO_2-PuO_2 fuel chute, 9. waste steel mold, 10. locks, 11. lock gates, 12. transfer chamber, 13. elevating mechanism for fuel subassemblies, 14. transfer chamber cooling gas inlet, 15. fuel subassemblies, 16. argon + fission product gas to recycle and storage, 17. pellet transport vessel, and 18. tilt-pour mechanism for crucible. ANL Neg. No. 308-2656.

B. Continuous Conversion of U/Pu Nitrates to Oxides

Conversion of uranyl nitrate hexahydrate (UNH) and plutonium nitrate solutions to powdered oxides suitable for the fabrication of fuel shapes (pellets) is a necessary and important step in the nuclear fuel cycle. With the projected increase in use of nuclear power, the demand for plutonium for LMFBR and plutonium-recycle fuel systems will increase. In addition, concern with the environment has focussed new attention on the problem of shipping plutonium as nitrate solution. These factors provide incentive for development of a new high-capacity, continuous conversion process.

A conversion process under investigation based on fluidized-bed technology developed in earlier ANL fluidization work[2] shows a high potential for meeting process requirements, including remote operation. Basic process steps include denitration by spraying uranyl nitrate-plutonium nitrate solution into a heated fluidized bed of oxide particles to form UO_3-PuO_2 powder, followed by fluidized-bed reduction of the UO_3-PuO_2 with hydrogen to UO_2-PuO_2 powder. The process appears to be applicable over the entire concentration range of uranium-plutonium nitrate solutions and to plutonium nitrate alone. An integrated laboratory and pilot-engineering program is in progress.

1. Laboratory Investigations

a. Examination of UO_2-PuO_2 Pellets

Laboratory studies were continued in several areas to provide a base of information for the engineering program. Earlier studies (see the preceding report in this series, ANL-7750, pp. 15-16) reported on the sinterability of UO_2-PuO_2 pellets prepared in a sequence of simulated process steps (dropwise denitration of uranyl nitrate-plutonium nitrate solution to produce UO_3-PuO_2, hydrogen reduction of the UO_3-PuO_2 powder to UO_2-PuO_2, pressing into 1/4-in.-dia pellets, and sintering of pellets). A density of 89% of theoretical was achieved.

A sample of a UO_2-20 wt % PuO_2 pellet with a density of 84% of theoretical, produced according to the above sequence of steps, has subsequently been chemically analyzed and also physically examined by X-ray diffraction and with an electron microprobe for homogeneity (uniformity of dispersion of the plutonium in the uranium matrix). The chemical analysis showed an oxygen-to-metal atom ratio of 1.98 and a uranium-to-plutonium atom ratio of 4.0.

X-ray diffraction analysis of the UO_2-PuO_2 pellet showed only a single set of diffraction lines, indicating that a single oxide phase

[2] A. A. Jonke, E. J. Petkus, J. W. Loeding, and S. Lawroski, Nucl. Sci. Eng. 2, 303 (1957).

was present. A lattice parameter of 5.4602 Å for the oxide pellet was measured. This value is in good agreement with a value (a_0 = 5.4610 Å) predicted by a mathematical relationship developed in a related program (see ANL-7750, p. 20).

Early LMFBR fuel specifications pertaining to homogeneity stated that isolated plutonium particles should have diameters no larger than 50 μm. This requirement was considered in evaluating results. A pellet was scanned by bombarding it with an electron beam from the electron microprobe and measuring the count rates for the characteristic uranium (Mα) and plutonium (Mβ) X-rays emitted. The ratio of the U/Pu count rates was a measure of the homogeneity of the material. Two different scanning procedures were used with a single beam size of 0.5 μm--(1) fixed counting at randomly selected spots and (2) continuous scanning of 8 by 10 μm and 80 by 100 μm areas.

In the initial series of measurements, both scanning procedures showed considerable scatter of the data, with a relatively high standard deviation of ~20% for U/Pu ratio, although no single spot of any size was found to contain only uranium or only plutonium. Standard deviations for U/Pu ratios determined from several additional sets of measurements near the center of the pellet ranged from ~8 to 12%. Scans of areas of 80 by 100 μm across an entire diameter of the pellet gave a standard deviation of 7.8% for a series of 65 measurements. Variability in the count ratio apparently indicated localized density differences rather than varying concentration since examination of individual uranium and plutonium X-ray count rates showed that generally the count rates for both elements increased or decreased in unison. This satisfied a key process requirement in that there was no localized enrichment of one of the constituents (i.e., no segregation of plutonium). Overall, results indicated that distribution of plutonium in the uranium matrix was uniform.

b. Solubility Limits for U/Pu Nitrate Solutions

A knowledge of the cosolubility of uranyl nitrate and plutonium nitrate in nitric acid solutions is important to the selection of the feed composition for the fluid-bed denitration process. The feed solution should be as concentrated as possible to increase the throughput of the fluid-bed denitration reactors. However, the feed solution should not be so concentrated that crystallization might occur, since this would probably interfere with feeding (spraying) of the solution and also might confound the nuclear safety design of the feed-storage system. Since little crystallization data are available in the literature for uranyl nitrate-plutonium nitrate solutions having high plutonium contents, crystallization temperatures were measured for a series of test solutions in the range of process interest, 1 to 2M (U+Pu).

The compositions and crystallization temperatures for these solutions are summarized in Table I-1. In these solutions, approximately 30% of the plutonium was present as the hexavalent (plutonyl) ion and the remainder as the tetravalent ion. The solution of current primary interest, 2.0M (U+Pu) and U/Pu ratio of 4, has a crystallization temperature of 18°C when the nitric acid concentration is 2.0M. For solutions of 1.4 and 1.6M (U+Pu), the crystallization temperature increased with increased nitric acid content in the acid range studied (2 to 5M), as may be seen in Fig. I-3. The crystallization temperature was lower when plutonium was substituted for uranium in a solution having a fixed total heavy metal ion content and a fixed nitric acid content, as shown in Fig. I-4; this trend is desirable in that increased plutonium concentration will lower the crystallization temperature and make precipitation less likely. Crystallization temperatures were also determined for plutonium totally in the tetravalent state and were found to be similar to those for 30% hexavalent-70% tetravalent plutonium.

TABLE I-1. Crystallization Temperatures for the Uranyl Nitrate-Plutonium Nitrate-Nitric Acid System

Solution Composition (M)				Crystallization Temperature
U	Pu	HNO_3	U/Pu	(°C)
1.6	0.2	2.0	8.0	13.2
1.6	0.3	2.0	5.3	15.9
1.6	0.4	2.0	4.0	18.0
1.4	0	3.4	-	12.6[a]
1.28	0.34	2.0	3.8	3.2
1.28	0.34	3.4	3.8	15.3
1.28	0.34	4.8	3.8	20.8
1.12	0.28	3.4	4.0	10.2
1.12	0.28	4.8	4.0	17.6
0.98	0.42	3.4	2.3	5.3
0.70	0.70	3.4	1.0	1.5

[a]Extrapolated from data on UNH solubility compiled by I. Dillon, Argonne National Laboratory, in 1950.

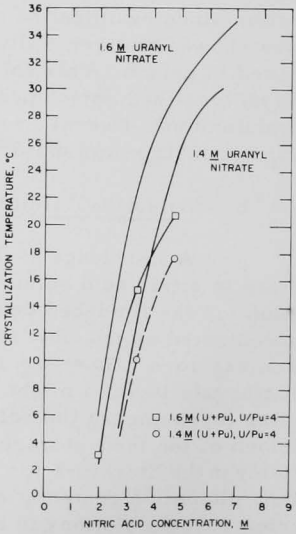

Fig. I-3

Effect of Nitric Acid Concentration on the Crystallization Temperature of Plutonium Nitrate-Uranium Nitrate-Nitric Acid Solutions. (The crystallization data for uranyl nitrate are from a compilation of data by I. Dillon, Argonne National Laboratory, 1950.)

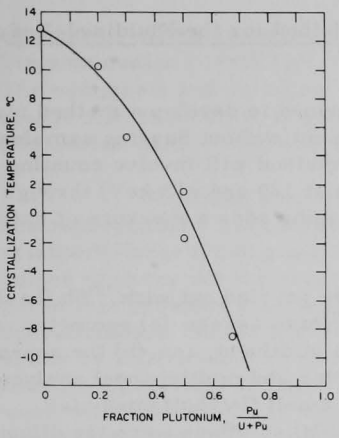

Fig. I-4. Effect of Increasing Plutonium Content on Crystallization Temperature of Uranium-Plutonium Solutions. Total U + Pu: 1.4M; HNO_3: 3.4M.

Identification of the Crystallized Phase. Tests were carried out to identify the crystallized phase in nitric acid solutions containing uranium and plutonium. This is of interest both from a general process standpoint and for criticality safety since precipitation of plutonium compounds in the feed solutions is highly undesirable.

The starting solution compositions and the analytical results obtained by liquid scintillation counting and X-ray fluorescence analyses after dissolving a portion of the crystallized phase are summarized in Table I-2. The relatively high U/Pu ratios, 8.4 to 20.2, in the crystallized phase compared with the approximate U/Pu ratios, 4, 2, and 1 in the starting solution, indicate that the crystallized phase is a uranium compound (probably UNH), even for starting solutions with a U/Pu ratio of one. The plutonium found in the crystallized phase is attributed to a sorption phenomenon, which is common when a salt is crystallized from a solution containing more than one species. The invariant point, which would be indicated by a U/Pu ratio of 1 in the crystallized phase, was not reached and apparently lies on the plutonium-rich side of the U-Pu-nitric acid system.

TABLE I-2. Identification of the Crystallized Phase in U/Pu Nitrate Solutions

Composition of Starting Solution (M)			% of Original Pu in Crystallized Phase	U/Pu Ratio in Crystallized Phase
U	Pu	HNO_3		
1.6	0.4	2.0	2.5	16.5
1.12	0.28	3.4	3.9	20.2
0.98	0.42	3.4	2.1	15.5
0.86	0.82	3.4	3.4	8.4

The solubility data, along with information on the identity of the crystallized phase, indicate that concentrations of current process interest can be handled safely at room temperature.

c. In-Box Plutonium Analysis Method for the Fluidized-Bed Denitration Pilot Plant

A laboratory study was performed to develop a method for analyzing process solutions for plutonium content without bagging samples from the pilot plant out of the glovebox. The method will involve counting the plutonium gamma activity (the ^{239}Pu peaks at 129 and 413 keV) through a glovebox glove. A procedure that avoids bagging adds a measure of safety to the pilot-plant operation and saves effort.

Preliminary experiments were carried out with ^{125}Sb (having peaks at 175 and 427 keV) as a stand-in for ^{239}Pu to assess (a) geometry and absorption effects due to sample size and type of diluent, and (b) the approximate lower limit of detection. A Ge-Li detector and multichannel analyzer were used, and the sample was contained in a small flat-bottomed vial. Water and 2.5M uranyl nitrate hexahydrate (UNH) solutions were the diluents and were added in 1-ml increments to a 0.1-ml water sample containing the antimony tracer. Semilog plots of gamma count rate versus volume (depth) of sample show straight-line relationships for the 175- and 427-keV gammas, i.e., a reduction of gamma activity with addition of either diluent.

Attenuations of the 175-keV gamma were 4 and 10% for 1-ml additions of water and UNH solution. Thus, the maximum error for a 1 ml sample due to the heavy metal content of the solution would be 6%, if no correction were made for the uranium present. If the measurement were made with the 427-keV gamma, the required correction would be even smaller. In practice, corrections will be made by the use of calibration curves.

In measurements of two dilute plutonium solutions (2.5 and 6.6 mg Pu/ml) with 1-ml samples 0.5 in. from the detector, the counting rate was 200 cpm/mg ^{239}Pu for the 129-keV peak. Since it should be possible to isolate a plutonium gamma peak equivalent to 20 cpm with the present equipment, a 1-ml sample with a plutonium concentration of 0.1 mg/ml can be assayed by this method.

These results indicate that this analytical method is suitable for the pilot-plant feed-makeup step but is not sufficiently sensitive to analyze the denitration condensate (which may have plutonium levels as low as 0.001 mg/ml). Further work is planned with this analytical procedure to improve its sensitivity.

2. Engineering Program

A pilot plant has been constructed to demonstrate the fluidized-bed denitration step in the proposed process for preparation of mixed U/Pu oxides for fuel application. The pilot plant comprises a 4-in.-dia fluidized bed denitration reactor, a feed make-up system, and associated

equipment, all housed in a 3- by 4-module glovebox of Chemical Engineering Division design (CENHAM).[3] (Each module is approximately a 3 1/2-ft cube.) The equipment and an initial shakedown series of denitration runs with uranyl nitrate solution at 300°C were described in the preceding report in this series (ANL-7750, p. 17).

Obtaining approval for startup of work with plutonium materials has represented a major effort during the current year. Because of the relatively large (7000 g maximum) inventory of plutonium that will be required to carry out the program, comprehensive documents had to be prepared that provided a general safety and nuclear safety analysis of the operations and the facility itself. These documents were reviewed successively by a Divisional committee, a Laboratory committee, and the AEC-Chicago Operations Office Criticality Hazards Committee. Approval for work with plutonium was obtained on the basis of the original array of equipment. However, the safety analysis itself suggested equipment changes that were made and were followed by further testing of the equipment.

Additional work with uranyl nitrate solutions suggested that some further minor modifications of the equipment would be desirable. New criticality computations indicated that the new equipment array has no higher reactivity than the original setup and that the new equipment can be operated safely. A second safety review, required by the changes, is nearly completed. (Assistance in the analysis was given by ORNL in the form of Monte Carlo computer calculations on various arrays of equipment.) Interim approval for startup with a maximum plutonium inventory of 2000 g was received October 28, 1971; approval of the use of up to 7000 g of plutonium is expected before the year's end.

Helium leak-testing of the glovebox and DOP (dioctyl phthalate) penetration (efficiency) tests on the glovebox and room ventilation filters (high-efficiency, AEC-type filters) have been carried out as recommended with satisfactory results.

Denitration runs were performed to obtain additional operating experience and to test procedures, specifically (1) to develop "standardized" startup procedures, (2) to check the reproducibility of the denitration operation (e.g., to observe particle-size effects), and (3) to explore the effect of spray-nozzle variations (i.e., the location of the nozzle with respect to the bed and the nozzle design). Nine denitration experiments were made with uranyl nitrate feed solutions during this report period. Equipment was operated through the gloves, employing the procedures that will be used in operations with plutonium materials. This work included the

---

[3] R. F. Malecha, H. O. Smith, J. H. Schraidt, J. V. Natale, N. E. Ross, and H. O. Brown, Jr., "Low-Cost Gloveboxes," in Proceedings of the Eighth Conference on Hot Laboratories and Equipment, Book 2, USAEC report TID-7599, p. 485 (1960).

preparation of 50-liter batches of feed solution to check out the mechanical operability of the feed makeup system. The feed makeup system functioned satisfactorily.

The runs to study the reproducibility of the operation were of relatively short duration, several being about 5.5 hr long (equivalent to about 1 1/2 bed displacements). Operating conditions were a bed temperature of 300°C, a feed rate of 80 cc/min, a feed solution composition of 1.9M UNH and 1M excess nitric acid, a starting bed weight of 8 kg of UO_3, and a fluidizing gas velocity of 1 ft/sec. Runs made under similar conditions gave fairly reproducible results as indicated by particle size effects, i.e., there were no significant trends with respect to growth or diminution in average bed particle size. About 5% of the UO_3 produced under the conditions used consisted of coarse (+20 mesh) UO_3 agglomerates and ~3% consisted of fine (-200 mesh) UO_3. In a production facility, methods for handling these fractions could be devised. For example, the coarse material could be ground before being processed in the subsequent reduction step or could be redissolved. Fines could be blended with the bed material and processed without further treatment.

No advantages of alternative nozzle positions (6 in. above the bottom of the bed as opposed to 9 in.) or alternative nozzle designs (standard two-fluid nozzle vs. extended liquid-tip nozzle) were apparent in the present exploratory work.

Work with plutonium materials is about to start at the interim approval level of 2000 g of plutonium. Because of this limit on the plutonium inventory in the facility, the production of UO_3-3% PuO_2 will be studied first. This work may also be of interest in connection with the recycle of plutonium in light water reactors. Subsequent work will be concerned with the preparation of UO_3-20% PuO_2 suitable for LMFBR applications.

C. In-Line Analysis in Fuel Fabrication

The development of rapid, precise, and accurate in-line nondestructive methods for analysis of critical fuel properties can lead to lower fuel fabrication costs and thereby help to improve the economic competitiveness of the LMFBR. The starting criteria in evaluating analytical methods are the specifications and associated precisions for preirradiated fuel properties for the Fast Fuel Test Facility (FFTF) project.

1. Plutonium/Uranium Ratio in Fuel

The determination by an X-ray fluorescence (XRF) procedure of the plutonium/uranium (Pu/U) ratio in UO_2-20 wt % PuO_2 fuel is being studied. The specification for plutonium concentration is 20.0 ± 0.1% of the actinide content, corresponding to a relative standard deviation (RSD)

of 0.5% in the analysis of solid oxide. To attain the desired RSD, effects on the fluorescence signal of properties of the solid, i.e., high absorption coefficients, enhancement (secondary fluorescence), crystallite size, bulk density, etc., must be proven insignificant or predictably measurable.

In initial investigations, ThO_2-UO_2 is being used as a stand-in for UO_2-PuO_2 to avoid the complications and delays of experiments with plutonium, which would have to be done in a glovebox. This substitution is practical because of the identical relationship of the atomic numbers and thus of the relevant properties for each pair of elements.[4] The relative intensities of Th$L\alpha$ and U$L\alpha$ fluorescence spectra are measured on a Norelco X-ray fluorescence spectrometer.

Experimental work during the report period has concerned the effects on fluorescence intensity of possible interfering impurities, equipment modifications, particle size, and bulk density.

Emission lines of impurity elements that might possibly interfere with the use of X-ray fluorescence analysis of U-Pu oxides have been identified as Sr, Pa, Np, and Am. However, these elements are not likely to be present in sufficient quantity in FFTF fuel to interfere with the analysis. The possibility remains that in future LMFBR fuels, the concentrations of these impurities will be high enough to contribute line intensities similar to those for plutonium.

Modifications of equipment or procedures that decrease the time required to reach a count corresponding to the desired precision improve the opportunity for in-line application, as well as the accommodation of higher production rates. One such equipment modification has been the design of an aluminum sample holder that provides reproducible loading. With this sample holder and a new loading procedure, the counting rate has been increased by a factor of 1.5 and the background count (from scattered X-rays) has been decreased by a factor of 3. Hence, analysis time has been decreased and precision improved.

A series of measurements was made to establish the X-ray spectrograph counting stability, the reproducibility of sample placement in the spectrograph, and the reproducibility of sample loading with the new sample holder. Counting stability was measured by repetitive counting of a sample of UO_2 for a fixed time. The relative standard deviation of ten measurements was 0.1%. The measurement of reproducibility of sample placement was done by withdrawing and replacing the sample carrier in the instrument and counting for a fixed time. The relative standard deviation of ten measurements was 0.1%. The reproducibility of sample loading was

[4] D. S. Webster et al., Chemical Engineering Division Fuel Cycle Technology Quarterly Report, July, August, September 1970, USAEC report ANL-7755, pp. 45-50 (October 1970).

tested by completely reloading the powder sample and counting for a fixed time. The standard deviation of ten measurements was 0.16%. At the 95% confidence level, $2\sigma = 0.34$, which is within the required total uncertainty.

In work to determine whether the relative standard deviation of ±0.5% for plutonium analysis can be achieved in the analysis of mixed-oxide fuel materials, an investigation was made of (1) the variability of XRF measurements of different pellets of the same nominal composition and (2) the variability of XRF measurements on the same pellet. The latter variability is ascribed to errors attributable to the method.

Four pellets each of ThO_2-10 wt % UO_2, ThO_2-20 wt % UO_2, and ThO_2-30 wt % UO_2 were prepared from mixed powders. A series of five measurements was performed on each of the four sintered pellets of three compositions and on four sintered pellets of pure UO_2. An analysis of variance[5] was performed in which it was assumed that the errors of the method and counting statistics are independent and that the variances are additive; this allowed the relative standard deviations of the method to be calculated from the variance of the measurements. Table I-3 presents, for the mixed-oxide pellets, the relative standard deviations for the measurements, for the counting statistics, and for the errors for the method, derived from both the uranium and thorium count rates. The relative standard deviation for the counting statistics ranged from 0.09 to 0.13%. Each count rate was corrected for dead time. Analysis of variance shows the XRF method to be reproducible to better than 0.5% for the same pellet. Thus, the variability in the results due to errors attributable to the method are adequately low.

TABLE I-3. Relative Standard Deviations for XRF Analysis of Fired ThO_2-UO_2 Pellets

ThO_2 (wt %)	UO_2 (wt %)	$\sigma_{measurement}$ (%) (within sample)	σ_{count} (%)[a]	σ_{method} (%)[b]
		Uranium Analyses		
0	100	0.14 (0.10-0.21)[c]	0.086	0.11 (0.051-0.19)[c]
70	30	0.15 (0.11-0.23)[c]	0.11	0.10 (0-0.20)[c]
80	20	0.34 (0.26-0.52)[c]	0.13	0.31 (0.22-0.50)[c]
90	10	0.33 (0.25-0.51)[c]	0.13	0.30 (0.21-0.49)[c]
		Thorium Analyses		
70	30	0.27 (0.20-0.41)[c]	0.11	0.24 (0.17-0.39)[c]
80	20	0.27 (0.19-0.40)[c]	0.10	0.24 (0.16-0.39)[c]
90	10	0.26 (0.20-0.41)[c]	0.099	0.24 (0.17-0.40)[c]

[a] RSD derived from average of three counts (~200,000) corrected for dead time.
[b] $\sigma^2_{method} = \sigma^2_{measurement} - \sigma^2_{count}$.
[c] 95% confidence limits.

[5] O. L. Davies (Ed.), Statistical Methods in Research and Production, 3rd ed., (1961).

The variability between pellets of 0.60 to 1.84% was greater than the variability of measurements of single pellets, and is probably due to mixing, sampling, or material properties of mixtures.

As expected, for the pure urania pellets, the variability between pellets is not statistically different from the variability within pellets. For pure UO_2 pellets, the RSD of the method, calculated from counting statistics and the RSD of the measurements, is 0.11%.

Five measurements of three samples of 70% ThO_2-30% UO_2 powder were subjected to an analysis of variance similar to that for pellets. The powder mixtures were prepared from pure ThO_2 and from UO_2 that had been reduced from NBS U_3O_8. Three sample cups were loaded with each powder and were counted sequentially.

The RSDs for the measurements for powder were 0.29% for thorium and 0.21% for uranium, leading to RSDs for the method of 0.27 and 0.17%, respectively. The RSDs at the 95% confidence level were again below 0.5%.

The variability of the method for pellets and 70% ThO_2-30% UO_2 powder has been shown to be adequately low to indicate that XRF has the potential to achieve better than 0.5% RSD at the 95% confidence level. However, the variability between samples of powder and between pellets is significantly larger than the variability of the method, indicating that a problem exists due to mixing, sampling, or material properties.

The effects on the XRF signal of particle size and bulk density were next evaluated under various conditions, using UO_2 powder. Since particle size and bulk density of powder samples are interrelated, these properties were investigated together. Measurements were made with UO_2 of mixed particle sizes and with samples of the same UO_2 having narrow particle size ranges (-10, 10-20, 20-30, 37-44 μm). The XRF intensities of the UO_2 samples with narrow particle size ranges were measured at different degrees of compaction (ranging from 25 to 36% of theoretical); the densities ranged from that obtained by loose packing to that obtained by the tightest packing obtainable by hand loading.

From these data, relative intensities (ratio of the intensity for oxide to the intensity for uranium metal, ~60 x 10^3 cps) were obtained at 25, 30, 35, and 40% of theoretical density by interpolation and extrapolation. These were plotted against the logarithm of particle size (Fig. I-5). Figure I-5 also includes a curve representing values calculated by Criss[6] from fundamental parameters.[7] Although the curves for experimental and

[6] J. W. Criss, private communication (January 1971).

[7] J. W. Criss and L. S. Birks, Anal. Chem. 40, 1080 (1968).

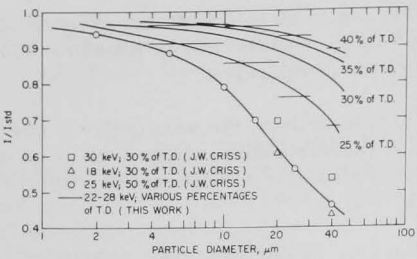

Fig. I-5. XRF Intensity Relative to Uranium Metal for Various UO_2 Particle Sizes and Percentages of Theoretical Densities

calculated values have the same general shape, the experimentally observed intensities differ from calculated values in the following two ways: (1) For the experimental data, a significant decrease in intensity (i.e., a decrease to 95% relative intensity) occurs for particle sizes of 10-20 μm or larger, but for the calculated values intensity decreases significantly at particles sizes of ~2 μm or larger. (2) In the region where particle size has an effect, the rate of decrease of intensity with increase in particle size is greater for the calculated values than for the experimental values.

At present, it is not clear how the experimental conditions differ from the conditions assumed in the model on which calculations were based. However, from a practical point of view, the general agreement indicates that particle size effects can be evaluated and that the influence of this variable on analytical precision can be determined. It appears that it will be necessary to pelletize powder to a controlled density to achieve a precision of 0.5% for the analysis.

D. Adaptation of Centrifugal Contactors in LMFBR Fuel Processing

Development work is continuing on a centrifugal contactor suitable for use in plutonium isolation steps in Purex-type solvent extraction processing of LMFBR fuel material. The contactor is a modification of the large centrifugal units in use in the Savannah River Plant (SRP). In the ANL design, criticality hazards caused by the high plutonium concentrations in the process streams will be controlled by limiting the diameter to a geometrically favorable size. This contactor has a small diameter in comparison with SR contactors, but has a higher length-to-diameter (L/D) ratio and operates at higher speeds to maintain a relatively high capacity. Expected advantages of centrifugal contactors are (1) reduced radiation damage to the solvent as a result of brief residence time in the contactor and (2) improved ease of operation (including rapid flushout at the end of a processing campaign).

The stainless steel contactor is shown in schematic outline in Fig. I-6. Figure I-7 is an overall view of the assembled contactor before installation in its test facility. The rotor and removable mixing paddle are shown in Fig. I-8. The rotor has a 4-in.-ID, a 12-in.-long settling zone, and a 3-in.-long weir section. The rotor, which is suspended from a shaft that penetrates the top of the contactor, spins within a cylindrical casing at speeds up to 3500 rpm. The mixing paddle (mounted on an extension of the rotor shaft) spins within a mixing chamb

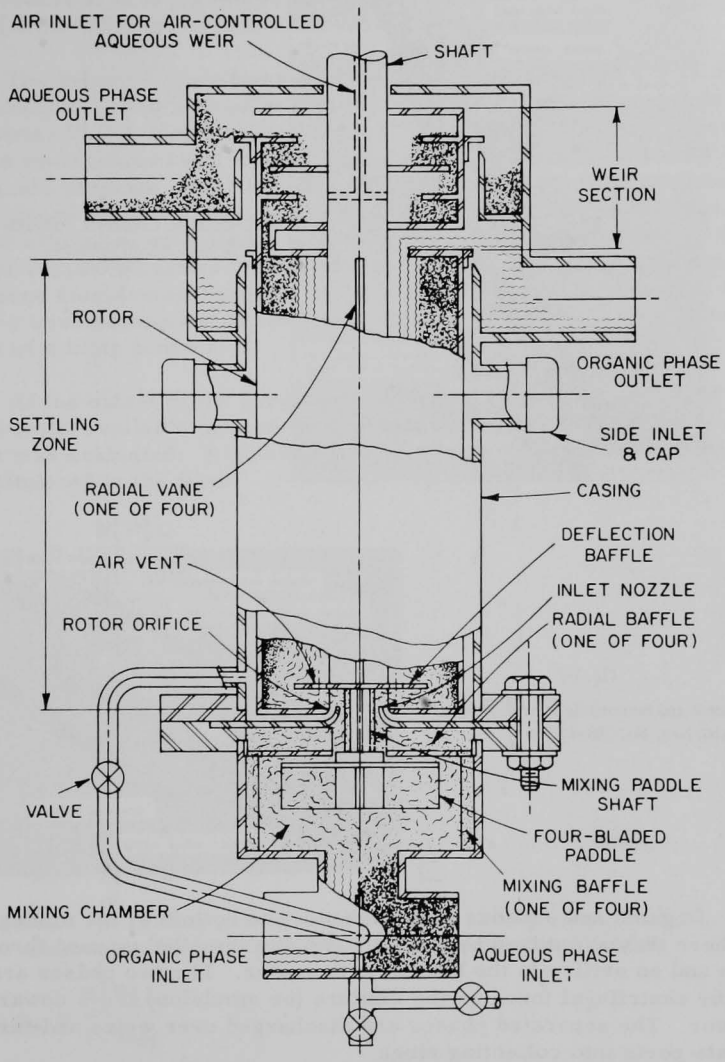

Fig. I-6. Experimental Centrifugal Contactor

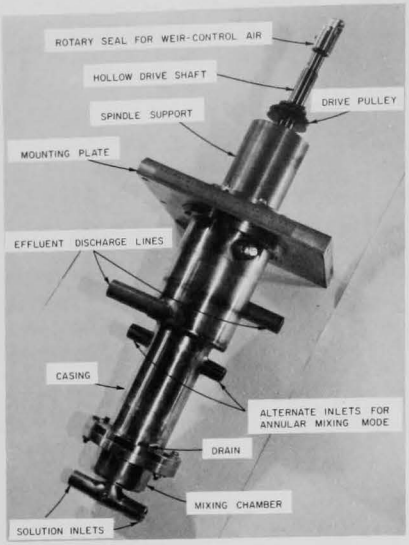

Fig. I-7

Centrifugal Contactor Assembly.
ANL Neg. No. 308-2361A.

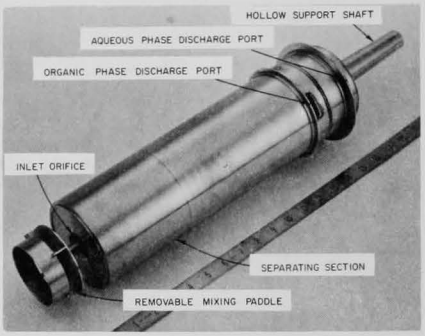

Fig. I-8

Rotor and Removable Mixing Paddle.
ANL Neg. No. 308-2354A.

Organic and aqueous streams enter the bottom of the mixing chamber where they are mixed by a paddle and are impelled upward through a nozzle and an orifice in the bottom of the rotor. The two phases are separated by centrifugal force as the mixture (or emulsion) flows upward through the rotor. The separated phases are discharged over weirs and through separate ports into collecting rings.

Air pressure is applied to the region of the aqueous-phase weir to position the unseparated emulsion band (interface) radially in the rotor. This feature (which was developed at Savannah River) permits operation over a wider range of phase densities and flow rates than could be achieved

with a fixed weir. A more detailed description of the contactor and of the facility where it is being tested appears in the preceding report of this series (ANL-7750, pp. 21-24).

The principal objectives of the development program are to determine mechanical and hydraulic operating characteristics of a high length-to-diameter (L/D), high-speed centrifugal contactor. The testing program includes measurements of separating capacity[8] during operation with aqueous and organic phases similar to those employed in Purex process flowsheets. Work planned for this program also includes tests to determine mass-transfer efficiency with uranyl nitrate solutions, an investigation of the effect of suspended solids upon performance using feed solutions containing manganese dioxide suspensions, and an investigation of the effect of mixing intensity upon separating capacity and mass-transfer efficiency using a variety of mixing paddles.

At the outset of the program, before the long-rotor contactor was designed, the available data on the performance of other centrifugal contactors was evaluated. A formula for estimating the separating capacity was postulated in the form

$$q_s = \frac{N_c^2 D_b^3 L}{10^5 N_m D_m}$$

where

q_s = separating capacity (gpm)

N_c = rotor speed (rpm)

D_b = rotor diameter (in.)

L = settling length of rotor (in.)

N_m = mixing paddle speed (rpm)

D_m = mixing paddle diameter (in.)

Since the mixing paddle and rotor are on the same shaft, $N_c = N_m$, and the expression for separating capacity can be simplified to

$$q_s = \frac{N_c^2 D_b^3 L}{10^5 D_m}$$

The group includes a conversion factor of 10^5 to give an approximate capacity in gpm. Although solution composition and aqueous-to-organic (A/O) flow ratios also affect separating capacity, the actual capacity is

[8]Separating capacity is defined as the maximum total flow throughput at which entrainment of each phase in the exit stream of the other phase reaches a maximum of 1 vol %.

expected to vary about the calculated capacity within a factor of two. On the basis of rotor and paddle size, the separating capacity of the ANL contactor was expected to be ~10 gpm at 3500 rpm. In the tests with the contactor, the capacity was found to be between 8 and 17 gpm, which is close to the predicted range.

Several sets of tests were made to measure separating capacity of the contactor. The first two sets covered a range of rotor speeds from 2000 to 3500 rpm and A/O flow ratios of 0.33 to 4.0. The aqueous phase was 0.5M HNO_3 and the organic phase was either 15 or 30% tributyl phosphate (TBP) in Ultrasene (refined kerosene).

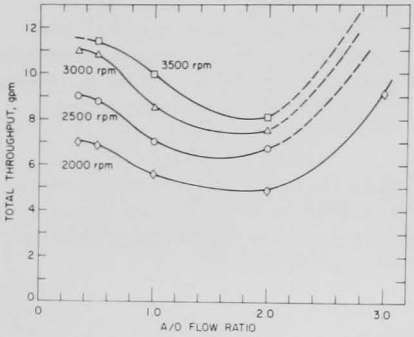

Fig. I-9. Separating Capacity of a 4-in.-dia Rotor Centrifugal Contactor with 15% TBP in Ultrasene and 0.5M HNO_3. (Total throughput measured at the 1% entrainment level.)

Results of the tests with 15% TBP are shown in Fig. I-9. In these tests, separating capacities were near their minimum values at A/O ratios of ~2 for all rotor speeds and ranged from ~5 to ~11.5 gpm. At rotor speeds above 2000 rpm, capacity was found to be limited by the size of the inlet piping (as indicated by the dotted-line extrapolations). The piping was subsequently enlarged from a 1-in. nominal pipe size to 1 1/2-in. nominal pipe size for the tests with 30% TBP.

In the tests with 30% TBP, the separating capacities over the range of rotor speeds from 2000 to 3500 rpm were lowest at an A/O ratio of ~1 (Fig. I-10). The larger inlet pipe lines permitted higher flow rates than had been attainable when 15% TBP was used. Accordingly, capacities as high as 17 gpm were attained at a rotor speed of 3500 rpm and an A/O ratio of 4.

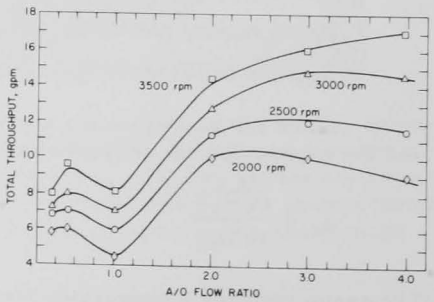

Fig. I-10. Separating Capacity of a 4-in.-dia Rotor Centrifugal Contactor with 30% TBP in Ultrasene and 0.5M HNO_3. (Total throughput measured at the 1% entrainment level.)

During these tests, rotational stability of the high-speed rotor was excellent, demonstrating that the design and fabrication tolerances were suitable for meeting dynamic balance requirements and critical speed limitations. Performance of the air-controlled weir was highly satisfactory, and the pressures required for

proper interface control ranged from 0 to 4 psig, conforming closely to the values calculated on the basis of formulas developed at Savannah River.[9]

Some operating difficulties were encountered during these runs as a result of flow surging, which is a phenomenon characteristic of centrifugal contactors of the SR design. Surging results from the fact that the mixing chamber (which functions as a centrifugal pump) must have a pumping capacity that exceeds the total input flow. Under the condition of excess pump capacity, the pump tends to gulp air, causing it to lose and regain its prime in a cyclic fashion which in turn results in uneven discharge into the separating rotor. Under these conditions, it is difficult to maintain a stable position for the emulsion band in the separating rotor, and measured separating capacities are lower than would be found under stable flow conditions. In the ANL contactor, surging was ameliorated by adding baffles to the mixing chamber (to reduce the pumping capacity) and by bleeding a small steady stream of air into the inlet tee (to prevent the pump from becoming fully primed). The addition of air simulated the operation of a bank of contactors of this type, in which the feed streams to each unit would contain air entrained when the stream is discharged from the adjacent contactors.

An additional change aimed at achieving steady hydraulic operation was to replace the dc variable-speed motor with an ac motor powered by a variable-frequency generator. During operation with the dc motor, speed had been difficult to control since the surging flow imposed a varying load on the drive. Any instability in the flow tended to persist because it created unstable rotor speeds. The new drive system maintains the rotor speed essentially constant at the desired level, even when throughput varies.

A new series of tests has been undertaken to investigate further the most suitable means for maintaining a steady and limited air input to the contactor mixing chamber. The effect of air in the emulsion discharged to the rotor is also being investigated. Because of the high L/D configuration of the rotor, its pumping capacity as well as its separating capacity is of concern when high throughput is a performance objective.

Tests are also currently being made to measure separating capacity using n-dodecane as a diluent in place of Ultrasene. Initial results indicate that the capacities will be close to those found in the tests with Ultrasene.

E. Electrolytic Reduction of Plutonium in Purex Processes

The Purex process is the commonly used method for reprocessing light-water-reactor fuel. Presently, it is being assessed for future fast-breeder reactors.[10] In the proposed sequence of process operations,

[9] A. A. Kishbaugh, Performance of a Multi-stage Centrifugal Contactor, USAEC report DP-841 (October 1963).
[10] W. E. Unger, R. E. Blanco, C. D. Watson, D. J. Crause, A. R. Irvine (comps.), LMFBR Fuel Cycle Studies Progress Report No. 27, USAEC report ORNL-TM-3456 (May 1971) and preceding reports in this series.

plutonium is reduced three times from the tetravalent state to the trivalent state and is reoxidized twice. Reduction and reoxidation are currently accomplished by chemical means. Owing to the requirement of a large stoichiometric excess of reductant, a substantial quantity of waste is formed that has to be disposed of as high-level radioactive waste. In LMFBR fuel reprocessing, processing problems are compounded by the high plutonium content of these fuels (ten times higher than for LWR fuels).

An electrolytic valence adjustment would reduce the total waste volume very substantially. In addition, it would facilitate conversion of decontaminated plutonium nitrate solution to new fuel. Electrolysis is precisely controllable, offering process convenience and operational safety.

Electrolytic reduction of plutonium has been accomplished experimentally on a laboratory scale by three groups.[11-13] In these studies the compositions of the electrolytes were somewhat different from those in a second- or third-cycle Purex stream, yet not different enough to put into question the feasibility of reducing plutonium in a nitric acid medium.

A major problem in the application of electrolytic reduction is the development of an electrolytic cell that allows an adequate reduction rate. Electrolysis is inherently slow, since a phase-boundary process is involved. The magnitude of the current in a flowing electrolyte is determined by mass transport. Levich has shown that an equation of the form

$$Sh = A\, Re^m Sc^n \qquad (1)$$

can be applied in electrolysis,[14] where Sh is the Sherwood number, Re is the Reynolds number, Sc is the Schmidt number, and A, m, and n are constants. The Sherwood number is defined here as $Sh = i_L L/NFDc$, and the Reynolds and Schmidt numbers have the usual definitions, i.e., $Re = Lv/\nu$ and $Sc = \nu/D$ where

i_L = limiting current density, A/cm^2

N = electric equivalents per mole of ions

F = Faraday constant, A-sec/equiv.

D = diffusion coefficient, cm^2/sec

v = linear flow velocity, cm/sec

[11] D. Cohen, Electrochemical Studies of Plutonium Ions in Perchloric Acid Solutions, J. Inorg. Nucl. Chem. 18, 207 (1961).

[12] M. B. Finlayson and J. A. S. Mowat, Electrolytic Reduction of Uranium (VI) and Plutonium (IV) Nitrate Solutions, Electrochem. Technol. 3, 148 (1965).

[13] G. Koch, W. Ochsenfeld, and E. Schwind, Flowsheet Studies on Processing of Plutonium Fuels by Solvent Extraction, German report KFK-990 (1969).

[14] V. G. Levich, Physicochemical Hydrodynamics, Prentice-Hall, Englewood Cliffs, N.J. (1962).

c = concentration of electroactive species, mol/cm^3

L = characteristic electrode dimension, cm

ν = kinematic viscosity of electrolyte, cm^2/sec.

Substituting the variables into Eq. 1 yields an equation for the limiting current density

$$i_L = \frac{ANFD^{(1-n)}v^m c}{L^{(1-m)}\nu^{(m-n)}} \qquad (2)$$

In this equation, N, F, D, c, and ν are determined by the conditions of the Purex process and cannot readily be altered to enhance the rate of electrolysis. However, the characteristic electrode dimension L and (within practical limits) the flow velocity v can be chosen freely. A small characteristic electrode dimension and a high flow velocity increase the current density.

Among the many possible electrode configurations, wire screens were chosen as the best compromise, because they have a small L and a reasonably small viscous drag on the flowing electrolyte. A schematic drawing of a slab-shaped conceptual reduction cell is shown in Fig. I-11. The cell has a cathode of several stacked wire screens, two diaphragms, and two anodes. The flow is directed back and forth through the cathode by baffles. Such a slab-shaped cell may be safe from the standpoint of nuclear criticality if the cell is less than 4 in. thick.

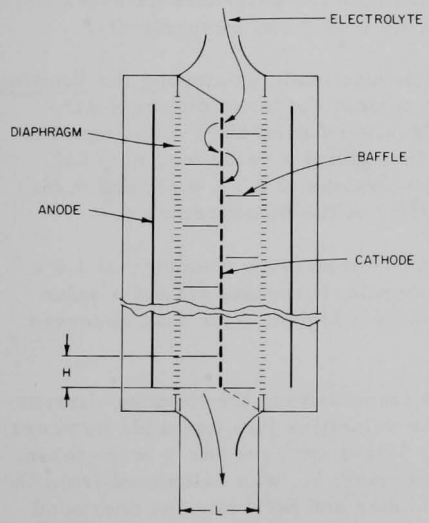

Fig. I-11. Schematic Drawing of Reduction Cell (H = separation of baffles; L = width of channel)

The outlet concentration of a reduced species is given by

$$c_{outlet} = c_{inlet}e^{-\varepsilon t} \qquad (3)$$

where t is the residence time of the electrolyte in the cell and

$$\varepsilon = \frac{AD^{(1-n)}v^m S}{L^{(1-m)}\nu^{(m-n)} V}$$

where S is the total electrode surface area and V is the volume of electrolyte in the cell.

To calculate the outlet concentration from Eq. 3, a knowledge

of the constants, A, m, and n, for wire screen electrodes is required. A value of 1/3 for n has been confirmed in numerous studies. Both A and m depend on the electrode geometry, and m is also somewhat affected by the Reynolds-number range of the system.

In our experimental work to determine A and m, limiting currents and limiting current densities were determined in an apparatus in which flow of electrolyte (at 25°C) over gold electrodes was controlled and measured. The interelectrode potentials were controlled with a potentiostat. Measurements were made at the Reynolds-number range of most interest to us, i.e., $1 < Re < 100$.

Separate tests were made with three gold wire cathodes of different diameters in an electrolyte of 0.01M $K_3Fe(CN)_6$, 0.01M $K_4Fe(CN)_6$, and 0.5M NaOH. This particular electrolyte was chosen because of its favorable electrochemical kinetics and because values for the diffusion coefficient and the viscosity were available from Bazán and Arvia.[15] In these tests, flow velocities were 0.45 to 28.8 cm/sec. These are corrected flow velocities,[16] the corrections being necessary because only a central segment of the electrode was exposed to the electrolyte.

Values of m (the slopes of log-log plots of limiting current density versus flow velocity) were 0.17, 0.19, and 0.24 for gold-wire cathodes having diameters of 1.2×10^{-2}, 2.4×10^{-2}, and 4.8×10^{-2} cm, respectively.

A further check on the value of m was made by plotting the limiting current densities at a constant velocity against the three different wire diameters, again on a log-log scale. Equation 2 predicts a slope equal to -(1-m). The plot indicated a slope of -0.8, giving a value for m of 0.2, which is in good agreement with the above values of 0.17, 0.19, and 0.24. This demonstrates the internal consistency of the measurements.

Limiting current densities for a 60-mesh (wire diameter of 1.8×10^{-2} cm) gold-plated wire screen were similarly measured, and a value of 0.33 was obtained for m. The reason for a higher value than observed with wires is not known.

The constant A was obtained by transforming the limiting current densities into Sherwood numbers and the velocities into Reynolds numbers. Values of 7.2×10^{-6} cm^2/sec for D and 0.0101 cm^2/sec for ν were taken from Bazán and Arvia.[15] The Schmidt number, Sc, was calculated from the same data. By dividing the Reynolds number and $Sc^{1/3}$ into the Sherwood number, the j-factor was computed; j-factors are a simple function of Re of the form

[15] J. C. Bazán and A. J. Arvia, The Diffusion of Ferro- and Ferricyanide Ions in Aqueous Solutions of Sodium Hydroxide, Electrochim. Acta 10, 1025 (1965).

[16] H. Schlicting, Boundary Layer Theory, p. 177, McGraw-Hill, New York (1968).

$$j = ARe^{(m-1)}$$

A plot of log j-factor versus log Re has an intercept of log A at a Reynolds number of 1; in our case, A was 1.3 for the wires and 0.86 for the screen.

Our data for A and m are characteristic of those for cylindrical electrodes at $1 < Re < 100$. No mass-transfer data exist in the literature for low flows and comparable geometries. However, two excellent heat-transfer studies exist for the conditions studied.

Heat transfer can be correlated to mass transfer by the j-factor. When plotted as functions of Reynolds number, the j-factors for heat and mass transfer have often been found to agree very closely. Hilpert[17] did extensive work on heat transfer from cylinders into air flowing transversely and provided data for A and m over the range of $1 < Re < 250{,}000$. Piret et al.[18] measured heat transfer to water for the same geometry in the range of $0.1 < Re < 10$. He reports A = 0.965 and m = 0.28.

Grassmann et al.[19] used a ferricyanide electrolyte and measured limiting currents to obtain mass-transfer data at high Reynolds numbers. Figure I-12 is a plot of log j-factor versus log Re for the data of Hilpert,

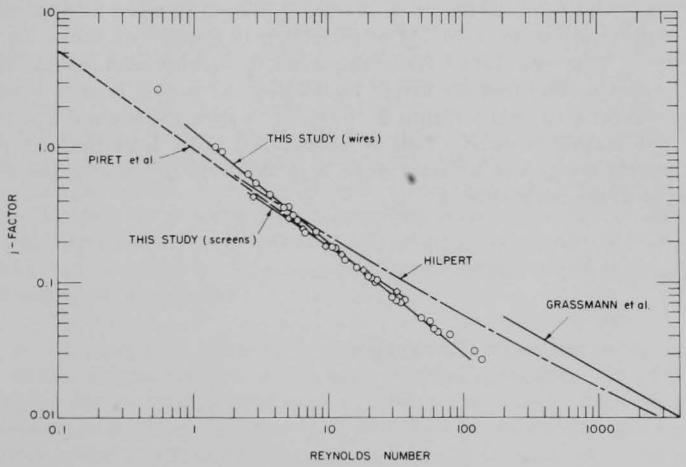

Fig. I-12. Correlation of Heat and Mass Transfer Data. ANL Neg. No. 308-2801.

[17] A. J. Chapman, Heat Transfer, MacMillan, N.Y. (1967).

[18] E. L. Piret, W. James, and M. Stacy, Heat Transmission from Fine Wires to Water, Ind. Eng. Chem. 39, 1098 (1947).

[19] P. Grassmann, N. Ibl, and J. Trüb, Elektrochemische Messung von Stoffübergangszahlen, Chem. Ingen. Technik 33, 529 (1961).

Piret, Grassmann, and the present work. For ease of comparison, the various A's and m's for the range of $4 < Re < 40$ have been tabulated.

	A	m
Hilpert[17]	0.821	0.385
Piret[18]	0.965	0.28
This work, wires	1.3	0.2
This work, screen	0.86	0.33

The correlation of the data for the screen with the heat-transfer data is better than that for the wires; however, there is no physical evidence for regarding one set of data as more accurate than the other.

For the practical purpose of predicting limiting current densities of plutonium in Purex processes by Eq. 2, the best values may be the arithmetic mean of all four determinations. These are $A = 1.0 \pm 0.1$ and $m = 0.30 \pm 0.05$. With these values, Eq. 2 becomes

$$i_L = \frac{1.0\ NFD^{0.66}v^{0.3}\nu^{0.03}c}{L^{0.7}} \tag{5}$$

The limiting current density on a 60-mesh standard wire screen at 2 cm/sec flow and a concentration of 0.1 $\underline{M}$ of $Pu(NO_3)_4$ is computed from Eq. 5 to be 0.057 A/cm^2. The residence time required to reduce plutonium (IV) to 1/2 of its inlet concentration would be 13 sec for a cell with a ratio of electrode surface to cell volume of 9 cm^{-1}. From residence time and flow velocity, the length of such a cell is calculated to be less than 36 cm. Such a cell is small enough to be practical, and the holdup time of the Purex stream appears acceptable.

II. SODIUM TECHNOLOGY

A. On-Line Monitoring of Impurities in Sodium

Argonne National Laboratory (ANL) is coordinating, as well as participating in, a national program for developing, testing, and establishing commercial availability of meters for use in FFTF and in other LMFBR systems. The meters being developed and characterized in this program are monitors for oxygen, carbon, and hydrogen impurities in sodium and a leak detector for steam generators. Meter modules that provide flow and temperature control are also being developed for FFTF.

In general, our program this year has turned from one of planning, design, and development to the actual characterization and proof-testing of devices that will be used on existing and future LMFBRs.

1. Oxygen Meter

The first objective of the oxygen-meter program has been the development of an improved solid electrolyte tube (isostatically pressed thoria-7.5 wt % yttria) for use in an electrochemical oxygen meter having a gas reference electrode. This objective has been substantially realized. The electrolyte-production process was developed at the Hanford Engineering Development Laboratory (HEDL), and 200 electrolyte tubes have been produced by the Zirconium Company of America (Zircoa). The 200 tubes were delivered to HEDL for characterization tests and, subsequently, selected tubes were sent to Westinghouse Research Laboratories (WRL) for incorporation into electrode assemblies. Westinghouse identified and solved a problem in the process for platinizing the tubes to form gas reference electrodes. The completed electrode assemblies were sent to ANL and Westinghouse Advanced Reactors Division (WARD) for installation in meter housings, and the meters are currently being tested in sodium. ANL is coordinating these efforts.

To provide a statistically significant measure of the calibration stability of the oxygen meter, 20 meters are being tested: 10 at ANL and 10 at WARD. Initial calibration curves at oxygen levels from <1 to 15 ppm will be determined for all meters at 370°C by the vanadium-wire equilibration method, which measures the oxygen activity in sodium. These calibrations will be repeated after three months of continuous operation at 370°C to determine calibration stability. The temperature coefficients of the meters will be measured at intervals during this period. Testing will continue for about a year, under conditions determined by results obtained during the first three months.

For the ANL tests, the ten meters are connected in series with a cold trap and a laboratory prototype carbon meter-equilibration (C-E) module in a system called the Oxygen Meter Rig (OMR). A piping diagram of the OMR is shown in Fig. II-1. In the OMR, the C-E module, which can

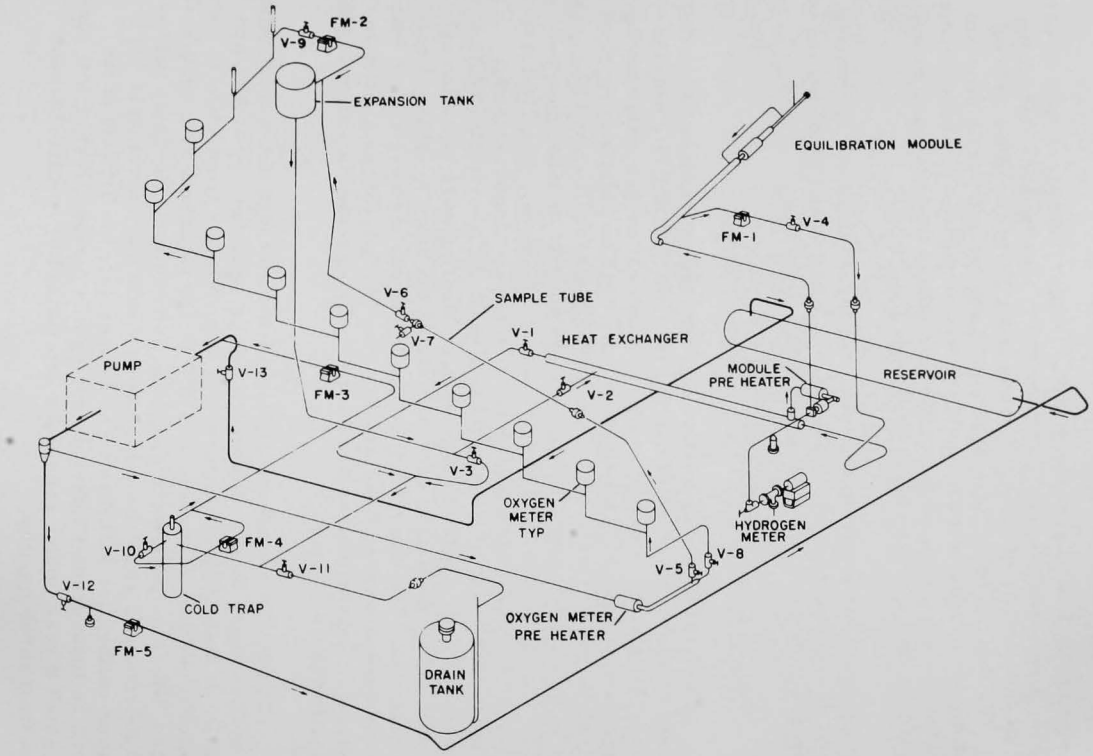

Fig. II-1. Piping Diagram of Oxygen Meter Rig (OMR)

be used either as a carbon-meter module or for equilibrating vanadium-metal specimens (the latter to be used for the calibration of oxygen meters).

The OMR was started up in October 1971. The sodium system at WARD was made operational at about the same time. After a break-in period to allow the meter voltages to stabilize, tests of calibration stability were begun. All 20 oxygen meters being tested on the two systems are operating satisfactorily.

2. Hydrogen Meter

The objective of this program is the development of an on-line meter for measuring the hydrogen activity in the primary and secondary sodium of LMFBR systems. The meter that has been developed at ANL operates on the principle of diffusion of hydrogen through a nickel membrane. A description of the meter was given in the preceding report in this series (ANL-7750, pp. 44-47).

The hydrogen meter can be operated in two modes. The first is a static mode, in which the equilibrium hydrogen pressure above the sodium is measured directly and related to hydrogen concentration in the sodium by Sieverts' law; the second is a dynamic mode, in which the hydrogen flux through the membrane is monitored by an ion pump.

Two series of experiments have been conducted in the Sodium Analytical Loop (SAL) to determine the Sieverts' law constant for the hydrogen-sodium system. Sieverts' law is expressed by the relation

$$S = KP^{1/2} \tag{1}$$

where

S = concentration of hydrogen in sodium, ppm

K = a constant, ppm $Torr^{-1/2}$ or ppm $cm^{-1/2}$

P = hydrogen pressure, Torr or cm

Our measurements of the constant, K, were conducted as follows. The sodium system was first cold trapped at about 100-120°C, and the equilibrium pressure above the sodium was measured. The cold trap was then isolated from the system by valving, and the hydrogen level of the sodium was increased stepwise by a series of hydrogen injections through a nickel membrane. The equilibrium pressure of hydrogen above the sodium before and after each injection was measured with the hydrogen-activity meter, which was operated at 450°C. After an addition of hydrogen, pressure measurements were continued until an equilibrium value was reached, i.e., until no further change in pressure occurred. In each case, equilibrium was attained within 10 min.

The amount of hydrogen added during each injection was obtained from standard pressure-volume gas measurements. The volume of the vessel used to add the hydrogen was accurately known, and the vessel was charged to a known hydrogen pressure, as measured by a calibrated pressure gauge. These values were corrected for losses resulting from (1) hydrogen solubility in the stainless steel of the loop and (2) permeation of hydrogen through various stainless steel and nickel components of other hydrogen meters operating in the dynamic mode on the loop.

Hydrogen losses to the cover-gas region above the sodium were assumed to be small, since the major portion of the cover-gas region was at 250°C, a temperature at which solid sodium hydride would not form at the equilibrium pressures studied.

The Sieverts' law constant, K in Eq. 1, was calculated after each hydrogen addition from values of the hydrogen pressure before and after the addition and from the amount of hydrogen added. The experimental data and the calculated values for the Sieverts' law constant are given in Table II-1. The total hydrogen concentration in the sodium in these experiments ranged from 0.006 to 0.8 ppm.

TABLE II-1. Determination of the Sieverts' Law Constant for the Hydrogen-Sodium System (temperature, 450°C)

Hydrogen Addition to Sodium, ppm	Equilibrium Hydrogen Pressure, Torr		Calculated Sieverts' Law Constant	
	Before Addition	After Addition	ppm $Torr^{-1/2}$	ppm $cm^{-1/2}$
0.1194[a]	1.0×10^{-4}	9.0×10^{-4}	6.0	19.0
0.1051	9.0×10^{-4}	2.4×10^{-3}	5.5	17.5
0.1094	2.4×10^{-3}	4.5×10^{-3}	6.0	19.1
0.1945	4.5×10^{-3}	1.0×10^{-2}	5.9	18.7
0.2019	1.0×10^{-2}	1.8×10^{-2}	5.8	18.5
0.1164[b]	1.2×10^{-6}	4.7×10^{-4}	6.3	19.9
0.1150	4.7×10^{-4}	1.6×10^{-3}	6.2	19.6
0.2103	1.6×10^{-3}	6.1×10^{-3}	5.8	18.4
			5.9 ± 0.8 (2σ)	18.7 ± 2.5 (2σ)

[a]First sequence of hydrogen additions.
[b]Second sequence of hydrogen additions.

The results of these studies indicate a value for the Sieverts' law constant of 18.7 ± 2.5 (2σ) ppm $cm^{-1/2}$ or 5.9 ± 0.8 (2σ) ppm $Torr^{-1/2}$ at 450°C. This may be compared with the values reported by Meacham et al.,[1] which varied from 4.7 to 17.7 ppm $cm^{-1/2}$, and that obtained by McClure and Halsey,[2] approximately 22 ppm $cm^{-1/2}$. We believe that the Sieverts' law constant obtained in the present work is the best value currently available.

[1]S. A. Meacham, E. F. Hill, and A. A. Gordus, The Solubility of Hydrogen in Sodium, USAEC report APDA-241, Atomic Power Development Associates (1970).

[2]D. W. McClure and G. D. Halsey, Jr., The Solubility of Hydrogen in Liquid Sodium, J. Chem. Phys. 69, 3542 (1965).

3. Carbon Meters

The long-range objective of this work is a commercially available on-line carbon meter that will indicate the probability of significant carbon transfer taking place in R & D and LMFBR systems. The more immediate objectives are the testing, calibration, and improvement of the United Nuclear Corporation (UNC) carbon meter, whose operation depends on the diffusion of carbon through an iron membrane. The meter will be incorporated into a module containing the necessary flow- and temperature-control devices for use on FFTF.

The UNC meter has been operated on a pumped-sodium system, the Test and Evaluation Apparatus (TEA) to determine its responses to system variables. The tests included separately increasing the cold-trap temperature, the loop temperature, and the primary sodium flow rate. Only transient increases in the carbon flux, some of these as large as 1000%, were obtained in all three instances.

These observations suggested that carbon or carbon-containing particulates are detached from the walls of the system by some disturbance and are released into the sodium and carried past the carbon meters. This hypothesis was supported by the results of two experiments. In the first, the system was disturbed by rapping the piping; in the second, the primary sodium flow rate was abruptly changed from 1 gpm (the normal flow rate) to 3 gpm. In both tests, the carbon flux increased rapidly after ~5 min (the time required for diffusion of carbon through the probe membrane).

Although it is generally agreed that carbon-containing particulates are present in sodium systems, their importance in carbon transfer is not fully understood. Nevertheless, it seems reasonable to assume that these particulates play some role in the transport of carbon.[3] Tests of the carbon meter on TEA have been temporarily deferred to implement meter-calibration studies (see below); however, further examination of the effects of carbon-containing particulates on meter response is needed.

Experiments are now under way to develop a method for calibrating the UNC meter by correlating flux readings with the carbon activity in sodium. With a standard calibration method, results obtained at various sites will be directly comparable. A direct method of activity measurement would provide intermittent on-line calibration capabilities for the continuously operating carbon meter; it could also supplement, and possibly replace, the traditional methods of analysis for carbon.

The method chosen to measure the activity of carbon in sodium, which is similar to that being used to measure the oxygen activity in

---

[3]R. Roy and G. P. Wolzadlo, Nucl. Technol. 10, 307 (1971).

sodium,[4] is based on the equilibrium distribution of carbon between a metal specimen and sodium. At equilibrium, the carbon activities in the metal and in the sodium are equal. From carbon analysis of the metal specimen and from the established relationship between carbon concentration and carbon activity in the specimen material, the carbon activity of the metal and consequently that of sodium can be derived.

Initial calibration experiments have been conducted in stirred vessels rather than a pumped-sodium loop, because of the difficulties in controlling the carbon concentration in a loop system. In the calibration experiments, two types of vessels were used: one was made of Type 304 stainless steel and the other of Croloy. The container fixes the activity of carbon in sodium, Type 304 stainless steel yielding a relatively low carbon activity and Croloy a high activity. Nickel and Fe-8 wt % Ni alloy in the form of 2-mil foils were chosen as metal specimens for equilibration.

Each vessel, equipped with a UNC carbon meter, was charged with about 700 g of reactor-grade sodium, heated to 750°C, and, after a constant carbon flux was obtained (usually overnight), a specimen holder (fabricated from the same materials as the containment vessel) with the foils attached was inserted into the liquid sodium. The foils were exposed to the sodium for ~65 hr. (This was, in general, ~10 times longer than the time to equilibrium calculated from diffusion theory.) The conditions of the experiments, carbon-meter flux readings, and carbon content of the foils after equilibration are given in Table II-2.

TABLE II-2. Initial Calibration of UNC Carbon-Meter Flux with Nickel and Fe-8 wt % Nickel Foils at 750°C

Sodium Container	Flux, $\mu g/(cm^2)(min)$	Final Carbon Concentration, ppm		Carbon Activity	
		Nickel	Fe-8 wt % Ni	Nickel	Fe-8 wt % Ni
Croloy	0.234	72	656	7×10^{-2}	1×10^{-1}
304 SS	0.003	27	47	3×10^{-2}	1×10^{-2}

The data show that both the carbon flux and the carbon content in the foils were higher with the Croloy vessel than with the Type 304 stainless steel vessel. In each experiment, the uptake of carbon was greater for the Fe-8 wt % Ni foils than for the nickel foil; thus, Fe-8 wt % Ni is a more sensitive indicator of carbon activity than nickel. The activities of carbon in the nickel and Fe-8 wt % Ni foils were calculated from their carbon contents and from the terminal solubilities of carbon in these materials. These activities also represent the activity of carbon in the sodium, since at equilibrium the activities of carbon in the foils and in sodium are equal. The results of these calculations are also included in Table II-2. The carbon activities derived from the data for nickel and Fe-8 wt % Ni are in fairly good agreement, but those derived from the Fe-8 wt % Ni foils are believed to be more accurate because of the higher carbon content. It

[4] D. L. Smith, An Equilibration Method for Measuring Low-Oxygen Activities in Liquid Sodium, Nucl. Technol. 11, 115 (May 1971).

should be noted that the carbon activities of the sodium/Type 304 stainless steel and sodium/Croloy system derived from the carbon contents of the Fe-8 wt % Ni foils differ by an order of magnitude, in agreement with the calculations of Natesan and Kassner.[5] Additional work is under way to examine other metals and alloys and to select the most suitable material for this application. However, these initial experiments indicate that the carbon-meter flux is a sensitive monitor of the carbon activity in sodium and that the equilibration method shows promise as a means of calibrating the carbon meter.

4. Meter Modules for FFTF

The objective of this work is to design, proof-test, and establish commercial availability for on-line meter modules to be installed at FFTF. These modules include meters for monitoring impurities and controls for flow and temperature which are required for proper meter operation. Two types of modules are being designed and tested: (1) an oxygen-hydrogen meter module, containing two oxygen meters and a hydrogen meter, and (2) a carbon meter-equilibration module, which houses either a carbon meter or a device for equilibrating metal specimens for meter-calibration purposes. The designs of these modules were described in the preceding report in this series (ANL-7750, pp. 41-42). Proof-testing is being carried out on laboratory sodium systems and on the Radioactive Sodium Chemistry Loop (RSCL) at EBR-II.

a. Oxygen-Hydrogen Meter Module

Two oxygen-hydrogen meter (O-H) modules have been built: one is being tested at ANL in the Test and Evaluation Apparatus (TEA); the other is being tested in radioactive sodium at EBR-II.

The module on TEA has been tested at sensor temperatures of 700, 800, and 900°F with an inlet sodium temperature of 700°F. The sodium in TEA has been cold-trapped at oxygen levels in the range of 0.5 to 10 ppm and hydrogen levels in the range of 0.025 to 1.0 ppm.

The two oxygen meters in the module had accumulated total operating times of 4920 and 4392 hr by December 1, 1971.

Periodic temperature-coefficient tests have been conducted to determine whether any changes had occurred in the behavior of the electrolyte tubes. Westinghouse has found that a progressive drop in the temperature coefficient from normal levels (±0.15 mV) to a large negative level (-1 mV/°F) indicates a progressive deterioration of the cell as a

[5] K. Natesan and T. F. Kassner, J. Nucl. Mater. 37(2), 223 (1970).

result of sodium corrosion.[6] The temperature coefficients of both meters at ~800°F have tended to drift toward more negative values; however, the changes are slight and are not expected to cause any difficulties.

In a series of calibration runs made at meter temperatures of 800°F and at several concentrations of oxygen in sodium, emfs of the meters were correlated with the oxygen concentration as determined by the vanadium-wire equilibration method.[4] Plots of emf versus oxygen concentration have slightly different slopes and are displaced somewhat from the theoretical values. For research and development studies, it is desirable to obtain equilibrations at two and preferably three concentrations to determine the slope accurately. However, in reactor systems, where large changes in oxygen concentration are not expected, a single equilibration of wires should suffice for meter calibration. Because of a decision to operate the O-H module at EBR-II at a meter temperature of 700°F, equilibration tests are also being made at this temperature to permit comparison of the data from TEA with data from EBR-II.

The hydrogen meter in the O-H module on TEA is being operated in the equilibrium mode to test its responses to changes in hydrogen concentration at various meter temperatures. Data for the hydrogen meter at three meter temperatures (700, 800, 900°F) and three hydrogen levels (0.55, 0.26, 0.14 ppm) indicate that the time to equilibrium is a function of sodium temperature at the meter and also, to a degree, the hydrogen concentration in the sodium.

Successful operation at elevated hydrogen levels was indicated by these experiments. Attempts will now be made to operate at low levels of hydrogen (<0.1 ppm) and at a temperature of 700°F; under these conditions, meter response for this unit has thus far been marginal.

The installation of the O-H module in Cell B of the RSCL has been completed. Checkouts of the module, the subsystem for Cell B, and the console for Cell B were accomplished after some modifications of heaters and power supplies for the solid-state alarm circuits. After these checkouts, the module was filled with sodium from RSCL and flow was initiated; operation at 700°F was attained on September 30, 1971. The O-H module was operated for 435 hr prior to a scheduled shutdown of the module. After 413 hr of successful operation, one of the oxygen meters failed; the other was operating properly at the time the module was shut down.

The main purpose of this first operation of oxygen meters on EBR-II was to determine whether radiation (primarily from ^{24}Na) had any effect on oxygen-meter performance. A comparison of oxygen-meter voltages during normal reactor operation and during a period of ^{24}Na decay after a planned reactor shutdown showed no significant differences in meter

[6] Instruction Manual, Westinghouse Liquid Metal Oxygen Meter, Model LM-II, WNICD-OM001 (December 1970)

operation. Similar, stable voltages were measured during shorter periods (several hours) of reactor shutdown and restartup. It is, therefore, tentatively concluded that direct radiation from ^{24}Na levels as high as 1400 μCi/g of sodium does not affect the oxygen-meter voltages.

The oxygen meter that failed had produced stable voltages during its 413 hr of operation. No transients were observed in the system variables that would unequivocally explain the failure; however, the meters did experience eight temperature decreases of >50°F, which were mainly caused by automated safety shutdowns of the RSCL and, hence, of the O-H module. These resulted in heater shutdown and a temperature decrease at the meters. It is possible, but unlikely, that these temperature decreases contributed to the short life of the failed meter. To avoid this possibility, steps are being taken to maintain the meters at a suitable temperature when the RSCL shuts down and also to lessen the frequency of automatic safety shutdowns on the RSCL.

The failed oxygen-meter electrode was replaced prior to restartup of the O-H module on December 1, 1971. The C-E module on the RSCL was also started up at that time, enabling oxygen-meter calibrations to be performed.

The hydrogen meter in the O-H module was operated only in the dynamic mode. The meter operation was stable except for a general drift from an initial reading of about 20 μA at 700°F to a stable value of 2-3 μA at 700°F after eight days of operation. The drift has been attributed to a general cleanup of hydrogen from the RSCL and module piping by the flowing sodium. No attempt was made to operate the meter in the equilibrium mode since the dynamic measurements indicated that the hydrogen content of the sodium was very low, possibly below 0.1 ppm. At these low levels of hydrogen, improved vacuum valves were needed. The original valves, which had polyimide seats and seals, were replaced with all-metal vacuum valves before the module was restarted. The all-metal valves will provide a lower background (less degassing) and, therefore, will make equilibrium measurements more feasible at the low concentrations of hydrogen in EBR-II sodium.

b. Carbon Meter-Equilibration Module

Two carbon meter-equilibration (C-E) modules have also been built: one is being tested at ANL on the Oxygen Meter Rig (OMR); the other will be tested at EBR-II in Cell C of the RSCL. Both will be used initially for calibrating oxygen meters by the equilibration of vanadium wires.

In initial tests of the C-E module on the OMR, the capabilities of the unit in meeting the temperature-control and flow requirements for FFTF were determined. In this module, the flow is controlled by a

manual throttling valve (to be automated for use at FFTF) and the incoming stream is heated by a regenerative heat exchanger and a high-intensity line heater. The module was designed to heat an incoming sodium stream with a flow rate of at least 0.1 gpm from 400 to 1382°F (750°C)[7] and to discharge the sodium at a temperature no more than 50°F above the inlet temperature. In the tests, the sodium inlet temperature was varied from 400 to 920°F and the maximum flow rate attainable with an inlet-to-outlet temperature rise of 50°F was measured. The results, plotted in Fig. II-2, show that the module meets the heat-transfer performance requirements.

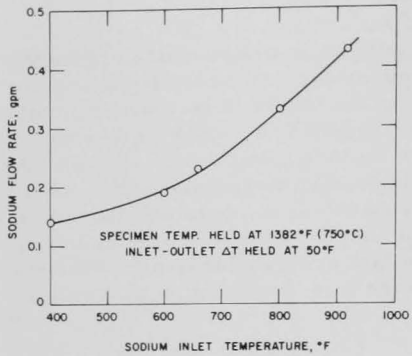

Fig. II-2. Sodium Flow Rate vs. Inlet Temperature for C-E Module [specimen temperature, 1382°F (750°C); inlet-outlet temperature differential, 50°F]

Another requirement for the module is that the vanadium wires be cooled quickly at the end of the equilibration period to avoid significant pick-up of additional oxygen by the wires during cooling. (The equilibrium oxygen content of the wires increases as the sodium temperature decreases.) Specimen cooling curves obtained by two different methods are shown in Fig. II-3. The cooling rate shown in the lower curve, obtained by simply turning off the module heaters and cooling the wires in the sodium stream, exceeds the rate suggested[4] as being adequate for cooling vanadium wires in sodium (the suggested cooling rate is shown in the figure as a dashed line). The cooling rate shown in the upper curve was obtained by stopping sodium flow through the module and displacing the sodium with argon. Although the latter cooling rate is lower than that obtained with flowing sodium, the method is equally satisfactory because oxygen transfer through the gas is negligible.

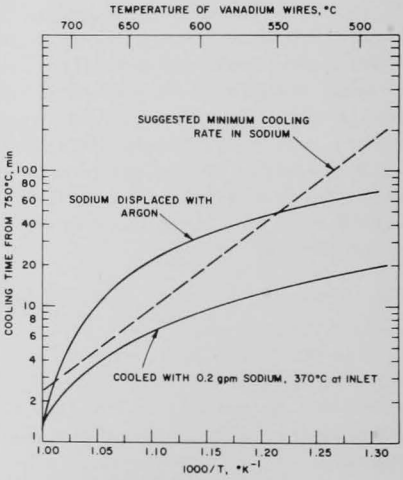

Fig. II-3. Cooling Rates of Vanadium Specimens in C-E Module

Checkouts of the C-E module and console for the RSCL were completed at ANL-Illinois, and the units and all components for Cell C

[7]Vanadium wires are equilibrated with the sodium for at least 4 hr at this temperature to determine oxygen activity.

were shipped to EBR-II. Installation was completed and the module was started up early in December 1971.

The proposed use of specimen-equilibration devices and modules on reactor systems has pointed up the need for a low cost equilibration device for other smaller sodium systems. Such a device is now being designed. It is expected that this apparatus can be adapted to fit existing equipment and provide for specimen equilibration with a minimum of expense.

c. Module Designs for FFTF

The O-H and C-E modules installed at EBR-II were originally designed to meet the performance and space requirements of FFTF; however, changes made by HEDL, principally, the addition of remote valve operators and changes in the module pipe size and inlet and outlet locations, have necessitated changes in the designs of these units. These changes have been completed and HEDL is now fabricating O-H and C-E modules according to the most recent designs for use in their test loops.

5. Detectors for Leaks in Steam Generators

A hydrogen meter has been developed for detecting leaks in sodium-heated steam generators. The leak-detector operation depends on diffusion of hydrogen from sodium through a nickel membrane into a dynamic vacuum system. Changes in the hydrogen level in the sodium are detected by changes in current in the ion pump that maintains the vacuum. The first steam-generator leak detector was built by ANL for use on the Sodium Components Test Installation (SCTI) at the Liquid Metal Engineering Center (LMEC).

A steam-generator leak detector has also been designed for installation on EBR-II and as a prototype for use on future LMFBRs. Design of various components is shown schematically in Fig. II-4. The overall

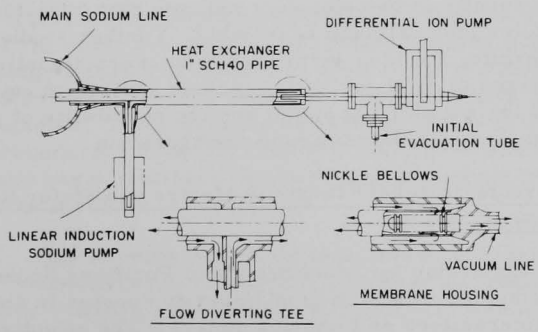

Fig. II-4. Hydrogen-Meter Leak Detector for Steam Generators

length of the unit is approximately 3.5 ft. It can be installed in a single penetration either on the steam-generator exit line or, with appropriate design changes, directly in the steam-generator module. Sodium enters the annulus and flows to the flow-diverting tee where it is diverted into the side leg in which the linear induction pump is located. Sodium entering the side leg is pumped down the annulus, up the center tube, and back to the tee. Flow continues through the heat-exchanger annulus, past the nickel membrane, and returns to the main sodium stream through the center tube of the heat exchanger.

The first model of this type of leak detector has been installed and tested on the Sodium Analytical Loop (SAL). The total test time was 1040 hr. During the tests, the hydrogen concentration in SAL was varied from 0.03 to 0.32 ppm, the range expected in a well cold-trapped system. The response of the leak detector over this range of concentrations has been very close to the predicted response.

A miniaturized hydrogen-meter leak detector has also been designed, constructed, and tested on SAL. The principle of operation of this device is the same as that of the larger version; however, in the miniaturized device, the ion-pump size was reduced from 11 liters/sec to 1 liter/sec, the surface area of the nickel membrane probe was reduced from 20 cm^2 to about 5 cm^2 and the shape of the membrane was changed from bellows-shaped to hemispherical for operation at high pressure.

Short-term tests in SAL of the miniaturized unit, with the nickel membrane operated at 450°C, indicated that the device operates satisfactorily. When the unit was operated on a sodium system containing approximately 0.8 ppm hydrogen, the ion-pump current generated was in good agreement (±30%) with that predicted from hydrogen-permeation calculations for the system. The stability of the ion-pump current for this system had a standard deviation of 0.016%, which is slightly better than that achieved with 11 liters/sec pumps.

The results of these studies indicate that miniaturization of the hydrogen-meter leak detector is feasible. Further studies are needed, however, to determine the long-term operating characteristics of this system. Advantages of miniaturization include savings in equipment costs, good stability of the smaller ion pump, and the possibility of providing a stronger and simpler nickel-membrane configuration.

6. Characterization of Impurity Meters and Meter Response to Impurity Species

The Apparatus for Monitoring and Purifying Sodium (AMPS) will be used to study the interaction of impurity species in sodium and the effects of such interactions on impurity meters. The effectiveness of cold traps for hydrogen removal will be studied to gain insight into the use of

cold traps for tritium removal and retention. Interaction of impurities with the stainless steel surfaces of the loop will be studied, as well as possible impurity sources in large sodium systems.

The design of AMPS has been completed except for a few minor details, and emphasis has shifted to the construction-and-assembly phase of the project. Major components now being fabricated include the cold traps, the hydrogen trap, the piping spool pieces, an O-H meter module, and a C-E module. Completed components include the main pressure vessels and component supports and stands.

B. Analytical Standards Program

Argonne National Laboratory has been given the responsibility of certifying sampling and analytical procedures for use throughout the national sodium technology program. The long-term objective of this program is a set of sampling and analytical methods which, when combined with corrosion and purification data, will constitute the basis for a final set of purity specifications for the operation of reactor and large nonreactor sodium systems. To achieve this objective, ANL has established an Analytical Standards Laboratory to handle the administrative and laboratory aspects of this program. The administrative aspects involve (1) coordination of contractor activities in the Analytical Standards Program and (2) generation of all RDT standards concerning sodium sampling, analysis and purity. The laboratory aspects involve (1) participation in the testing of interim sampling and analytical methods to satisfy the near-term needs of EBR-II, FFTF, and contractor laboratories and (2) the development of standard methods that fully satisfy the long-range needs of the sodium technology effort.

1. Administrative Activities

a. National Standards Working Group

Successful implementation of the analytical standards program requires the close cooperation of all laboratories participating in the sodium technology effort. Accordingly, ANL organized an advisory group (the National Standards Working Group) to represent both reactor and nonreactor laboratories. ANL, with the assistance of this group, has prepared a manual of procedures[8] to be used for the analysis of sodium and cover-gas systems and has established mechanisms for sample interchange programs to test the methods.

Participants in the first sample interchange, which was termed a "pilot study," were ANL-Illinois, EBR-II, the Hanford Engineering Development Laboratory (HEDL), and the Liquid Metal Engineering Center (LMEC).

[8] Interim Methods for the Analysis of Sodium and Cover Gas, ANL/ST-6 (January 1971).

Samples of EBR-II sodium, which were provided by EBR-II personnel, were analyzed for oxygen, carbon, hydrogen, and trace metals.

Results of the pilot study were evaluated using the criteria of "familiarity" and "intercomparability" generated by ANL. Familiarity with a given method was considered satisfactory when the precision within a laboratory was found to be equal to or less than 1.5 times the precision stated in ANL/ST-6. Intercomparability of the results was considered acceptable when the mean value of the participating laboratory agreed, within the calculated precisions, with the mean value obtained by a control laboratory. The pilot study evaluation indicated intercomparability of results of hydrogen, carbon, and oxygen analyses for all participating laboratories; however, familiarity by all participating laboratories was found only for the oxygen method, which indicated that experience with the hydrogen and carbon methods was insufficient. The evaluation also indicated a problem with the trace-metal analysis. The results reported for 15 trace metals by the four participating laboratories were only irregularly comparable. The cause of this irregularity is now being sought. The Working Group is now considering changes in procedural details of some of the methods, as well as additions of new methods to the manual.

b. RDT Standards for Sodium Sampling, Analysis, and Purity

ANL has the responsibility for generating all RDT standards related to purity specifications for sodium and gases used in reactors or other sodium systems. These documents will specify the impurity levels that are acceptable for the purchase of sodium and cover gas and for the operation of sodium and cover-gas systems. They will also specify the sampling and analytical methods to be used to monitor all impurities and to demonstrate that certain impurities (for which methods of control exist) are at or below the acceptable levels.

Preliminary specifications were generated and published in an informal document (ANL/ST-5) entitled "Interim Purity Specifications for Large Operating Sodium Systems." This document contains specifications for (a) purity of purchased sodium, (b) measurement and control of the level of selected impurities in sodium, (c) measurement of the level of other impurities in sodium, (d) measurement of the levels of impurities in cover gas, and (e) frequency of analysis of sodium and cover gas. These preliminary specifications, along with the procedures specified in ANL/ST-6, will be used as a basis for generating and/or revising the RDT standards discussed below.

Sodium Purchase Specifications. An amended version of RDT-M13-1T "Reactor Grade Sodium--Purchase Specifications," was distributed in 1971. The contents of this standard were discussed with and are acceptable to all three potential suppliers[9] of reactor-grade sodium.

[9] E. I. duPont de Nemours & Co., U.S.I. Chemicals, and Ethyl Corp.

This document now contains (1) overall requirements for sodium purity, (2) maximum impurity levels for elements detrimental to sodium and reactor systems, (3) detailed sampling instructions, and (4) appropriate references to analytical procedures in ANL/ST-6.

Reviews of the amended version of RDT M13-1T by potential users and RDT revealed that (1) a more stringent specification for uranium in sodium was desirable and (2) a reevaluation of the sampling and analysis requirements with respect to cost was appropriate. ANL has established by analysis of several sources of sodium that sodium usually contains <0.01 ppm uranium and has agreed to lower this specification from 1 to 0.01 ppm. A cost analysis of several sampling and analytical schemes made by ANL, and the findings of the cost analysis have been submitted to RDT for review.

Cover-Gas Specifications. ANL has completed a draft of RDT M14-1, entitled "Sodium Cover Gas--Purchase Specifications." This document specifies acceptable impurity levels in argon, helium, and nitrogen when they are used as cover gases for sodium.

Included in these specifications are the acceptable levels of xenon, krypton, and neon. These potential impurities in argon are of particular interest to HEDL, because isotopic mixtures of each of these gases may eventually be used as tags to identify subassemblies containing faulty fuel pins in FFTF. It is important, therefore, that the background from natural isotopic mixtures of these gases be kept low (below the parts-per-million level) so that the tags will be identifiable.

Purity Specifications for Operating Sodium Systems. Some of the specifications of ANL/ST-5 have been incorporated into a draft of RDT A1-5, "Purity Specifications for Operating Sodium Systems." This draft contains specifications for both large and small loops throughout the sodium technology program, and prescribes separate sampling and analysis schedules for systems operating with and without on-line impurity monitors.

Interim Methods for the Analysis of Sodium and Cover Gas. The document ANL/ST-6 entitled "Interim Methods for the Analysis of Sodium and Cover Gas" is in the process of being converted into an RDT standard, RDT F3-40.

2. Laboratory Activities

The Analytical Standards Program's laboratory efforts have been directed toward investigations in the following areas: (1) establishing a metal-specimen equilibration technique as an analytical method for determining carbon activity in sodium, (2) applying the uranium-getter technique[10]

[10] H. S. Isaacs, J. Nucl. Mater. 36, 322 (1970).

to the determination of oxygen in circulating sodium systems, (3) developing a gas-chromatographic separation of ^{23}Ne from xenon and krypton isotopes for analysis of reactor cover gas, (4) establishing the effect of sample line length on the concentration of trace impurities in sodium, (5) developing a method for the collection and analysis of particulates in sodium, and (6) decreasing the analysis time of the vanadium-wire equilibration method for oxygen in sodium by employing a commercial oxygen analyzer. The first two investigations are in preliminary stages of evaluation, and the third is described elsewhere in this report (Section II.D). The work on effects of line length, particulate analysis, and determining oxygen in vanadium is described below.

a. Effects of Line Length on Sample Validity

One of the ANL lead assignments related to FFTF needs is the determination of the effects of the length of a sampling line on sample validity. Of principal interest are the effects on the determination of (1) nonmetallic impurities, mainly oxygen, hydrogen, and carbon, (2) metals and halides, and (3) radioactive species.

The effect of line length on the oxygen content of sodium has been investigated in a flowing sodium system at 350, 450 and 565°C. The equipment consisted of a main loop of ~15-gal capacity and a smaller bypass loop of ~1-gal capacity. The two loops were interconnected so that they could be operated independently or in series. The smaller loop consisted of 100 ft of 5/8-in.-OD (9/16-in.-ID) Type 304 stainless steel tubing with an electrochemical oxygen meter located at each end of the 100-ft section. Before the line-length experiments were performed, these meters were calibrated against each other by changing the cold-trap temperature and recording the equilibrium meter readings. The experiments were performed by operating the two systems independently at different oxygen levels and then quickly (in ~2 sec) interconnecting the systems in series by means of a valving sequence. The emf response of the oxygen meters was then recorded as a function of time.

The experiments at each temperature were conducted at two different sodium flow rates (2.5 and 5 gpm) and with the initial oxygen concentration in the main loop both higher and lower than in the bypass loop (all oxygen levels were between 1 and 10 ppm). In each experiment, the response of the inlet meter was rapid and the response time of the outlet meter corresponded closely to the time calculated for the passage of sodium through the 100 ft of tubing at the known flow rate. The changes in oxygen-meter readings were the same for both cells, within experimental error. From these data, it is concluded that at these temperatures, flow rates, and oxygen levels, no significant loss in accuracy is incurred by the use of a sample-line length of 100 ft and that the oxygen-meter response to a change in oxygen level is limited only by the time required for the sodium to move through the line.

In the experiments at 450 and 565°C, hydrogen meters are also installed in the small loop to study the effect of line length on hydrogen concentration. The data indicate that, for hydrogen concentrations between 0.1 and 10 ppm, line length has no effect on hydrogen concentration at these temperatures and flow rates.

b. Particulate Analysis

As a part of the Analytical Standards Program, ANL will specify a method of particulate analysis for use in sodium technology programs. Most of the aspects of such a procedure have been reasonably well established; however, the recovery of the particulates unchanged from a filter device is an unsettled procedural problem.

Particulate recovery by the common practice of using a polar solvent such as alcohol or water to remove residual sodium could alter the form or composition of particulates; therefore, other methods, namely, distillation, dissolution in mercury, and dissolution in liquid ammonia, were investigated. Dissolution of residual sodium in mercury presented problems in the subsequent filtration and complete removal of mercury. Dissolution in liquid ammonia resulted in the formation of considerable quantities of sodium amide. Distillation, on the other hand, provided an effective separation of excess sodium from the filter. Effort is now being directed toward devising a method of rapidly and reproducibly separating the particulate from the filter following distillation of the sodium. At present, a procedure involving ultrasonic removal of the particulate is under investigation.

Filter assemblies have been designed for EBR-II, for the Core Components Test Loop (an ANL facility being used to test FFTF subassemblies), and for smaller loops in the ANL sodium technology effort. The EBR-II assembly was installed and operated on EBR-II for ~2 days, during which time more than 1000 gal of sodium was filtered. This EBR-II test indicated that minor design changes were desirable to improve the operation of the filter.

The filter from the EBR-II assembly is presently being used to investigate ultrasonic removal of particles, particularly radioactive species, from the filter.

c. The Vanadium-Wire Equilibration Method for Determining Oxygen Activity in Sodium

In the vanadium-wire equilibration method,[11] a vanadium wire is exposed to sodium until equilibration of oxygen between the wire and sodium has been attained. The oxygen activity in the sodium is then obtained

[11] D. L. Smith, Nucl. Technol. 11(1), 115-119 (1971).

from the oxygen content of the vanadium and from data on the distribution coefficient of oxygen between vanadium and sodium.

During the development of the vanadium-wire method, the oxygen content of the wires, after equilibration in sodium, was determined by an inert-gas fusion method that employs a platinum bath.[12] Recently, a LECO RO-16 Oxygen Determinator was purchased and set up to perform the inert-gas fusion analysis. This instrument decreases the analysis time by a factor of four.

In the procedure used with the LECO instrument, the metal is first fused in a graphite crucible at a temperature in excess of 2500°C. Nitrogen carrier gas sweeps the released oxygen (as CO), nitrogen, and hydrogen from the furnace through an Ascarite trap and over hot copper oxide. Hydrogen is oxidized to water and absorbed in anhydrone while the carbon monoxide is oxidized to CO_2 and measured by a thermal-conductivity cell. The output of this detector is integrated and displayed on an electronic digital voltmeter.

Initial tests with the new instrument revealed that the vanadium-wire samples did not completely fuse; however, the addition of ~0.5 g of high-purity iron chips provided complete fusion of the wires. The graphite crucible and iron are outgassed near the operating temperature prior to adding the sample. The sample is then added without exposure of the crucible and its contents to the atmosphere and fused during a second "burn" in the same crucible.

Results of analyses of samples of vanadium wires using the LECO instrument were compared with results from duplicate samples previously analyzed by the manual inert-gas fusion technique. This comparison showed that the LECO analyzer gives values that are within 2% of those obtained by the established manual method.

A study of the precision of the LECO method was also made by examining the results of 51 determinations on 20 different vanadium samples. The average difference between duplicates was 2.7%. The range between the high and low results on the triplicates averaged 2.9%, and the range of the quadruplicates was 3.2%. The triplicate sets of data yielded an average relative standard deviation of 3.9%. These tests indicate that both the precision and accuracy obtained with the LECO instrument are adequate for determining the oxygen content of the vanadium wires.

C. Sodium Chemistry

The program on the chemistry of liquid sodium is directed toward understanding the behavior of impurities in sodium pertinent to

[12] B. D. Holt and H. T. Goodspeed, Anal. Chem. 35, 1510 (1963).

(a) the development and evaluation of analytical methods, (b) the interpretation of oxygen- and hydrogen-meter readings, and (c) the purification of cover gas. In this connection, recent effort has been devoted to (1) elucidating the phase relations in the sodium-rich corner of the Na-Na_2O-NaOH-NaH system, (2) developing vacuum distillation as an analytical method for impurities in sodium, and (3) determining the solubility of krypton, a fission-product gas, in liquid sodium.

1. The Na-Na_2O-NaOH-NaH System

Interest in the Na-Na_2O-NaOH-NaH phase relations stems from the need to understand the behavior of oxygen- and hydrogen-bearing species in liquid sodium. The results will assist in the development and evaluation of analytical methods for monitoring oxygen and hydrogen impurities in sodium and will provide a base for future investigations of cold-trapping, caustic stress corrosion, and other related studies.

A careful review of the literature indicated that previous work on this system was fragmentary and not self-consistent. Nevertheless, we constructed several tentative working versions of the Na-Na_2O-NaOH-NaH corner of the sodium-oxygen-hydrogen ternary system, each of which was in agreement with some aspects of the literature data. Several arbitrary, but reasonable, assumptions were made in creating the diagrams. The Na_2O-NaOH binary section of Bouaziz, Papin, and Rollet[13] and the NaOH-NaH binary section of Mikheyeva and Shkrabkina[14] were assumed to be correct. The allotropic transformations of Na_2O and NaOH were ignored. The Na-Na_2O and Na-NaH binary sections were drawn as monotectic systems to maintain agreement with Shikov.[15] Two of the diagrams included the transformation of Na and NaOH into Na_2O and NaH with decreasing temperatures. Subsequent experimental evidence indicated that this transformation actually occurs and that it is described by the Class II four-phase equilibrium[16] reaction $Na(\ell) + NaOH(\ell) \rightleftharpoons Na_2O(s) + NaH(s)$ where $Na(\ell)$ and $NaOH(\ell)$ are terminal liquid solutions and $Na_2O(s)$ and NaH(s) are the pure solids.

The resultant phase diagram, shown in three sections in Figs. II-5, -6, and -7, is thus a schematic that most reasonably combines the previously cited conclusions and that has been confirmed in principle by our experimentation. The diagram is in fundamental agreement with the thermodynamic analyses of the sodium-oxygen-hydrogen system by Jansson[17] and, therefore, is in disagreement with much of the diagram given by Shikhov.[15]

---

[13] R. Bouaziz, G. Papin, and A. P. Rollet, Compt. Rend. 262C, 1051 (1966).
[14] V. I. Mikheyeva and M. M. Shkrabkina, Russ. J. Inorg. Chem. 7, 1251 (1962).
[15] B. A. Shikov, Russ. J. Inorg. Chem. 12, 545 (1967).
[16] F. N. Rhines, Phase Diagrams in Metallurgy, McGraw-Hill Book Co., New York (1956).
[17] S. A. Jansson, Corrosion by Liquid Metals, p. 523, Plenum Press, New York (1970).

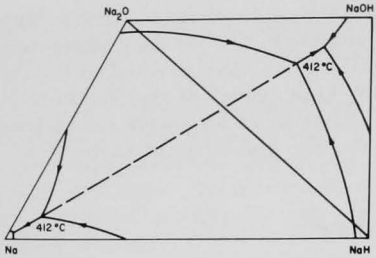

Fig. II-5

Liquidus Valleys of the Na-Na_2O-NaOH-NaH System [the transformation Na(ℓ) + NaOH(ℓ) ⇌ Na_2O(s) + NaH(s) is shown to occur at 412°C]

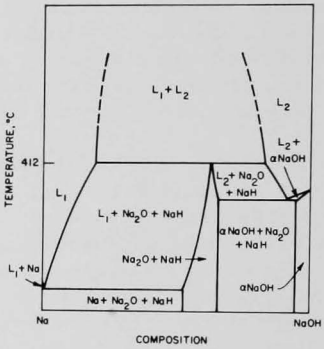

Fig. II-6

Vertical Section Na-NaOH of the Na-Na_2O-NaOH-NaH System

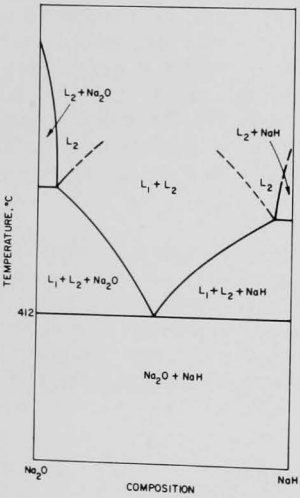

Fig. II-7

Vertical Section Na_2O-NaH of the Na-Na_2O-NaOH-NaH System (as viewed from the Na-rich corner)

Experimental verification of the proposed diagram centered around the characterization of the transformation of Na and NaOH into Na_2O and NaH with decreasing temperature. The two Class I four-phase equilibria[16] (ternary eutectics) were not investigated. One of these, near pure Na, presumably occurs so near the melting point of pure sodium that it is difficult to detect, and the other, near NaOH, is not in a region of current interest.

In the experimental work, mixtures of Na, Na_2O, NaOH, and NaH were heat-treated and then examined at room temperature by X-ray diffractometric methods. Pure reagent-grade materials were weighed and sealed into nickel capsules, which were then placed inside a rotatable cradle in a rocking furnace. Hence, the materials within the capsules were both rotated and rocked to ensure complete mixing during the heat treatment. In the initial experiments, it was observed that, regardless of which reactant phases were chosen to produce a mixture of given composition, the reactant phases found after a 24-hr treatment at 550°C were the same; hence, all subsequent samples received a 550°C normalizing heat treatment. The capsules were then maintained at various temperatures from 250 to 750°C for about 10 days and water-quenched. The temperature of the capsules was measured with a calibrated thermocouple. During the entire heat treatment, a hydrogen pressure corresponding to the equilibrium hydrogen dissociation pressure of NaH at the temperature of treatment was maintained within the capsules.

After the heat treatment, the capsules were opened in a helium drybox and the contents crushed and ground into a fine powder. A sample of the powder was loaded into a gas-tight diffractometer cassette with a beryllium window for X-ray analysis.

In all the capsules quenched from above 412°C, large amounts of free sodium were observed visually, and NaOH was the major component found in the diffractometer samples. Little NaH was detected. On the other hand, in all capsules quenched from below 412°C, very little free sodium was observed and NaH was the major component in the diffractometer samples. Little NaOH was detected. Samples quenched from 412°C were composites of the components described above; therefore, 412°C is believed to be the transformation temperature. Sodium monoxide (Na_2O) was detected in minor amounts in all samples. From these results, it was concluded that liquid sodium and liquid sodium hydroxide transform on cooling into solid Na_2O and solid NaH at 412 ± 2°C under an equilibrium hydrogen pressure of 182 ± 10 Torr. This temperature, which is shown in the phase diagrams, is in agreement with that predicted by Jansson[17] using thermodynamic arguments.

2. Vacuum Distillation as an Analytical Method for Impurities in Sodium

The work of Walker et al.[18,19] has demonstrated that vacuum distillation is a useful method for determining oxygen in sodium and that it has potential for determining carbon in sodium. Walker's work[18] has shown that, provided the oxygen exists in sodium as Na_2O or Na_2CO_3, it can be determined indirectly by this method; however, the possibility has not been explored that the presence of other impurities, especially those known to exist in the sodium, might introduce errors in the analysis. Other experiments have shown that carbon in the form of either carbonate[20] or elemental carbon[18] is not lost (due to degradation of the carbonate or formation of carbon monoxide via the reaction of elemental carbon with sodium oxide) during distillation at 350°C. Tests to demonstrate that similar results are obtainable regardless of the form of the carbon or the type and concentration of other impurities in the sodium have not been done.

Clearly, to exploit the full potential of this method for oxygen and carbon analyses and to place the method on a firm and fully tested basis, experiments are needed that examine the effects of added carbon, oxygen, hydrogen, and nitrogen impurities on the composition of the residue. Accordingly, a program has been undertaken to characterize the impurity reactions that may occur in the evaporation-concentration step of the distillation analysis and to determine whether or not such reactions lead to significant errors in analyses for nonmetallic elements in sodium.

The requisite tests will involve adding measured quantities of carbon-, oxygen-, hydrogen-, and nitrogen-bearing impurities, singly and in combination, to 1 kg of sodium, heating the mixture inductively to distill away the sodium, analyzing the off-gas with a residual-gas mass analyzer, collecting the residue, and analyzing it by either X-ray or infrared methods. The 1-kg still that has been assembled for this purpose is shown in Fig. II-8. It consists of four basic parts: (1) a nickel crucible, (2) a condenser, (3) a vacuum adapter, and (4) an induction heater.

The crucible consists of two pieces--a 3.75-in.-OD by 8.69-in.-high cylinder and a 3.75-in.-OD by 0.50-in.-thick bottom piece. The cylinder and its base are joined through a leak-tight Inconel O-ring gasket. The crucible was made with a detachable base so that distillation residues, which tend to concentrate in the bottom of a crucible, can be easily removed for analysis.

The condenser is fabricated of Type 304 stainless steel and is water-cooled. The cooling coil, which is welded to the condenser, is

---

[18] J. J. Walker, E. D. France, and W. T. Edwards, Analyst 90, 727 (1965).
[19] J. J. Walker and E. D. France, Analyst 90, 228 (1965).
[20] V. M. Sinclair, J. L. Drummond, and A. W. Smith, TRG-Report-1185(D) (1966).

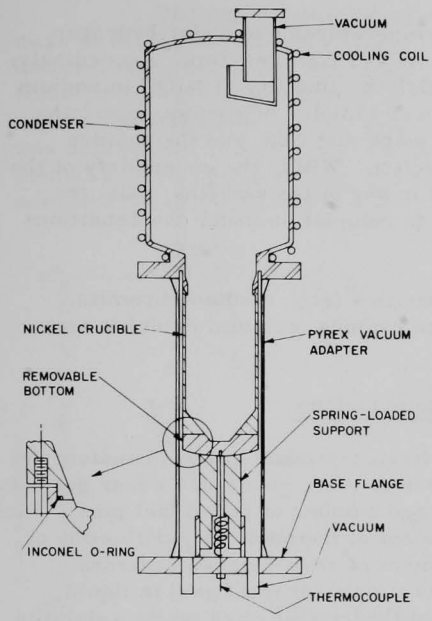

Fig. II-8. Sodium Still

1/4-in.-OD stainless steel, sprayed with copper to maximize cooling efficiency. The lower lip of the condenser is lapped and mated to the upper lip of the crucible, which is also lapped. The crucible, in turn, is held on a spring-loaded support to provide leak-tight mating of the lapped surfaces and, thereby, prevent leakage of sodium out of the condensing region.

The vacuum adapter is a flanged Pyrex pipe that is gasketed to the condenser at the top and to the base support at the bottom. It provides a vacuum-tight, nonconducting envelope for the inductively heated crucible. Vacuum is obtained with a mechanical pump separated from the still by a hydrocarbon trap and a cold trap in series.

The induction heater, which is also water-cooled, is a coil of 1/4-in.-diameter copper tubing wrapped around the vacuum adapter. The power source for the heater is a 2.5-kW Lepel high-frequency oscillator. The temperature of the crucible is monitored by a sheathed thermocouple located in a well within the base of the crucible.

Not shown in Fig. II-8 is a quadrupole, residual-gas mass analyzer, with which the gases evolved during distillation are analyzed.

Tests of the still have shown that 1 kg of sodium can be distilled at ~350°C in about 6 hr. Also, virtually all of the residue collects in the bottom of the crucible; hence, the residue can be removed for examination simply and conveniently by detaching the crucible's base.

Initial effort is being concentrated on the effect of added impurities on analysis for oxygen. Conventionally, oxygen is determined from acid titration of the residue after distillation, assuming that the residue consists only of sodium oxide. The presence of other titratable impurities would obviously result in error. One such impurity is NaOH. The work in the preceding subsection suggests that at the temperature (~350°C) and pressure ($<1 \times 10^{-3}$ Torr) of the distillation, NaOH should react with sodium to form Na_2O and NaH. (Subsequent decomposition of the hydride during the distillation is expected.) However, little information is available on the kinetics of this reaction, and the presence of hydroxide has been reported in

sodium samples taken from loops at temperatures and under hydrogen pressures that favor the $NaOH + Na \rightarrow Na_2O + NaH$ reaction. Accordingly, experiments were performed to establish the stability of NaOH in sodium under our distillation conditions. Several samples of sodium containing known quantities (1-500 ppm) of NaOH were distilled, and the residue analyzed for hydroxide by X-ray diffraction. Within the uncertainty of the X-ray method, no hydroxide was found in any of the samples; thus, the NaOH-Na reaction appears to proceed to completion under the conditions of the distillation.

The influence of other impurities (e.g., sodium chromite, sodium ferrite, sodium carbide, sodium cyanide, calcium oxide) is now being investigated.

3. Solubility of Krypton in Liquid Sodium

Data on the solubilities of fission-product gases in sodium are needed to estimate how the concentration of these gases in a cover gas may vary with conditions (e.g., fuel burnup and number of failed fuel pins). Such estimates are essential to the development of methods for purification of cover gas and, thereby, to the development of zero-release reactors. Accordingly, the solubility of krypton (a fission-product gas) in liquid sodium was measured earlier.[21] Recent theoretical work on the solubility of gases in liquid sodium[22] suggested the possibility that these measurements may have yielded solubilities that were somewhat low. To test this possibility, the solubility of krypton in sodium was redetermined using the refined techniques that have evolved since the earlier krypton study.

The method employed was adapted from Grimes et al.,[23] who had applied it to the determination of the solubility of noble gases in molten salts. The method has been described in detail elsewhere[24] and has been used to measure the solubility of helium,[24] argon,[24] xenon,[25] and nitrogen[26] in liquid sodium. Briefly, this method involves the following basic steps: (1) saturation of liquid sodium with a gas at a preselected temperature and pressure, (2) transfer of the saturated sodium to a container where the solution is stripped of the dissolved species by sparging with an inert gas, (3) concentration of the desired component of the resulting gas mixture by selective adsorption, and (4) quantitative assay.

---

[21] S. K. Dhar in Chemical Engineering Division Semiannual Report, January-June 1964, ANL-6900, p. 125 (1964).

[22] H. C. Schnyders and H. M. Feder in Chemical Engineering Division Physical Chemistry of Liquid Metals and Molten Salts Semiannual Report, January-June 1971, ANL-7823, p. 16 (1971).

[23] W. R. Grimes, N. W. Smith, and G. M. Watson, J. Phys. Chem. 62, 862 (1958).

[24] E. Veleckis, S. K. Dhar, F. A. Cafasso, and H. M. Feder, J. Phys. Chem. 75, 2832 (1971).

[25] E. Veleckis and W. Kremsner in Sodium Technology Quarterly Report, July, August, September 1970, ANL/ST-4, p. 44 (December 1970).

[26] E. Veleckis, K. E. Anderson, F. A. Cafasso and H. M. Feder, "Solubilities of Nitrogen Gas and Sodium Cyanide in Sodium," in Proc. Int. Conf. on Sodium Technology and Large Fast Reactor Design, ANL-7520, Part I, p. 295 (1968).

Our exploratory measurements indicated that the early data were at least a factor of four too low and, hence, that the solubility should be remeasured over the entire temperature range of interest. Accordingly, solubilities were measured at ~7 atm pressure[27] and at approximately 50-degree intervals between 400 and 550°C. Each equilibration temperature was approached from higher and lower temperatures; within the experimental uncertainty of the septuplicate determinations made at each temperature, no effect of this variation was observed. This finding lends support to the conclusion that the measurements were made under equilibrium conditions.

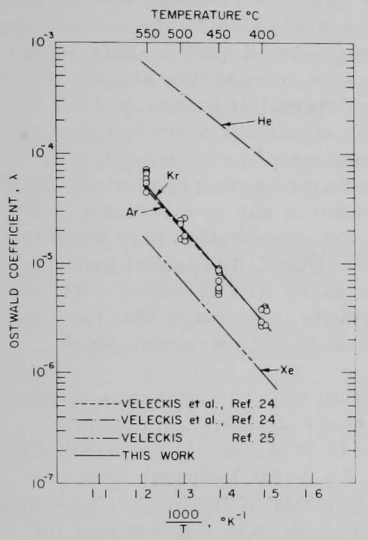

Fig. II-9. Solubility of Noble Gases in Liquid Sodium

The results of 28 determinations for krypton were fitted by the method of least squares to the following linear equations:

$$\log \lambda = 1.430 - 4711\ T^{-1} \qquad (1)$$

and

$$\log K_H = -2.413 - 4374\ T^{-1} \qquad (2)$$

where T is absolute temperature, and λ and K_H are, respectively, the Ostwald coefficient[28] and Henry's law constant[29]--two units in which gas solubilities are conventionally expressed. The data are given in Fig. II-9 as a plot of Ostwald coefficient versus reciprocal temperature. The heat of solution of krypton in sodium calculated from Eq. 1, in which the standard state of krypton is taken as one gram-atom of ideal gas in a volume equal to the molar volume of sodium, is 21.6 ± 1.6 kcal/mol; the heat of solution calculated from Eq. 2, in which the standard state corresponds to one gram-atom of ideal gas at 1 atm, is 20.0 ± 1.5 kcal/mol.

In Fig. II-9, the solubility of krypton is also compared with the solubilities of helium, argon and xenon in liquid sodium. Note that the

[27]The applicability of Henry's law to noble gas–sodium solutions to at least 9 atm pressure has been amply demonstrated (see ANL-7675, p. 64, 1970 and ANL-7750, p. 32, 1971); hence, a study of the dependence of krypton solubility on pressure was considered to be unnecessary, and selection of 7 atm as the working pressure was based on convenience.

[28]The Ostwald coefficient is defined as the volume of gas dissolved per unit volume of solvent, both solute and solvent being at a defined temperature and pressure.

[29]The Henry's law constant is defined as the atom fraction in solution per atmosphere of gas pressure.

solubility of krypton is smaller than that of helium, larger than that of xenon, and, within experimental uncertainty, identical to that of argon between 400 and 550°C. Although this finding is surprising, it is reconcilable in a qualitative way, in terms of a solution model currently under development at Argonne by Schnyders and Feder.[30] (Earlier published solution models were shown by Veleckis et al.[24] to be inadequate for treating the thermodynamics of rare gas-liquid sodium solutions.) In the model of Schnyders and Feder, the difference between two work terms--the electronic work done on creating, in a solvent, a cavity of size appropriate to accommodate a solute atom and the attractive work done by the solute atom in the cavity when it polarizes the surrounding solvent atoms--determines the excess free energy of formation of a gas in a solvent like sodium. The size of a solute atom plays an important role in determining the size of the cavity and hence in determining the magnitude of the electronic work term. Similarly, the polarizability of a solute atom is important in determining the magnitude of the attractive work term. The major contribution to the excess free energy of solutions of rare gases in sodium is due to electronic work; the attractive work begins to make a significant contribution only when the polarizability of an atom becomes very large. Hence, the model predicts, qualitatively, that the solubilities of the rare gases will decrease with increasing size unless an increase in polarizability is so large that the size effect (electronic work) is offset or neutralized by the attractive work.

We hypothesize that a neutralization effect is operative in the case of the argon-krypton pair. The hard-sphere diameter of krypton (2.0 Å) is only 4.5% larger than that of argon (1.91 Å) but its polarizability is 34% greater (11.09 a.u.[31] for argon vs. 16.7 a.u. for krypton); hence, a reasonable qualitative explanation for the similarity of the argon and krypton solubilities is offered by this model. Moreover, despite the fact that the model is still undergoing refinement, quantitative agreement between theory and experiment is good.[22]

D. Fission-Product and Cover-Gas Technology

Detection and characterization of fuel-element failures in fast reactors such as FFTF are necessary to prevent gross contamination of the primary coolant with fission products and fuel and to limit possible progressive damage to adjacent fuel pins. To this end, methods are currently being developed for monitoring both the cover gas and the sodium in FFTF and future LMFBR's. The proposed method for monitoring the cover gas for fission products consists of (1) collection of a sample of the gas on a specially constructed chromatographic column, (2) elution of ^{23}Ne [produced by the reaction ^{23}Na(n,p)^{23}Ne] with argon carrrier gas, and (3) counting of the xenon and krypton isotopes remaining on the column by means of a lithium-drifted germanium diode [Ge(Li)] detector. The proposed method

[30] ANL-7675, p. 130 (1970); ANL-7823, p. 16 (1971).
[31] Atomic units.

for monitoring the sodium consists of sparging a sample of sodium with argon to remove dissolved xenon and krypton isotopes and analyzing the sparger effluent by the method used for the cover gas. In a continuation of the sparging, the ^{135}I content of the sodium can be determined by analysis for its daughter, ^{135m}Xe. An abnormally high concentration of ^{135}I in the sodium indicates contact of the fuel by sodium.

A plan for development and testing of these systems for fuel-failure monitoring at FFTF has been submitted to RDT. This plan provides for (1) development of an automatic gas-chromatographic and gamma-ray counting system for efficient analysis of fission gases, (2) development of a system for analysis of sodium by stripping the soluble gases from the sodium, (3) development of computer software for automatic control of the equipment and for analysis of the data from the gamma spectrometer, and (4) installation and testing of the cover-gas-analysis and sodium-sampling systems on the Radioactive Sodium Chemistry Loop (RSCL) of EBR-II.

1. Proposed System for Fuel-Failure Detection and Characterization on FFTF

A preliminary design description has been written for the system proposed for detecting and characterizing fuel failures on FFTF. The system is divided into three subsystems: (1) a spectrometer-computer, (2) a reactor cover-gas analyzer, and (3) a sparger and sparge-gas analyzer. A functional description of each of the subsystems follows.

(1) Spectrometer-Computer. The functions of the spectrometer-computer are to acquire, store, and analyze the data from the Ge(Li) detectors on both the cover-gas and sparger systems; to control the gas-sampling processes for both the cover-gas and sparger systems; to control the sequence of valve operations in the sparger; and to provide results in an output form useful for denoting the type and severity of a fuel failure. During operation at EBR-II, experience gained from response of the computer system to fuel failures is expected to provide information for devising a program to analyze the data for the type and severity of failure.

(2) Reactor Cover-Gas Analyzer. Cover-gas analysis will be done on a semicontinuous basis with a cycle time of 2 to 4 min. Neon-23 removal will be accomplished by a high-speed chromatographic technique, in which xenon and krypton are retained on the adsorbent after neon has been eluted. Xenon and krypton isotopes will be determined by gamma spectrometry using a Ge(Li) detector adjacent to the specially designed adsorbent column. Saturation of the Ge(Li) detector by a high counting rate will be avoided by automatic reduction of the sample size. The computer will exercise control of this operation.

(3) Sparger and Sparge-Gas Analyzer. Gases dissolved in or generated in the sodium coolant will be sparged from a sodium sample and

analyzed on a semicontinuous basis with a cycle time of 4 to 6 min. The analysis will be done by the method used for the cover-gas system. Iodine-135 in the sodium will be determined subsequently from analysis of the sparger effluent for ^{135m}Xe.

2. Analysis of Cover Gas

The background level of ^{23}Ne [from the reaction $^{23}Na(n,p)^{23}Ne$] in the cover gas at FFTF may be considerably higher than that at EBR-II. When there is high turbulence at the sodium-cover gas interface in the closed loops, the normal background level of ^{23}Ne may be 10^6 times as great as the background level of krypton and xenon fission products. Because of the large cover-gas volume in the main heat-transport system and the short half-life of ^{23}Ne (38 sec), the ^{23}Ne may be less abundant in the cover gas of that system than in the closed-loop system. However, the likelihood of a high ^{23}Ne background presents a problem in the normal assay of the activity of fission-product gases.

To detect and measure the fission-product noble gases with minimum delay, a gas-chromatographic technique is being developed for rapidly separating ^{23}Ne from the fission gases prior to the fission-product assay with a Ge(Li) detector system. The feasibility of this approach is well founded in that the retention time of rare gases on chromatographic columns increases with increasing atomic weight.

The present concept of the operation of a gas-chromatographic neon-discrimination device is as follows: (1) introduce a sample of reactor cover gas onto a chromatographic column, (2) flow argon carrier gas through the column for a preestablished period of time so that the ^{23}Ne activity remaining on the column is no more than 10^{-6} as much as that originally introduced, (3) stop the carrier gas flow and obtain a gamma spectrum of the radioactive species on the column, (4) immediately introduce another sample (the krypton and xenon from the previous sample will be eluted as the chromatographic process continues), and (5) repeat the cycle.

The development of the chromatographic column, which will also serve as the counting chamber, will require (1) selecting the column material and the length of column necessary to provide adequate separation, (2) investigating, in laboratory experiments, tailing effects (retention of small quantities of gas for relatively long times, common in gas chromatography) and the decontamination factors (DFs) obtainable, and (3) designing and testing a column to optimize sample size, flow rate, and counting efficiency. (The geometry of the column has a marked effect on the counting efficiency and the rate of change of efficiency as an isotope moves through the column.)

Several preliminary gas-chromatographic separations were performed with nonradioactive neon, krypton, and xenon using various

absorbents, argon carrier gas, and a thermal-conductivity detector. A 1-ft Molecular Sieve column yielded the best resolution per unit length of column, and was, therefore, selected for further evaluation.

Several factors complicate the direct investigation of tailing effects of neon and demonstration of DFs of neon from krypton and xenon in laboratory experiments: (1) Investigations must be performed with neon, krypton, and xenon concentrations expected in reactor cover gases (~1 to 10 ppm in argon). (2) Conventional chromatographic detectors are operating at or below their detection limits at these concentrations, and hence are not useful in obtaining the required information. (3) Although radioactive tracers provide the requisite sensitivity, the longest-lived radioactive isotope of neon (^{24}Ne, 3.4 m) has too short a half-life to be practical in laboratory experiments. (4) A preliminary assessment of the chromatographic approach was needed quickly to furnish design information for a neon-discrimination device to FFTF on schedule.

To facilitate rapid accumulation of design information, an indirect approach was taken. This involved (1) selection of column material, column length, flow rate, sample size, and counting geometry that were consistent with reactor design requirements and that provided the best separation between ^{85}Kr (10.7 y) and ^{135}Xe (5.3 d), and (2) projection of these selections to a neon-xenon separation using as a basis our preliminary experiments, which had indicated that the neon-xenon separation is at least an order of magnitude better than the krypton-xenon separation.

Two series of experiments were conducted with ^{85}Kr and ^{133}Xe to investigate tailing effects and to demonstrate the DFs obtainable; one series was conducted with a 1-ft column, the other with a 3-ft column. In each series, a column packed with Molecular Sieve 5A was coiled in a flat spiral of ~2-in. OD and placed next to a Ge(Li) detector, which had a computer-controlled multichannel analyzer. From these experiments, it was determined that a DF of 10^3 would be obtained in 1 min with the 1-ft column, and a DF of 4.5×10^3 in 3 min with the 3-ft column.

Projection of the data for the 3-ft column (a DF of 4.5×10^3) to a neon-xenon separation involved (1) calculating the fraction of ^{23}Ne which would decay during the 3-min separation (~97%) and (2) incorporating the factor of ten difference between the krypton-xenon separation and a neon-xenon separation. These calculations yielded a projected DF of ~10^6 for the separation of ^{23}Ne and ^{133}Xe (the xenon isotope of principal interest in reactor application). Since the ^{23}Ne level in the FFTF cover gas is expected to be no more than 10^6 times greater than the krypton and xenon isotope levels, this demonstrated DF should be adequate for FFTF application.

With the procedure described above, subsequent samples could be introduced onto the column immediately after the ^{133}Xe count is completed, since >95% of the ^{133}Xe is flushed off the column in one additional minute

of flow. This procedure would have a total cycle time of 4 min--1 min sample introduction, 2 min additional flow to elute the neon, and 1 min counting time.

It is believed that additional experimental work will improve the chromatographic system. An improved separation would decrease the cycle time and increase the decontamination factor.

3. Analysis of Sodium by Sparging

When oxide fuel is exposed to sodium by a breach in the fuel cladding, many fission-product elements, including the halogens, the alkaline earths, and tellurium, are leached from the fuel and enter the sodium-coolant stream. The detection of these elements in the coolant should, therefore, provide an indication of sodium-fuel contact prior to extensive fuel washout.

A study of the various isotopes available for detection of fuel-element failures indicated that iodine in sodium could be determined from the rate of generation of its xenon daughter, which is sparged from the sodium and counted. The iodine and xenon isotopes of principal interest for reactor application are ^{135}I (6.7 hr) and ^{135m}Xe (15.6 min). The advantages of these isotopes over other iodine-xenon pairs has been discussed in a previous report in this series (ANL-7750, p. 49). The method is briefly as follows. An isolated sodium sample containing the ^{135}I is sparged with an inert gas to strip out all the dissolved gases in the sample including the ^{135m}Xe. This initial flow of sparge gas is analyzed for fission-gas content by the same technique that is described above for the cover gas. As sparge-gas flow continues, the only fission-gas isotopes present in the sparge gas are those coming from the decay of the halogens dissolved in the sodium sample. Xenon-135m produced from ^{135}I decay is separated from the sodium by the sparge gas, collected in a chromatographic column and counted by means of a Ge(Li) detector. From the collection time, the counter efficiency, and the recorded counts, the amount of ^{135}I in the sample is calculated. The use of a sodium sampling/sparging system in conjunction with a cover-gas analysis system is expected to provide rapid detection and characterization of fuel-element failures.

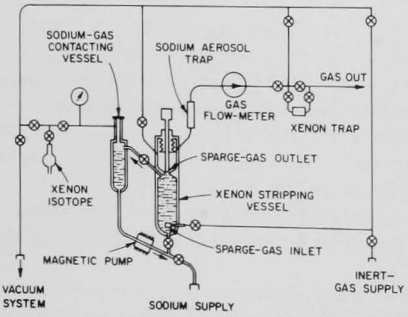

Fig. II-10. Flow Diagram for Xenon-Stripping Apparatus. ANL Neg. No. 308-2725.

To assess this method of on-line monitoring, information was needed on the rate at which dissolved xenon is removed from sodium by inert-gas sparging. A prototype batch sparger and associated apparatus required for these kinetic tests was constructed. A flow diagram of the apparatus is shown in Fig. II-10.

This apparatus has been used to obtain data on xenon-removal rates from sodium samples at 350 and 450°C. In these laboratory tests, the samples were sparged with helium, and for convenience, 5.3-day ^{133}Xe was used instead of ^{135m}Xe, which has a short half-life (15.6 min). Xenon was dissolved by pumping sodium through the sodium-gas contacting vessel, which contained 0.1% xenon (~3 x 10^{-3}% ^{133}Xe, initially) in helium. The system sodium was circulated through the stripping vessel. After some of the xenon had dissolved, a sample of sodium (500 cm^3) was isolated in the stripping vessel, and helium was bubbled through the sodium. The helium (at rates of 450 to 2000 cm^3/min) was passed upward through an aerosol trap, a filter, and then through a liquid-nitrogen-cooled trap of activated charcoal. The charcoal trap was then gamma-counted with a Ge(Li) detector connected to a computer-controlled multichannel analyzer system. The analyzer system was programmed for repeated counting of the trap at short, preselected time intervals (typically, between 3 and 7 sec). The trap/detector geometry was fixed during each experiment.

Ten experiments on removal kinetics were completed. For each experiment, the time constant for xenon removal (defined as the time to decrease the xenon concentration in the sodium by a factor of e^{-1}) was calculated from a plot of xenon activity accumulated in the trap as a function of time. Data from a typical experiment are given in Fig. II-11.

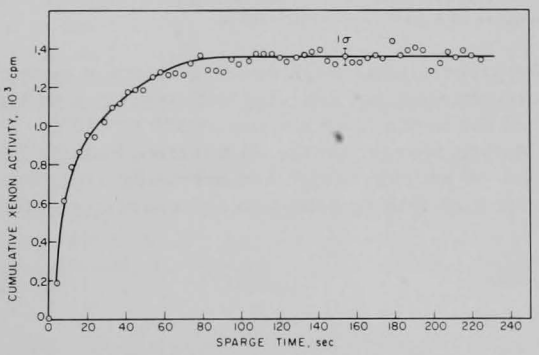

Fig. II-11. Data from Xenon-Stripping Experiment (Expt. 7; sodium temperature, 450°C; helium sparge rate, 1000 cm^3/min). ANL Neg. No. 308-2726.

Experimental conditions and the times for xenon removal from sodium are summarized in Table II-3. For 99% removal, 4.6 time constants are required. Comparison of the data for 99% removal from 350°C sodium indicates that the removal time is decreased from approximately 1.5 to 1 min by increasing the sparging rate from 450 to 2000 cm^3/min. On the other hand, increasing the temperature of the sodium to 450°C reduces the sparging time required for 99% xenon removal only slightly. Deviations

between single experiments conducted under similar conditions are attributed primarily to inaccuracies in counting at the low count rates obtained when xenon first enters the charcoal trap. Calculations have indicated that argon sparge gas would remove xenon more rapidly than helium because argon forms smaller bubbles in sodium. Preliminary experiments, recently conducted with argon, have confirmed these calculations, and argon will be used as the sparge gas for xenon removal.

TABLE II-3. Time Required for Removal of Dissolved Xenon from Sodium by Helium Sparging

Expt.	Helium Sparge Rate, cm^3/min	Sodium Temp., °C	Time Constant for Removal,[a] sec	Time for 99% Removal, sec
1	2000	350	15	69 } 62 (Av)
2	2000	350	12	55
3	2000	350	(>12)[b]	
4	1000	350	21	97 } 94 (Av)
5	1000	350	24	110
8	1000	350	16	74
9	450	350	24	110 } 99 (Av)
10	450	350	19	87
6	1000	450	17	78 } 85 (Av)
7	1000	450	20	92

[a]Defined as time to decrease xenon concentration by a factor of e^{-1}.
[b]Value suspect because of experimental difficulties.

The experimental work on the kinetics of xenon removal from sodium has demonstrated that sparging with inert gas will rapidly strip essentially all of the xenon from sodium at 350 to 450°C. Present plans are to install a prototype sparger on the Radioactive Sodium Chemistry Loop (RSCL) at EBR-II to provide design and operating experience for an automated system for fuel-failure detection and characterization to be installed on FFTF.

III. MATERIALS CHEMISTRY AND THERMODYNAMICS

A. High-Temperature Thermodynamic Phase and Kinetics Studies

The objective of this program is to obtain phase-diagram, thermodynamic, and chemical data that can be used to interpret and evaluate performance of fast-breeder-reactor fuels. This information will aid in understanding and in selecting methods for control of sodium-fuel interactions, fission-product distribution in the fuel, cladding attack by corrosive fission products, plutonium segregation, and fuel swelling. In addition, these data will help to identify phases formed in fuel under operating conditions and to choose additives for controlling the chemical potentials of fuel anions and those fission products which are deleterious to prolonged fuel-pin lifetimes.

The high-temperature investigations of U-Ce-O, U-Pu-O-Na, and U-O fuel-fission product-sodium systems include mass-spectrometric vapor-pressure measurements, phase-diagram studies, kinetic studies, and activity measurements by transpiration experiments.

1. The Effect of Fuel Burnup on Oxygen Potentials

The objective of this research is to measure the effect on the oxygen potential of the substitution of rare earth fission products for plutonium and uranium in the fuel lattice. These results will help to determine the initial oxygen concentrations in the fuel required to yield reasonable burnup levels before reaching undesirably high oxygen potentials.

a. Oxygen Partial Pressure Measurements

Measurements of oxygen partial pressure over oxygen-deficient compositions in the U-Ce-O system were obtained by means of a flowing-gas technique with H_2-H_2O mixtures to fix the oxygen potential in the gas stream.

The results of preliminary measurements at 1807°K for the solid solution $U_{0.89}Ce_{0.11}O_{2-x}$, prepared by pressing and sintering UO_2 + CeO_2 powders, are summarized in Table III-1. For comparison, we have included approximate relative partial molar free-energy values of diatomic oxygen in hypostoichiometric mixed-oxide fuel compositions, $U_{0.89}Pu_{0.11}$, estimated from the work of Rand and Markin,[1] as well as $\Delta\bar{G}(O_2)$ values for hypostoichiometric urania.[2,3] It should be noted that urania compositions in the range from $UO_{1.93}$ to $UO_{1.96}$ lie within the univariant system $[U(\ell) + UO_2(s)]$ at 1807°K.

---

[1] M. H. Rand and T. L. Markin, "Some Thermodynamic Aspects of $(U,Pu)O_2$ Solid Solutions and Their Use as Nuclear Fuels," in Thermodynamics of Nuclear Materials, 1967, p. 637, IAEA, Vienna (1968).

[2] A. E. Martin and R. K. Edwards, J. Phys. Chem. 69, 1788 (1965)

[3] R. J. Ackermann, E. G. Rauh, and M. S. Chandrasekharaiah, J. Phys. Chem. 73, 762 (1969).

TABLE III-1. Oxygen Partial Pressures and Oxygen Potentials for the $U_{0.89}Ce_{0.11}O_{2-x}$ System at 1807°K

$U_{0.89}Ce_{0.11}O_{2-x}$					UO_{2-x}[a]	$U_{0.89}Pu_{0.11}O_{2-x}$
Experiment No.	Time, hr	-log $p(O_2)$, atm	O/M	$-\Delta\bar{G}(O_2)$, kcal	$-\Delta\bar{G}(O_2)$, kcal	$-\Delta\bar{G}(O_2)$, kcal
5	8.3	14.72	1.93	121.7	181.7	144
6	6.9	14.30	1.95	118.2	181.7	140
7	8.3	14.26	b	117.9	-	-
8	4.4	13.9	1.96	114.9	181.7	137

[a] $[U(\ell) + UO_2(s)]$.
[b] Sample lost during analysis.

The experimental results show that the oxygen potentials of the system $U_{0.89}Ce_{0.11}O_{2-x}$ are considerably higher than those for urania and the U-Pu-O system for the corresponding O/M ratios. It may be tentatively concluded that substitution of rare-earth fission products for U and Pu in U-Pu oxide fuel will increase the oxygen potential of the system. Measurements are planned for the U-Pu-Ce-O system to determine the effects of substituting Ce for Pu in the U-Pu-O fuel.

2. Phase and Reaction Studies of U-O-Na and U-Pu-O-Na Systems

Interaction of sodium coolant with reactor fuel could cause fuel swelling and cladding rupture in the event of a breach in the cladding. The severity of the problem may determine how long failed fuel elements can be left in the reactor core and whether or not failed fuel elements can be stored in the reactor sodium coolant.

In the 1970 Research Highlights report (ANL-7750), we described work on the phase relations in the U-O-Na system and the preparation of Na_3UO_4 for calorimetry and mass-spectrometric investigations (discussed in Section III.A.2.b below). It was shown in ANL-7750 that Na_3UO_4 is the product of reaction between sodium and UO_{2+x} and that $Na_3U_{1-y}Pu_yO_4$ is the product of the reaction between U-Pu oxide fuel and sodium. Further studies of these systems are described below.

a. Oxygen/Metal Ratio of U-Pu Oxide Fuel in Contact with Sodium

An objective of this study is to establish the oxygen-to-metal (O/M) ratio of U-Pu mixed oxide in equilibrium with sodium as a function of temperature and of the Pu/(U + Pu) ratio of the mixed oxide. A lattice-parameter method is being used. The reaction products are treated with ethyl alcohol to remove free sodium and then are examined by X-ray diffraction. The lattice parameter of the mixed-oxide phase is measured, and from a plot of lattice parameter versus O/M ratio, the O/M composition of the mixed-oxide phase is established.

The literature data on the relationship of lattice parameter to O/M composition for the hypostoichiometric mixed-oxide phase with a Pu/(U + Pu) composition of 0.20 were not definitive enough for this study. Consequently, standards were prepared by the hydrogen reduction of pellets at temperatures up to 1930°C in a Brew tungsten resistance furnace. The pellets were analyzed for oxygen by a fusion method. The lattice parameter of the mixed-oxide phase was measured to establish a calibration curve.

In the equilibrium study, the O/M composition of the initial U-20% Pu oxide powder was 1.99_5. The powder was charged with chunk sodium in a ratio by weight of about 1 part oxide to 0.6 part sodium into nickel capsules which were welded shut. These operations were carried out in a purified helium atmosphere. The capsules were then heated for various time periods at temperatures up to 1100°C to reach equilibrium. The data are summarized in Table III-2.

TABLE III-2. The O/M Composition of the Uranium-Plutonium Mixed-Oxide Phase, Pu/(U + Pu) = 0.20, after Reaction with Sodium in Nickel Capsules[a]

Reaction Conditions		Data on Product Mixed-Oxide Phase	
Time, days	Temperature, °C	Lattice Parameter, a_0	O/M Composition, deduced from a_0
7	800	5.4663	1.958
3	900	5.4662	1.959
0.17	1100	5.4663	1.958

[a]The mixed oxide was initially in the form of a powder (100% -100 mesh and 43% -270 mesh) with O/M = 1.995.

The values in Table III-2 can be compared with calculated values listed in Table III-5. The calculated values were also for oxide with a Pu/(U + Pu) ratio of 0.20 and were based on thermodynamic data including data derived from calorimetric[4-6] and mass spectrometric studies of Na_3UO_4. The experimental data from 800 to 1100°C based on lattice-parameter measurements are in good agreement with the calculated values.

b. Mass-Spectrometric Study of Sodium-Fuel Interaction

The objective of this study is to obtain equilibrium thermodynamic data on the products of reaction between sodium and fuel. In

[4]D. W. Osborne and H. E. Flotow, J. Chem. Thermodyn. (accepted for publication).

[5]P. A. G. O'Hare, W. A. Shinn, F. C. Mrazek, and A. E. Martin, J. Chem. Thermodyn. (accepted for publication).

[6]D. R. Fredrickson and M. G. Chasanov, J. Chem. Thermodyn. (accepted for publication).

particular, the studies are concerned with determination of the oxygen and sodium partial pressures (activities) in equilibrium with the reaction product, liquid sodium, and $(U,Pu)O_2$. Knowledge of the sodium and oxygen partial pressures will permit us to calculate the O/M ratio below which reactions will not occur.

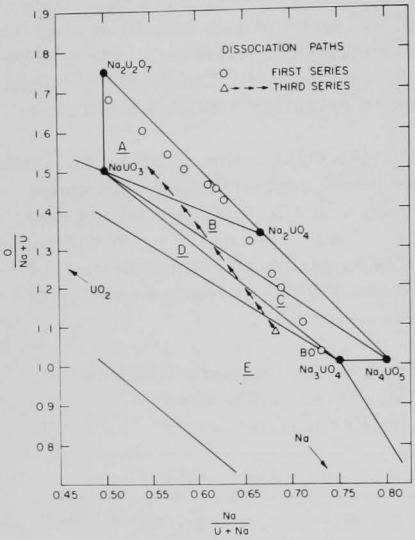

Fig. III 1. Na-U-O Phase Diagram; Three-Phase Regions Studied by Mass Spectrometry are Labeled A through E

Measurements were carried out on the U-O-Na system to establish data applicable to U-Pu-oxide fuels for low concentrations of plutonium. Three series of measurements (with two initial compositions) were made in which Na_3UO_4 and UO_2 disproportionated to sodium gas and to other U-O-Na condensed phases. The two paths of dissociation are shown in Fig. III-1. During the experiments, sodium pressures were measured by mass spectrometry and by weight loss of an effusion cell. Partial molar heats were also found by measuring ion intensities as a function of temperature. Oxygen pressures are high enough to measure in only one of the three-phase regions traversed in these experiments (i.e., $NaUO_3$-$Na_2U_2O_7$-Na_2UO_4; see ANL-7750, Fig. III-2, p. 55). In all the other regions, the oxygen pressures were computed from the sodium pressures and the equilibria between sodium, oxygen, and the condensed phases. The data are summarized in Table III-3.

TABLE III-3. Sodium and Oxygen Pressures and Partial Molar Enthalpies in the U-O-Na System at 1000°K

Three-Phase Regions in Fig. III-1	A	B	C	D	E
Phases	$Na_2U_2O_7$, $NaUO_3$, Na_2UO_4	Na_2UO_4, $NaUO_3$, Na_4UO_5	Na_4UO_5, $NaUO_3$, Na_3UO_4	Na_3UO_4, $NaUO_3$, UO_2	Na_3UO_4, UO_2, Na
P_{Na} (atm)	9.55×10^{-10}	5.25×10^{-8}	1.15×10^{-7}	5.50×10^{-7}	0.170
P_{O_2} (atm)	1.59×10^{-11}[a]	5.26×10^{-15}[b]	5.01×10^{-16}[b]	9.58×10^{-19}[b]	3.24×10^{-35}[b]
$\Delta\bar{H}_{Na}$ (kcal)	63.88 ± 2.75	61.00 ± 1.33	63.10 ± 1.92	63.06 ± 1.14	23.64[c]
$\Delta\bar{H}_{O_2}$ (kcal)	92.89 ± 2.65	98.7 ± 6.7[d]	92.3 ± 8.5[d]	92.5 ± 8.0[d]	210.7 ± 6.6[d]

[a]Measured above 1160°K and extrapolated to 1000°K.
[b]Calculated from sodium pressures and oxygen pressure in Region A.
[c]Reference 7.
[d]Calculated from the sodium partial molar enthalpies and the oxygen partial molar enthalpy in Region A.

c. Enthalpies and Entropies of Formation of Na-U-O Compounds

The enthalpies and entropies of formation at 1000°K of the five Na-U-O compounds shown in Fig. III-1 were calculated by two methods. In the first method, the enthalpy of formation of UO_2[7] corrected to 1000°K[8-10] and the measured slopes, RT^2 d ln p/dT, and intercepts for the vaporization of sodium in Regions A to E and oxygen in Region A were used to compute the enthalpy and entropy of formation. In the second procedure, the entropy of the compound was assumed to equal the sum of the entropies of the separate oxides, i.e., Na_2O,[8] UO_3,[11] and $UO_{2.5}$. For $UO_{2.5}$, a mean value between UO_2[9] and UO_3[11,12] was used. The enthalpies were computed from the sodium and oxygen pressures in Table III-3, enthalpy of formation of UO_2, and the estimated entropy of formation.

The results are summarized in Table III-4 where both sets of enthalpies and entropies of formation are tabulated for the compounds $NaUO_3$, $Na_2U_2O_7$, Na_2UO_4, Na_4UO_5, Na_3UO_4, and UO_2. The third-law enthalpy of formation for Na_3UO_4 based on our oxygen pressures is also listed. The third-law entropy of formation at 1000°K was computed from the entropies (at 1000°K) for Na_3UO_4,[4] Na and O_2,[8] and UO_2.[9]

d. Correlation of Data to the Sodium-Fuel Reaction

The thermodynamic properties of Na_3UO_4 have been measured to provide data for equilibrium calculations of the reaction between sodium and the mixed-oxide fuel (UO_2-PuO_2) of liquid-metal fast-breeder reactors (LMFBRs). The product formed when sodium reacts with $(U,Pu)O_2$ has been identified as $Na_3U_{1-y}Pu_yO_4$(Na_3MO_4) (ANL-7750), which is isomorphous with Na_3UO_4 with plutonium substituted for some of the uranium. The Pu/U atom ratio in Na_3MO_4 appears to be about the same as in the fuel [$(U,Pu)O_2$] from which it was formed.

The plutonium oxide content of the fuel is expected to be <30%, and since the thermodynamic properties of PuO_2 (i.e., enthalpy, entropy, heat capacity, and enthalpy of formation) are reasonably close to those of UO_2, it is expected that the thermodynamic properties of $Na_3U_{1-y}Pu_yO_4$ will not differ substantially from those of Na_3UO_4.

---

[7] E. J. Huber, Jr. and C. E. Holley, Jr., J. Chem. Thermodyn. 1, 273 (1969).

[8] JANAF Thermochemical Data, The Dow Chemical Co., Midland, Mich. (1963).

[9] D. R. Fredrickson and M. G. Chasanov, J. Chem. Thermodyn. 2, 623 (1970).

[10] R. Hultgren, R. L. Orr, P. D. Anderson, and K. K. Kelley, Selected Values of Thermodynamic Properties of Metals and Alloys, John Wiley & Sons, Inc., New York (1963).

[11] K. K. Kelley and E. G. King, Contributions to the Data on Theoretical Metallurgy, Bulletin 592, Bureau of Mines, U. S. Government Printing Office, Washington, D. C. (1961).

[12] K. K. Kelley, Contributions to the Data on Theoretical Metallurgy, Bulletin 584, Bureau of Mines, U. S. Government Printing Office, Washington, D. C. (1960).

TABLE III-4. Enthalpies and Entropies of Formation of Compounds in the Na-U-O System at 1000°K

Compound	Calculated from Slopes and Intercepts		Calculated from Pressures and Estimated Entropies		Literature Values at 298°K	
	$-\Delta H_f^\circ(1000°K)$, kcal mol^{-1}	$-\Delta S_f^\circ(1000°K)$, cal mol^{-1} K^{-1}	$-\Delta H_f^\circ(1000°K)$, kcal mol^{-1}	$-\Delta S_f^\circ(1000°K)$, cal mol^{-1} K^{-1}	$-\Delta H_f^\circ(298°K)$, kcal mol^{-1}	
UO_2[a]	258.5	40.6				
$NaUO_3$	344 ± 8[b,c]	60[b]	350	66[d]	357[e]	273[f]
$Na_2U_2O_7$	735 ± 15[b]	142[b]	745	152[d]		760[f]
α-Na_2UO_4	431 ± 13[b]	84[b]	439	92[d]	478[g]	448[f]
Na_4UO_5	555 ± 19[b]	116[b]	563	124[d]		577[f]
Na_3UO_4	469 ± 13[b]	94[b]	474	99[d]		
Na_3UO_4	479 ± 5[h]	103.3				

[a]Enthalpy and entropy of formation of 298°K[7] corrected to 1000°K.[8-10]
[b]Calculated from slopes and intercepts of sodium and oxygen logarithmic pressure curves and enthalpy of formation of UO_2.
[c]Uncertainties are two standard deviations.
[d]Entropies of Na-U-O compounds are assumed to equal the sum of entropies of Na_2O, UO_3, and $UO_{2.5}$ where $S_{UO_{2.5}} = (S_{UO_2} + S_{UO_3})/2$.
[e]King, Siemans, and Richardson,[13] preliminary value.
[f]Cordfunke and Loopstra.[14]
[g]Ippolitova et al.[15]
[h]Calculated from oxygen pressures and free energy functions and the enthalpy of formation of UO_2.

The equilibrium reaction in the three-phase region (UO_2-Na-Na_3UO_4) may be written as

$$3\ Na(\ell) + UO_2(c) + O_2\ (\text{in } UO_2) = Na_3UO_4(c) \tag{1}$$

The data from this study and three additional studies[4-6] are used to calculate the equilibrium oxygen pressure as a function of temperature and sodium activity,

$$\ln P_{O_2}(\text{atm}) = \frac{-220{,}500}{RT} + \frac{62.7}{R} - 3 \ln a_{Na} \tag{2}$$

where the quantity -220,500 is the difference in the enthalpies of formation for Na_3UO_4 and UO_2, and the quantity 62.7 is the corresponding difference in the entropies of formation. If the sodium is in contact with or at the

[13]E. G. King, R. E. Siemans, and D. W. Richardson, Quarterly Metallurgical Progress Report No. 51, April 1, 1971, June 30, 1971, U. S. Bureau of Mines report USBM-RC-1516 (1971).
[14]E. H. P. Cordfunke and B. O. Loopstra, J. Inorg. Nucl. Chem. 33, 2427 (1971).
[15]E. A. Ippolitova, D. G. Faustova, and V. I. Spitsyn, "Determination of Enthalpies of Formation of Mono Uranates of Alkali Elements and Calcium," in Investigations in the Field of Uranium Chemistry, V. I. Spitsyn, Ed., ANL-Trans.-33, p. 170 (1964).

same temperature as the oxides, the last term is zero. When there is a temperature gap, the sodium activity will be lowered.

The equilibrium oxygen content of $U_{0.8}Pu_{0.2}O_{2-x}$ in contact with sodium and Na_3MO_4 has been calculated from Eq. 2 and extrapolated data of Rand and Markin[1] for the O/M atom ratio of the fuel as a function of oxygen pressure. These values are given in Table III-5 together with the oxygen content of the sodium, which is discussed below. In this calculation, it is assumed that the Na-U-O system approximates the Na-U-Pu-O system for low concentrations of plutonium [i.e., Pu/(U + Pu) < 0.3].

TABLE III-5. Calculated Oxygen Content of $(U_{0.8}Pu_{0.2})O_{2-x}$ and of Na in Equilibrium with Na_3MO_4

Temperature, °K	Equilibrium Oxygen Pressure,[a] atm	$-\Delta\bar{G}_{O_2}$, kcal/mol	O/(U + Pu) Ratio[b]	Oxygen Conc. in Na,[c] ppm
600	2.4×10^{-67}	183	1.92	0.07
700	7.3×10^{-55}	177	1.93	0.12
800	2.9×10^{-47}	170	1.94	0.9
900	1.4×10^{-40}	164	1.94_5	4.5
1000	3.3×10^{-35}	158	1.95	16
1100	7.8×10^{-30}	151	1.95_5	47
1200	3.5×10^{-27}	145	1.96	110

[a]Calculated from Eq. 2.
[b]Extrapolated from Rand and Markin's data.[1]
[c]Calculated from Eq. 3.

The equilibrium oxygen content (in ppm) of sodium in contact with UO_2 and Na_3UO_4 is given by

$$\ln [O](\text{ppm}) = \frac{-11{,}550}{T} + 14.33 \qquad (3)$$

This equation was derived from the free energy of formation of Na_2O,[8] the solubility of Na_2O in Na,[16] and Eq. 2 for the oxygen pressure in equilibrium with the three-phase region Na-UO_2-Na_3UO_4. The calculated oxygen concentrations are listed in Table III-5.

To control the undesirable sodium-fuel reaction in a liquid metal fast-breeder reactor, the oxygen-to-(U + Pu) ratios for the fuel and oxygen content of the sodium (at thermodynamic equilibrium) must be held below the levels given in Table III-5. An important result of our research is the requirement for using lower oxygen concentrations in the fuel and in the sodium as the temperature is decreased.

[16]T. F. Kassner and D. L. Smith, ANL-7335 (1967).

Since control of the sodium-fuel reaction may significantly affect the specifications for oxygen content in the initial fuel and in coolant sodium, it is important that the equilibrium oxygen contents be firmly established. To be sure that the Na-U-O data can be applied to the system containing plutonium, we are studying the Na-U-Pu-O system. Mass-spectrometric studies are being carried out using a procedure parallel to that used with the Na-U-O system.

3. Partial Relative Ion Cross Sections of U and U-O Molecules and Partial Pressures over the U-Pu-O System

For LMFBR U-Pu-O fuel, it is important to know the partial pressures of gases over the fuel in order to establish the conditions (temperature and fuel oxygen concentration) for redistribution of uranium and plutonium by vapor transport. The data can also be used to calculate oxygen pressures of the fuel as a function of oxygen concentration at high temperatures.

Mass-spectrometrically measured ion intensities were previously reported[17] for UO_2-20 wt % PuO_2. To calculate pressures from ion intensities, the following are needed: ionization probabilities, fragmentation patterns, and relative ion cross sections. These quantities were measured in the study reported here.

The equipment for the measurements consisted of an inductively heated Knudsen cell, a Granville-Phillips Spectra Scan 750 quadrupole mass spectrometer, and an Airco Temescal quartz crystal balance in an ultrahigh vacuum system. The system, with the exception of the quartz balance and mass spectrometer, was described previously.[18]

A tungsten Knudsen cell, filled with a weighed sample of known oxygen content, was used as a molecular beam source. An iridium liner was used for UO_{2+x} samples. The collimated beam passed through the ionizing section of the mass spectrometer and impinged on the quartz balance. With this arrangement, both the rate of effusion and the mass spectrum of the molecular beam could be measured simultaneously. Samples used in these measurements were initially $UO_{2.1}$, $UO_{1.96}$, UO_{2-x} plus U, and U. Vapor over the $UO_{2.1}$ sample at 1560°C consisted of $UO_3(g)$ and oxygen, with less than 0.01% $UO_2(g)$ and U(g), based on literature data.[19,20] The vapor over the uranium metal sample was all U(g). By suitable choice of sample and corrections for fragmentation of the other U-O gases, it was possible to establish curves for UO_2 and UO, even though these two gases are never present alone.

---

[17] J. E. Battles, W. A. Shinn, P. E. Blackburn, and R. K. Edwards, in Plutonium 1970 and Other Actinides, p. 733, W. N. Miner, Ed., Institute of Mining, Metallurgical, and Petroleum Engineers, New York (1970).

[18] R. K. Edwards, M. S. Chandrasekharaiah, and P. M. Danielson, High Temp. Sci. 1, 98 (1969).

[19] R. J. Ackermann, E. G. Rauh, and M. S. Chandrasekharaiah, A Thermodynamic Study of the Urania-Uranium System, ANL-7048, p. 30 (1965).

[20] K. Hagemark and M. Broli, J. Inorg. Nucl. Chem. 28, 2837 (1966).

The ionization probabilities of U, UO, UO_2, and UO_3 were computed from the measurements and normalized for each molecule to its maximum value. These values were used, together with some additional measurements (described below), to establish the partial relative ion cross sections as a function of ionizing voltage (see below).

a. Fragmentation of Uranium Oxide Molecules

Fragmentation patterns as a function of electron energy were obtained from analysis of the vapor over $UO_{2.1}$, $UO_{1.96}$, and UO_{2-x} plus U. Ratios of ion fragments to ion parents as a function of electron energy are given in Table III-6.

TABLE III-6. Fragmentation as a Function of Electron Energy

Ion Precursor	Ion Fragment	Electron Energy, eV								
		10	12	14	16	18	20	25	30	40
		Fragment Ion/Precursor Ion Ratio								
UO	U^+			0.02	0.05	0.13	0.20			
UO_2	UO^+		0.027	0.11	0.22	0.36	0.46	0.74	0.78	0.9[a]
UO_3	UO_2^+	0.64	1.03	2.05	2.4	2.3	2.4	2.7	3.1	3.4
UO_3	UO^+			0.042	0.086	0.10	0.26	0.68	1.4	2.3

[a]Estimated.

b. Partial Relative Ion Cross Sections

The product of the mass-spectrometer multiplier efficiency and the partial relative ion cross sections of U, UO, UO_2, and UO_3 was determined from the simultaneous measurement of the mass-spectrum ion intensities and rate of condensation on the quartz-crystal balance. The partial relative ion cross sections here refer only to the probability of forming an ionized parent molecule (ion fragments are not included).

The total deposition rate, G_T, for U, UO, UO_2, and UO_3 can be calculated from

$$KG_T = \frac{I_U+\sqrt{238T}}{\gamma_U\bar{\sigma}_U} + \frac{I_{UO}+\sqrt{254T}}{\gamma_{UO}\bar{\sigma}_{UO}} + \frac{I_{UO_2}+\sqrt{270T}}{\gamma_{UO_2}\bar{\sigma}_{UO_2}} + \frac{I_{UO_3}+\sqrt{286T}}{\gamma_{UO_3}\bar{\sigma}_{UO_3}} \qquad (4)$$

where the four γ's, the four $\bar{\sigma}$'s, and four I^+'s are multiplier efficiency, partial relative ion cross sections, and ion intensities, respectively, of each of the gases, T is the absolute temperature, and K is a constant.

In determining the product of the multiplier efficiency and the partial relative ion cross section for $UO_3(g)$, the $UO_{2.1}$ sample was used

where the vapor consists of $UO_3(g)$ and O_2 only. During the experiment, UO_3^+ was found along with WO_3^+, WO_2^+, and WO^+ ions from oxidation of the tungsten outer cell. X-ray fluorescence analysis of the deposit on the quartz crystal and mass-balance treatment of the tungsten Knudsen cell, iridium liner, and UO_{2+x} sample established that the UO_3 constituted 75 ± 5 wt % of the depositing vapor.

The integrated ion-intensity curve at an electron energy of 20 eV, temperature, weight change, and the UO_3 fraction of the total weight change were used in Eq. 4 to obtain the product $K\gamma_{UO_3}\bar{\sigma}_{UO_3}$. In this case, the first three terms on the right side of Eq. 4 were equal to zero.

A similar treatment was used with only uranium vaporizing at an electron energy of 10 eV to obtain $K\gamma_U\bar{\sigma}_U$. It was not possible to measure UO_2 or UO alone. Instead, nine measurements were obtained with 10-eV ionizing electrons and varying amounts of U, UO, and UO_2 in the vapor. These data were fitted by least squares to Eq. 4 with the UO_3 term deleted. From this treatment, values were obtained for $K\gamma_U\bar{\sigma}_U$, $K\gamma_{UO}\bar{\sigma}_{UO}$, and $K\gamma_{UO_2}\bar{\sigma}_{UO_2}$.

The product of the multiplier efficiency and partial relative ion cross section ($\gamma_U\bar{\sigma}_U$) was normalized to 1 for the uranium at its maximum value. Table III-7 lists the products of multiplier efficiency and partial relative ion cross section as a function of electron energy. The partial relative ion cross sections relative to uranium are smaller than the total relative ion cross sections (which include ion fragments). For example, at 40 eV the total cross section ratio σ_{UO_3}/σ_U is ~0.5 compared with ~0.07 for the corresponding partial ratio. The factors measured here--ionization probability, fragmentation, and the product of multiplier efficiency and the partial relative ion cross section--are used to correct the uranium oxide pressures measured over $U_{0.8}Pu_{0.2}O_{2-x}$. These new values in turn are used to calculate oxygen pressures for the fuel at high temperatures.

TABLE III-7. Product of Multiplier Efficiency and Partial[a] Relative Ion Cross Section as a Function of Electron Energy

	Electron Energy, eV										
	6	8	10	12	14	16	18	20	25	30	40
	Product of Multiplier Efficiency and Partial Relative Ion Cross Sections[b]										
$\gamma_U\bar{\sigma}_U$	-	0.25	0.66	0.89	0.98	0.98	0.91	0.88	0.61	0.42	0.23
$\gamma_{UO}\bar{\sigma}_{UO}$	0.94	1.32	1.29	1.23	1.23	1.12	0.97	0.84	0.42	0.30	0.15
$\gamma_{UO_2}\bar{\sigma}_{UO_2}$	0.31	0.33	0.31	0.30	0.30	0.28	0.26	0.22	0.18	0.09	0.05
$\gamma_{UO_3}\bar{\sigma}_{UO_3}$	-	-	0.0021	0.0122	0.0206	0.027	0.034	0.038	0.037	0.028	0.016

[a]Calculated with parent ions only (ion fragments are not included).
[b]Normalized to $\gamma_U\bar{\sigma}_U$ = 1 at 15 eV.

c. Calculation of UO_3, UO_2, and O_2 Pressures over $U_{0.8}Pu_{0.2}O_{2-x}$

Table III-8 lists the UO_2 and UO_3 pressures calculated with fragmentation and multiplier efficiency cross-section corrections and pressures calculated without these corrections to illustrate the effect of the corrections on the calculated pressures. In the absence of cross-section data for PuO and PuO_2, it was assumed that the $(PuO + PuO_2)/(UO_3 + UO_2)$ ratio is equal to the corresponding ion-intensity ratio.

TABLE III-8. Partial Pressures of UO_2 and UO_3 and Oxygen Potentials over UO_2-20 wt % PuO_2 as Function of Oxygen-to-Metal (O/M) Ratio at 2240°K

			Pressure, 10^{-6} atm					
			Uncorrected		With Ion Cross Section and Fragmentation Corrections		$-\Delta\bar{G}_{O_2}$, kcal/mol	
Run No.	Gas Fusion Analysis, O/M	Smoothed O/M[a]	UO_2	UO_3	UO_2	UO_3	This Research	Rand & Markin[b]
4A-2	1.973	1.98	11.3	1.9	3.7	9.3	79	97
4A-4	1.964	1.97	9.2	1.1	3.6	6.4	82	100
4A-6	1.962	1.96	7.9	0.68	3.8	5.0	85	104
4A-8	1.952	1.95	6.4	0.34	3.8	3.0	89	109
4A-10	1.909	1.94	5.7	0.21	3.8	2.1	92	114
4A-12	1.934	1.93	5.3	0.15	3.9	1.7	95	119
5A-3	1.977	1.98	12.1	2.5	3.5	11.1	77	98
5A-5	1.954	1.97	9.0	1.1	3.4	6.7	81	100
5A-7	1.977	1.97	6.6	0.49	3.3	3.7	86	103
5A-9	-	1.96	5.2	0.22	3.4	2.1	91	106
5A-9A	1.971	1.96	5.6	0.21	3.8	2.1	88	108
5A-9B	2.017	1.95	5.2	0.17	3.5	1.8	93	109
5A-11	1.934	1.95	5.8	0.24	3.8	2.3	91	113
5A-13	1.930	1.94	5.0	0.14	3.6	1.5	95	116
5A-15	1.934	1.93	5.6	0.13	4.2	1.5	96	119
5A-17	1.922	1.93	5.0	0.11	3.9	1.3	97	122

[a]The smoothed O/M ratios were calculated by least-squares fit to a linear equation in the sets of measurements in each of the series 4A and 5A. Standard deviation of calculated O/M is ±0.020.
[b]Extrapolated from 1000°C using data in Ref. 1.

The newly calculated data indicate that UO_2 pressures are nearly constant over the composition range measured. This is consistent with Raoult's law and Gibbs-Duhem treatment as it applies to the behavior of the 80% UO_2 solvent. The UO_2 pressures are also in reasonable agreement with those calculated from the literature[19] for pure UO_2. At 2240°K, the calculated pressure over UO_2 is 3.7×10^{-6} atm.

The UO_3 and UO_2 pressures were used to calculate oxygen pressures at 2240°K. These were calculated from the reaction

$$2\ UO_3(g) = 2\ UO_2(g) + O_2$$

The equilibrium constant for this reaction was calculated from the data of Ackermann, Rauh, and Chandrasekharaiah.[19]

Oxygen potentials computed from the calculated oxygen pressures are listed in Table III-8 with the extrapolated oxygen potentials

of Rand and Markin.[1] We also calculated the average partial molar enthalpy for oxygen to be -186 kcal/mol of O_2 from the partial molar enthalpies of vaporization of UO_2 and UO_3 gas.[17]

B. Chemistry of Irradiated Fast-Reactor Fuels and Materials

The chemical behavior of irradiated fast-reactor fuels is being studied to gain an understanding of the complex processes that occur in these fuels during irradiation. Effort is being directed toward the study of irradiated uranium-plutonium oxide fuels, with particular emphasis on investigating the effect of oxygen potential on the distribution of fission products and establishing the relationship between fission-product migration and fuel-cladding interactions.

1. Ion Microprobe Analysis of Stainless Steel

An ion microprobe mass analyzer (IMMA) is being procured by the Chemical Engineering Division. With this instrument, sample atoms are ionized by a finely focused ion beam that impinges on the sample surface. Ions of many different elements can be used for sample bombardment, the choice depending on the matrix and on the element to be determined. The sample ions are collected and mass-analyzed in a double-focusing mass spectrometer with a high collection efficiency.

The IMMA will supplement the capabilities of the electron probe microanalyzer for analyzing irradiated fuels in several important ways. The IMMA provides uniform sensitivity of detection at the parts-per-million level for the full mass range of elements. This is especially important for the low mass range; with the electron probe microanalyzer, the elements hydrogen to carbon cannot be detected and the elements from carbon through oxygen can be detected only with low sensitivity. Furthermore, since the IMMA collects isotopic data, it provides a direct means for differentiating between fission products and structural materials.

Before final plans had been made to purchase the IMMA, several sections of Type 304 stainless steel capsules that had previously contained cesium oxide were used to assess the capabilities of the IMMA for analyzing samples of interest to the fuels program. These capsules[21] had been heated at 690°C for various lengths of time under otherwise identical conditions to examine the action of cesium oxide[22] on stainless steel. The two sections that we examined with the IMMA had been heated for 25 and 72 hr. It should be emphasized that the quantity of cesium and the pressure of oxygen used in these out-of-pile experiments had been significantly greater than those calculated for irradiated fuels. The higher concentrations had been employed

[21] Capsule tests were performed by P. S. Maiya, Materials Science Division, ANL.
[22] The cesium oxide material used in these tests was richer in oxygen than is Cs_2O.

to accelerate any chemical reactions that might occur and cause their effects to be more visible in the limited time of the experiments.

The capsule sections were analyzed[23] with the IMMA for cesium and oxygen using a nitrogen-ion beam having a diameter of 20 ± 5 μm. Each sampled location was first thoroughly "cleaned" by etching with the nitrogen-ion beam to ensure that the area being analyzed was free of surface contamination. After a consistent analysis had been obtained in a given location, digitized data were collected at selected mass positions.

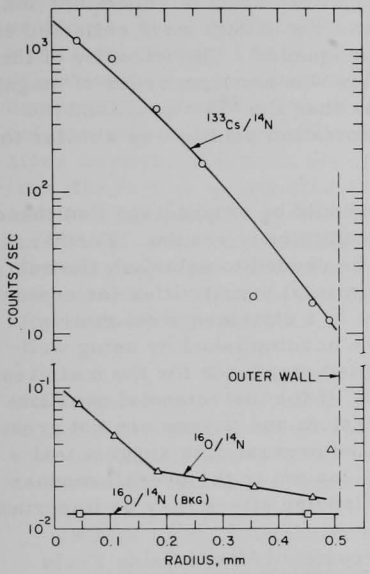

Fig. III-2. Ion-microprobe Analysis for ^{133}Cs and ^{16}O in Stainless Steel Exposed to Cesium Oxide at 690°C for 72 hr. ANL Neg. No. 308-2786.

Data for cesium and oxygen were collected across the radius of each capsule cross section from the inner surface to the periphery to determine the concentration gradients of these elements in the stainless steel. (The wall thickness of the capsules was 0.508 mm.) Relative concentrations of ^{133}Cs and ^{16}O for the sample heated for 72 hr are presented in Fig. III-2 and similar data for the sample heated for 25 hr, in Fig. III-3. Each datum point was normalized against the ^{14}N ion-beam count rate. The profiles are similar in both samples, with expected increases in the observed concentration of ^{133}Cs and ^{16}O for the sample that had been at temperature for the longer time period. Each sample exhibits easily detected concentrations of cesium across the capsule wall and a gradient in the cesium concentration of about two orders of magnitude. The level of cesium at the outer surface of the capsule is still some two orders of magnitude above that in the blank. The rapidity with which cesium had penetrated the capsule wall is of considerable interest. The mechanism for the cesium transport has not yet been established but is under investigation.

The levels of oxygen found in the stainless steel are considerably lower (by a factor of ~10^5) than those of cesium, the levels of oxygen at the outer surface of the capsule approaching the background level. The oxygen had penetrated deeper into the capsule wall in the longer term experiment.

The data may be interpreted to indicate that cesium is preceding oxygen in its diffusion into the stainless steel, probably along the grain

[23] Analyses were performed by the Applied Research Laboratories, Santa Barbara, California.

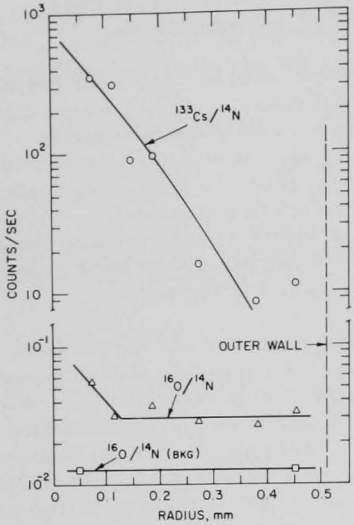

Fig. III-3. Ion-microprobe Analysis for ^{133}Cs and ^{16}O in Stainless Steel Exposed to Cesium Oxide at 690°C for 25 hr. ANL Neg. No. 308-2785.

boundaries. The diffusion of oxygen is possibly slowed by competing reactions as it too moves along a grain boundary. A number of competitive reactions can occur in the stainless steel to tie up oxygen, e.g., formation of chromium and iron oxides. Some data were collected on these oxide species. The intensity of the CrO species was about an order of magnitude higher than the ^{16}O signal, and the CrO concentration profile was similar to that of ^{16}O.

It should be emphasized that these are only preliminary results. Further work will be needed to establish the relative instrumental sensitivities for cesium and oxygen in a stainless steel matrix. This can be accomplished by using well-characterized standards for the matrices of interest. If the instrumental sensitivities for cesium and oxygen are not greatly different, the present data suggest that the role of cesium in the overall mechanism for cladding attack may be important.

2. Oxygen Potential Gradients in Irradiated Mixed Oxide Fuels

a. Electron Microprobe Analysis of Irradiated Fuels

The electron probe microanalyzer, which accomplishes microsampling and microanalysis directly, is being used to study fission-product distributions in irradiated fuels. The instruments used in these studies (Applied Research Laboratories Models EMX and EMX-SM) are equipped with shielding to handle irradiated fuel specimens having gamma activities as great as 1 R/hr at 1 ft.

The Model EMX microprobe has been adapted for computer control to facilitate its operation. Spectrometer movement, data acquisition, and readout onto punched paper tape are controlled through a simple set of instructions entered through the teletype keyboard. Data reduction to net counting rate, complete with an estimate of the standard deviation, is accomplished by a "DISCOM" program which accepts as input the paper tape generated by the computer-controlled microprobe.

Recent emphasis has been placed on the detailed examination of NUMEC fuel element C-15. This mixed-oxide pellet fuel, which had a

density of 85% of theoretical and an initial oxygen-to-metal (O/M) ratio of 1.998, was irradiated in EBR-II to 9.4 at. % burnup at a maximum linear power rating of 12.9 kW/ft.

Electron microprobe analyses were carried out on the metal inclusions that have often been observed in irradiated fuels and have previously been identified by electron microprobe analysis.[24-26] Inclusions were first examined to determine their elemental compositions. The microprobe analysis established that these inclusions were homogeneous for each component. Of particular interest in this study were the inclusions in the columnar-grain region of the fuel; the principal components of these inclusions were molybdenum, technetium, ruthenium, rhodium, palladium, and iron (the iron is an impurity in the fuel). Count-rate data for each element and for a standard of each element were processed on a computer using the MAGIC (Microprobe Analysis General Intensity Correction)[27] program to yield weight percent of each component in the alloy. The MAGIC program corrects the X-ray data for absorption, fluorescence, and atomic-number effects due to the matrix.

The compositional data (in weight percent) for the inclusions examined in fuel element C-15 are given in Table III-9 as a function of radial distance from the fuel center. A comparison of the data in Table III-9 with calculated fission-yield ratios reveals that the concentrations of molybdenum in the inclusions are extremely low in relation to the concentrations

TABLE III-9. Composition of Metal Inclusions in Columnar-Grain Region of NUMEC Element C-15

Sample No.	Distance from Center,[a] mm	Composition, wt %					
		Mo	Tc	Ru	Rh	Pd	Fe
1	0.89	7.31	21.4	52.1	14.4	4.57	0.26
2	1.00	8.61	21.2	50.3	16.9	2.60	0.32
3	1.09	8.11	23.4	47.0	18.7	2.38	0.37
4	1.26	9.49	18.5	47.8	20.9	2.85	0.38
5	1.42	10.5	18.7	43.5	24.0	2.73	0.48
6	1.67	11.6	18.1	40.3	25.4	3.73	0.77
7	1.78	11.0	24.5	38.6	21.3	3.48	1.16
8	1.96	6.99	29.1	41.4	16.4	3.72	2.35

[a]Fuel radius = 2.794 mm.

[24]N. R. Stalica and C. A. Seils, Proc. Amer. Ceram. Soc., Washington, May 7, 1969, p. 215 (1969).
[25]J. I. Bramman, R. M. Sharpe, D. Thom, and C. Yates, J. Nucl. Mater. 25, 201 (1968).
[26]D. R. O'Boyle, F. L. Brown, and J. E. Sanecki, J. Nucl. Mater. 29, 27 (1969).
[27]J. W. Colby in Advances in X-Ray Analysis, Vol. 11, p. 287, Plenum Press, New York (1968).

of the noble-metal fission products. The relatively constant concentrations of molybdenum in the inclusions found in the columnar-grain region suggest that equilibrium had been attained between metallic molybdenum in the inclusions and oxidized molybdenum in the contiguous fuel-oxide matrix (this is discussed in the following section).

Accordingly, the oxide matrix of NUMEC C-15 was analyzed for molybdenum by means of the automated electron probe. Determination of the low concentrations of molybdenum found in the matrix, which has been a difficult and time-consuming task in the past, is readily accomplished with the automated probe. The results of the analyses are given in Table III-10. The molybdenum concentration ranges from 0.05 wt % at the central void edge to a low of about 0.03 wt % at the cool end of the columnar-grain region and then increases sharply in the equiaxed region to a maximum concentration of 0.45 wt % in the outer, cooler region of the fuel.

TABLE III-10. Molybdenum Concentration in UO_2-PuO_2 Fuel Matrix of NUMEC Element C-15

Distance from Fuel Center, mm	Molybdenum Concentration, wt %
0.844	0.0489
0.880	0.0496
0.922	0.0506
1.084	0.0593
1.391	0.0359
1.411	0.0441
1.497	0.0390
1.643	0.0376
1.900	0.0421
1.972	0.0266
2.118	0.0241
2.207	0.0517
2.277	0.0564
2.403	0.0733
2.528	0.123
2.626	0.235
2.738	0.265
2.738	0.381
2.738	0.447

The concentration profile for molybdenum is similar to the profiles observed previously for fission-product krypton and cesium.[28] These

[28] C. E. Johnson, D. V. Steidl, and C. E. Crouthamel, Distribution of Gaseous Fission Products in Irradiated Mixed-Oxide Fuels, Trans. Amer. Nucl. Soc. 14 (Suppl. 1), 27 (April 1971); see also, ANL-7833, p. 5.10.

data are consistent with our present understanding of the migration behavior of molybdenum. Near the central void, migration is influenced by pore migration as pores pile up in this region of decreasing thermal gradient. Migration throughout the rest of the fuel is influenced by the local oxygen activity, which, in turn, is influenced by the thermal gradient. In the equiaxed and undisturbed regions, an additional influence on migration is the formation of cesium molybdate, which serves to stabilize the molybdenum in a local area.

b. Estimation of Oxygen Potential Gradient in Irradiated Mixed-Oxide Fuel from Distribution of Molybdenum

The most important single chemical property of a mixed urania-plutonia fuel with respect to its usage as a nuclear fuel is its oxygen potential. In irradiated oxide fuels, the chemical form of the fission products, which is strongly dependent on the oxygen potential, determined (1) their chemical reactivity, and hence, the extent of fuel-cladding interaction; and (2) their specific volume, and hence, the extent of solid fuel swelling. The oxygen potential also governs the extent of fuel-sodium reaction in the event of a cladding rupture.

The large radial temperature gradient that exists in a fuel during irradiation will lead to a gradient in the oxygen potential, which may be expressed as follows:

$$\Delta\overline{G}_{O_2} = RT \ln p_{O_2}$$

where p_{O_2} is the partial pressure of oxygen (in atm) of the system. Because of the existence of this oxygen potential gradient, a redistribution in the oxygen occurs. Rand and Markin[29] have proposed that the oxygen potential of an oxide fuel in a temperature gradient can be calculated if it is assumed that local equilibrium exists everywhere between the solid fuel and a gaseous CO_2-CO-O_2 mixture in which the CO_2/CO partial-pressure ratio is constant. (The source of the CO and CO_2 is a carbon impurity in the fuel.) Studies of unirradiated urania-plutonia mixtures under temperature gradients,[30] have indicated that the oxygen redistribution can be only partially predicted by the Rand and Markin model, and that the oxygen distribution depends not only on the initial O/M ratio of the oxide and the temperature gradient but also on the length of time the specimen has been in the temperature gradient. The uncertainties introduced by the buildup of fission-product elements in the fuel makes the computation of the oxygen potential gradient in an irradiated fuel by any of the current models highly inaccurate.

---

[29] M. H. Rand and T. L. Markin, in Thermodynamics of Nuclear Materials, 1967, pp. 637–650, IAEA, Vienna (1968).

[30] E. A. Aitken and S. K. Evans, GEAP-12047 (June 1970).

We have developed a new method for calculation of the oxygen potential, based on the distribution of molybdenum in the fuel (see preceding section). The basic concept of the method involves the assumptions that (1) at each point in the fuel during irradiation (i.e., under a temperature gradient), a local equilibrium exists between the oxidized and reduced forms of a fission product that function as a "redox-indicator" system and (2) the system is frozen into place when the fuel pin is cooled. The Mo-MoO_2 system was chosen as the redox-indicator system for the following reasons:

(1) The oxygen potential of the Mo-MoO_2 system is in an appropriate range for the mixed-oxide fuel system.

(2) The reduced and oxidized forms of molybdenum, a fission product with a high yield, exist in the cooled fuel pin in separate phases (metallic inclusions and fuel matrix) at concentrations that can be determined by the electron microprobe.

(3) The mobility of both the reduced and oxidized forms of molybdenum decreases rapidly as the temperature of the fuel decreases and hence are quenched into position.

(4) The oxidized form has a relatively high mobility in the fuel.

(5) The Mo-MoO_2 system is not sensitive to chemical reaction during the preparation of the fuel specimens for microprobe examination.

With the assumption, stated above, that at each point in the fuel during irradiation, a local equilibrium exists between the reduced (metallic) molybdenum in the noble-metal alloy inclusion and the oxidized molybdenum in the oxide matrix, the following equation may be used to calculate the oxygen potential at each position in the fuel pin:

$$\Delta\overline{G}_{O_2} = \Delta Gf^{\circ}_{MoO_2} + RT \ln \frac{a_{MoO_2}}{a_{Mo}}, \qquad (1)$$

where $\Delta Gf^{\circ}_{MoO_2}$ is the standard free energy of formation of MoO_2,[31] a_{Mo} is the activity of molybdenum in a noble-metal alloy inclusion, and a_{MoO_2} is the activity of molybdenum (as the dioxide) in the oxide matrix adjacent to the metallic inclusion. To compute the oxygen potential from Eq. 1, the temperature of the fuel at the location of the alloy inclusion must be estimated, and the molybdenum contents of the alloy inclusion and oxide matrix as determined by electron microprobe analysis must be converted into activities.

[31] JANAF Thermochemical Data, Dow Chemical Co., Midland, Mich. (June 30, 1967).

The radial temperature profile of a given fuel-pin section was computed[32] assuming a steady-state heat flow in cylindrically symmetrical geometry. The temperatures were computed stepwise by dividing the oxide fuel into small cylindrical segments and assuming that the thermal conductivity of each segment was constant. The value of the thermal conductivity for each segment was computed by an iterative procedure using the equation reported by Baily et al.[33] The dimensions of each region (columnar-grain, equiaxial-grain, and unrestructured regions) were obtained as a part of the electron microprobe analyses. The starting density of the unirradiated fuel (85% of theoretical) was used for the density of the unrestructured region, whereas the densities of the equiaxial- and columnar-grain regions were assumed to be 96.0 and 98.5% of theoretical, respectively.

The activity of molybdenum in the noble-metal alloy inclusions was computed from the molybdenum atom fraction and an estimated value for the activity coefficient. These noble-metal inclusions are known[34] to be hexagonal, close-packed (epsilon), solid-solution alloys of molybdenum, ruthenium, technetium, rhodium, and palladium containing a small amount of iron. The integral free energy equation based on the regular solution model given by Kaufman and Bernstein[35] was differentiated to obtain an equation for the partial molar free energy of molybdenum in the above five-component alloy (the small iron content was neglected). The lattice-stability and interaction parameters for molybdenum, ruthenium, rhodium, and palladium reported by Kaufman and Bernstein[35] were used in these calculations; parameters for technetium were estimated.

It was assumed that, in the columnar-grain region, the molybdenum present in the oxide matrix forms a solid solution in the mixed-oxide fuel when the fuel pin is at irradiation temperatures. From preliminary studies of the composition of the gaseous species in equilibrium with a mixture of urania and MoO_2 as determined by a Knudsen effusion-mass-spectrometric study,[36] it was estimated that the activity coefficient of MoO_2 is 0.5_2 at 1693°K. The regular solution model was used to estimate the activity coefficients at temperatures of interest in the present study.

These activity coefficients, along with the concentrations of molybdenum in the inclusions and oxide matrix determined by electron microprobe analysis, were used to compute the oxygen potential in the columnar-grain region of the fuel element. The results are given in Table III-11. Since the irradiated fuel also contains cesium, the possibility

---

[32]The assistance of R. H. Land, Computer Applications Group, CEN, is gratefully acknowledged.

[33]W. E. Baily, E. A. Aitken, R. R. Asamoto, and C. N. Craig, Int. Sym. on Plutonium Fuels Technology, Nuclear Metallurgy, Vol. 13, p. 297, (Eq. 5), AIME (1968).

[34]D. R. O'Boyle, F. L. Brown, and A. E Dwight, J. Nucl. Mater. 35, 257–266 (1970).

[35]L. Kaufman and H. Bernstein, Computer Calculation of Phase Diagrams, Academic Press, New York (1970).

[36]Chemical Engineering Division Fuels and Materials Chemistry Semiannual Report, January–June 1971, ANL-7822, p. 15 (1971).

that some of the molybdenum might be present as cesium molybdate was investigated by a consideration of the reaction:

$$[MoO_2]_{oxide}\ (s) + O_2(g) + 2\ Cs(g) = Cs_2MoO_4(\ell) \qquad (2)$$

TABLE III-11. Calculated Oxygen Potential for Fuel Element NUMEC C-15

Location			Molybdenum Activity		
No.	Distance from Center, mm	Temp, °K	Alloy	Oxide	$\Delta\bar{G}_{O_2}$, kcal/mol
1	0.84	2368	0.023	8.5×10^{-4}	-61.7
2	0.89	2363	0.023	7.9×10^{-4}	-62.2
3	1.00	2353	0.028	7.0×10^{-4}	-64.0
4	1.09	2338	0.026	6.3×10^{-4}	-64.4
5	1.26	2293	0.032	5.3×10^{-4}	-67.5
6	1.42	2238	0.036	4.6×10^{-4}	-70.1
7	1.67	2118	0.039	4.0×10^{-4}	-74.2
8	1.73	2028	0.032	3.9×10^{-4}	-76.0
9	1.96	1943	0.016	4.1×10^{-4}	-75.5

The cesium partial pressure was computed using the values of the MoO_2 activity and oxygen potential shown in Table III-11 together with an estimate of the enthalpy and entropy of formation of Cs_2MoO_4. It was found that for locations 1 to 7 (see Table III-11) the cesium pressure was about 1 atm, but decreased to about 0.2 atm for location 9. It seems unlikely that the cesium pressure would be greater than the vapor pressure of metallic cesium at the cladding, which at 600°C is about 0.6 atm. Therefore, it is concluded that, in most of the columnar grain region, cesium molybdate does not form as a separate phase and, therefore, the molybdenum concentration in the oxide matrix can be used to estimate the molybdenum activity for this region of the fuel, as described above. However, in the cooler regions of the fuel (the equiaxial-grain and unrestructured regions), cesium molybdate probably does form, and the MoO_2 activity is no longer directly proportional to the molybdenum concentration. The rapid rise in molybdenum content of the oxide matrix in the outer, cooler regions of the fuel (see Table III-10) probably reflects the formation of cesium molybdate in these regions.

C. Reactor Safety and Physical Property Studies

The primary objective of these studies is to provide physical-property data for use in evaluating the safety of various fast-breeder-reactor materials. The property data obtained experimentally at temperatures above normal operating conditions of reactors will also be extrapolated

to the much higher temperatures involved in accident situations. In addition, reactor material-fuel phase studies at high temperatures are under way to provide chemical information needed on fission-product distribution between molten fuel and other reactor materials for use in post-accident heat-removal calculations.

1. Enthalpies and Heat Capacities by Drop Calorimetry

Three complementary calorimetric systems for the measurement of high-temperature enthalpy increments are available for our use. Depending on the material to be studied and the temperature range to be covered, one may choose

(1) the resistance-heated drop-calorimetric system (600-1600°K),

(2) the electron-beam-heated drop-calorimetric system (1300-2500°K), or

(3) the induction-heated drop-calorimetric system (2500-3600°K).

During this period, systems (1) and (3) have been used for making measurements.

a. Resistance-Heated Calorimetric System

The compound Na_3UO_4 is a product of a reaction that can occur when liquid sodium contacts uranium oxide reactor fuel material. This compound could materially affect the coolant flow because of volume changes resulting in possible fuel-pin swelling. Thermodynamic data are needed for assessing the effects of this reaction product on various proposed fast-breeder-reactor materials. We have determined enthalpy increments for this compound by drop calorimetry.

The sample used for this work was the same material used by this Division's Calorimetry Group in their heat-of-formation studies (see Section III.C). The enthalpy of Na_3UO_4 (relative to 298.15°K) was measured from 523 to 1213°K. Using the constraints that $H^\circ_T - H^\circ_{298} = 0$ at 298.15°K and that $C^\circ_p = 41.35$ cal/(mol)(°K),[37] we obtain the following equation as a fit to the experimental data:

$$H^\circ_T - H^\circ_{298.15} = 45.1484T + 3.00894 \times 10^{-3}T^2 + 4.97148 \times 10^5 T^{-1} - 15395.91 \text{ cal/mol}. \quad (1)$$

[37] D. W. Osborne and H. E. Flotow, Thermodynamic Investigation of Trisodium Uranium (V) Oxide (Na_3UO_4), Part II, J. Chem. Thermodyn. (accepted for publication).

Temperature, T, is in degrees Kelvin. The standard deviation for Eq. 1 is 43 cal/mol or 0.22%. The derived heat capacity from Eq. 1 is

$$C_p = 45.1484 + 6.01788 \times 10^{-3}T - 4.97148 \times 10^5 T^{-2} \text{ cal/(mol)(°K)} \quad (2)$$

b. Induction-Heated Drop-Calorimeter System

The induction-heated drop calorimeter has been modified for work with plutonium-containing materials; the details of the modified system are described in an ANL report.[38] The system has been used to measure enthalpy increments for the compound $(U_{0.8}Pu_{0.2})O_{1.97}$, a leading candidate for fuel in LMFBRs.

Enthalpy data were obtained from 2348 to 3041°K. The sample heated to 3041°K showed clear signs of melting, while the sample heated to the next lower temperature, 3005°K, gave no indication of melting. The solidus temperature for this oxide material thus lies between 3005 and 3041°K. The data for the solid samples were fitted by the method of least squares to the following equation (temperature in degrees Kelvin):

$$H^\circ_T - H^\circ_{298.15} = -4470.04 + 14.6470T + 9.51929 \times 10^{-4}T^2 + 6.95191 \times 10^{-7}T^3 \text{ cal/mol} \quad (3)$$

Equation 3 satisfies the constraints that $H^\circ_T - H^\circ_{298.15} = 0$ when $T = 298.15$°K and $C_p^{298.15} = 15.4$ cal/(mol)(°K), the latter being obtained by taking the weighted sum of values for UO_2, PuO_2, and Pu_2O_3. The standard deviation for this fit is 221 cal/mol or about 0.4%. Heat capacities derived from Eq. 3 are in good agreement with values estimated by assuming simple additivity of the heat capacities of UO_2 and PuO_2.

Work has commenced on the measurement of enthalpy increments for this mixed oxide in the liquid state. The same type double-wall tungsten capsule used previously for our molten-UO_2 studies is being employed in these experiments.

2. Speed of Sound in Molten Reactor Materials

Experiments are in progress to measure the speed of sound in molten reactor materials with the initial efforts being directed to sodium. Compressibility data for molten fuel materials and coolant for use in conjunction with the Grueneisen equation of state will be available from these measurements. These speed-of-sound data will also be of value in assessing shock propagation through molten fuel and coolant, as well as in analyzing two-phase flow of coolant.

[38] D. Fischer, L. Leibowitz, and M. Chasanov, USAEC report ANL-7896 (in press).

Measurements of the speed of sound in molten sodium from 736 to 1489°C were made using a pulse-echo technique. The cell used in these studies was fabricated from a tantalum-10% tungsten alloy (60 metal) chosen because of its strength. This is a necessary property since high vapor pressures are developed in the sample cell at the upper temperatures (37 atm at 1489°C). The data obtained are presented in Fig. III-4; the plot clearly shows a departure from linear dependence on temperature at the higher temperatures. Nonlinearity with temperature has, however, been previously observed by other investigators in speed-of-sound measurements on liquid metals.[39]

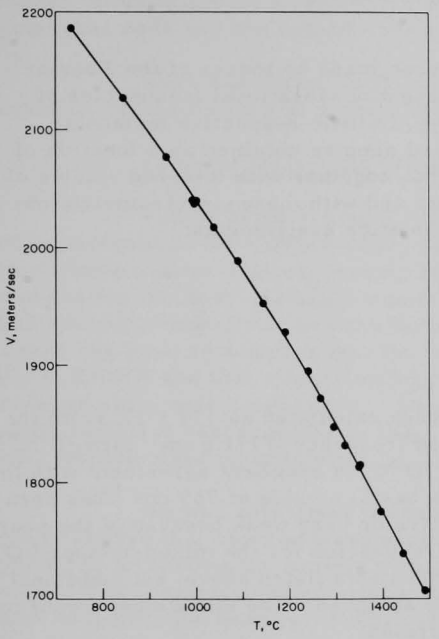

Fig. III-4. Speed of Sound in Liquid Sodium as a Function of Temperature. ANL Neg. No. 308-2593.

The data shown in Fig. III-4 can be represented by the following empirical equation:

$$V = 2437.6 - 0.20385t - 0.19322 \times 10^{-3}t^2 \qquad (4)$$

where the velocity, V, is given in meters per second and the temperature, t, is in degrees centigrade. The standard deviation for this equation is 4.1 m/sec. Extrapolation of this equation beyond the upper limit of the experimental temperatures is not recommended because of the unknown effect of increasing temperature on the velocity-vs.-temperature curve.

3. Matrix-Isolation Spectroscopy

The thermodynamic properties of the vapor species of fuel oxides are important in determining equation-of-state relationships used in projecting the results of certain fast-breeder-reactor design-basis accidents. Application of statistical mechanical techniques to spectroscopic data for these species presents a useful way of determining their thermodynamic properties at temperatures beyond the range of direct experimental measurements. Consisting of trapping molecules in frozen inert-gas lattices, the matrix isolation method allows low-temperature pseudo-gas phase studies to be carried out on molecules normally present

[39] M. B. Gitis and I. G. Mikhailov, Soviet Phys. Acoust. English Transl. 12, 14 (1966).

in large gas-phase concentrations only at very high temperatures. Because population of excited rotational quantum levels is eliminated under these low-temperature conditions, interpretation of the simplified infrared and visible spectra is greatly facilitated.

Substantial progress has been made by means of the Fourier transform spectrometer in the assignment of vibrational frequencies of vapors observed above condensed $UO_{2\pm x}$ to their respective molecular species. Careful studies of the infrared spectra obtained as a function of the O/M ratio of the condensed material, together with infrared studies of full and partially ^{18}O-substituted urania and with mass-spectrometric observations, have led to the following tentative assignments:

776 cm^{-1}: $U^{16}O_2(\nu_3)$

853 cm^{-1}: $U^{16}O_3(\nu_1)$

746 cm^{-1}: $U^{16}O_3(\nu_3)$

In addition, a bond angle for UO_2 has been calculated as 174 ± 10° from the ratio $\nu_3(U^{16}O_2)/\nu_3(U^{18}O_2)$. The observed frequency of 771.6 cm^{-1} for $\nu_3(U^{16}O^{18}O)$ has yielded a calculated value of $\nu_1(U^{16}O^{18}O)$ in excellent agreement with the observed value at 728.4 cm^{-1}. On this basis, a value of 765 cm^{-1} has been calculated for $\nu_1(U^{16}O_2)$, which is inactive or very weak because of the near-linear O-U-O bond angle. Observed frequencies for the mixed-isotope UO_3 molecules are consistent with the assignments listed above, but additional work is needed before all peaks can be assigned. The vibrational frequency for diatomic UO has not yet been confirmed.

4. Theoretical Extrapolation of Measured Physical-Property Data to Higher Temperatures

A computational algorithm has been constructed which predicts the vapor pressures and oxidation states of fast-breeder-reactor fuel and fission-product elements. These data are of importance in the areas of fuel-cladding interaction, possible fuel failure propagation, fuel-coolant interaction, and reactor disassembly calculations. The calculations, which consider a three-phase (condensed oxide, condensed non-oxide, and vapor) closed thermodynamic system, are based on the assumptions of ideal solution theory and temperature uniformity. On the basis of available thermodynamic data and extrapolations to 6000°K, and the assumption of 100% retention of fission-product gases within the closed system, vapor pressures, oxygen-to-metal ratios of the fuel, and oxidation states of condensed fission products have been computed as a function of initial fuel composition, burnup, and fuel density. Results of these calculations indicate the noble gases to be the major contributors to the total pressure at temperatures below 4000°K. Above 5000°K, gaseous UO_2 becomes the principal contributor to the vapor pressure at low (5%) burnup. The total pressures are

relatively insensitive to initial fuel composition [O/M and Pu/(U + Pu) ratios] and to the exactness of the calculated oxygen partial pressure even at the higher temperatures. A report has been prepared which describes this computational code and the results obtained with it so far.

Work has commenced on the evaluation of existing sodium equation-of-state data and extrapolation techniques.

5. Thermal Diffusivity of Reactor Materials

Values of the thermal diffusivity of UO_2 in the liquid state are of importance to the reactor safety program. This information is needed to evaluate means of safely cooling the core of an LMFBR in the event of a meltdown incident. Reliable experimental values of thermal diffusivity and thermal conductivity are available for solid UO_2 up to about 2300°K. There has been speculation that the thermal conductivity of UO_2 will increase above 2300°K and that a contributing factor to such an increase would be increased electronic conductivity. There is also considerable uncertainty about radiative heat transfer in UO_2. It is hoped that the present research will resolve these uncertainties.

We will determine thermal diffusivity of liquid UO_2 from the phase change in a thermal wave passing through a sample; this wave is produced by heating the sample with a sinusoidally modulated electron beam. The thermal conductivity is calculated using the thermal diffusivity, heat capacity, and density. Modification of a twin-beam electron furnace for use in this work has been completed. All electronic equipment for modulation and electron-beam sample scan during heating has been tested. Phase-shift measurements have been made using tungsten samples, and the calculated thermal-diffusivity values agree with literature values. An empty tungsten cell, of the type which will be used to contain uranium dioxide, has been tested by heating with both electron beams. The entire cell was held above 3100°C. The cell remained intact and there was no surface buckling. A disk of uranium dioxide has been successfully enclosed in a similar cell by electron-beam welding.

6. Reactor Materials-Fuel Phase Studies at High Temperatures

In the event of an LMFBR core meltdown, simultaneous failure of multiple safeguards and loss of effective cooling could lead to melting of the oxide fuel, the stainless steel cladding, the core-support steel, and the concrete which will be below the reactor core. Knowledge of the distribution of fission products to the phases produced in such a hypothetical incident and of the distribution of the phases is required to predict the fission-product heat distribution and to be able to assure that means are available for cooling the products of the meltdown. Consideration must also be given to the possible

dissolution of concrete in the molten UO_2-PuO_2 layer, thereby forming a liquid less dense than molten steel. This program seeks to provide this information.

Experimental studies of the distribution of inactive fission products between molten iron (representing fuel cladding) and molten UO_2 (representing reactor fuel) have been completed using an arc-melting furnace. Experiments have shown that when molten uranium dioxide is contacted with molten iron, the elements yttrium, lanthanum, strontium, barium, zirconium, praseodymium, cerium, and some of the niobium are distributed to the oxide phase. Molybdenum, ruthenium, and some of the niobium are distributed to the metal phase. The first group of elements is characteristic of the alkaline earths, transition metals, and rare earths that have stable oxides under the experimental conditions. The second group is characteristic of the noble metals. The results are in general accord with the conclusions that have been drawn from thermodynamic data. A report, ANL-7864, has been prepared which discusses these experiments in detail.

A study of the distribution of fission products between a molten UO_2-concrete mixture and iron is in progress.

D. Calorimetry

The calorimetric program is directed toward the experimental, empirical, or theoretical determination of thermodynamic properties of substances that are of interest in high-temperature chemistry and nuclear technology. Measurements are being made of standard enthalpies of formation (ΔHf°_{298}) of the substances. Complementary experimental determinations of high-temperature increments ($\Delta H^\circ_T - \Delta H^\circ_{298}$) are reported in Section III.C of this report. Complementary low-temperature thermal measurements (of C°_p, S°, and ΔH°_{tr}) are being performed in the ANL Chemistry Division and elsewhere. Quantum chemical investigations are also being carried out on some related binary systems.

1. Na_3UO_4

The failure of the fuel cladding in an oxide-fuel, sodium-cooled reactor is postulated to lead to the reaction

$$3Na + O_2 + (U,Pu)O_2 \rightarrow Na_3(U,Pu)O_4 \qquad (1)$$

This reaction leads to swelling of the fuel and, possibly, obstruction of the reactor coolant channel. A knowledge of the thermodynamic properties of the four species in the reaction enables one to calculate the oxygen pressure, one of the critical parameters of the process. It is believed that if the Pu content of the fuel is ~20% or less, the thermodynamic properties of

$Na_3(U,Pu)O_4$ ought to be very close to that of Na_3UO_4. For this reason, a sample of Na_3UO_4 was prepared[40] and characterized (see Section III.A of this report) and its enthalpy of formation determined[40] by enthalpy-of-solution measurements in an aqueous HCl solution of XeO_3. $\Delta Hf^\circ_{298}[Na_3UO_4(c)]$ was found to be -477.7 ± 0.9 kcal mol^{-1}. Other thermodynamic properties measured on the sample include low-temperature heat capacity and entropy,[41] high-temperature enthalpy,[42] and dissociation vapor pressures.[43]

2. Na_2O

The enthalpy of formation of disodium oxide, Na_2O, is also an important datum for use in the elucidation of the thermodynamics of the sodium-uranium-oxygen system, the importance of which was indicated above. Because of this importance and because the literature data are discordant, a sample of Na_2O was purchased, heated under vacuum at 510°C for 40 hr to remove excess sodium and any NaOH present, and its enthalpy of solution measured. From the measurements, the enthalpy of formation was calculated to be $\Delta Hf^\circ_{298}[Na_2O(c)] = -99.15 \pm 0.05$ kcal mol^{-1}.

3. $CsHC_2$

Values for the enthalpies of formation of the sodium acetylides Na_2C_2 and $NaHC_2$ were reported in the preceding report (ANL-7750, p. 68). They were determined because Na_2C_2 has been postulated as playing an important role in the transport of carbon in sodium-cooled reactors. A similar study was planned for the cesium acetylides because the techniques for the measurements were available and because cesium is a high-yield fission product and the dicesium acetylide might be formed in carbide fuel systems. Further, literature data on fission-product carbides are so sparse that any addition would be an aid in estimating thermodynamic values that do not now exist. However, preparation of a sample of Cs_2C_2 was not achieved and measurements were made only on $CsHC_2$. Calorimetric measurements of the enthalpy of reaction of $CsHC_2$ with 0.018 N CsOH were combined with auxiliary thermochemical data to obtain the enthalpy of formation, $\Delta Hf^\circ_{298}[CsHC_2(c)] = +18.55 \pm 0.2$ kcal mol^{-1}.

---

[40] P. A. G. O'Hare, W. A. Shinn, F. C. Mrazek, and A. E. Martin, Thermodynamic Investigations of Trisodium Uranium (V) Oxide (Na_3UO_4). Part I. Preparation and Enthalpy of Formation, J. Chem. Thermodyn. (accepted for publication).

[41] D. W. Osborne and H. E. Flotow, Thermodynamic Investigations of Trisodium Uranium (V) Oxide (Na_3UO_4). Part II. Heat Capacity, Entropy, and Enthalpy Increment from 5 to 350K. Gibbs Energy of Formation at 298.15K, J. Chem. Thermodyn. (accepted for publication).

[42] D. R. Fredrickson and M. G. Chasanov, Thermodynamic Investigations of Trisodium Uranium (V) Oxide (Na_3UO_4). Part III. Enthalpy to 1200K by Drop Calorimetry, J. Chem. Thermodyn. (accepted for publication).

[43] J. E. Battles, W. A. Shinn, and P. E. Blackburn, Thermodynamic Investigations of Trisodium Uranium (V) Oxide (Na_3UO_4). Part IV. Mass Spectrometric Study of the Na-U-O System, J. Chem. Thermodyn. (accepted for publication).

4. ThS

As part of an effort to alleviate the scarcity of thermodynamic data on actinide compounds, the determination of the enthalpy of formation of thorium monosulfide is being carried out by the Chemical Engineering Division by measurement of the enthalpy of solution of ThS in 6M HCl. This is part of a cooperative study of the thermodynamic properties of ThS: the sample was prepared by R. R. Walters;[44] low-temperature C_p° and S° measurements have been made by D. W. Osborne and H. E. Flotow;[44] high-temperature vapor pressure measurements were planned by R. J. Thorn (Walters, Osborne, Flotow and Thorn are all members of the ANL Chemistry Division). A preliminary value has been obtained for the enthalpy of formation, $\Delta Hf^\circ_{298}[ThS(c)] \simeq -97.0$ kcal mol^{-1}.

5. N≡SF

Two years ago, measurements of the enthalpy of formation of thiazyl trifluoride, $N{\equiv}SF_3$, were made[45] on a sample prepared by Professor O. Glemser and I. Wegener of the University of Göttingen, Germany. From the enthalpy of formation of $N{\equiv}SF_3$ and some mass-spectrometric appearance-potential data[46] for both the thiazyl tri- and monofluorides, a value was calculated[45] for the enthalpy of formation of the monofluoride, N≡SF. Since then, Professor Glemser has prepared a sample of $Hg(NSF_2)_2$ (from which N≡SF can be obtained by thermal decomposition) in order that the enthalpy of formation of N≡SF could be measured directly. A preliminary value, determined by us during the past year, is $\Delta Hf^\circ_{298}[N{\equiv}SF(g)] \simeq -5.2 \pm 0.9$ kcal mol^{-1}. This value differs by about 40 kcal from the calculated one[45] and points to a serious error in one of the appearance-potential reaction assignments.[46] The appearance potential of NSF^+ from $N{\equiv}SF_3$ must be assigned to the reaction

$$N{\equiv}SF_3 + e^- = N{\equiv}SF^+ + 2F + 2e^- \qquad (2)$$

rather than to

$$N{\equiv}SF_3 + e^- = N{\equiv}SF^+ + F_2 + 2e^- \qquad (3)$$

as originally postulated.

6. XeF_6, XeF_4, and XeF_2

The discovery of the xenon compounds in the early 1960's has been followed by a decade of intensive study of their properties, much of

[44] H. E. Flotow, D. W. Osborne, and R. R. Walters, J. Chem. Phys. 55, 880 (1971).
[45] P. A. G. O'Hare, W. N. Hubbard, O. Glemser, and I. Wegener, J. Chem. Thermodyn. 2, 71 (1970).
[46] O. Glemser, A. Müller, D. Böhler, and B. Krebs, Anorg. Allg. Chem. 357, 184 (1968).

it done in the ANL Chemistry Division. A number of the studies have involved determinations of the enthalpies of formation of the xenon fluorides by calorimetric techniques, by equilibrium techniques, and by mass-spectrometric techniques. Because the samples used in many of the earlier studies were impure and because there were considerable differences in the values obtained, it was decided to determine the enthalpies of formation of XeF_6, XeF_4, and XeF_2 in a cooperative effort with John Malm of the ANL Chemistry Division, one of the pioneers in the field. The samples were prepared and purified by Malm and contained no detectable impurities. The reaction between the fluorides and gaseous PF_3 was chosen for the study. The main reaction studied was

$$XeF_n(c) + n/2\ PF_3(g) \rightarrow n/2\ PF_5(g) + Xe(g) \qquad (4)$$

The enthalpy of this reaction, combined with n/2 times the enthalpy of the reaction of $PF_3(g)$ with fluorine,

$$PF_3(g) + F_2(g) \rightarrow PF_5(g) \qquad (5)$$

leads directly to the enthalpy of formation of the xenon fluoride. The enthalpies of Reaction 4 found were -113.08 ± 0.20, -240.12 ± 0.15, and -375.12 ± 0.49 kcal mol^{-1} for the di-, tetra-, and hexafluoride, respectively. The enthalpy of Reaction 5 had been previously determined at this laboratory to be -151.99 ± 0.16 kcal mol^{-1}. Another measurement in the course of the present work yielded a value of -151.98 ± 0.07 kcal mol^{-1}. The derived heats of formation are $\Delta Hf^{\circ}_{298}[XeF_n(c)]$ = -38.90 ± 0.21, -63.84 ± 0.21, and -80.82 ± 0.53 kcal mol^{-1} for the di-, tetra-, and hexafluorides, respectively.

7. BrO_3F

The recent synthesis of perbromic acid and the alkali perbromates by E. H. Appelman[47,48] of the Chemistry Division has led to the preparation of perbromyl fluoride, BrO_3F. Inasmuch as the perbromates were thought previously to be nonexistent, their thermodynamic properties are of fundamental interest. The thermodynamic properties of potassium perbromate and the aqueous perbromate ion have already been determined in this laboratory.[49] During the past year, the enthalpy of formation of BrO_3F has been determined by measurement of its enthalpy of hydrolysis to be $\Delta Hf^{\circ}_{298}[BrO_3F(\ell)]$ = +26.78 ± 0.25 kcal mol^{-1}.

8. Quantum-Chemical Investigations

In support of other calorimetric studies, quantum-chemical investigations have continued with calculations on the nitrogen-fluorine, silicon-fluorine, nitrogen-sulfur, and nitrogen-oxygen systems.

---

[47] E. H. Appelman, J. Amer. Chem. Soc. 90, 1900 (1968).
[48] E. H. Appelman, Inorg. Chem. 8, 223 (1969).
[49] G. K. Johnson, P. N. Smith, E. H. Appelman, and W. N. Hubbard, Inorg. Chem. 9, 119 (1970).

IV. ANALYTICAL AND REACTOR CHEMISTRY

A. Dosimetry

On July 1, 1971 a dosimetry program was established within the Chemical Engineering Division. The objective of this program is to develop and apply experimental and analytical techniques for characterizing fast-neutron irradiation environments in terms of flux, fluence, and neutron spectrum. The program is divided into two primary areas of responsibility: (1) to investigate systematic errors in foil-activation techniques and develop methods for measuring integral reaction rates in operating power reactors to an accuracy of ±3% and (2) to establish the capability for a routine, coordinated dosimetry service for all Argonne National Laboratory (ANL) experimenters using EBR-II.

1. Development of Dosimetry

The principal means by which dosimetry methods will be developed and evaluated is by participation in the Interlaboratory LMFBR Reaction Rate (ILRR) program. The ILRR program objective is to systematically compare all available methods for measuring fission rates and for characterizing irradiation environments. Accordingly, a coordinated program has been set up among laboratories that have wide experience in these techniques. The techniques to be evaluated and the laboratories involved are as follows: (1) foil activation, Hanford Engineering Development Laboratory and ANL; (2) solid-state fission track recorders, ANL; (3) ion chambers, National Bureau of Standards; (4) proton recoil, Aerojet Nuclear Corp.; and (5) neutronics calculations, Los Alamos Scientific Laboratory and Aerojet Nuclear Corp. Because the instrumental techniques, namely, track-recorder, ion-chamber, and proton-recoil, cannot be used for in-core power-reactor measurements, the philosophy is to perform measurements with all techniques in well-established, permanent, critical facilities. From these measurements, the absolute accuracy of each technique should be defined and the data will be used to "standardize" or "calibrate" the foil-activation and neutronics-calculation techniques for use in fast power reactors such as EBR-II and FFTF.

Our efforts are emphasizing the use of solid-state track recorders (SSTR) and foil activation. The SSTR technique has been shown to have an accuracy of 1-3% under ideal conditions;[1] however, the ultimate accuracy achievable in critical-assembly reactor environments has yet to be demonstrated. The technique involves placing a thin, uniform deposit of a fissile material in contact with a suitable dielectric such as mica. As fissions occur, the recoil fission fragments produce damage tracks in the

[1]R. Gold, R. J. Armani, and J. H. Roberts, Nucl. Sci. Eng. 34, 13-22 (1968).

dielectric which, upon suitable chemical etching, are enlarged and are visible under a microscope. Thus, the SSTR serves as a fission monitor that integrates the number of fissions during the course of an irradiation.

The accuracy obtainable with SSTRs is largely defined by the accuracy with which the number of fissile atoms exposed to the recorder is known. We are, therefore, developing improved techniques for uniformly plating nanogram amounts of ^{235}U, ^{238}U, ^{237}Np, and ^{239}Pu onto thin backing materials and establishing the number of plated atoms. The ^{237}Np and ^{239}Pu atoms can be determined by low-geometry alpha counting. Because ^{235}U and ^{238}U are not sufficiently active for accurate alpha counting, these isotopes will be determined by spiking the solutions with known amounts of ^{234}U before plating and alpha counting.

Another important consideration in the accuracy of the SSTR measurements is that the amount of all materials of construction in the irradiation packages be minimized. This is necessary to minimize perturbations of the neutron field in which measurements are made. Several different packages have been designed and are now being constructed. Initial evaluations of these packages will be made in tests at NBS, in which the packages will be irradiated simultaneously with highly calibrated ion chambers. Selection of the final design of the SSTR package will be made on the basis of these tests.

Reaction-rate measurements by all ILRR participants are scheduled to begin in February 1972 in the Coupled Fast Reactivity Measurement Facility (CFRMF) at Aerojet Nuclear Corporation.

2. Service Dosimetry

This effort is committed to establishing a capability for routine dosimetry measurements at ANL, performing dosimetry measurements in EBR-II for ANL experimenters, and for coordinating ANL's overall dosimetry effort. At present, this work includes radiochemical measurements of reaction rates from various neutron dosimeters exposed in various neutron environments and determination of flux, fluence, and neutron spectrum from these reaction rates. In the near future, we expect to provide the capability for determining the number of atomic displacements (Frankel pairs) produced in a neutron-irradiated material and for determining the burnup of a fuel specimen by means of specific dosimeter foils.

During the past year, most of our effort was devoted to two extensive series of measurements conducted and supported by the EBR-II project. The first included foil-activation-rate measurements from dosimetry foils irradiated in strategic locations in each of four critical-assembly mockups of EBR-II. More than 600 individual reaction rates were measured. The objectives of this work were to examine heterogeneity effects within

the reactor, to provide integral data that could be compared with neutronic calculations of the mockup assemblies, and to provide reaction-rate data that could be compared directly with similar measurements in EBR-II to establish the validity of the mockups.

The second experiment, the EBR-II flux-mapping test, consisted of measurements essentially identical to the mockup tests, except that they were conducted in EBR-II. The specific objectives of our participation in this test were (1) to provide data that could be compared directly with those of the mockup tests, (2) to examine the effects of reactor power level upon neutron spectrum and reaction rates, (3) to provide data to examine flux-depression effects in structural subassemblies, and (4) to generate a store of data and experience to enable more accurate and reliable dosimetry monitoring of individual irradiation experiments in EBR-II.

The dosimetry program is responsible for designing the dosimetry aspects of all ANL experiments conducted in EBR-II. In this regard, we have designed and planned the dosimetry monitoring for five experiments. The effort included defining the location, types, and number of dosimetry monitors and providing suitable foil materials to the experimenters. Reaction rates have been measured on dosimetry monitors from one completed materials-property test conducted in EBR-II.

B. Fast-Reactor Cross-Section Measurements

1. Spectrum-Averaged Measurements

An understanding of fast-neutron processes that occur during irradiation is essential to the design and development of LMFBRs. The objective of our program is to provide measurements of spectrum-averaged reaction rates, cross sections, and cross-section ratios; these are determined by means of irradiations carried out in various fast-neutron spectra, e.g., in EBR-II or in critical assemblies. During 1971, effort was devoted to completing a series of experiments whose purpose was to provide data on integral (spectrum-averaged) capture-to-fission ratios (alpha) of the major fissile and fertile isotopes; such data are needed to evaluate breeding characteristics of potential LMFBR fuels. In these experiments, which were begun in 1964, a total of 64 samples of ^{233}U, ^{235}U, ^{238}U, ^{239}Pu, ^{240}Pu, and ^{242}Pu were irradiated in various positions in the core and blanket of EBR-II for periods of 0.5 to 1.6 yr. The samples were analyzed to determine the number of captures, the number of fissions, and their ratio, alpha. A topical report describing this work has been published.[2]

Considerable effort at Argonne has been devoted to developing the capability for calculating the irradiation environment of EBR-II, and the

[2] R. R. Heinrich, J. Williams, A. A. Madson, and N. D. Dudey, Integral Measurements in EBR-II of Capture Rates, Fission Rates, and Alpha for ^{235}U, ^{238}U, ^{239}Pu, ^{240}Pu, and ^{242}Pu, ANL-7791 (1971).

data obtained in the alpha experiments provide an important means for evaluating the accuracy of these calculations. Such an evaluation is being made in a collaborative effort between the Chemical Engineering Division and the EBR-II Project. Experimental[3] and calculated[4] values of the capture-to-fission ratios of ^{233}U, ^{235}U, and ^{239}Pu at various radial locations in EBR-II have been reported; a comparison[4] of these results is given in Fig. IV-1. The comparison shows good agreement for ^{233}U and ^{239}Pu but points up some discrepancies between the measured and calculated values for ^{235}U. More detailed comparisons and analysis of the individual capture rates, fission rates, and spectrum-averaged cross-section ratios for ^{233}U, ^{235}U, ^{238}U, ^{239}Pu, ^{240}Pu, and ^{242}Pu are in progress.

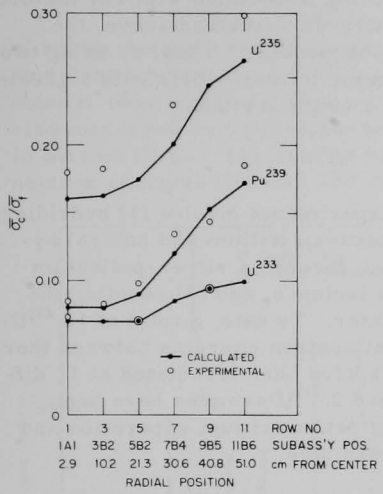

Fig. IV-1. Comparison of Calculated and Measured Capture-to-Fission Ratios of ^{233}U, ^{235}U, and ^{239}Pu in EBR-II Core and Radial Blanket. ANL Neg. No. 104-294.

2. Fast-Neutron Fission Yields of Tritium

Data on the fast-neutron fission yields of tritium are needed for predicting tritium production rates in LMFBRs. This information is important because of the problems of tritium disposal in fuel reprocessing plants. Our work is being directed primarily toward the measurement of the fission yield of tritium as a function of neutron spectrum and fissioning nuclide. Two independent methods are being examined for establishing tritium yields. The first method is a radiochemical technique in which the tritium is separated from other sample constituents and counted. The second method is an on-beam, particle-identification technique for measuring the number and energy of all low-mass particles (^1H, ^2H, ^3H, ^3He, ^4He, and ^6He) emitted in fission. Both methods involve irradiation of the fissile nuclides in a beam of monoenergetic neutrons at several different energies to establish the energy dependencies. During the past year, both methods have emphasized measurements of tritium yields from fast-neutron fission of ^{235}U.

Accurate measurements of tritium yields as a function of neutron energy are complicated because of (1) the very low yields of tritium relative to those of virtually every other fission product, (2) the long

---

[3] N. D. Dudey, R. R. Heinrich, J. Williams, Trans. Amer. Nucl. Soc. 14, 816 (1971).

[4] D. Meneghetti and R. H. Rempert, Trans. Amer. Nucl. Soc. 14, 817 (1971).

half-life and low decay energy of tritium, and (3) the possibility of interferences from tritium originating from sources other than fission. These complications result in significant errors being associated with any method for measuring tritium yields. In the two methods described above, the errors, even though large, are completely independent. Thus, by using two widely different methods, we hope to determine tritium yields with a greater reliability than would be achieved by using a single method.

a. Radiochemical Method

The radiochemical-yield experiments involve (1) hydriding an irradiated sample to provide exchange between tritium and natural hydrogen, (2) pumping the hydrogen and tritium through a silver-palladium valve, which is permeable only to hydrogen isotopes, and (3) counting the tritium in a low-level gas proportional counter. To date, a total of 16 ^{235}U samples have been irradiated at 12 different neutron energies between thermal energies and 770 keV; 12 ^{239}Pu samples have been irradiated at 11 different energies between 230 and 770 keV; and 3 ^{233}U samples have been irradiated between 540 and 420 keV. The effort on tritium separation and counting has been concentrated on the ^{235}U samples.

A demonstration of the validity of the radiochemical method was made by measuring the yield of tritium from thermal fissioning of ^{235}U. Measurements of the thermal yield have been reported by several investigators with results ranging from 0.80×10^{-4} to 1.1×10^{-4} tritons per fission (T/f). Our evaluation of these reported experiments indicate that the lowest value, $(0.80 \pm 0.096) \times 10^{-4}$ T/f, as measured by Sloth et al.,[5] is the most reliable thermal yield value. This evaluation was based on the assigned errors, the methods employed, and reproducibility of replicate measurements.

The thermal measurement is complicated by the fact that the mean free path of thermal neutrons is quite short in ^{235}U, so that most fissions would occur near the surface of a sample. Since the kinetic energy of the tritons can exceed 15 MeV, a large fraction of the tritons will recoil out of the target. For this reason we irradiated a 2-mil foil of 93% enriched ^{235}U sandwiched between two 10-mil foils of ^{238}U, which acted as a tritium recoil catcher. This package was irradiated in the Argonne Thermal Source Reactor for about 5 min. Both the sample and the catcher foils were counted on high-resolution Ge(Li) detectors to determine the number of ^{140}Ba atoms produced in the irradiation. From this value and the thermal yield of ^{140}Ba, the number of fissions occurring in the sample was determined. The sample and catchers were than analyzed individually for tritium. The value obtained for the thermal tritium yield was $(0.85 \pm 0.09) \times 10^{-4}$ T/f, which is in excellent agreement with the value of Sloth et al.[5] On

[5] E. N. Sloth, D. L. Horrocks, E. J. Boyce, and M. H. Studier, J. Inorg. Nucl. Chem. 24, 337 (1962).

the basis of these results, we conclude that our radiochemical method for determining tritium yields is valid.

In the fast-neutron irradiations, monoenergetic neutrons of known energy were used to initiate the fission process. The irradiated samples were analyzed for the number of fissions and tritium content in a manner identical to the thermal irradiations. The number of fissions was also measured by solid-state track recorders. (This method is described in Section IV.C.) The results of tritium-yield measurements for ^{235}U at 6 neutron energies between 420 and 770 keV are shown in Fig. IV-2, along with results obtained by the particle-identification technique (both sets of results are discussed in the following subsection). The rather large errors in the data result primarily from the tritium counting statistics. Typically, a one-week irradiation of a 1-g sample of ^{235}U yields a tritium count rate of 1-2 dpm.

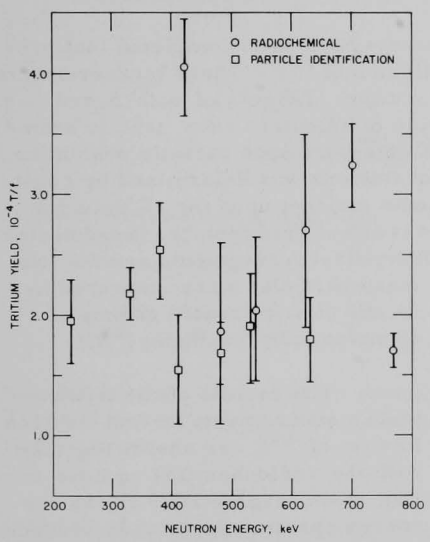

Fig. IV-2. ^{235}U Fission Yield of Tritium as a Function of Bombarding Neutron Energy

b. <u>On-Beam Particle Identification Yield Method</u>

The particle-identification method differs from the radiochemical method in that all low-mass charged particles emitted during fission are detected and identified on-line, and the kinetic energy of each particle is determined. The data obtained by this method will aid in understanding the mechanism of low-mass-particle production in fission; however, our major interest is in understanding the dependence of tritium production in fast-neutron fission on neutron energy and fissioning species. Accordingly, two types of fission are being studied: spontaneous fission (e.g., of ^{252}Cf) and monoenergetic neutron-induced fission of ^{235}U and ^{239}Pu over the energy range from 200 to 4000 keV. The initial objectives of these studies are to measure the number of particles emitted per fission and the energy distributions of ^{1}H, ^{2}H, ^{3}H, ^{3}He, ^{4}He, and ^{6}He as a function of neutron energy for ^{235}U.

The principle of particle identification takes advantage of the differences in the rate of energy loss of charged particles as a function of their charge and mass. The detector system employs two diffused-junction silicon detectors, a thin (30-60 μm) ΔE and a thick (500 μm) E detector, as well as a two-detector telescope. A particle traversing the telescope produces signals from the detectors that are proportional to the

energy lost in each detector. The two energy signals (ΔE and E) resulting from this traversal are such that the total energy of the particle is (ΔE + E) and the relationship between ΔE and (ΔE + E) uniquely defines the mass and charge of the particle.

The primary advantage of the particle-identification method is that fission tritons are clearly differentiated from tritons produced by other reactions, e.g., $^{6}Li(n,T)$, by means of the measured energy distributions. The principal errors in the method are related to absolute calibration of the solid angle (geometry) of the detector telescope and the practical limitation on accelerator time needed to provide adequate statistics.

Two series of experiments have been completed that produced useful data on the fast-neutron fission of ^{235}U. These measurements involved a total of 130 hr of accelerator time. Targets of both 3 and 0.4 mg/cm^2 of ^{235}U and two different sets of detectors were used to examine the effects of the thicknesses of ΔE detectors upon particle resolution. For these measurements the number of fissions was determined by counting the number of heavy fission fragments incident upon the ΔE detector and the number of low-mass particles was determined from the two-detector telescope. The solid angles for both heavy fission fragments and the low-mass particles were measured by means of a calibrated source of spontaneously fissioning ^{252}Cf.

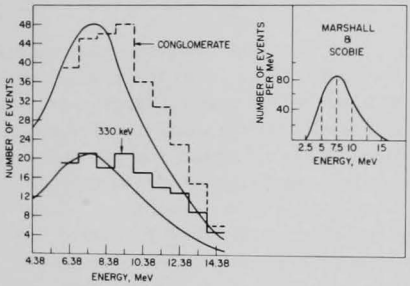

Fig. IV-3. Energy Spectra of Tritons Emitted in Fast-Neutron Fission of ^{235}U. (The smoothed curves represent a tritium energy spectrum for thermal neutron fission of ^{235}U.[6]) ANL Neg. No. 308-2741.

The results of the tritium-yield measurements for fast-neutron fission of ^{235}U are shown together with the radiochemical results in Fig. IV-2. Figure IV-3 shows the energy spectrum of tritium produced by 330-keV neutrons and a conglomerate tritium spectrum of the sum of all spectra collected for a variety of energies. The inset in Fig. IV-3 shows a tritium energy spectrum reported for thermal-neutron fission of ^{235}U;[6] these data have also been normalized to each of our energy spectra and are shown as the smoothed curves in the main body of the figure. One important fact defined by the energy spectra is that tritium must indeed come from fission rather than any possible light-element contaminants.

Our results to date, from both the radiochemical and particle-identification experiments, indicate that a tritium yield of 2.25 x 10^{-4} ($\pm$20%) tritons per fission of ^{235}U is the best available estimate of

[6] M. Marshall and J. Scobie, Phys. Letters 23, 583 (1966).

tritium production rates in LMFBRs. Because of the large uncertainties in the absolute-yield measurements, it is difficult to define an energy dependence in the tritium yields for ^{235}U over the energy region encompassed by fast-reactor spectra. However, the possibility of energy dependence cannot be ruled out at this time. Two conclusions can be drawn from our work to date: (1) the tritium yield in fast-neutron fission of ^{235}U is between two and three times larger than the thermal-neutron fission yield, and (2) calculations that predict the tritium production rates of EBR-II, which are based on a yield of $(0.8\text{-}0.9) \times 10^{-4}$ T/f, are clearly underestimating the tritium production in ^{235}U-fueled fast reactors such as EBR-II.

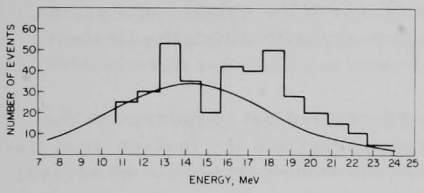

Fig. IV-4. Energy Spectrum of Alpha Particles Emitted in Fission of ^{235}U with 410-keV Neutrons. (The smoothed curve is an alpha-particle spectrum for thermal-neutron fission of ^{235}U.[6]) ANL Neg. No. 308-2740.

Figure IV-4 presents our measurements of the energy spectrum of alpha particles emitted in ^{235}U fission with 410-keV neutrons. (The smoothed curve represents the energy spectrum of alpha particles from thermal fission of ^{235}U.[6]) An interesting feature of our data is that the alpha-particle spectrum appears to break into two distinct components. This feature has been observed in both series of irradiations at neutron energies between 400 and 480 keV. Such an effect is not observed at other neutron energies and has not been previously observed. These data may indicate the presence of channel (resonance) effects in the fission process.

As part of our efforts to understand the mechanism of low-mass atom production in fission, we are collaborating with the Chemistry Division in an experiment to measure accurately the angular distribution of the alpha particles produced in fission relative to the massive fragments as a function of the mass split. In this experiment, the mass of a heavy fission fragment is determined from its time of flight and total energy, and the angular distribution of an emitted alpha particle is measured relative to that of the heavy fragment by a position-sensitive detector that records energy and angle. Preliminary results indicate narrower angular distributions than heretofore measured in other experiments, which were more indirect attempts to define the angular distributions. If our preliminary results are substantiated, serious reconsideration of the mechanisms leading to long-range particle emission will be required, and some of the popular models used to calculate angular distributions of long-range particles will not be adequate.

C. Determination of Fast-Neutron Fission Yields

Accurate determinations of the number of fissions that occur in a specimen of fissile material during irradiation are needed not only for determining burnup of power-reactor fuels, but also for monitoring fission rates in critical-assembly experiments and in power-reactor dosimetry measurements. The number of fissions is determined by measuring the number of atoms of a particular fission product and dividing by the fractional fission yield. For fission-rate measurements, the number of atoms of a short-lived fission product, e.g., ^{140}Ba(12.8 d), is determined from a gamma-activity assay. The accuracy with which the number of fissions can be determined is dependent on the accuracy with which the fission yields are known.

An experimental program has been carried out to determine the yields of the short-lived gamma-active nuclides from the fast-neutron fission of ^{235}U, ^{238}U, and ^{239}Pu. The irradiations were carried out at several locations in Assemblies 60 and 61 of Argonne's Zero Power Reactor-3 (ZPR-3); the neutron spectra corresponded to those in Row 2 (core) and Row 7 (core-blanket interface) of EBR-II.

A detailed description of the irradiation capsules and the methods used to measure the number of fissions and the number of fission product atoms formed was presented in a previous report in this series (ANL-7750, pp. 82-83). The number of fissions per gram of fissile nuclide was determined by irradiating nanogram amounts of the fissile nuclide in contact with mica fission-track recorders and subsequently measuring the amounts of fissile material by chemical analysis and counting, under a microscope, the number of fission tracks induced in the mica. The number of fission-product atoms per gram of fissile nuclide was determined by irradiating gram amounts of fissile material (metal foils) in close proximity to the fission-track recorders and subsequently measuring the gamma activities of the fission products by means of a calibrated Ge(Li) detector-multichannel analyzer system.

Fast-neutron yields from fissioning of ^{235}U and ^{239}Pu have been determined for those nuclides that have (1) relatively high fission yields (>3%), (2) half-lives ranging from 1 to 65 days, and (3) well-established ratios of photon emission to disintegration; these fission yields are summarized in Tables IV-1 and IV-2. Averaging of the fission-yield values for the three neutron spectra is justified by previously obtained information (see ANL-7750, pp. 82-85), namely, that within the neutron-energy range encompassed by these measurements, the fission yields do not vary with neutron energy.

TABLE IV-1. ^{235}U Fast-Fission Yields of Short-Lived Gamma-Active Fission Products

ZPR-3 Assembly and Location[a]	Fission Yield, %						
	^{95}Zr	^{97}Zr	^{99}Mo[b]	^{103}Ru	^{131}I	^{132}Te	^{140}Ba
60 Core (446)	6.49	-	-	3.36	3.46	4.56	5.75
61 Core (442)	6.46	5.56	5.67	3.28	3.51	4.91	5.61
61 Interface (293)	6.27	5.49	-	3.22	3.36	4.84	5.65
Average	6.41	5.53	5.67	3.29	3.44	4.77	5.67
S.D.	±0.24	±0.44	±0.20	±0.11	±0.14	±0.29	±0.17

[a]The numbers in parentheses are median fission energies (in keV) at these locations.
[b]Determined by radiochemical separation and beta counting.

TABLE IV-2. ^{239}Pu Fast-Fission Yields of Short-Lived Gamma-Active Fission Products

ZPR-3 Assembly and Location[a]	Fission Yield, %					
	^{95}Zr	^{97}Zr[b]	^{103}Ru	^{131}I	^{132}Te	^{140}Ba
60 Core (446)	-	-	7.03	4.69	5.12	5.19
61 Core (442)	4.78	(4.87)	7.11	4.77	5.31	5.31
61 Interface (293)	4.76	(4.85)	7.01	4.84	5.65	5.26
Average	4.77	(4.86)	7.05	4.77	5.36	5.25
S.D.	±0.18	±0.32	±0.25	±0.17	±0.32	±0.16

[a]The numbers in parentheses are median fission energies (in keV) at these locations.
[b]Calculated values based on measurement of ^{95}Zr yield and measured ^{97}Zr-to-^{95}Zr thermal fission-yield ratio. (The ^{97}Zr gamma ray was subject to interference from a ^{239}Pu gamma ray.)

Of the nuclides whose fission yields have been measured, ^{95}Zr(65 d), ^{97}Zr(17 h), and ^{140}Ba(12.8 d) are the fission products that are used most frequently to determine fission rates for experiments in zero-power critical assemblies and for dosimetry measurements in fast reactors such as EBR-II. Our values for these fission yields are compared in Table IV-3 with literature values[7] and with values which were obtained from earlier work[8] in this program of yields of the stable daughters of these nuclides, ^{95}Mo, ^{97}Mo, and ^{140}Ce. On the basis of mass-charge distribution theory, it is predicted that the cumulative independent fission yields of the daughters of ^{95}Zr, ^{97}Zr, and ^{140}Ba are each less than 0.2% (relative) of the total chain yield. We have confirmed this experimentally for ^{97}Nb(72 m), the short-lived daughter of ^{97}Zr.

[7]F. L. Lisman, R. M. Abernathy, W. J. Maeck, and J. E. Rein, Nucl. Sci. Eng. 42, 191 (1970).
[8]Chemical Engineering Division Semiannual Report, January–June 1964, ANL-6900, p. 337 (1964) and Chemical Engineering Division Research Highlights, May 1964–April 1965, ANL-7020, p. 232 (1965).

TABLE IV-3. Comparison of ^{235}U and ^{239}Pu Fission Yields of ^{95}Zr, ^{97}Zr, and ^{140}Ba with Fission Yields of ^{95}Mo, ^{97}Mo, and ^{140}Ce

	Fission Yields, %				
	^{235}U			^{239}Pu	
Mass No.[a]	ZPR-3	Lisman et al.	ANL	ZPR-3	Lisman et al.
95	6.41	6.47	6.50	4.77	4.78
97	5.53	6.13	6.13	4.87	5.47
140	5.67	6.21	5.69	5.25	5.59

[a]The mass numbers refer to ^{95}Zr, ^{97}Zr, and ^{140}Ba for ZPR-3 and to ^{95}Mo, ^{97}Mo, and ^{140}Ce for Lisman et al. and ANL.

The data in Table IV-3 show good agreement, for both ^{235}U and ^{239}Pu, between the fission yields of ^{95}Zr and ^{95}Mo. However, significant differences exist between the yield values for ^{97}Zr and ^{140}Ba obtained in the ZPR-3 irradiations and the corresponding values for the stable products ^{97}Mo and ^{140}Ce. The discrepancies in the ^{97}Zr values, about 10%, appear to be due to an error in the decay scheme of ^{97}Zr to ^{97}Mo, rather than in the fission yield of ^{97}Mo. In the determinations of molybdenum yields, the ^{95}Mo and ^{97}Mo were determined simultaneously and, if a 10% positive error occurred in the determination of the fission yield of ^{97}Mo, there would also be a 10% positive error in the value of ^{95}Mo. Moreover, the decay of ^{97}Zr (17 h) to ^{97}Mo (stable) is particularly complicated and an error in one of the branches of the published decay scheme could easily account for the discrepancy between the ^{97}Zr and ^{97}Mo yields.

The differences between the ^{235}U and ^{239}Pu fission yields of ^{140}Ba obtained in the ZPR-3 irradiations and the values of Lisman et al. for the stable product ^{140}Ce, -9 and -6%, respectively, do not appear to be due to an error in the decay scheme of ^{140}Ba to ^{140}Ce, which is comparatively simple. Since there is agreement between the ^{235}U fission yield of ^{140}Ba and the ANL value of ^{140}Ce, it is suggested that the values of Lisman et al. for the ^{235}U and ^{239}Pu fission yields of ^{140}Ce are high.

The ^{238}U fast fission yields determined in the ZPR-3 experiments are given in Table IV-4. No information is available on the corresponding fission yields of the stable daughters. Existing fission-yield values are based on determinations of the same nuclides as those given in Table IV-4, and calculations of chain yield are based on the assumption that the chain yield is the same as that of the short-lived fission-product parent. A comparison of our ^{238}U fast fission yield values with recommended values from the compilation by Meek and Rider[9] reveals significant differences. This is

[9]M. E. Meek and B. F. Rider, Summary of Fission Yields for ^{235}U, ^{238}U, ^{239}Pu, and ^{241}Pu at Thermal, Fission Spectrum, and 14 MeV Neutron Energies, APED-5398A, Nucleonics Laboratory, General Electric Co., Pleasanton, California (1968).

not surprising since the ^{238}U values that Meek and Rider used to make their evaluations are not taken from recent work. We believe that our ^{238}U fission-yield values, which were determined by the use of mica fission-track recorders, sophisticated multichannel analyzer systems, and accurately calibrated radioactive standards, are the most reliable data available at present.

TABLE IV-4. ^{238}U Fast-Fission Yields of Short-Lived Gamma-Active Fission Products

ZPR-3 Assembly and Location	Fission Yield, %						
	^{95}Zr	^{97}Zr	^{99}Mo[a]	^{103}Ru	^{131}I	^{132}Te	^{140}Ba
60 Core[b] (446)	5.47	-	6.14	6.26	3.62	5.27	5.96
61 Core (442)	5.41	5.91	5.92	6.32	3.68	5.46	5.88
S.D.	±0.21	±0.35	±0.20	±0.20	±0.16	±0.15	±0.17

[a]Determined by radiochemical separation and beta counting.

[b]The Assembly 60 core values are recommended (the precision of fission-track counting was ±0.6% R.S.D. for the Assembly 60 core vs ±2.0% for the Assembly 60 core).

V. PHYSICAL INORGANIC CHEMISTRY

A. Thermodynamics of Lithium-Chalcogen Systems

Experimental and theoretical studies dealing with molten-salt systems have formed an on-going program in the Chemical Engineering Division. Whereas most previous work has dealt with all-salt or salt-metal systems, recent work has concentrated on the behavior of systems involving the interaction of salts with semimetals or nonmetals. This work has particular application in electrochemical energy conversion and storage devices using alkali metal-chalcogen couples (see Section VI).

1. Phase-Equilibrium Studies of Binary Lithium-Chalcogen Systems.

a. Lithium-Sulfur System

Preliminary thermal data on the lithium-sulfur system were previously reported.[1] Those data identify the thermal invariants of the system which provide the basic form of the phase diagram, as indicated in Fig. V-1. Recent work has been directed toward determining the extent of the miscibility gap which exists on the sulfur-rich side of Li_2S above 365°C and the location of the upper liquidus separating liquid 2 (L_2) and solid Li_2S.

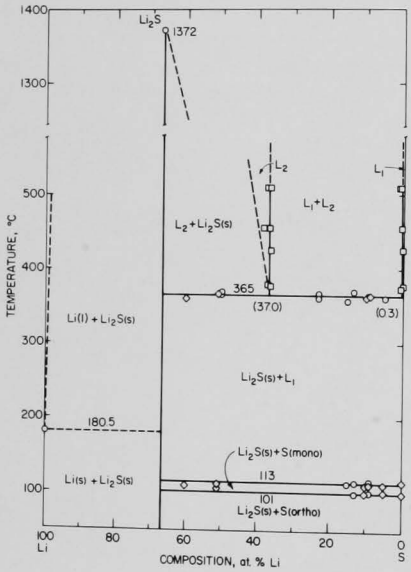

Fig. V-1. Partial Phase Diagram of the Lithium-Sulfur System. □ Chemical analysis data; ○ heating and cooling curve data; and ◇ differential thermal analysis data. ANL Neg. No. 308-2702.

Previous efforts to determine the extent of the miscibility gap by chemical analysis of quenched samples were frustrated by failure of the two phases to separate completely under normal gravity. This difficulty was overcome by use of a high-temperature centrifuge.

After centrifuging and quenching, the samples contained two distinctly different zones, presumably representing the two liquid phases present prior to quenching. Each zone was analyzed by flame photometry for lithium content, the sulfur being obtained by difference. The analytical results, which are shown

[1] Chemical Engineering Division Annual Report--1970, USAEC report ANL-7775, Section V.A.1.a.(2) (in press).

in Fig. V-1 as the square symbols, define the limits of the miscibility gap. The miscibility gap can be seen to extend from less than 0.5 at. % lithium to about 36.8 at. % lithium at 365°C and does not appear to have narrowed significantly at 508°C.

Location of the upper liquidus has proven to be difficult because the thermal effects associated with the liquidus crossing were not observed, and quenched samples have not been polished well enough to permit microscopic methods to be used.

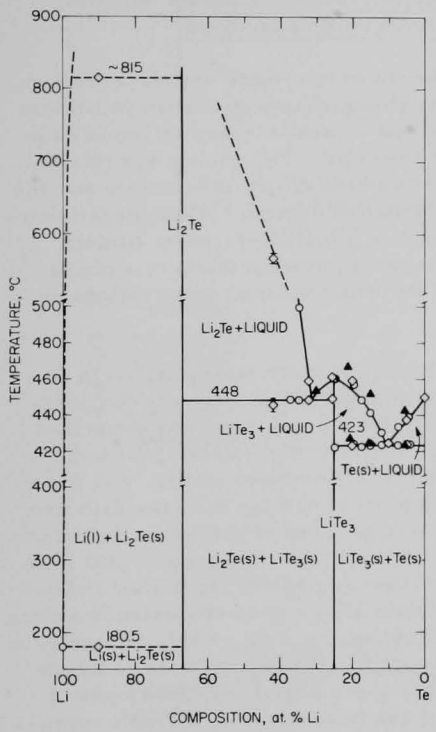

Fig. V-2

Partial Phase Diagram of Lithium-Tellurium System. ▲ Heating and cooling curve data (previous work, see Ref. 2); ○ heating and cooling curve data (present work); and ◇ differential thermal analysis data (present work). ANL Neg. No. 308-2703.

b. Lithium-Tellurium System

Preliminary work on the lithium-tellurium phase diagram was previously reported.[2] Investigation of this system has been reinstituted to obtain a more accurate and more complete phase diagram. Classical thermal and X-ray techniques are being used. The phase diagram shown in Fig. V-2, while it contains recent data, is essentially the same as previously reported.[2]

The presence of the intermediate phase $LiTe_3$, which was tentatively identified[2] earlier, has been substantiated by the present work. At room temperature, this phase has a body-centered cubic structure with a lattice constant of 6.162 Å. The density of $LiTe_3$, as measured with an air-comparison picnometer, was found to be 5.29 (±0.25) g/cm^3, which is in reasonable agreement with the calculated density of $LiTe_3$ (5.531 g/cm^3) based on the X-ray data.

The results of recent thermal measurements are shown in Fig. V-2 along with previously reported data. The previous data appear to have been systematically high, expecially in the temperature of the liquidus crossing. This is attributed to a lack of vigorous stirring since similar effects have been observed during the present work when samples were not stirred.

[2] Chemical Engineering Division Annual Report--1968, USAEC report ANL-7575, pp. 140-142 (1969).

Attempts to measure the melting point of Li_2Te have been unsuccessful because of the difficulty of preparing a pure sample. The melting point appears to be higher than 825°C. Preliminary DTA results on samples more lithium-rich than Li_2Te indicate that the lithium melting point is not measurably depressed by the addition of tellurium.

2. Thermodynamics of the Pseudo-Ternary Lithium Selenide-Selenium-Alkali Halide System by Emf Methods

Ambiguities arising in attempts to correlate emf data from reversible electrochemical cell work with phase-diagram studies in lithium selenide-selenium systems have shown that it is necessary to include the influence of the electrolyte on emf cell behavior. The reason for this influence is the significant mutual solubility of the halide electrolyte and the lithium-rich liquid (L_2) in the lithium-selenium system.[3] Consideration of the electrolyte mixture as one component in a pseudo-ternary lithium selenide-selenium-electrolyte (halide eutectic) system leads to a phase diagram which is consistent with all of the experimental observations on this system.

Emf measurements on the Li/LiBr-RbBr (eutectic)/Li in Se cell at 360°C have been conducted in the high selenium-low salt composition region using a three-compartment H cell, which has been described previously.[4] The emf values of three Li/LiBr-RbBr (eutectic)/Li in Se cells as a function of cathode composition are presented in Fig. V-3 for a temperature of 360°C. In the right-hand portion of Fig. V-3, the data are presented on a linear scale of emf vs. atom percent of lithium in selenium in the cathode compartment. The principal utility of this type of plot is in locating the intersections of the straight-line regions at the higher lithium concentrations. Comparison of the emf data shows good consistency among the data for cells of different Se-to-salt ratios, $n_{Se}/(n_{Se} + n_E)$. Notably, in the dilute-lithium region designated $L_1 + L_3$ (L_1, L_2, and L_3 refer to liquid fields in the pseudo-ternary phase diagram; see Fig. V-4), the slopes of emf vs. logarithm of composition exhibit the Nernst slope, RT/nF, corresponding to ~63 mV/decade. This slope is required for a two-electron ($n = 2$) reaction, which may be written: $2\ Li + xSe \rightarrow Li_2Se_x$. In the three-phase region labeled $L_1 + L_2 + L_3$, the slight downward trend of emf vs. cathode composition (which should be horizontal for a three-phase region in a three-component system) is thought to be caused by exchange of rubidium and lithium at the electrolyte-cathode interface in the cathode chamber. The formation of some Rb_2Se_x would be expected to lower the cell potential slightly as the lithium concentration increases in the cathode alloy. The discontinuous changes in the slopes $dE/d \ln x_{Li}$ denote the locations of phase boundaries. For Cell No. 2164F-72, a change in slope occurs

[3] Chemical Engineering Division Annual Report--1970, USAEC report ANL-7775, Sec. V.A.1.a.(1) (in press); P. T. Cunningham, S. A. Johnson, and E. J. Cairns, J. Electrochem. Soc. 118, 1941 (1971).

[4] E. J. Cairns et al., Physical Chemistry of Liquid Metals and Molten Salts, Chemical Engineering Division Semiannual Report--January-June 1971, USAEC report ANL-7823, pp. 29

at x_{Li} = 0.04; Cells No. 2258F-32 and 2258F-41 indicate phase boundaries by changes of slope at x_{Li} = 0.023, x_{Li} = 0.252, and x_{Li} = 0.298.

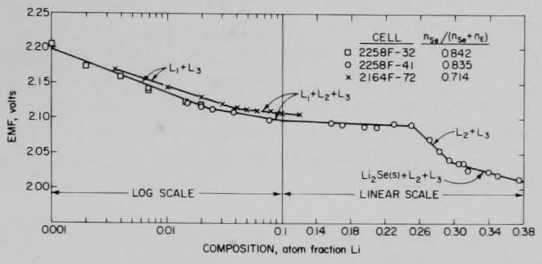

Fig. V-3. Emf Measurements at 360°C as Function of Cathode Composition for Three Li/LiBr-RbBr/Li in Se Cells. ANL Neg. No. 308-2705.

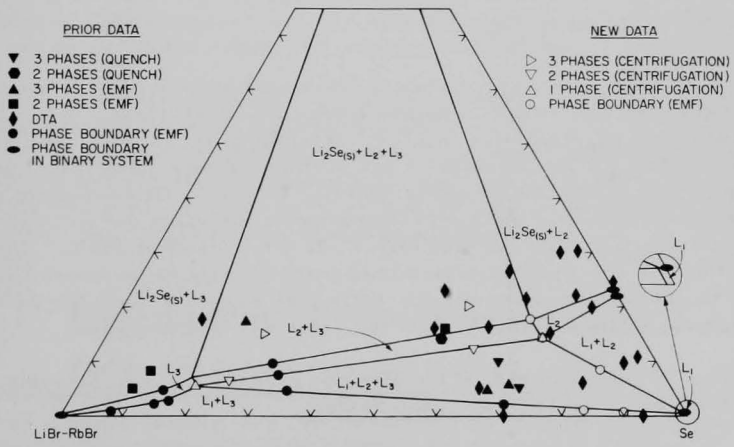

Fig. V-4. Li_2Se-Se-(LiBr-RbBr Eutectic) Pseudo-Ternary Phase Diagram

The highest $n_{Se}/(n_{Se} + n_E)$ ratio studied was 0.903. Distinct changes in slope occurred at x_{Li} = 0.008 and 0.152. The slope for the low x_{Li} region is in agreement with both the previous data obtained in the L_1 + L_3 region and the Nernst slope of RT/2F. After passing through the L_1 + L_2 + L_3 phase region and into a two-phase region, L_1 + L_2, the cell potential continued to increase at a low rate (~0.5 mV/hr) to unreasonably high values. This behavior was probably caused by the absence of L_3 in the cathode compartment, resulting in a relatively large driving force for the transfer of L_3 (or electrolyte) from the center compartment into the cathode chamber, and conversely of L_2 into the electrolyte contained in the center compartment.

The various phase regions and boundaries determined by the changes in slope of emf-vs.-composition plots of Fig. V-3 can be understood on the basis of the pseudo-ternary phase diagram shown in Fig. V-4. The results shown in Fig. V-3 for $n_{Se}/(n_{Se} + n_E) = 0.714$ (Cell No. 2164F-72) correspond to a line parallel to the Li_2Se-Se side of the diagram at 71.4 mol % Se in Fig. V-4. The values for x_{Li} corresponding to changes in slope (indicating phase boundaries) have been converted to mole percent Li_2Se. Using all available data, the phase boundaries shown in Fig. V-4 were located and are found to conform with the results of thermal analyses[4] and centrifugation experiments.

From the data in the $L_1 + L_3$ region, such as those of Fig. V-3, it can be determined that $dE/d \ln x_{Li} = -RT/2F$, indicating that two electrons and two lithium atoms are involved in the cell reaction, $2\ Li + xSe \rightarrow Li_2Se_x$. The corresponding Nernst equation (with pure lithium as the reference electrode) is

$$E = -\frac{RT}{2F} \ln \gamma_{Li_2} x_{Li_2}.$$

The activity coefficient γ_{Li_2} has been calculated to be 6×10^{-32} from the Nernst equation and results obtained from Li/LiBr-RbBr/Li in Se cells at 360°C at lower $n_{Se}/(n_{Se} + n_E)$ ratios.[5] Assuming the activity coefficient of salt in L_2 and L_3 to be constant, it has been possible to determine the free energy of formation, ΔG_f, of Li_2Se (360°C). Using the Gibbs-Duhem equation to correct the free energy of formation to the value for unit activities of lithium and selenium, we find $\Delta G_f^\circ = -94.0$ kcal/mol at 360°C.[4] It can be shown that ΔG_f° for $Li_2Se(s)$ determined from the emf value where $Li_2Se(s)$ begins to precipitate, namely 2.042 volts (see Fig. V-3, Cell No. 2258F-41), is within approximately 0.3 kcal of the value of -94.0 kcal/mol.

3. Phase Diagram of the Pseudo-Ternary Lithium Selenide-Selenium-Alkali Halide System

Phase-equilibrium studies have been conducted to determine the compositions of the terminal phases in the Li_2Se-Se-(LiBr-RbBr eutectic) pseudo-ternary system. Some difficulties in separating the various liquid and solid phases were encountered in early experiments. Nearly quantitative separation of these phases was accomplished using the high-temperature centrifuge assembly described previously.[6]

By centrifuging and chemical analysis, the compositions of the terminal phases were only roughly located (±5%) because of uncertainties

[5] Chemical Engineering Division Annual Report--1970, USAEC report ANL-7775, Section V.B.1.c (in press).
[6] E. J. Cairns et al., Physical Chemistry of Liquid Metals and Molten Salts, Chemical Engineering Division Semiannual Report--January-June 1971, USAEC report ANL-7823, p. 40 (1971).

in the analytical techniques. To locate the phase boundaries more accurately, mixtures of Li_2Se, Se, and LiBr-RbBr eutectic with compositions in the vicinity of the analytically determined values for the terminal phases were equilibrated, centrifuged, and examined microscopically until a nearly single-phase sample was produced. Results of these studies are plotted in Fig. V-4 and appear to be in good agreement with the results of the other studies.

B. Lithium-Hydrogen-Metal Systems of Importance to Fusion Reactors

Liquid lithium appears to be uniquely suited to act as the blanket material in present conceptual designs for deuterium-tritium fueled fusion reactors. Because much of the thermodynamic information on the lithium-hydrogen, -deuterium, and -tritium systems is fragmentary, particularly for conditions that are projected for fusion reactors, we have initiated a program to study chemical activities and phase equilibria in these systems. The results of these studies are expected to provide useful information for the design of thermonuclear-reactor fuel-cycling and recovery processes and to add to our understanding of solutions of hydrogen in liquid metals.

In advance of our studies of the thermodynamics of the lithium-hydrogen system, attempts have been made to estimate (1) tritium partial pressures in tritium-lithium solutions as a function of temperature and composition and (2) tritium permeation rates under the conditions anticipated for fusion reactors. Results of these calculations are presented, and their implications with regard to the design of thermonuclear devices are discussed.

1. Thermodynamics of Lithium-Hydrogen Systems

The paucity of literature data for the Li-LiH, Li-LiD, and Li-LiT systems has been indicated elsewhere.[7] In the Li-LiH system there are three studies dealing with the dissociation pressure of hydrogen as a function of temperature and composition: Hill[8] obtained a pressure-composition isotherm at 700°C; Perlow[9] measured two isotherms at 770 and 825°C; and, more recently, Heumann and Salmon[10] redetermined Hill's isotherm at 700°C. The data of these investigations lack consistency, particularly in the dilute regions, where the disagreements result in the crossing of the isotherms.

Our present experimental program is intended to produce a more consistent set of isotherms amenable to thermodynamic interpretation. In anticipation of our results, we have made a thermodynamic analysis

---

[7] Ibid., p. 14.
[8] L. L. Hill, Ph.D. dissertation, The University of Chicago (1938).
[9] M. R. J. Perlow, Ph.D. dissertation, The University of Chicago (1941).
[10] F. K. Heumann and O. N. Salmon, USAEC report KAPL-1667 (1956).

of the existing data in the Li-LiH system and derived the following semi-empirical equation:

$$\ln \sqrt{P} = -\ln K + \ln \frac{N_{LiH}}{1 - N_{LiH}} + \frac{1}{T} \sum_{i=0}^{k} B_i N_{LiH}^i \qquad (1)$$

where P is the pressure of hydrogen (atm), N_{LiH} is the mole fraction of LiH, T is the Kelvin temperature, K is an equilibrium constant for the equilibrium $Li + 1/2\ H_2 \rightleftharpoons LiH$, and the B_i's are coefficients. For $i \neq 0$, the B_i's are related to the coefficients in the Margules equation.[11]

Equation 1 expresses, in an analytical form, the pressure-composition-temperature relationship for the Li-H_2 system. In order to evaluate the constants, we fit the quantity $\ln \sqrt{P} - \ln [N_{LiH}/(1 - N_{LiH})]$ obtained from Eq. 1, as a function of N_{LiH}, using the data of Heumann and Salmon and truncating the sum at k = 1, 2, 3, etc. Statistical F-tests have indicated that the cubic term is the last one of significance. Therefore, similar plots were made using k = 3 for the data of Hill (700°C) and of Perlow (770 and 825°C).

Since it was felt that the quality of the more recent work of Heumann and Salmon is superior, we elected to use, for the B_i coefficients, the values obtained from their data. In order to evaluate the constants, a constraint was introduced: at 825°C, and at the critical composition $N_{LiH} = 0.768$ (see below), the value of hydrogen pressure was taken to be 435 Torr, which is the approximate dissociation pressure in the plateau region of the experimental 825°C isotherm.[9] The constraining condition, when applied to Eq. 1, yielded $(-\ln K + B_o/T) = 1.789$ at 825°C, which compares with $(-\ln K + B_o/T) = 0.822$ at 700°C. Parameters obtained from the solution of these two simultaneous equations lead to Eq. 2

$$\ln \sqrt{P}\,(\text{atm}) = 9.324 + \ln \frac{N_{LiH}}{1 - N_{LiH}} + \frac{1}{T}\left(-8274 - 7931\, N_{LiH} + 11754\, N_{LiH}^2 - 9775\, N_{LiH}^3\right). \qquad (2)$$

Equation 2 was used to calculate isotherms at 700, 770, and 825°C. They are compared with the experimental data in Fig. V-5.

In the dilute region ($N_{LiH} \ll 1$) of the Li-LiH phase diagram, Eq. 1 reduces to

$$\ln \sqrt{P} = -\ln K + \ln N_{LiH} + B_o/T \qquad (3)$$

[11] J. H. Hildebrand and R. L. Scott, The Solubility of Nonelectrolytes, 3rd ed., p. 34, Reinhold Publishing Co., New York (1950).

or

$$\sqrt{P} = K_S N_{LiH} \tag{4}$$

where $K_S = [\mathrm{Exp}(B_o/T)]/K$ is the Sieverts' law constant. The law appears to hold up to 0.1 mol % LiH; at 0.1 mol %, the deviations were not larger than 1%. Since the dilute solutions (~10 ppm) of LiH in Li are of special interest in the tritium inventory problems in the fusion-reactor blankets, the Sieverts' law constants and hydrogen pressures at $N_{LiH} = 10^{-5}$ are listed in Table V-1.

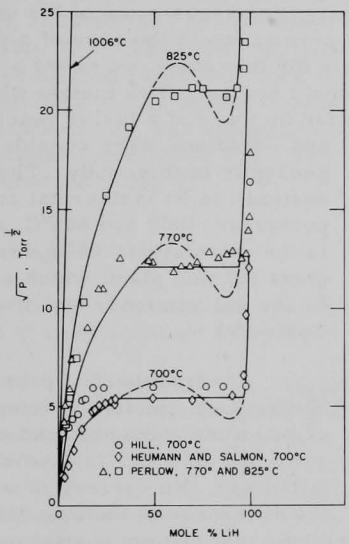

Fig. V-5

Comparison of the Calculated Isotherms with the Experimental Data for the System Li-LiH

TABLE V-1. Sieverts' Law Constants and the Corresponding Hydrogen Pressures at $N_{LiH} = 10^{-5}$ for Solutions <0.1 mol % LiH in Li

Temp., °C	Sieverts' Constant, $(\mathrm{Torr})^{1/2}$ (mole fraction)$^{-1}$	Pressure, Torr
600	23.7	5.61×10^{-8}
700	62.7	3.93×10^{-7}
800	138	1.92×10^{-6}
900	267	7.14×10^{-6}
1000	465	2.16×10^{-5}

2. Some Estimates of the Consequences of Tritium Permeation in the Core of a D-T Fusion Reactor

A number of preliminary studies[12-16] have appeared in which attempts have been made to evaluate the major problem areas confronting the designers of fusion-reactor facilities. Among the materials-related problems that have been identified, the permeation of hydrogen isotopes, particularly tritium, through the materials of construction is of considerable importance because of its bearing on structural integrity, fuel economy, and safety of operation.

In what follows, we attempt to assess some of the consequences, beneficial or otherwise, of tritium permeation in the core of a deuterium-tritium fueled reactor. As the basis for this study, we chose a 2500-MW(t) plant with a low-β toroidal confinement system. Two metals which appear promising as structural materials for the core of a fusion reactor, niobium and vanadium, were considered independently in this study. The blanket was assumed to be isothermal and two temperatures, 1000 and 800°C, were used in the calculations. The design parameters for this plant, which are important to the calculations, are listed in Table V-2.

TABLE V-2. Fusion Reactor Plant Parameters

Power and Energy Parameters	
Fuel cycle	50%D-50%T
Thermal power	2,500 MW(t)
Heat load on vacuum wall	10 MW(t)/m^2
Energy released per fusion reaction	22.4 MeV
Dimensions	
Area of vacuum wall	2.5 x 10^6 cm^2
Major radius of plasma chamber	435 cm
Minor radius of plasma chamber	145 cm
Thickness of vacuum wall	5 mm
Thickness of lithium blanket	60 cm
Area of blanket outer wall	3.5 x 10^6 cm^2
Thickness of blanket outer wall	5 mm
Breeding Parameters	
Number of fusion reactions per second	7 x 10^{20}
Tritium breeding ratio	≈1.1
Tritium breeding rate (in blanket)	≈8 x 10^{20} tritons/sec
Tritium Partial Pressures (TPP)	
TPP in plasma chamber	>10^{-3} Torr
TPP in vacuum annulus	≤10^{-4} Torr

Tritium partial pressures in the blanket as a function of temperature and composition were obtained using the results in Table V-1 for hydrogen solutions in lithium. No correction was made for the difference in isotope, although the results of Heumann and Salmon[10] indicate that tritium partial pressures may be 1.5 to 2 times higher than hydrogen partial pressures over lithium for

[12] J. E. Draley et al., in 1971 Intersociety Energy Conversion Engineering Conference Proceedings, p. 1065, Society of Automotive Engineers, Inc., New York (1971).

[13] D. J. Rose, On the Feasibility of Power by Nuclear Fusion, USAEC report ORNL-TM-2204 (1968).

[14] D. J. Rose, Science 172, 797 (1971).

[15] D. Steiner, A Review of ORNL Fusion Feasibility Studies, USAEC report ORNL-TM-3222 (1970).

[16] (a) A. P. Fraas, in Nuclear Fusion Reactor Conference Proceedings, p. 1, British Nuclear Energy Society, UKAEA, Culham Laboratory, Abingdon, Berkshire (1969).

(b) R. F. Post, ibid., p. 88.

(c) F. L. Ribe et al., ibid., p. 242.

(d) E. F. Johnson, ibid., p. 441.

(e) R. W. Werner et al., ibid., p. 449.

(f) R. W. Werner, ibid., p. 536.

the same composition and temperature. Hydrogen permeation rates through niobium and vanadium were determined using the equation

$$\varphi = \frac{C'}{X}\left(\sqrt{P_H} - \sqrt{P_L}\right) \exp(-Q/RT) \tag{5}$$

where φ is the permeation rate in atoms/(sec)(cm)^2, X is the wall thickness in mm, P_H and P_L are the tritium partial pressures in Torr on each side of the wall ($P_H > P_L$), Q is the activation energy in calories per mole, and T is the Kelvin temperature. Values of the proportionality factor C' and of Q were computed from the results given by Webb[17] for niobium and by Heinrich, Johnson, and Crouthamel[18] for vanadium. These values are listed in Table V-3. Since the constants in Table V-3 are based on data for hydrogen permeation rates, the atom fluxes were corrected for isotopic effects by dividing by the square root of the tritium-to-hydrogen mass ratio. In the calculations, P_L was set equal to 10^{-4} Torr and the values of P_H were determined from Table V-1. The total tritium fluxes, F_A (tritons/sec), were computed using Eq. 6:

$$F_A = \sqrt{\tfrac{1}{3}}A\varphi \tag{6}$$

where A is the total outside area (cm^2) of the wall being permeated by the tritium and φ is determined from Eq. 5.

TABLE V-3. Values of C' and Q for Niobium and Vanadium

	C', (atom)(mm)/(sec)(cm)^2(Torr)$^{1/2}$	Q, cal/mol
Niobium	5.63×10^{17}	3,430
Vanadium	2.66×10^{20}	14,200

A plot of the flux of tritium atoms through the outer wall of the blanket as a function of the concentration of tritium in the blanket is shown in Fig. V-6 at 1000°C and 800°C for both niobium and vanadium. The tritium production rate in the blanket of the fusion-plant concept considered here is also indicated in Fig. V-6. It can be seen that if a tritium concentration in the lithium in the range of 10 to 20 ppm is tolerable from the standpoint of materials compatibility and overall plant safety, the tritium can be recovered at a rate equal to the production rate in the blanket for niobium or vanadium structures at 1000°C. If operating temperatures are limited

[17] R. W. Webb, Permeation of Hydrogen through Metals, NAA-SR-10462 (1965).
[18] R. R. Heinrich, C. E. Johnson, and C. E. Crouthamel, J. Electrochem. Soc. 112, 1071 (1965).

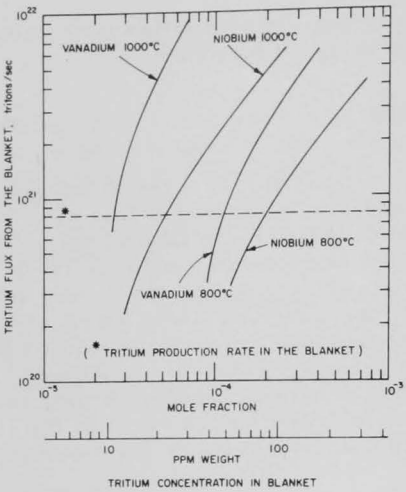

Fig. V-6. Tritium Flux through the Blanket Outer Wall as a Function of the Tritium Concentration in the Blanket

to 800°C, then tritium concentrations in excess of 40 ppm may have to be maintained in the blanket in order to reach a steady state.

One of the obvious advantages of the tritium-recovery scheme implied above is that the lithium blanket is static, thus avoiding pumping-power losses associated with the circulation of a liquid metal through magnetic field lines. We must stress, however, that these calculations are subject to errors associated with lengthy extrapolations of experimental data. A detailed assessment of the consequences of hydrogen isotope permeation in fusion devices will have to await the results of studies of (1) the chemical activity (partial pressure) of tritium in lithium at low concentrations (ppm range) and high temperatures (up to 1000°C) and (2) the permeability of hydrogen isotopes through various candidate structural materials as a function of temperature and differential driving pressure, particularly at low hydrogen pressures ($<10^{-3}$ Torr). The effect of radiation damage on permeation rates will also require investigation.

C. Structure Investigations by Spectroscopic Methods

The program of Raman spectroscopic studies has added much to our knowledge of the structure of molten salts. The existence of complex equilibria in Mg(II)- and Pb(II)-halide systems has been demonstrated, and in some cases the structures of the predominant complexes have been elucidated. Studies of polyatomic anions and their interaction with various cations in the molten state have revealed pertinent information on the nature of contact "ion-pairs" and cation polarization effects. These studies contribute to a better understanding of transport properties, distribution coefficients, and phase-equilibrium behavior in molten-salt systems. Recent results have been of particular importance to nuclear-fuel reprocessing programs, studies of species in contact with liquid sodium, and systems of potential utility as galvanic cell cathodes.

1. Studies of Divalent Metal Halide Melts

Raman investigations of divalent metal halide melts have continued with the completion of studies on the $MgBr_2$-KBr, MgI_2-KI, $PbCl_2$-KCl, and $PbBr_2$-KBr systems. The results of Raman spectroscopic and

normal-coordinate examinations for the $MgCl_2$-KCl system (reported previously in ANL-7775, Section V.B.2) confirmed the existence of tetrahedral $MgCl_4^{2-}$. These studies have since been extended to include $MgBr_2$-KBr and MgI_2-KI melts. Complete Raman spectra of $MgBr_4^{2-}$ and MgI_4^{2-} have been obtained for melts with a halide/magnesium(II) mole ratio of 4.0. The observed frequencies are listed in Table V-4. As in the case of $MgCl_4^{2-}$, one high-intensity polarized band and three low-intensity depolarized bands are observed for the bromide and iodide complexes. Normal-coordinate analyses were carried out for each of these species based on a tetrahedral configuration and using a Urey-Bradley force field[19] with the conditions F' = -0.1 F and H = 0. Matrix elements used in the calculations were identical to those given by Nakamoto.[20] The calculated frequencies for $MgBr_4^{2-}$ and MgI_4^{2-} are given in Table V-4 together with those previously determined for $MgCl_4^{2-}$, and the force constants for all three species are listed in Table V-5.

TABLE V-4. Observed and Calculated Frequencies for MgX_4^{2-} (X = Cl, Br, and I)

Symmetry Species	Frequencies,[a] cm^{-1}					
	$MgCl_4^{2-}$		$MgBr_4^{2-}$		MgI_4^{2-}	
	Observed	Calculated	Observed	Calculated	Observed	Calculated
ν_1 (A_1)	250 p	250	150 p	152	111 p	114
ν_2 (E)	94 dp	92	50 dp	52	40 dp	38
ν_3 (F_2)	325 dp	325	282 dp	282	263 dp	262
ν_4 (F_2)	130 dp	132	83 dp	79	59 dp	59

[a]p = polarized, dp = depolarized.

TABLE V-5. Force Constants for MgX_4^{2-} (X = Cl, Br, and I)

Complex	Force Constants,[a] millidynes/Å		
	K	H	F
$MgCl_4^{2-}$	0.669	0	0.158
$MgBr_4^{2-}$	0.629	0	0.113
MgI_4^{2-}	0.584	0	0.095

[a]Urey-Bradley Force Constants: K = Mg-X bond-stretching constant, H = X-Mg-X bond-bending constant, and F = X....X repulsion constant.

[19]K. Nakamoto, Infrared Spectra of Inorganic and Coordination Compounds, p. 55, John Wiley & Sons, New York (1970).

[20]Ibid., p. 318.

The observation of four Raman-active bands (one polarized and three depolarized) is consistent with the existence of a tetrahedral MgX_4^{2-} species in each of the magnesium halide systems studied. The excellent agreement between observed and calculated frequencies obtained with the simplified Urey-Bradley force field adds support to the conclusion of this study (and an earlier one[21]) that these species are indeed tetrahedral.

The existence of complex ions in PbX_2-KX melts (X = Cl and Br) has been investigated by Raman spectroscopy. No Raman bands were observed for pure molten $PbCl_2$, in agreement with previous results of Balasubrahmanyam and Nanis.[22] When additions of KCl were made to the $PbCl_2$ melts, a single polarized band was observed in the region from 200 to 240 cm^{-1}. This band, centered near 218 cm^{-1}, appeared to increase in intensity as the Cl^{1-}/Pb^{2+} mole ratio was increased from 2.3 to 4.0. This behavior is illustrated in Fig. V-7. Similar results were obtained for the $PbBr_2$-KBr melts. An extremely weak, polarized band was observed in pure $PbBr_2$. This band, centered near 144 cm^{-1}, increased in intensity as the Br^{1-}/Pb^{2+} mole ratio was increased from 2.0 to 4.0.

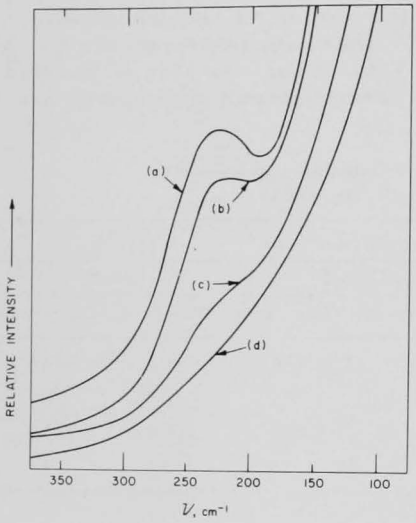

Fig. V-7

Raman Spectra of $PbCl_2$-KCl Melts: (a) 33 mol % $PbCl_2$ in KCl at 590°C, (b) 50 mol % $PbCl_2$ in KCl at 520°C, (c) 75 mol % $PbCl_2$ in KCl at 520°C, (d) Pure Molten $PbCl_2$ at 520°C

Pure molten $PbCl_2$ and $PbBr_2$ appear to have very little bonded structure. The single polarized band observed in the systems $PbCl_2$-KCl and $PbBr_2$-KBr, which increases in intensity with increasing amounts of potassium halide up to 67 mol % KX in PbX_2, is attributed to the symmetric stretching motion of a simple species of the type $PbCl_n^{(2-n)}$. In the absence of additional vibrational bands, it is not possible to deduce a structure for this species. Nevertheless, the results of this study substantiate

[21] V. A. Maroni, E. J. Hathaway, and E. J. Cairns, J. Phys. Chem. 75, 155 (1971).
[22] K. Balasubrahmanyam and L. Nanis, J. Chem. Phys. 40, 2657 (1964).

the conclusion drawn from other physicochemical investigations[23-28] that complex ions exist in $PbCl_2$-KCl and $PbBr_2$-KBr melts.

2. Reactions of Iodine-Containing Species with Molten Nitrates

The reaction of elemental iodine and other iodine-containing species with silver nitrate at 200°C is of particular interest because of its role in the silver nitrate-impregnated scrubber towers used to strip ^{131}I from the gases released during the reprocessing of nuclear fuels.[29] These towers are capable of iodine-removal efficiencies of better than 99.5% principally because of the following reaction:[30]

$$6\ AgNO_3 + 3\ I_2 \rightarrow 4\ AgI + 2\ AgIO_3 + 6\ NO_2.$$

However, the expense associated with the use of silver makes it worthwhile to examine the possibility of using molten alkali metal nitrates in place of the silver nitrate. Accordingly, we have continued our investigations of the interactions of iodine-containing species with molten nitrates in order to develop an understanding of the reactions involved in molten-nitrate-packed scrubber towers.

In a previous report,[31] we showed that I_2O_5 (very probably an intermediate in the reaction of elemental iodine and iodine-containing species with molten nitrates) reacts nearly quantitatively with alkali metal, silver(I), and thallium(I) nitrates at temperatures just above their melting points to produce an iodine-containing oxyanion, presumably IO_3^{1-}. The reaction assumed to occur was the following:

$$I_2O_5 + 2\ MNO_3 \rightarrow 2\ MIO_3 + 2\ NO_2 + 1/2\ O_2.$$

Infrared spectra (650-950 cm^{-1}) of KIO_4, KIO_3, and two pre-equilibrated (at 350°C) mixtures (15 mol % KIO_4-KNO_3 and 15 mol % KIO_3-KNO_3) were obtained on samples that were pressed into KBr pellets. The spectra were recorded using a Beckman IR-4 infrared spectrophotometer. These spectra are shown in Fig. V-8. The spectrum of KIO_4 (Curve b) has a strong band centered at 855 cm^{-1} which is attributed to ν_3 for tetrahedral IO_4^{1-}.[32] Infrared spectra of KIO_3 and the pre-equilibrated KIO_4-KNO_3 and KIO_3-KNO_3

---

[23] M. F. Lantratov and O. F. Moiseeva, Zh. Fiz. Khim. 34, 171 (1960).

[24] I. G. Murgulescu and St. Zuca, Rev. Roum. Chim. 10, 129 (1965).

[25] M. F. Lantratov and A. F. Alabyshev, J. Appl. Chem. USSR English Transl. 26, 235 (1953).

[26] H. Bloom and A. J. Easteal, Aust. J. Chem. 18, 2039 (1965).

[27] J. L. Barton and H. Bloom, Trans. Faraday Soc. 55, 1792 (1959).

[28] H. Bloom and J. W. Hastie, Aust. J. Chem. 21, 583 (1968).

[29] W. A. Rodger and S. L. Reese, Reactor and Fuel-Processing Technology 12(2), 173 (1969).

[30] J. W. Lacksonen, W. H. Kerby, and C. E. Dryden, Iodine Vapor-Silver Nitrate Reaction Mechanisms and Phase Equilibria, USAEC report TID-16914 (1962).

[31] V. A. Maroni and E. J. Hathaway, in Chemical Engineering Division Annual Report--1970, ANL-7775, Section V.B.2.b (in press).

[32] K. Nakamoto, Infrared Spectra of Inorganic and Coordination Compounds, 2nd ed., p. 111, John Wiley & Sons, New York (1970).

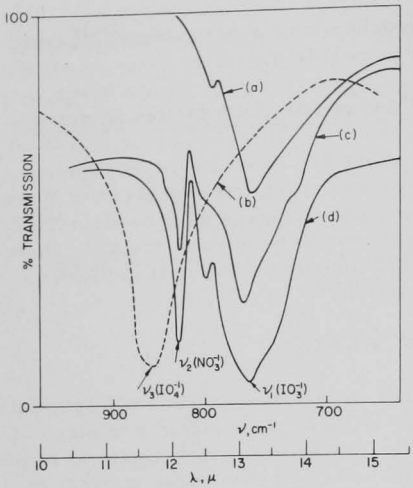

Fig. V-8

Infrared Transmission Spectra of KIO_3 (Curve a), KIO_4 (Curve b), Premelted Mixture of 15 mol % KIO_3-85 mol % KNO_3 (Curve c), and Premelted Mixture of 15 mol % KIO_4-85 mol % KNO_3 (Curve d) Pressed into KBr Pellets. ANL Neg. No. 308-2317.

mixtures (Curves a, c, and d) are essentially the same with a broad band centered near 755 cm^{-1}, which is indicative of IO_3^{1-}.[33]

The occurrence of the 755-cm^{-1} band for both the unheated KIO_3 and the pre-equilibrated KIO_3-KNO_3 mixture, together with the previously presented results[31] of Raman studies of alkali metal, silver(I), and thallium(I) iodate-nitrate melts, demonstrates that IO_3^{1-} has appreciable stability in these melts. The similarity of Curves c and d indicates that IO_4^{1-} is reduced to IO_3^{1-} in the presence of nitrate at elevated temperatures.

3. Cation Effects on the Structure of the Iodate Ion in Molten Nitrates

Raman spectra of the iodate ion in molten alkali metal, silver(I), and thallium(I) nitrates[31] were found to be consistent with the existence of a pyramidal IO_3^{1-} species. Comparison of the spectral features of the IO_3^{1-} and NO_3^{1-} ions indicated that the nature and magnitude of the cation-iodate ion and cation-nitrate ion interactions are remarkably similar. In this earlier study, the extent of cation-anion interaction was determined from the frequency shift of the totally symmetric stretching vibrations, $\nu_1(IO_3^{1-})$ and $\nu_1(NO_3^{1-})$, upon change of the cation.

Recently, James and Leong[34] measured the relative intensities of the symmetrical stretching frequency (ν_1) of the nitrate ion in melts containing univalent metal cations. They found that for the alkali nitrates, the intensity gradually decreased with increasing values of z/r of the cation (z = ionic charge, r = cationic radius). In Fig. V-9, we have plotted the ratio of the integrated intensities of the IO_3^{1-} and NO_3^{1-} symmetrical stretching frequencies[35] against the IO_3^{1-}/NO_3^{1-} mole ratio for those MIO_3-MNO_3 samples (M = Li, Na, K, and Rb) which we were able to analyze iodometrically for IO_3^{1-}. (Some decomposition was noted in the $CsIO_3$-$CsNO_3$ sample; consequently results for this sample were not included in Fig. V-9.) The

[33] Ibid., p. 94.

[34] D. W. James and W. H. Leong, Trans. Faraday Soc. 66, 1948 (1970).

[35] See Ref. 3 for details of the Raman spectral measurements.

ratios of the relative band intensities of $\nu_1(IO_3^{1-})$ and $\nu_1(NO_3^{1-})$ are found to be proportional to the ratio of their molar concentrations and independent of the alkali cation present. This implies that the interaction of each alkali cation with an iodate ion is strikingly similar to the interaction of that cation with a nitrate ion in terms of its effect on the intensity of the oxyanion symmetrical stretching vibration.

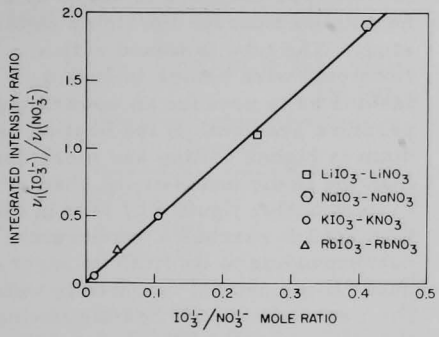

Fig. V-9

Ratio of the Integrated Intensities of $\nu_1(IO_3^{1-})$ and $\nu_1(NO_3^{1-})$ Plotted against the IO_3^{1-}/NO_3^{1-} Mole Ratio. ANL Neg. No. 308-2737.

D. Nucleation Studies

There are a number of examples of bubble-nucleation phenomena important to reactor technology, such as the superheating and boiling of liquid sodium coolant and the release of dissolved fission products from fluid coolants or fuels. In an effort to better understand such phenomena, both for pure systems and for mixtures, an experimental and theoretical study has been initiated of the homogeneous nucleation of vapor bubbles in superheated liquids.

1. Measurements of the Limit of Superheat of Liquids

The experimental program in bubble nucleation involves measurement of the limit of superheat of various pure liquids and binary liquid mixtures to test existing theories of nucleation. Hydrocarbon systems are convenient for this purpose. The apparatus, which is being used to determine the vaporization temperature corresponding to the homogeneous limit of superheat, is shown in Fig. V-10. It is constructed of Pyrex and based on the designs of Wakeshima and Takata,[36] Skripov et al.,[37,38] and Blander et al.[39] In a superheating experiment, droplets of the liquid under study are produced in the lower chamber by dispersion in an immiscible liquid medium. For current experiments on hydrocarbons, a dispersion medium of

[36] H. Wakeshima and K. Takata, J. Phys. Soc. Japan 13, 1398 (1958).
[37] V. P. Skripov and V. I. Kukushkin, Russ. J. Phys. Chem. 35, 1393 (1961).
[38] V. P. Skripov and E. N. Sinitsyn, Sov. Phys. Usp. English Transl. 7, 887 (1964-65).
[39] M. Blander, D. Hengstenberg, and J. L. Katz, J. Phys. Chem. 75, 3613 (1971).

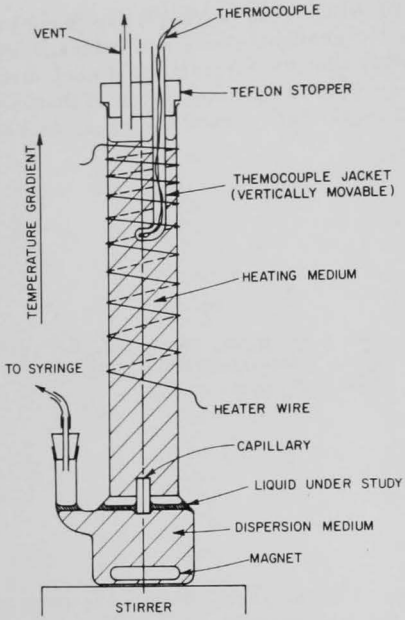

Fig. V-10. Apparatus for Determination of the Vaporization Temperature for the Homogeneous Limit of Superheat

glycerin or glycol is being used. By exerting pressure on the side arm, dispersed droplets can be pushed through the capillary tube into the upper heating tube. The heating tube is filled with the same liquid as that in the lower chamber to serve as a heating medium for the liquid under study. The tube is wound with a Nichrome wire heater in such a fashion as to produce an upward temperature gradient. If the heating medium is higher boiling and more dense than the liquid under study, then a droplet of this liquid will rise in the tube until it reaches a temperature corresponding to its limit of superheat. If the droplet completely wets (i.e., spreads on) the heating medium, then the nucleation of vapor bubbles will occur homogeneously within the body of the liquid droplet. This condition is met if

$$\gamma_L < \gamma_M - \gamma_{ML} \tag{7}$$

where γ_L is the surface tension of the liquid under study, γ_M is the surface tension of the medium, and γ_{ML} is the interfacial tension between the medium and the liquid. If the liquid does not completely wet the medium then

$$\gamma_L > \gamma_M - \gamma_{ML} \tag{8}$$

and nucleation will tend to occur heterogeneously at the liquid-liquid interface.

Measurements have been made of the vaporization temperature, T_v, for a variety of saturated hydrocarbons and the results are shown in Table V-6. A number of these determinations have been made in both glycerin and glycol in our study as well as in sulfuric acid in other studies.[36-43] The close agreement between the results in different media strongly suggests homogeneous nucleation. In Table V-6, T_v is compared with the

[40] V. P. Skripov and G. B. Ermakov, Russ. J. Phys. Chem. 37, 1047 (1963).
[41] V. P. Skripov and G. B. Ermakov, Russ. J. Phys. Chem. 38, 208 (1964).
[42] V. P. Skripov and E. N. Sinitsyn, Russ. J. Phys. Chem. 42, 167 (1968).
[43] E. N. Sinitsyn and V. P. Skripov, Russ. J. Phys. Chem. 42, 440 (1968).

boiling temperature, T_b, at the ambient pressure of these measurements (~748 Torr) and with the increment of superheat, $\Delta T = T_v - T_b$. A correlation has been developed which relates T_v, T_b, and the critical temperature, T_c. It takes the form of a linear relationship between the reduced vaporization temperature, T_v/T_c, and the reduced boiling temperature, T_b/T_c, as is shown in Fig. V-11. This correlation permits the simple estimation of the vaporization temperature corresponding to the homogeneous limit of superheat from the boiling and the critical temperatures.

TABLE V-6. Superheat Determinations for a Variety of Hydrocarbons

Liquid	T_b, °K	T_v, °K	ΔT, °K	T_c, °K
n-butane	272.3	378.2	105.9	425.2
n-pentane	308.8	420.1	111.3	469.6
n-hexane	341.7	455.6	113.9	507.4
n-heptane	371.1	486.7	115.6	540.2
n-octane	398.2	513.0	114.8	568.8
n-nonane	423.5	538.5	115.0	594.6
2,2-dimethylpropane	282.3	386.6	104.3	433.8
2,3-dimethylbutane	330.7	446.4	115.7	499.9
2,2,4-trimethylpentane	372.4	488.5	116.1	543.9
1-pentene	303.2	417.2	114.0	464.7
1-octene	394.5	510.3	115.8	566.6
Cyclohexane	353.9	492.8	135.3	553.4
Methylcyclohexane	374.1	510.4	136.3	572.1

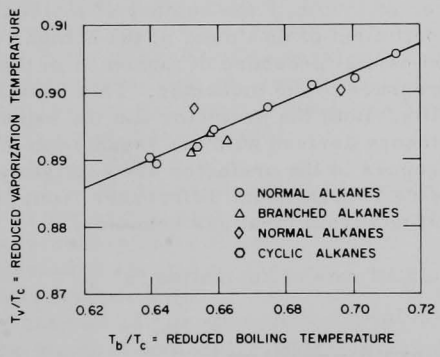

Fig. V-11

Reduced Vaporization Temperature versus Reduced Normal Boiling Temperature for Various Pure Liquids

Experiments have also been performed on binary mixtures of n-octane with n-pentane. The results are shown in Fig. V-12. Of the twelve mixtures studied, ten were superheated in glycerin and two in glycol. The results show no significant difference attributable to the medium. The limit of superheat as a function of mole fraction shows a positive deviation from linearity which is skewed toward the more volatile hydrocarbon.

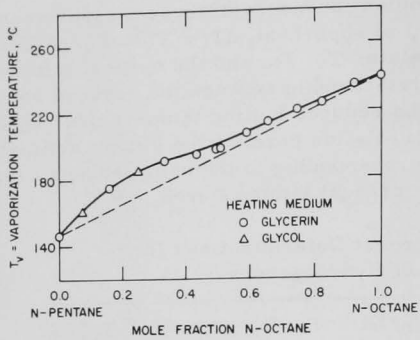

Fig. V-12

The Vaporization Temperature versus Mole Fraction for Mixtures of n-pentane with n-octane

2. Theory for Homogeneous Nucleation Involving Nonideal Gases

Equations were derived for the rate of homogeneous nucleation in the processes of condensation and boiling for cases in which the gas phase is not ideal. The calculations were considerably simplified by the use of the formalism discussed by Hill[44] and Mayer[45] where all deviations from ideal behavior can be rigorously ascribed to the presence of "mathematical" polymers. Utilizing a method of calculation used by Katz et al.,[46] we derived the equation for J, the rate of nucleation per unit volume in condensation,

$$J = \frac{p_1}{dkT}\left(\frac{2\sigma m}{\pi}\right)^{1/2} \Sigma i^{3/2}\alpha_i n_i \exp\left\{-\frac{16\pi}{3}\left(\frac{\sigma}{kT}\right)^3\left(\frac{m}{d}\right)^2\left[\frac{1}{\ln\,(p_1/p_{1\infty})}\right]^2\right\} \qquad (9)$$

where d is the liquid density in the critical-sized droplet, σ the surface tension, m the mass of a monomer molecule, i the number of molecules in a polymer, α_i the condensation coefficient of an i'mer, n_i the number density of an i'mer, p_1 the supersaturated partial pressure of monomer in the vapor, and $p_{1\infty}$ the equilibrium partial pressure of the monomer. This equation is valid for any type of gas nonideality. Both the prefactor and the exponential differ from classical nucleation theory derived with the assumption of ideality of the gas phase. The differences in the prefactor are negligibly small. However, the factor $\ln\,(p_1/p_{1\infty})$ leads to significant differences from classical theory, especially for large deviations from ideal gas behavior.

For boiling, the calculated rate of nucleation is

$$J = N_o\left(\frac{2\sigma}{\pi m B}\right)^{1/2} \frac{\Sigma i^{3/2}\alpha_i n_{ic}}{\Sigma i n_{ic}} \exp\left[\frac{-16\pi\sigma^3}{3kT(p_c - p_o)^2}\right] \qquad (10)$$

---

[44] T. L. Hill, Statistical Mechanics, McGraw-Hill, New York (1956).
[45] J. E. Mayer and M. G. Mayer, Statistical Mechanics, p. 292, John Wiley and Sons, New York (1940).
[46] J. L. Katz, H. Saltsburg, and H. Reiss, J. Colloid. Interface Sci. 21, 560 (1966).

where N_o is the number density of the liquid, p_c is the gas pressure inside a critical-sized bubble, p_o is the external pressure on the liquid, n_{ic} is the number density of i'mers in a critical-sized bubble, and B is given by

$$B = 1 - \frac{1}{3}\left(1 - \frac{p_o}{p_c}\right)\Sigma i^2 N_{ic}/(\Sigma i N_{ic})^2 \tag{11}$$

where N_{ic} is the mole fraction of i'mer in the critical-sized bubble. The exponential factor is identical with that of classical theory, as has been shown by Moore;[47] the pre-exponential factor differs from classical theory and the form differs from Moore's calculations, which were based solely on thermodynamic reasoning. However, only for mixtures and other cases where the exponential factor is not a very strong function of temperature, are the differences between classical theory and Eq. 10 significant.

E. Theoretical Studies in Thermodynamics

1. Gas Solubility in Liquid Metals

Interest in devising improved models for the prediction of the solubility of noble gases in liquid metals is continuing because of the technological need for such predictions in connection with liquid-metal-cooled fast reactors. Such systems also serve as simplified models for basic investigations of alloy-formation thermodynamics. The model so far developed[48] has yielded far better predictions than previous ones based on molecular considerations only. This improvement is brought about by the incorporation of concepts specific to solutions in metals, i.e., the energetics of the expulsion of the conduction electrons from the vicinity of the solute atom. Some of the detailed predictions, however, showed small but significant deviations from the experimentally observed behavior of solutions of helium, argon, and xenon in liquid sodium;[49] further attention has been given to these discrepancies.

In our earlier models we had taken the size of the cavity occupied by the solute atom to be given either by geometric factors (i.e., sum of hard-sphere radii of solute and solvent atoms) or by a balance between the pressure exerted on the cavity walls by the confined solute atom and the internal pressure of the solvent. Neither of these two models constitutes more than an ad hoc approximation; in recent work, these have been replaced by the thermodynamically exact requirement that the cavity size be that which minimizes the sum, g^{xs}, of the relevant atomic free-energy terms.

---

[47] G. R. Moore, Ph.D. dissertation, The University of Wisconsin (1956).

[48] Chemical Engineering Division Research Highlights, USAEC report ANL-7750, p. 90 (1971).

[49] A discrepancy of a factor of 10 between the predicted and measured solubility of krypton in sodium caused the data for this case to be questioned; the solubility of krypton was therefore remeasured. See Section II.C.3.

Furthermore, an additional simplification had been made which, in essence, assumed that the partial atomic volume of solution, $\bar{v}$, is identical with the cavity volume, δV. This approximation, which affected the calculation of the change in kinetic energy of the conduction electrons, has now been replaced by the thermodynamically exact relation

$$\bar{v} = \beta_T kT + \beta_T n_o (\partial g^{xs}/\partial n_o)_T \tag{12}$$

where β_T is the isothermal compressibility of the solvent and n_o is the number density of solute particles. Because g^{xs} is a function of both $\bar{v}$ and δV, the calculations incorporating the exact thermodynamic relations are lengthy. They are now in progress.

a. Equation of State of Simple Fluids

The work done, w_{attr}, by the attractive forces acting between the solute molecule and the solvent is a significant term in our model describing noble gas solubilities in liquid metals, but it is not the dominant term. Consequently, the comparison of our calculated results with the experimental data in these systems does not provide a means for ascertaining the accuracy of our calculation of this term. It occurred to us that many of the concepts employed in our model could equally well be applied to a model description of the cohesive free energies of the pure liquefied noble gases.

Consider one mole of a noble gas at temperature T and having a molar volume v_g. The first step of our model process for the condensation of this gas will be the (conceptual) discharging of the attractive intermolecular forces at constant density (see Fig. V-13). The result is one mole of a gas of "soft" spheres (the molecules interact via long-ranged repulsive forces only) at v_g and T. The corresponding Helmholtz energy change for this process is

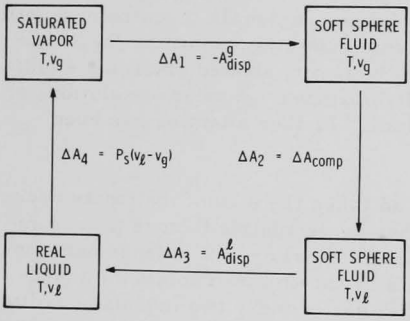

Fig. V-13. Helmholtz Energy Cycle for Model Process of Condensation

$$\Delta A_1 = -A^g_{disp} \tag{13}$$

The second step is the isothermal compression of the soft-sphere fluid from v_g to the molar volume of the real liquid v_ℓ, which is accompanied by a molar Helmholtz energy change of

$$\Delta A_2 = \Delta A_{comp} = A^{xs}_\ell - A^{xs}_g + RT \ln \frac{v_g}{v_\ell} \tag{14}$$

where A^{xs} is the molar excess Helmholtz energy of a soft-sphere fluid relative to the ideal gas at the same temperature and density. The last term in Eq. 14 is the well-known entropic change accompanying the compression of an ideal gas. In the third step, the attractive forces between molecules, assumed to be induced multipolar dispersion forces, are "turned on" at constant density with a molar Helmholtz energy change,

$$\Delta A_3 = A^{\ell}_{disp} \tag{15}$$

The sum of Eqs. 13-15 represents the molar Helmholtz energy at condensation. The fourth step is the isothermal vaporization of one mole of the liquid to the saturated vapor state (T, v_g). The Helmholtz energy change for this step is

$$\Delta A_4 = \Delta A_{vap} = \Delta G_{vap} - \Delta(PV) = -\Delta(PV) \tag{16}$$

since along the saturated vapor curve, the Gibbs energy change, ΔG_{vap}, equals zero.

The sum of the Helmholtz energy changes for the four steps in the cyclic process must be zero, i.e.,

$$A^{\ell}_{disp} - A^{g}_{disp} + A^{xs}_{\ell} - A^{xs}_{g} + RT \ln \frac{v_g}{v_\ell} - P_s(v_g - v_\ell) = 0 \tag{17}$$

where we have replaced $-\Delta(PV)$ by $-P_s(v_g - v_\ell)$, P_s being the saturated vapor pressure. For convenience, we shall consider only saturated vapors at densities low enough for the ideal gas law to hold, i.e., $P_s v_g = RT$. (At greater densities of the vapor phase, one must use higher order terms in the virial expression for $P_s v_g$.) For these low-density vapors, deviations from ideality being negligible, A^{xs}_g and A^{g}_{disp} may also be set equal to zero. One can then rearrange Eq. 17 as follows:

$$-A^{\ell}_{disp} = A^{xs}_{\ell} + RT\left(\ln \frac{RT}{P_s v_\ell} + \frac{P_s v_\ell}{RT} - 1\right) \tag{18}$$

The left- and right-hand sides of Eq. 18 may be evaluated independently, and the deviation from equality then serves as a measure of the accuracy of our evaluation of A^{ℓ}_{disp}.

Consider the Linder method[50] of approximating A^{ℓ}_{disp}. For a molecule B of static polarizability, $\alpha_B(O)$, in the center of a spherical cavity of radius a in a solvent continuum, the frequency-dependent reaction field $R_A(\omega)$ is given by

[50] B. Linder and D. Hoernschemeyer, J. Chem. Phys. 46, 784 (1967).

$$R_A(\omega) = \left[\frac{2\epsilon_A(\omega) - 2}{2\epsilon_A(\omega) + 1}\right]\frac{1}{a^3} \tag{19}$$

where $\epsilon_A(\omega)$ is the frequency-dependent dielectric function of the solvent. The generalized potential, φ, experienced by the molecule B is given by Linder's equation

$$\varphi = -\frac{3}{4}h\frac{\bar{\omega}_A\bar{\omega}_B}{\bar{\omega}_A + \bar{\omega}_B}\alpha_B(O)\, R_A(O) \tag{20}$$

where $\bar{\omega}_A$ and $\bar{\omega}_B$ are mean dielectric response frequencies of the solvent and solute molecules, respectively. Charging the molecules to this potential at constant volume V is equivalent to adding molecules (at the potential appropriate to the density at the time of addition) until N_o (Avogadro's number) are added so that $v_\ell = V/N_o$. It is clear that φ is proportional to a^{-3}, which in turn is proportional to the volume per molecule, so that φ may be set equal to CN/V, where N is the number of molecules in V and C is a proportionality constant. The Helmholtz energy change for the charging process of step three in the cycle is given by the integral

$$A^{\ell}_{disp} \cong \int_0^{N_o} \varphi(N)dN = C\int_0^{N_o} NdN = 1/2\, N_o\varphi \tag{21}$$

The "solute" molecule B and the "solvent" molecule A being the same, $\bar{\omega}_A$ is equal to $\bar{\omega}_B$, and we may substitute Eq. 21 into Eq. 20 to obtain

$$A^{\ell}_{disp} = -3/16\, \hbar\bar{\omega}_A\alpha_A(O)\, R_A(O) \tag{22}$$

where $R_A(O)$ is evaluated at the density of the liquid.

Calculations have been carried out for the noble gases Ar, Kr, and Xe by means of these equations and an approximation to the term A^{xs}_{ℓ}, which denotes the excess molar Helmholtz energy change for the formation of the soft-sphere fluid. The latter approximation involved the assumption of an inverse twelfth-power repulsive potential. For argon, the balance implied by Eq. 18 was obtained within a few percent when the experimental liquid density was used, and vapor pressures within a factor of two of the experimental values were calculated. Details, i.e., the density and compressibility of the liquid were, however, inadequately described. This failure has been shown to be caused by the inaccuracy of the inverse twelfth-power repulsion law. Accordingly, we have joined forces with A. C. Wahl of the Chemistry Division to calculate the repulsive potential quantum mechanically. If these calculations are sufficiently accurate, it may be hoped that the equation of state of a simple fluid may be obtained for the first time entirely from a first-principles calculation.

VI. ENERGY CONVERSION

A. Lithium/Sulfur Cells for Electric Vehicle Propulsion

A program has continued under the sponsorship of the Division of Advanced Automotive Systems Development of the Office of Air Programs, Environmental Protection Agency (EPA) to develop the technology for the construction and testing of a high-temperature (380°C) lithium/sulfur battery suitable for powering an electric family automobile. Table VI-1 presents both the battery and single-cell performance goals. These single-cell goals were developed from an analysis of the energy and power requirements of an automobile operated in an urban area.

TABLE VI-1. Lithium/Sulfur Battery Development Program Goals

Assembled battery	
Specific energy (at the 4-hr rate)	220 W-hr/kg
Specific power (at the 1-hr rate)	220 W/kg
Cost[a]	$10/kW-hr
Lifetime	3-year minimum
Cycle life	300-1000 cycles
Single cell	
Specific energy	220 W-hr/kg
Specific power	220 W/kg
Cost[a]	$9/kW-hr
Capacity density (at 1-hr rate)	0.4 A-hr/cm^2
Sulfur utilization (above 1-V cut off)	70%
Capacity per unit volume of cathode	1.0 A-hr/cm^3
Cycle life	1000 minimum

[a]Capital equipment cost of installed capacity; not direct energy cost.

The principal objective of the cell program during the past year has been to improve cell performance, particularly in the areas of capacity per unit volume of cathode, sulfur utilization, cycle life, and lifetime. Most of the investigations during the year concerned the design of, and materials used for, the cathode structure.

1. Cell Studies

Electrical performance tests were made on cells of the types Li/LiX/S, Li/LiX/S-Tl, Li/LiX/S-Se-Tl, and Li/LiX/S-Se-Pb, where LiX represents a molten alkali halide mixture containing lithium cations. The experimental cells, with electrode areas of 1 to 5 cm^2, were operated at temperatures of 375 to 400°C in a helium atmosphere. Various cathode

designs were investigated by means of electrical performance tests. In general, the anode consisted of liquid lithium contained in stainless steel or nickel Feltmetal.[1] The cathode was molten sulfur or a mixture of sulfur with additive materials (such as selenium, thallium, or lead) contained in a porous material, such as graphite, which served both to immobilize the cathode reactant and to provide current-conducting paths to the reaction sites at the cathode-electrolyte interface. The anode and cathode assemblies were immersed in the molten-salt electrolyte with an interelectrode distance of about 1 cm.

The principal variables investigated in the cell tests were the design of the cathode current collector and the effects of additive materials to the sulfur. Table VI-2 summarizes the electrical performance, physical characteristics, cycle life, and materials of cathode construction for selected cell experiments.

a. Geometry of Cathode Current Collectors

Several different cathode current collector designs that were used in the experimental cells are illustrated in Fig. VI-1. The simplest of all is the disk design (Fig. VI-1a). This type of cathode has typically yielded a capacity density near 0.2 A-hr/cm^2, which is below the goal of 0.4 A-hr/cm^2. A number of more complicated cathode current collector designs were investigated in an attempt to increase the interfacial area between the sulfur and the electrolyte, and thus provide a greater area for the transport of reactants to and products from the sites of the electrochemical reaction, which should increase the capacity density. The laminated cathode design (Fig. VI-1b) provides an interfacial area between the sulfur and the electrolyte which is several times greater than can be obtained with the disk cathode. Initially, the laminated cathode consisted of stainless steel Feltmetal laminates alternately filled with sulfur and electrolyte. The later designs employed alternating layers of molybdenum foam, which were wet preferentially by the electrolyte, and porous graphite or carbon, which were wet by the sulfur.

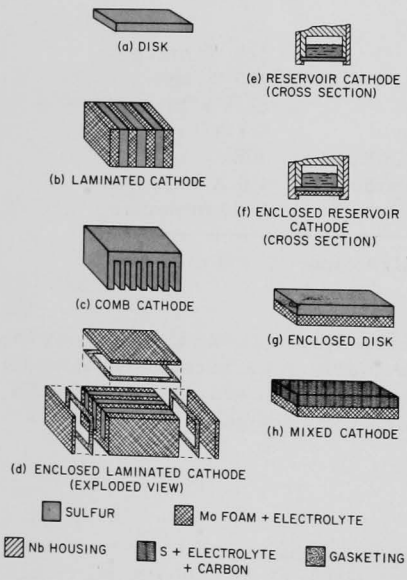

Fig. VI-1. Schematic Diagrams of Some Cathode Current Collector Designs

[1]Product of the Brunswick Corp.

TABLE VI-2. Characteristics and Performance of Selected Lithium/Sulfur Cells

Cell No.	Structure Type	Cathode Reactant	Electrolyte	Cathode Depth, cm	Materials[a] & Thickness, mm	Area,[b] cm^2	Theoretical Capacity Density, A-hr/cm^2	Capacity Density >1 V Cutoff, A-hr/cm^2	Capacity per Unit Volume of Cathode, A-hr/cm^3	Average Cell Voltage,[c] V	Current Density,[c] A/cm^2	Cycle Life, Cycles	Life, hr
37	Laminated	100% S	LiBr-RbBr	1.1	A,1.6; C,0.45	0.96	2.06	0.52	0.47	1.5	0.52	3	6
44	Laminated	100% S	LiBr-RbBr	1.1	E,0.91; A,1.6	1.31	0.76	0.33	0.30	1.3	0.25	6	26
45	Comb	100% S	LiBr-RbBr	1.3	E,1.8; -0.64	1.89	1.45	0.40	0.31	1.5	0.53	4	24
55	Enclosed laminated	100% S	LiCl-LiI-KI	2.1	E,1.5; G,3	2.53	0.33	0.17	0.08	1.8	0.20	803	1100
L-1	Enclosed laminated	100% S	LiF-LiCl-KCl	0.51	E,0.31; G,0.20	1.38	0.19	0.12	0.24	2.1	0.09	7	31
50	Reservoir	100% S	LiCl-KCl	0.8	E,0.63	1.00	1.48	0.28	0.35	1.9	0.30	6	8
56	Enclosed reservoir	100% S	LiCl-LiI-KI	1.3	F,3.0; G,4.0	1.00	1.00	0.52	0.40	1.6	0.27	600	750
62	Enclosed reservoir	100% S	LiCl-LiI-KI	1.3	F,3.0; G,3.3	1.00	2.07	0.17	0.13	1.9	0.20	131	340
75	Enclosed disk	92.0 at. % S 5.7 at. % Se 2.3 at. % Tl	LiF-LiCl-KCl	1.9	I,12.7; G,6.3	2.00	1.2	0.73	0.38	1.8	0.20	>400	>2000
77	Enclosed disk	100% Li_2S	LiF-LiCl-KCl	1.8	I,12.7; G,5.6	2.00	0.46	0.41	0.23	1.9	0.20	85	330
78	Enclosed disk	92.0 at. % S 5.7 at. % Se 2.3 at. % Pb	LiF-LiCl-KCl	1.0	I,9.6; G,0.6	2.00	1.31	1.07	1.07	1.8	0.20	33	160
L-5	Mixed cathode	100% S[d]	LiF-LiCl-KCl	0.50	E; G[d]	1.28	0.23	0.10	0.20	1.7	0.28	22	146

[a]The materials are given first for the sulfur-bearing then for the electrolyte-bearing laminae. The meanings of the code letters are given below.

A = 302 SS, 80% porosity, 30 μm mean pore size, Huyck Metals Co.
B = 304 SS, 85%, 40 μm, Brunswick Corp.
C = 304 SS, 83%, 25 μm, Brunswick Corp.
D = 347 SS, 90%, 67 μm, Huyck Metals Co.
E = Grade AX graphite, 63%, 1.4 μm, Poco Graphite Co.
F = FC-14 graphite, 49%, 3.5 μm, Pure Carbon Co.
G = Mo foam, 78%, 25 μm, Spectra-Mat, Inc.
H = Mo foam, 75%, 20 μm, Spectra-Mat, Inc.
I = PG 25 graphite, 48%, 120 μm, Union Carbide Corp.

[b]The area given is the area facing the anode (the projected area).

[c]The average power density at the 1-hr rate is the product of the average voltage and current density.

[d]Cathode mixture: 36 vol % sulfur, 57 vol % electrolyte, 8 vol % graphite, 4 vol % molybdenum.

The comb design (Fig. VI-1c) embodies the same concept, but in this case the electrolyte-containing layers are eliminated to decrease the cathode weight and to provide the bulk electrolyte with direct access to the sulfur at the surface of the graphite current collector. The laminated and comb designs both resulted in improved capacity densities (0.4-0.5 A-hr/cm^2) initially, but lost capacity rapidly. The loss in capacity was attributed to the escape of sulfur from the cathode structure. This sulfur loss was confirmed in a later series of experiments which showed that during cell startup, when the sulfur (m.p. ~119°C) is molten before the electrolyte (m.p. ~345°C), some sulfur can escape from porous carbon and disperse into the molten-salt electrolyte, which becomes a clear, yellow liquid. To minimize the rate of migration of sulfur into the electrolyte, the enclosed laminated cathode (Fig. VI-1d) was built and tested. This design greatly reduced (or eliminated) the sulfur loss by the cathode and significantly extended the cell life. A cell of this design was operated for 803 cycles (1100 hr), but during this period the cell did not maintain the desired performance level (the typical capacity density was ~0.17 A-hr/cm^2).

To minimize the volume and weight of the current collector, another cathode design was used to explore the possibility of relying upon sulfur transport from a reservoir to the cathode-electrolyte interface in the current collector. The reservoir cathode (Fig. VI-1e) consisted of a thin, porous carbon current collector that confined liquid sulfur within a reservoir. As sulfur was consumed by the cell reaction at the current collector-electrolyte interface, additional sulfur was wicked through the current collector to the site of the reaction. This design, however, allowed significant sulfur losses, probably by the same mechanism as that in the laminated and comb designs (Figs. VI-1b and VI-1c). This problem was eliminated by introducing a porous molybdenum layer, which is wet preferentially by the electrolyte (Fig. VI-1f), at the cathode-electrolyte interface. Cells of this design performed well and produced capacity densities of up to 0.52 A-hr/cm^2 and lives of 600 cycles (~750 hr). Their main performance failure was the gradual loss of capacity over the operating life.

The enclosed disk cathode (Fig. VI-1g) consisted of a porous graphite current collector, which was impregnated with liquid sulfur, and a porous molybdenum layer to prevent sulfur loss. This design provided more graphite matrix for conduction of electric current per unit volume of the cathode than was used in the reservoir cathode. The best performance in terms of energy density, W-hr/cm^2, was achieved with this type of cathode design. One of these cells has operated at high performance levels for more than 400 cycles (>2000 hr). Another variation designed to substantially increase the sulfur-electrolyte interfacial area was the mixed cathode (Fig. VI-1h). In this design, the cathode reactant (sulfur), electrolyte, and current conductor (graphite or metal) are brought into intimate contact as a mixture of 100- to 200-μm-dia powders. In general, cathodes of this type have performed poorly after the first few cycles. This poor

performance is probably caused by inadequate current collection (discontinuities in the conductor) or by insufficient dispersion of the electrolyte in the reacting mixture. Promising results have recently been obtained by a new homogenization procedure, in which the sulfur is contained within porous graphite particles, and part of the electrolyte is contained within porous metal particles. A high proportion of electrolyte in the mixture appears to be necessary for high sulfur utilization, at least if the depth of the cathode mixture is of the order of 1 cm or more.

b. Additives to the Cathode Reactants

The addition of sulfur and thallium to a selenium cathode was shown to improve the performance of lithium/selenium cells.[2] In the lithium/sulfur cells, mixtures of selenium-thallium and selenium-lead have been tested as candidate additives to increase cell performance by decreasing the viscosity, increasing the diffusion rate of cell reaction products, or increasing the conductivity of the cathode. Cells with these additives appear to outperform cells with pure sulfur cathodes and produce cell capacity densities above 0.4 A-hr/cm^2 for more than 100 hr and 30 cycles.

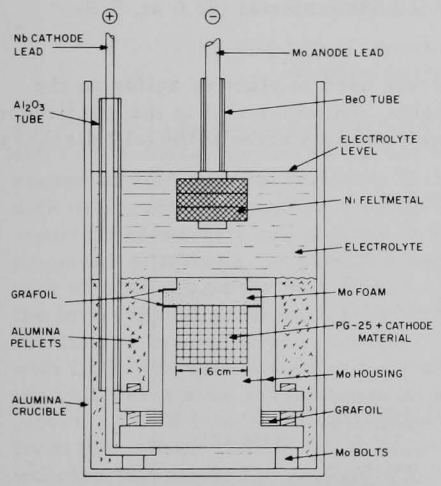

Fig. VI-2. Schematic Diagram of Cell No. 75

Cell No. 75, with an enclosed-disk cathode, was tested using a sulfur-selenium-thallium cathode mixture (92.0 at. % S-5.7 at. % Se-2.3 at. % Tl). A schematic drawing of the enclosed-disk cell is shown in Fig. VI-2. On the first discharge, the cell showed a high capacity density, 0.71 A-hr/cm^2 (above a 1.0-V cutoff), at a current density of 0.10 A/cm^2 with a sulfur utilization of more than 48%. Its performance declined within a few cycles and stabilized at a capacity density of about 0.35 A-hr/cm^2 at a current density of 0.40 A/cm^2. This performance continued for about 300 hr and 50 cycles, at which time the capacity density improved by 30% to 0.50 A-hr/cm^2 for the above discharge conditions. For the next 50 cycles and 300 hr, the cell maintained capacity densities above 0.4 A-hr/cm^2 at 0.4 A/cm^2, the 1-hr rate. During this experiment the charging current density was kept constant at 0.25 A/cm^2.

[2]USAEC report ANL-7777, p. 19 (1971).

The cell performance deteriorated in the subsequent 50 cycles or 400 hr because of a high moisture content of the glovebox in which the cell was being operated. When this problem was corrected, the cell anode and electrolyte were replaced and the charge cutoff voltage was increased from 2.85 V (IR included) to 3.05 V (IR included) or 2.85 V (IR free). The cell improved in performance from that time, and after some variation reached a capacity density of 1.0 A-hr/cm^2 (above a 1.0-V cutoff) at a current density of 0.4 A/cm^2 on the 280th cycle. Even at the high current density of 2 A/cm^2, a capacity density of 0.8 A-hr/cm^2 was achieved. The capacity density of Cell No. 75 is shown in Fig. VI-3 as a function of cycle number and time. Selected voltage-capacity density curves for Cell No. 75, taken at various current densities, are shown in Fig. VI-4. The cause of the improvement in cell performance is not known at this time. However, the improved performance of this cell suggests that studies on additives should be continued.

Results similar to those for Cell No. 75 were obtained for a shorter period with Cell No. 78, which contained a small amount of lead in addition to selenium in its starting cathode material (92.0 at. % S-5.7 at. % Se-2.3 at. % Pb).

Lithium sulfide (Li_2S) was used in place of sulfur as the starting cathode material in several cells. This material is the end product of the cell reaction; therefore, these cells were started in the fully discharged

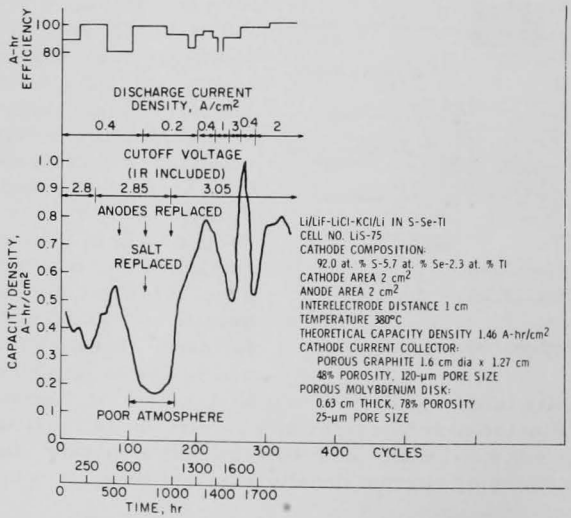

Fig. VI-3. Capacity Density of Cell No. 75 as a Function of Time and Cycle Number

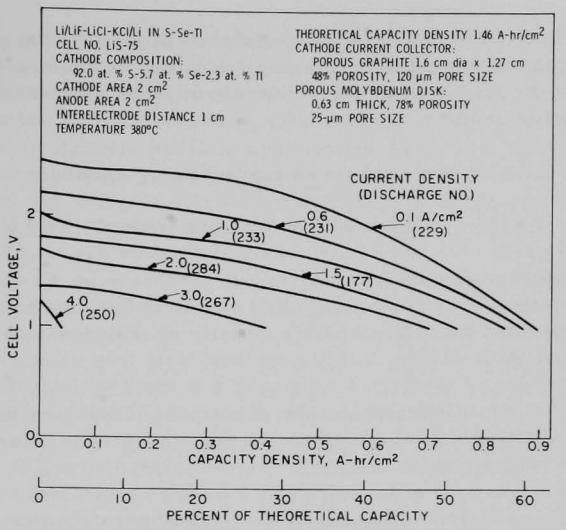

Fig. VI-4. Voltage-Capacity Density Curves for Cell No. 75 for Various Current Densities

state. The Li_2S has a very low vapor pressure at temperatures below 400°C; therefore, its use as the starting cathode material prevents the escape of sulfur by vaporization during startup. Cell No. 77, an enclosed-disk cell, contained Li_2S as the starting cathode material. The basic construction of the cell was similar to that of Cell No. 75. The cathode was prepared as follows. A porous graphite disk was impregnated with a mixture of Li_2S and sulfur at 370°C in a sealed quartz tube. After removal of the impregnated graphite disk from the tube, the sulfur was removed from the disk by heating under vacuum. The porous graphite disk, impregnated with Li_2S, was then placed in the cathode assembly. The performance of the cell was stable with capacity densities ranging from 0.2 to 0.4 A-hr/cm^2 (above a 1.0-V cutoff) at a current density of 0.2 A/cm^2. No loss of sulfur from the cathode during the operation was observed. This result seems to indicate that the use of Li_2S as a starting material should be investigated further.

At present the effects of various additives, including selenium, thallium, lead, and aluminum, in the starting cathode materials continue to be investigated. It appears that chemical and physical changes in the sulfur caused by the additives are significant and can result in significantly improved cell performance.

c. Scale-Up Studies

Until a few months ago, the cells operating in this program were generally small (<20-cm^2 electrode area) and unsealed. Recently,

some effort has been devoted to the scale-up of cells to larger sizes and to the development of methods for hermetically sealing the larger cells so that they may be operated in air rather than in the inert-atmosphere glove-boxes now being used.

The scale-up investigation being conducted are as follows:

a) On the basis of the small, single-cell test results, larger-sized cells (30- to 60-cm^2 active electrode areas) are being designed for use in single-cell tests and for later use in a 1- to 2-kW battery. Electrical performance tests are being conducted to determine the voltage-current density and voltage-capacity density characteristics, cycle life, and lifetime of the cells.

b) Hermetic seals, electrical insulators, and feedthroughs are being evaluated in sealed cells with respect to ease of assembly, lifetime, and performance.

Six scaled-up cells have been operated, one of which was a sealed cell. These cells contained a sulfur-selenium-thallium cathode mixture (92.0 at. % S-5.7 at. % Se-2.3 at. % Tl) held in a porous-graphite current collector. Cell No. S-1 was operated for 800 hr and 250 cycles, at which time operation was terminated for examination of its components. The highest capacity density delivered by Cell No. S-1 was 0.46 A-hr/cm^2 (40% of the theoretical capacity density) at a current density of 0.27 A/cm^2 to a 1.0-V cutoff. The maximum short-time peak power density was 1.5 W/cm^2.

The first sealed lithium/sulfur cell, Cell No. S-7, was operated for 242 hr and 62 cycles. The highest capacity density delivered by this cell was 0.44 A-hr/cm^2 (58% of the theoretical capacity density) at a current density of 0.20 A/cm^2 to a 1.0-V cutoff. Typically, a capacity density of 0.22 A-hr/cm^2 (29% of the theoretical) was measured at a current density of 0.21 A/cm^2 to a 1.0-V cutoff. The A-hr efficiency was generally greater than 0.9 until the cell failed as a result of electrical shorting caused by lithium contacting both the anode and the cathode.

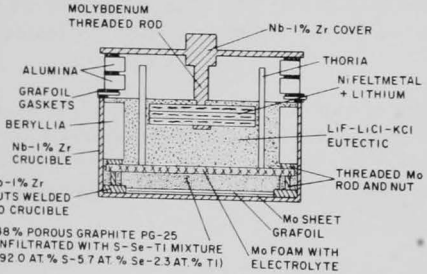

Fig. VI-5. Cross Section of Sealed Cell No. S-7

The configuration of Cell No. S-7 is shown in Fig. VI-5. A graphite current collector containing the sulfur-selenium-thallium mixture (92.0 at. % S-5.7 at. % Se-2.3 at. % Tl) was bolted to a niobium-1% zirconium

crucible for good electrical contact, and Grafoil[3] was used between the current collector and crucible to minimize the corrosion rate of the crucible. A molybdenum foam disk was used to prevent free lithium contact with sulfur in the cathode. A ThO_2 tube contained any free lithium which floated to the electrolyte surface and was not absorbed by the anode current collector during charging. A BeO liner was used to prevent free lithium which escaped the ThO_2 tube from bridging to the niobium crucible. The cell was sealed with spring-loaded stainless steel clamping rings.

A summary of the capacity density data with continuous cycling for Cell No. S-7 is shown in Fig. VI-6. The cell was initially discharged at a current density of 0.12 A/cm^2 to a 1.0-V cutoff and charged at a current density of 0.10 A/cm^2 to a 2.9-V cutoff. The capacity density increased with cycling from 0.076 to 0.24 A-hr/cm^2 as shown in Fig. VI-6. The discharge current density was then increased to 0.20 A/cm^2. As cycling was continued the capacity density reached a maximum of 0.44 A-hr/cm^2 (58% of the theoretical value) and then decreased to 0.31 A-hr/cm^2. The discharge and charge current densities were increased to 0.26 and 0.18 A/cm^2, respectively, and the charge cutoff voltage was increased to 3.05 V. The capacity density decreased from 0.27 to 0.20 A-hr/cm^2 between Cycles No. 17 and 27. The discharge and charge current densities were then reduced to 0.22 and 0.15 A/cm^2, respectively. The charge cutoff voltage was gradually increased and was set at 3.5 V (IR-included) for

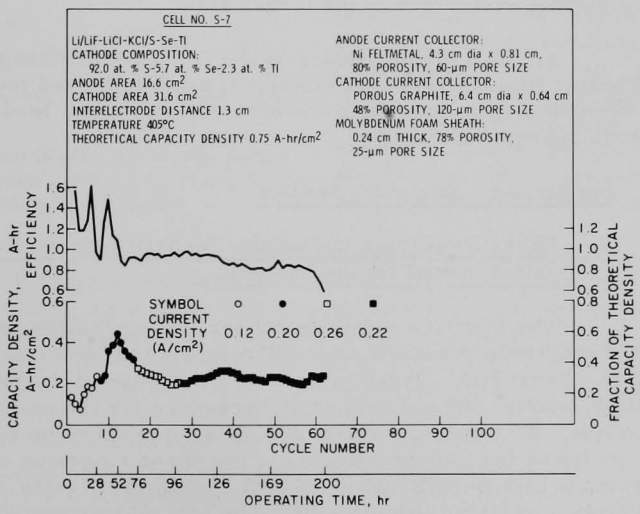

Fig. VI-6. Cell Capacity Density vs. Cycle Number for Cell No. S-7

[3]Product of the Union Carbide Corp.

Charge No. 58. The estimated IR-free voltage was slightly greater than 3.1 V. The discharge capacity density was nearly constant at approximately 0.22 A-hr/cm^2 for Cycles No. 28 to 62. The initial rise in the capacity density may have been caused by displacement of trapped gas from the cathode and subsequent improved wetting of the cathode current collector by the electrolyte. The cause of the later decrease in capacity density to the nearly constant value of 0.22 A-hr/cm^2 has not been identified.

Operation of Cell No. S-7 was terminated because of electrical shorting. The ThO_2 tube cracked and lithium or some other electrically conductive material contacted the niobium crucible. Sealed-cell experiments are continuing with various cell designs in an attempt to develop sealed cells with a consistent capacity of 0.4 A-hr/cm^2 at a current density of 0.4 A/cm^2 to a 1.0-V cutoff for at least 100 cycles.

Based on the above results, the following areas of investigation require further work:

1) The nickel Feltmetal anode current collector sometimes appears to provide inadequate absorption of the lithium during recharge, resulting in occasional electrical short circuits.

2) An improved cathode current collector is required to reduce the internal resistance of the larger cells.

3) Corrosion studies in the cell environment are needed to identify better lithium-resistant electrical insulators, and techniques should be developed to reduce the corrosion rates of metal leads attached to the cathode current collector.

2. Supporting Laboratory Studies

a. Phase Equilibria in Pseudo-Ternary Lithium Sulfide-Sulfur-Alkali Halide Systems

The long-life requirement for lithium/sulfur cells can best be met if the electrode reactants and cell reaction products have low solubilities in the electrolyte. Therefore, some knowledge of the phase diagrams involving Li_2S, sulfur, and electrolyte is necessary for the selection of the best electrolyte. Emf measurements and phase-equilibration techniques were used to define the salient features of the phase diagrams of the pseudo-ternary systems Li_2S-S-(LiX-MX), where LiX-MX represents several alkali halide mixtures containing lithium ions. The emf measurements were performed with a quartz H-cell having a lithium-aluminum alloy anode and a cathode containing a lithium-sulfur mixture whose composition was varied coulometrically by charging or discharging the cell. The reference electrode was also a lithium-aluminum alloy containing 5 to 45 at. % lithium. The half-cell potential of the lithium-aluminum alloy is constant over this range.

The phase equilibration experiments were performed as follows. A Li_2S-sulfur-alkali halide mixture was prepared, and weighed amounts of this mixture were sealed in quartz capsules. The capsules were heated, agitated, equilibrated at 360 or 400°C, centrifuged at temperature when necessary, quenched, and then sectioned for microscopic examination and/or chemical analysis of the individual phases.

Preliminary results from the emf measurements indicated that the phase diagram of the pseudo-ternary Li_2S-S-(LiF-LiCl-LiI) system is very similar to that of the corresponding Li_2Se-Se-(LiF-LiCl-LiI) system (ANL-7750, p. 106). The results of the phase-equilibration experiments suggest that the general features of the diagram are the same for several different alkali-halide electrolytes, but the locations of the phase boundaries differ somewhat. A 400°C isothermal section of the pseudo-ternary Li_2S-S-(LiCl-KCl) diagram which has been constructed from the phase-equilibration results is shown in Fig. VI-7. The binary Li_2S-S system is characterized by the occurrence of one compound (Li_2S) and a miscibility gap from <0.3 to 29 mol % Li_2S.[4] Three liquid phases, L_1, L_2, and L_3, and one solid phase, Li_2S, are found in the pseudo-ternary system at this temperature. The L_1 phase consists essentially of pure sulfur, which does not dissolve in any of the other phases to a significant extent; L_2 is composed of sulfur, Li_2S, and a small amount of electrolyte; L_3 is an electrolyte-rich phase containing small amounts of Li_2S and sulfur.

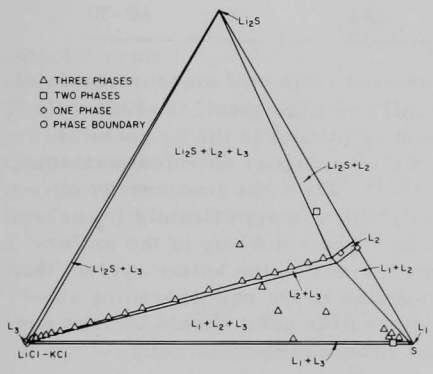

Fig. VI-7. Phase Diagram of the Pseudo-Ternary System Li_2S-S-(LiCl-KCl) at 400°C. ANL Neg. No. 308-2814.

To minimize chemical self-discharge of a lithium/sulfur cell, the solubility of the cathode reactant in the electrolyte should be as low as possible. This solubility corresponds to the location of the phase boundary between L_3 and $L_2 + L_3$. The phase-equilibration technique was used to locate this boundary for various electrolytes. The results shown in Table VI-3 indicate that those electrolyte systems having only small anions (chloride and fluoride) have much less tendency to dissolve sulfur-bearing species than do those having large anions (bromide and iodide). Thus, it appears that chlorides and fluorides are the best electrolytes for minimizing the self-discharge rate.

[4] E. Cairns et al., Chemical Engineering Division, Physical Chemistry of Liquid Metals and Molten Salts Semiannual Report, January-June 1971, USAEC report ANL-7823, p. 4 (1971).

TABLE VI-3. Extent of L_3 Phase in the Presence of 29.3 mol % Li_2S-70.7 mol % S Mixture

Electrolyte Composition, mol %	M.P., °C	Mol % Electrolyte in Saturated Solution	
		360°C	400°C
3.5 LiF-56.0 LiCl-40.5 KCl	347	-	>99
58.8 LiCl-41.2 KCl	352	-	>99
57.5 LiCl-13.3 KCl-29.2 CsCl	265	>99	98
11.7 LiF-29.1 LiCl-59.2 LiI	340.9	-	70-80
59 LiBr-41 RbBr	278	92	70
8.5 LiCl-59.0 LiI-32.5 KI	264	94	60-70

Thermodynamic data derived from emf measurements of the pseudo-ternary Li_2S-S-(LiF-LiCl-LiI) and Li_2Se-Se-(LiF-LiCl-LiI) systems show that the activity coefficient of lithium in the L_1 phase is much lower in the sulfur system than in the analogous selenium system, where it has an estimated value of 6×10^{-32}. Also, the free energy of formation of Li_2S is about -100 kcal/mol, which is significantly lower than the value of -94.0 kcal/mol for Li_2Se. The solubility of the sulfur-bearing species in the electrolyte is much lower in the sulfur system than the solubility of the selenium-bearing species in the corresponding selenium system, which indicates that lithium/sulfur cells should be less susceptible to chemical self-discharge than lithium/selenium cells.

b. Sulfur Species in Molten-Salt Solutions[5]

A study was undertaken to investigate the sulfur-bearing species that are formed when sulfides and polysulfides are dissolved in molten alkali halide salts. Since complex equilibria undoubtedly occur between species such as S_n, S^{2-}, and S_n^{2-}, the initial effort was directed toward the preparation of S^{2-}, free of excess sulfur in molten LiCl-KCl eutectic. An attempt to generate a known concentration of S^{2-} coulometrically by the reaction

$$Ag_2S + 2\,e^- \rightarrow 2\,Ag + S^{2-}$$

resulted in low yields of S^{2-}. However, subsequent efforts employing the reaction

$$NiS + 2\,e^- \rightarrow Ni + S^{2-}$$

[5]Work performed by D. M. Gruen, R. L. McBeth, and A. J. Zielen of the ANL Chemistry Division.

gave good results with a Nernstian response corresponding to the expected two-electron reaction. The potential of the Ni/Ni^{2+} electrode vs. a Pt/Pt^{2+} reference electrode at 400°C was -0.79 V, the solubility product of the NiS was 2.1×10^{-15} $(mol/liter)^2$, and the amount of S^{2-} found by chemical analysis was 94.2% of the theoretical value based on the coulometric measurement.

During the course of this work, an analytical method was needed to determine the S^{2-} concentration in quenched samples of the salt. Potentiometric titrations with standard $AgNO_3$ solution in 1M NH_4OH plus 0.1M NaOH with an Orion sulfide-selective electrode gave satisfactory results. An alternative procedure involving reaction of the sulfide with standard iodate, followed by back-titration with standard thiosulfate, proved difficult to execute, but with sufficient care accurate results were obtained. Chloride ion was shown not to interfere with this procedure.

Absorption spectra were determined for molten LiCl-KCl eutectic containing a known initial concentration of S^{2-} ion in equilibrium with various partial pressures of sulfur at temperatures of 500 to 800°C. The spectra responded reproducibly and reversibly to changes in the partial pressure of sulfur and the temperature. The spectra were resolved into two Gaussian absorption peaks at 390 and 585 nm. A mathematical analysis of the data indicated that they were in best accord with the following equilibria involving the supersulfide ions, S_2^- and S_3^-:

$$2\ S^{2-} + 3\ S_2 \rightleftharpoons 4\ S_2^-$$

$$2\ S^{2-} + 5\ S_2 \rightleftharpoons 4\ S_3^-$$

$$K_2 = (S_2^-)^4/(S^{2-})^2 \cdot p^3$$

$$K_3 = (S_3^-)^4/(S^{2-})^2 \cdot p^5$$

The 390- and 585-nm peaks were assigned to S_2^- and S_3^-, respectively. Although some interference due to other species (possibly S_2 or some other form of zero-valent sulfur) appeared to occur at the lowest temperature (500°C), the data were reasonably consistent with the above equilibria. Preliminary estimates of the values of K_2 and K_3 based on these data are as follows:

T, °C	K_2	K_3
500	1.51×10^5	4.59×10^2
600	1.74×10^3	1.70×10^0
700	9.07×10^1	2.64×10^{-2}
800	1.74×10^1	1.18×10^{-3}

where the concentrations are in moles per liter and the partial pressure of sulfur is in atmospheres. The molar absorptivities for S_2^- and S_3^- are estimated to be in the general ranges of 10^2 and 10^4, respectively.

c. Cathode Material Studies

Small-scale cell tests have shown that elemental sulfur alone can be used as the active cathode material in lithium/sulfur cells. It may be desirable, however, to use certain additives to increase the electrical conductivity and decrease the vapor pressure of the sulfur, which should increase the electrical performance of the cell and possibly permit the use of a simpler, lighter-weight cathode current collector. Iron was investigated briefly as a potential additive, but, contrary to literature data,[6] practically no iron was found in solution (<0.01 wt %) when FeS was equilibrated with liquid sulfur for several days at 450°C. The conductivity of the solution was $<10^{-7}$ ohm^{-1} cm^{-1}, compared with a value of $\sim 10^{-9}$ ohm^{-1} cm^{-1} for high-purity sulfur.

Sulfur-thallium mixtures are reported to have a high conductivity of ~1 ohm^{-1} cm^{-1} at 400°C.[7] These data, however, apply to relatively high thallium concentrations (>37.5 at. %), which would be undesirable in a lithium/sulfur cell because of the high atomic weight of thallium (204.37 g/g-atom). The thallium-sulfur system was therefore investigated in the region of lower thallium concentrations, where a liquid-liquid miscibility gap is reported to exist.[8] The presence of a miscibility gap was confirmed experimentally by observing two liquid phases in a nominally 20 at. % thallium-sulfur mixture at ~350°C. The boundaries of the gap were redetermined by analyzing quenched samples of the two liquids for thallium. The results were as follows:

Equilibration temp., °C	310	344	350
Thallium concentration, at. %			
Upper phase	<0.08	0.09	<0.02
Lower phase	26.0	26.9	26.5

These results indicate that the solubility of thallium in sulfur is considerably lower than the literature values, and that the thallium content of the higher-density phase is slightly less than that reported in the literature. The conductivity of the upper (sulfur-rich) phase was $\sim 10^{-9}$ ohm^{-1} cm^{-1} at 345°C and that of the lower (thallium-rich) phase was 4×10^{-1} ohm^{-1} cm^{-1} at 367°C.

Conductivity measurements were also made on sulfur containing 3.5 wt % Vulcan SC-72R carbon black,[9] which was supplied by the Freeport Sulphur Co., Belle Chasse, La., and was claimed to have a conductivity of $\sim 10^{-1}$ ohm^{-1} cm^{-1} at 130°C.[10] Preliminary tests with a

[6] F. A. Shunk, Constitution of Binary Alloys, Second Supplement, p. 344, McGraw-Hill Book Co., N.Y. (1969).

[7] A. A. Velikanov and V. A. Tertykh, Electrical Conductivity, Polarization, and Electrolysis of Thallium-Sulfur Melts, Zh. Fiz. Khim. 43, 2580 (1969).

[8] M. Hansen and K. Anderko, Constitution of Binary Alloys, p. 1168, McGraw-Hill Book Co., N.Y. (1958).

[9] A product of the Cabot Corp.

[10] T. K. Wieriorowski, Electric Conductivity of Carbon Black Suspensions in Molten Sulfur. J. Electrochem. Soc. 118, 1711 (1971).

volt-ohmmeter showed the material to be conductive both when molten and at room temperature after it had solidified. Subsequent measurements with an impedance bridge gave values of 1.23×10^{-3} ohm^{-1} cm^{-1} at 136°C and 1.43×10^{-3} ohm^{-1} cm^{-1} at 158°C. Higher-temperature measurements were not possible because of a tendency for the material to segregate and to form gas bubbles in the cell.

The above results indicate that iron is unlikely to be a useful additive to the cathodes of lithium/sulfur cells. Thallium shows some promise, and the sulfur-carbon black mixtures may be useful if their tendency to segregate and to release gases can be overcome.

Investigations were also conducted on various porous carbons and graphites that are under consideration as cathode current-collector materials. Two important characteristics of a cathode current collector are the amount of sulfur it can contain per unit volume or weight and its electrical conductivity. Comparative data on the absorption of sulfur were obtained by immersing preweighed specimens in liquid sulfur at 150°C for 1 hr and weighing them again after they had been removed and cooled. It had been shown earlier that essentially all of the uptake of sulfur occurred within the first 5 min of exposure. Conductivity measurements were also made on selected porous graphites and carbons, using a four-probe dc method. The results of the sulfur absorption and conductivity measurements are summarized in Table VI-4. In general, the amount of sulfur absorbed per unit volume increased and the conductivity decreased with increasing porosity of the material. The pore size had no clearly defined effect on either property. As expected, the graphites had considerably higher conductivities than did carbons of the same porosity.

TABLE VI-4. Sulfur Absorption and Conductivity Data for Porous Graphites and Carbons[a]

Material	Porosity, %	Mean Pore Diameter, μm	Sulfur Absorbed, g/cm^3	Conductivity, ohm^{-1} cm^{-1}		
				25°C	350°C	450°C
PG-60[b] graphite	48	33	0.85	467	610	600
PC-60[b] carbon	48	33	0.97	64	76	76
PG-25[b] graphite	48	120	0.90	270	320	325
PC-25[b] carbon	48	120	0.82	79	89	88
FC-14[c] graphite	49	3.5	0.67	-	-	-
Poco AX[d] graphite	65	1.4	0.48	-	-	-
FC-20[c] carbon-graphite	77	20	1.04	-	-	-
FPA-20[b] graphite	91	53	1.31	16	18	19
FPB-3[b] carbon	98	100	1.31	3.0	-	-
FRA-3[b] carbon	98	600	0.38	2.5[e]	-	-

[a]Absorption measurements were conducted for 1-hr exposures at 150°C.
[b]Product of Union Carbide Corp.
[c]Product of Pure Carbon Co.
[d]Product of Poco Graphite Co.
[e]Literature value (Union Carbide Tech. Info. Bull. 463-204 A1).

d. Mass-Transport Studies

Since the cycle life of lithium/sulfur cells has been increased markedly by improvements in the cathode design, a frequent cause of cell failure has been an inability to transport lithium back into the anode current collector structure after extensive charge-discharge cycling. Four special-purpose cells were built and operated to investigate this problem. These cells consisted of a conventional lithium anode, a molten-salt electrolyte, and an aluminum counter electrode. As the cells were discharged, lithium was transferred from the Type 302 stainless steel Feltmetal anode (90% porosity, 67-μm mean pore diameter) to the aluminum electrode, creating a lithium-aluminum alloy. The aluminum counter electrode was used to eliminate possible effects resulting from the sulfur in a conventional cathode, thereby permitting an evaluation of the lithium anode alone.

Three different electrolytes were used in the various cells: LiCl-KCl (58.5-41.5 mol %); LiCl-LiI-KI (8.5-59.0-32.5 mol %); LiF-LiCl-KCl (3.5-56.0-40.5 mol %). The operating temperatures ranged from 390 to 425°C. The first cell, which used the LiCl-KCl electrolyte and an Al_2O_3 insulator, failed after 10 cycles (~100 hr) when lithium could not be charged back into the Feltmetal anode because of poor wetting. The second and third cells, which used the LiCl-LiI-KI electrolyte and BeO insulators, failed for the same reason after less than five cycles. In the fourth cell, the LiF-LiCl-KCl salt was used as the electrolyte and BeO as the insulator. This cell performed well for 139 cycles (480 hr) at which point 10 g of the LiCl-LiI-KI salt was added to the electrolyte. Immediate bubbling of the electrolyte was observed upon the addition of this salt, and the cell performance deteriorated. Operation of this cell was terminated after 202 cycles (675 hr).

The results of these tests suggest that the use of Al_2O_3 as an insulator may result in contamination of the lithium anode, causing poor wetting of the stainless steel by the lithium. The use of iodide salts in the second and third cells and the addition of iodide in the fourth cell appeared to cause a similar dewetting of the anode structure by the lithium. It appears that this effect may result in part from the very strong tendency of iodide salts to take up moisture, even from helium atmospheres containing only a few (<10) ppm of water vapor. It is also possible that the presence of iodide increases the ability of the electrolyte to displace lithium from the stainless steel Feltmetal. Regardless of the exact mechanism involved in the dewetting of lithium from stainless steel, these results indicate that the problem may be solved or at least greatly diminished by avoiding iodide-containing electrolytes and Al_2O_3 insulators.

3. Materials and Components

a. Corrosion Tests

Lithium/sulfur cells will probably require an electrical insulator resistant to lithium, electrolytes, and cathode mixtures. Previously BeO and BN were the only insulators which had demonstrated any appreciable lifetime in cell service, and BN is not thought to be useful in long-lived cells because of a corrosion mechanism which produces an electrically conducting film on the insulator surface. Although BeO has operated very well in cell service, alternative insulators were sought because of the cost and health hazard associated with BeO.

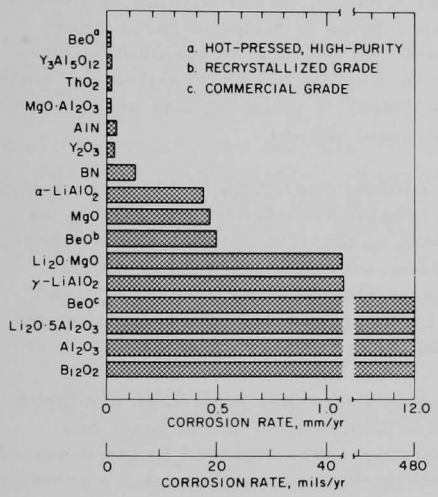

Fig. VI-8. Corrosion Resistance of Electrical Insulators to Molten Lithium

The results of 300-hr tests conducted recently to determine the corrosion resistance of several potential electrical insulators to molten lithium at 375°C are shown in Fig. VI-8 and compared with materials previously tested. The tests indicated that γ-$LiAlO_2$, high-purity Al_2O_3, $Li_2O \cdot 5\ Al_2O_3$, $Li_2O \cdot MgO$ spinel structures, and $B_{12}O_2$ are not resistant to molten lithium. These materials have been eliminated from further consideration as lithium/sulfur cell insulators.

Three insulators, Y_2O_3, $Y_3Al_5O_{12}$, and the $MgO \cdot Al_2O_3$ spinel, were translucent before testing and darkened during testing but otherwise resisted attack very well. The observed corrosion rates of less than 0.06 mm/yr compare favorably with those of BeO and other insulators tested to date. Yttria was further tested in sulfur, LiCl-KCl electrolyte, and a 20 at. % Li-S mixture for 327 hr at 375°C. In all tests the observed corrosion rate was less than 0.008 mm/yr. Yttria will undergo testing in operating cells because of its excellent corrosion resistance and availability. The performance in these corrosion tests was strongly affected by the preparation method. In general, hot-pressed oxides were superior in corrosion resistance to ceramics fabricated by other techniques.

Although the above results on corrosion rates are useful in screening candidate materials for cell components, it must be recognized that the observed rates are not necessarily those that would be found in an

operating cell where electrochemical effects can result from potential differences within the cell. A case worthy of note involved the loss of insulating properties of BeO during use and its subsequent structural degradation in cell operation. It was ascertained that these phenomena were typical of the poorer grades of beryllia, and independent observations indicated that conductivity arose from surface contact with the electrolyte whereas the structural degeneration was accelerated by contact with metallic components.

b. Feedthroughs and Insulators[11]

Changes in cell design occur simultaneously with materials evaluation and specification and require a capability for making cell components. Little difficulty exists in the fabrication of metallic parts where pieces are either machined or purchased. In the case of insulators, however, problems were encountered in obtaining corrosion-resistant ceramics in shapes that are useful in cell construction. A program was undertaken to develop the capability for producing ceramic shapes.

Lithium aluminate (α-$LiAlO_2$) and yttria (Y_2O_3) were selected for study because of their excellent corrosion resistance, availability as high-purity powder, nontoxicity, and ease of fabrication. Generally, these powders are blended with organic binders, vibrated into rubber molds, pressed isostatically, degassed and then sintered at temperatures high enough to give the desired densities. In this processing it is the isostatic pressing that contributes to the flexibility in fabricating shapes.

To date, $LiAlO_2$ rings and Y_2O_3 tubes have been produced. In processing, it is difficult to control all dimensions and at least one grinding step has been necessary. The rings were sintered to the required 73.6-mm OD x 64.6-mm ID; the desired thickness was obtained by grinding. The tubes were sintered to produce the desired length and ID, and the OD was ground to size. Both components are now being used in cell development programs--the rings as insulators in cells and the tubes as feedthroughs. Feedthrough development is also being conducted. A feedthrough consists of a metallic current conductor electrically insulated from a housing or sleeve. Current ideas on cell design require at least one feedthrough that is chemically inert and corrosion resistant to all cell reactants. These feedthroughs are not commercially available and are not likely to be developed by commercial sources soon enough for present needs.

On the basis of previous corrosion studies, molybdenum and niobium were chosen to be used as metallic components and Y_2O_3 as the insulator. A braze selected on the basis of the same studies showed promise of being relatively inert to cell environments. Simple feedthroughs that were leak tight were fabricated and withstood failure for 100 hr in static corrosion tests. In the progression to designs adaptable to use in cell

[11]Work performed by D. E. Walker, EBR-II Project and T. L. Wilson, Resident Associate from Gould, Inc.

development it was noted that stresses were generated that caused cracking during the braze cycle. An analysis of the stress system indicated that niobium was to be preferred over molybdenum because of its better match (with Y_2O_3) in the thermal-expansion coefficient. Heavier ceramic sections are necessary for stress-bearing purposes and are presently being fabricated into feedthroughs.

4. Electric Automobile Performance Calculations

Calculations were made to estimate the performance that might be expected of a family automobile powered by a lithium/sulfur battery. These calculations differed from others of this type in that cognizance was taken of the fact that the deliverable energy of the battery is a function of operating power level of the battery. The effect of different operating power levels associated with different manners of operating an automobile (commonly termed the driving profile) is significant. For example, our calculations estimate a range of 530 km (329 miles) when a specified vehicle is operated at a constant velocity of 45 km/hr (28 mph). The range of this same vehicle drops to about 158 km (98 miles) on a driving profile typical of urban driving conditions with frequent stops, starts, low-speed driving, and accelerations. The vehicle and battery characteristics used for this study are presented in Table VI-5.

TABLE VI-5. Electric Automobile Characteristics

Vehicle		
Curb weight of vehicle	1950 kg	4300 lb
Vehicle test weight (W)	2086 kg	4600 lb
Weight of power plant (included in curb weight)		
Motors	68.0 kg	150 lb
Controls	90.7 kg	200 lb
Transmission and drive train	31.8 kg	70 lb
Air conditioner and heater	36.3 kg	80 lb
Miscellaneous	11.3 kg	25 lb
Battery[a]	487.6 kg	1075 lb
Total	725.7 kg	1600 lb
Accessory power		
None	0 kW	
Lights, windshield wipers, blower, etc.	0.250 kW	0.33 hp
Above plus air-conditioning	2.983 kW	4 hp
Constants		
Air drag coefficient (C_D)	0.5	
Frontal area of vehicle (A_f)	2.23 m^2	24 ft^2
Efficiency (battery output to wheels, $E_m \cdot E_e$)	0.82	
Total accel./linear accel.	1.1	
Air density/g (ρ_A)	9.6×10^{-9} kg-hr^2/m^4	

[a]Battery---Cell Type: laminated cathode, Size: 350 cm^2/cell, Number: 498 cells, and Weight: 0.91 kg (2 lb)/cell.

The results of the calculations for three of the profiles are shown in Fig. VI-9. Under urban driving conditions averaging around 32 km/hr (20 mph) and for an accessory load of 2.983 kW (4 hp) with air conditioning, the vehicle range is 158 to 248 km (98 to 154 miles), depending upon the exact driving conditions. At the lower accessory load of 0.250 kW (without air conditioning), the range increases to around 322 km (200 miles). Urban driving requires peak power levels of 99 to 150 W/kg (45 to 68 W/lb); the battery delivers 120 to 195 W-hr/kg (54 to 89 W-hr/lb) with the greater energy capability and longer ranges obtained at the lower power levels.

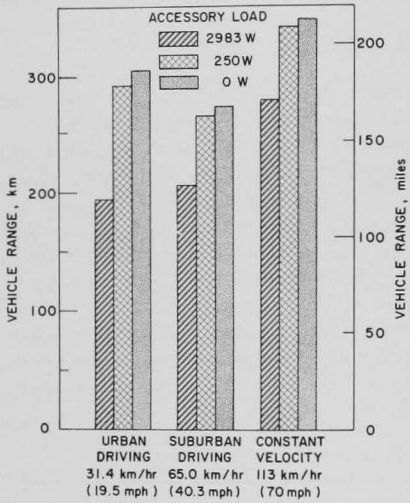

Fig. VI-9. Vehicle Range under Selected Driving Profiles. ANL Neg. No. 308-2595.

Suburban driving averages around 64 km/hr (40 mph) and requires higher peak power levels of up to 162 W/kg (73 W/lb). The higher power levels reduce the delivered specific energy of the battery (at the 2.983-kW accessory power level) to as low as 97 W-hr/kg (44 W-hr/lb), and the vehicle range drops to 142 to 206 km (88 to 128 miles).

Constant-speed driving, even at the higher velocities of 96 to 113 km/hr (60 to 70 mph), is not as demanding on the battery as some of the other profiles because the average power level is lower than the peak power demands of the other profiles. Once the initial power required to accelerate the vehicle to its velocity has been satisfied, the power requirement drops off so that, at a constant velocity of 113 km/hr (70 mph) and an accessory load of 2.983 kW, the range of the vehicle increases to 277 km (172 miles). At lower constant velocities of 32 to 40 km/hr (20 to 25 mph), the vehicle's range is over 483 km (300 miles). The range falls off rapidly at velocities above 88 km/hr (55 mph), primarily because of the increased retarding effect of air drag.

The conclusions that can be drawn from these calculations are that lithium/sulfur cells possess the potential for powering an all-electric vehicle of good performance. Laboratory cells have been shown to have a sufficient power density to accomplish all driving profiles tested. Energy storage, however, should be improved to increase the range of the vehicle somewhat.

B. Lithium/Chalcogen Cells for Hybrid-Vehicle Propulsion

Since May 1969, the U. S. Army Mobility Equipment Research and Development Center at Fort Belvoir, Virginia, has been supporting a program in the Chemical Engineering Division for the development of a lithium/chalcogen (sulfur, selenium) battery to be used in military vehicles. This application involves a hybrid propulsion system in which a gas turbine would provide power during normal operation, and a lithium/chalcogen battery would provide additional power in situations such as acceleration and hill climbing, where high power is required for a relatively short time. The hybrid system is expected to weigh less and cost less than either a battery or turbine designed to do the job alone. Existing batteries are incapable of meeting the requirements of high specific power (watts per pound of battery weight) and specific energy (watt-hours per pound of battery weight) for this application.

The present effort is directed toward the development of lightweight sealed cells, approximately 7.5-cm diameter, capable of delivering (a) short-time peak power densities of 1 to 3 W/cm^2, (b) energy densities of 0.5 $W\text{-}hr/cm^2$ at the 1-hr discharge rate (0.27 A/cm^2) to a 1.0-V cutoff and 40% utilization of the theoretical capacity, (c) lifetimes of 1000 to 2000 hr, and cycle lives of 500 to 1000 charge-discharge cycles. These cells will eventually be components of a 1-kW battery.

The progress made in this program during the past year includes (a) the extension of the cell lifetime, through the use of sulfur and thallium additives to the selenium, from about 100 hr to more than 2500 hr, (b) the development of a liquid-electrolyte cell of improved capacity density and power density, and (c) the attainment of all of the cell performance goals (per unit electrode area) in unsealed 7.5-cm-dia cells.

1. Cell Studies

a. Cathode Composition Studies

The cause of the short cell life encountered in this program and the NHLI Program (see Section VI.C) was found to be related to the solubility transport of selenium through the electrolyte to the lithium electrode. A series of paste-electrolyte cell tests was performed to study the effect of various additives to selenium on cell performance. The interest in additives to selenium was stimulated by early experiments which indicated that the transport rate of selenium-additive mixtures through the paste electrolyte had been considerably lower than that of pure selenium. Also, solubility tests conducted by other investigators at Argonne[12] indicated that additives such as phosphorus reduced the solubility of sulfur in lithium-halide electrolytes. The available phase-diagram data for lithium-additive and

[12] V. A. Maroni, private communication (1970).

selenium-additive systems were studied in an attempt to identify those systems with low melting points over reasonable composition ranges (an apparent requirement for high utilization of the cathode reactant). The additives selected for experimental testing included P, P_4S_{10}, As, Te, and Tl.

Table VI-6 shows the various cathode compositions tested in paste-electrolyte cells. Most of the cell tests were of brief duration since the available paste electrolytes were not capable of maintaining complete physical separation of the anode and cathode phases for long periods. Phosphorus, tellurium, and thallium were found to be effective additives to selenium and sulfur for reducing the transfer rate of cathode material. Tellurium and thallium additives showed the most promise of meeting the short-time peak power density goal of 1 to 3 W/cm^2. Thallium, however, appeared to be more attractive than tellurium because of its much lower corrosion rates in cell tests using niobium current collectors. Since the electrical performance of the paste-electrolyte cells using thallium additive (Tl_2Se_3 and TlS_2 compositions tested) was poor, it appeared that a major change in cell design or a reduction in thallium concentration would be required for this system. The use of thallium additive was recommended for testing in the NHLI cell lifetime study (Section VI.C.1). It was shown in the NHLI work that Se-10 at. % Tl was effective in reducing selenium transport, and long cell lifetimes were achieved at acceptable performance levels. It was concluded that the use of thallium additive represented an acceptable solution to the solubility transport problem.

TABLE VI-6. Cathode Compositions Tested in the Additive Investigation

	Cathode Composition, wt %								
Cell No.	Se	S	P_4S_{10}	P	As	Te	Tl	Li_2Se	Salt Additive[a]
23	11.9					29.4		58.7	
24	56.7					43.3			
29			100.0						
L-4	30.0					70.0			
30	55.9				11.7				32.4
31	52.2			8.0					39.8
34	87.7			8.9				3.4	
36			100.0						
38			100.0						
43	36.6						63.4		
45		23.9					76.1		
48		23.9					76.1		

[a]The LiCl-LiBr-LiI-KI-CsI eutectic.

A significant decrease in the average voltage during discharge (to a 1.0-V cutoff) was observed in early cell tests with Se-Tl alloys. Sulfur additions to the Se-Tl cathode were made in an attempt to increase the average voltage. All tests involving $S_6Se_7Tl_3$ (atom ratio) cathodes resulted in higher average voltages as well as in improved capacity densities.

A subsequent cell test involving S-50 at. % Se with trace Tl (less than 0.1 at. %) was found to result in even better electrical performance than the cells using S-Se-Tl cathodes. This cell (Army Cell No. 73) has achieved over 2500 hr of stable operation and is described in detail below. It has been tentatively concluded that the S-50 at. % Se alloy is a better cathode material than either sulfur or selenium alone. Additional tests will be required to determine the optimum S/Se ratio and whether the thallium addition can be eliminated completely.

b. Cell Performance Studies

A total of 73 single cells of approximately 7.5-cm diameter have been tested in this program. The first 53 cells used paste electrolytes and generally experienced either short cell lifetimes or poor electrical performance characteristics. Paste-electrolyte cell studies were discontinued after Cell No. 53 pending further progress in the preparation of high-quality pastes. Cells No. 54 to 73 were liquid-electrolyte cells in which the cathode material was immobilized by either (1) containment within a porous graphite current collector or (2) formation of a thick adherent coating on corrugated niobium expanded-mesh disks. Cell performance and lifetime generally improved as improvements in design and procedure were incorporated into the later tests. Table VI-7 summarizes performance data for selected liquid-electrolyte cells. The best sustained performance to date has been achieved with Cell No. 73, which is described below.

TABLE VI-7. Summary of Performance Data for Selected Liquid-Electrolyte Cells[a]

(Temperature ≈400°C)

Cell No.	Discharge No.	Current Density, A/cm^2	Capacity Density, A-hr/cm^2	Cutoff Voltage, V	Cycle Life	Lifetime, hr	Cathode Composition, wt %	Interelectrode Distance, cm
56	5	0.11	0.054	1.1	40	140	36.7 Se-63.3 Tl	0.63
64	51	0.15	0.26	0.4	71	380	47.2 Se-52.8 Tl	0.64
68	7	0.15	0.15	0.6	63	144	14.3 S-40.7 Se-45.0 Tl	1.1
70	3	0.29	0.24	1.0	313	310	14.3 S-40.7 Se-45.0 Tl	0.63 to 2.22
72	46	0.36	0.30	1.05	150	450	14.3 S-40.7 Se-45.0 Tl	0.63 to 2.22
73	1389	0.30	0.475	1.00	>1400[b]	>2500[b]	30 S-70 Se	0.63 to 2.22

[a]The cell performances are maximum values and do not represent average values.
[b]Test still continuing.

c. Cell No. 73

Cell No. 73, shown schematically in Fig. VI-10, contained 3.0 g of lithium and 66.8 g of S-50 at. % Se alloy containing <0.1% Tl. The anode consisted of nickel Feltmetal (Huyck Metals Co., 80% porosity, 60-μm mean pore size) loaded with lithium at 550°C. The cathode current collector consisted of a comb-shaped structure (approximately 0.95-cm thick and 7-cm diameter) made of PG-25 porous graphite (Union Carbide Corp., 48% porosity, 120-μm average pore diameter) filled with the S-Se alloy. The cathode was assembled as follows: (1) about 10 g of the S-Se-Tl alloy was loaded into the niobium cup; (2) the graphite current collector

was put in place; (3) the remaining S-Se alloy was loaded on the graphite structure; (4) 135.0 g molten LiF-LiCl-KCl eutectic was poured into the niobium cup; and (5) the cathode assembly was heated for approximately 3 hr at 400°C to allow the cathode alloy to infiltrate the graphite structure.

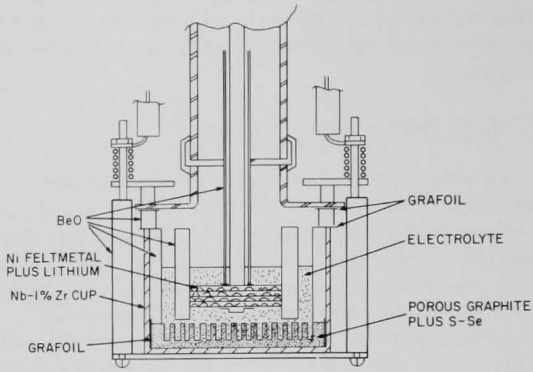

Fig. VI-10. Cross Section of Cell No. 73

A summary of the capacity density data for the first 2000 hr and 1400 cycles of operation of Cell No. 73 is shown in Fig. VI-11. Since the first 100 cycles and ~250 hr, Cell No. 73 has consistently achieved a capacity density of 0.30 A-hr/cm^2 or greater at the 1-hr rate. The cell is still in operation at this writing.

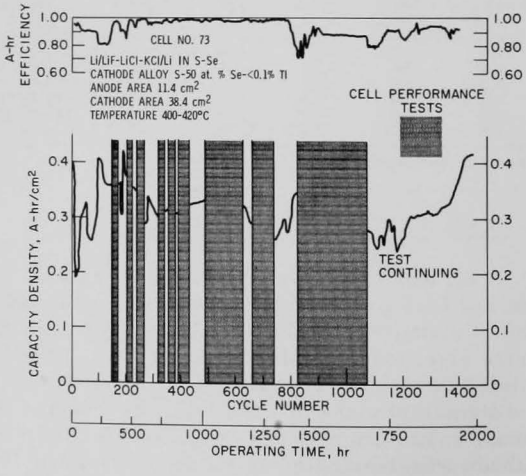

Fig. VI-11. Capacity Density Data for Cell No. 73

The cell performance improved during the first two weeks of operation as a result of a gradual decrease in the internal resistance. After about 2 months of operation, a slight decline in electrical performance and a corresponding increase in internal resistance was observed. The decreases in internal cell resistance may be due to an improvement in the wetting of the anode and cathode current collectors during the early cycles, resulting in a lower contact resistance.

A major goal of the Army hybrid vehicle program has been the development of a battery which can operate at a peak power of about 50 kW (equivalent to 1-3 W/cm^2) for periods of 1-3 sec. Figure VI-12 shows pulse duration vs. power level data taken after 350 hr of operation of Cell No. 73. Pulses of greater than 1.5 W/cm^2 were maintained for periods exceeding 60 sec with the pulse duration dropping sharply with increasing power level. The power density varied by about 10% during each pulse and average values are shown in Fig. VI-12. It appears that the hybrid vehicle peak power requirements can be readily achieved with lithium/chalcogen cells.

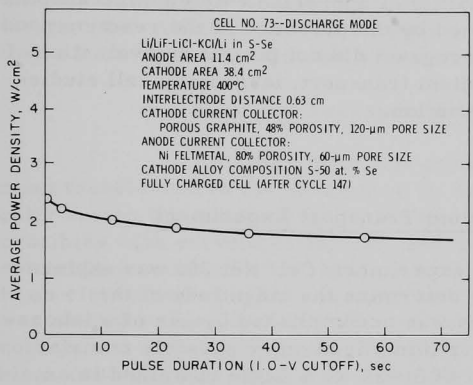

Fig. VI-12. High-Power Pulse Data for Army Cell 73

Present emphasis in this program is being devoted to the construction and testing of high-performance, lightweight, sealed cells. The excellent performance and long lifetime of recent laboratory cells (not sealed) have provided confidence that the cells being developed will achieve the goals of the Army program.

C. Lithium/Selenium Batteries for Implantation

The program to develop a lithium/selenium battery suitable for use as an implantable, rechargeable power source for an artificial heart or heart-assist device was continued. This effort has been supported by the National Heart and Lung Institute (NHLI) under the Medical Devices Applications Program. For this application, the critical measures of performance are the specific energy (W-hr/kg), the energy density (W-hr/cm^3), and the cycle life (number of charge-discharge cycles before failure). The specific power (W/kg) objective is less critical, with a total power of 10-30 W required for an electrically driven heart-pump system. The specific energy goal is about 110 W-hr/kg, which would permit operation of an artificial heart for 10 hr with a battery weight of 1.1 kg if the average

power demand were 10 W. The battery is to be recharged by transmitting electromagnetic energy inductively through intact skin.

In the first year's program, the major emphasis was on the development and testing of full-sized (31.6-cm^2 active area) cells and batteries employing paste electrolytes. These cells and batteries generally exhibited excellent performance during the first cycle; however, lifetime problems were experienced and a good second cycle was not achieved in any of the tests. The difficulty was traced to selenium transport through the paste electrolyte, forming Li_2Se at the anode. Phase-diagram studies (see Section V.A.2) suggested the possibility of appreciable selenium transport via a solubility mechanism, enhanced by the presence of the reaction product, Li_2Se. Since the cell-testing program did not permit an evaluation of the mechanism or kinetics of selenium transport, laboratory cell studies were performed to yield this information.

1. Cell Lifetime Studies

a. Exploratory Selenium Transport Experiment

The first lifetime experiment, Cell No. 20, was exploratory in nature and was designed to determine the magnitude of the solubility-transport problem. This was accomplished by use of a laboratory cell design which eliminated or minimized other possible transfer mechanisms. In this test, an ingot of Se-22 wt % Li_2Se contained in an alumina crucible was immersed in a bath of "viscous" LiCl-KCl electrolyte at 375°C. The viscous electrolyte consisted of a mixture of salt and a sufficient amount of inert $LiAlO_2$ powder to increase the viscosity of the electrolyte in order to eliminate convective mixing currents during the experiment. The viscous electrolyte provided a liquid seal, preventing vaporization transport of selenium species as well as avoiding the wicking and other physical transport mechanisms associated with paste electrolytes. After the top surface of the salt was sampled, an anode consisting of a 2.5-cm-dia stainless steel Feltmetal soaked with lithium was placed in contact with the electrolyte. The cathode area was 5.0 cm^2 and the interelectrode distance was 3 cm. After about 6 hr of operation at 375°C and a discharge of 0.21 A-hr, the system was rapidly cooled to room temperature. The cell was sectioned and a very dark mushroom-shaped phase was observed to be emanating from the top of the inner alumina crucible. This phase, which also filled the inner crucible, had advanced more than 1.5 cm toward the lithium electrode and had a somewhat homogeneous appearance. The upper portion of this dark phase was analyzed and found to be very rich in selenium. It was concluded that solubility transfer of selenium to the lithium electrode was very rapid and may have been responsible for the brief lifetimes experienced in the cells and batteries tested previously in this program.

b. Electrolyte Studies

Three experiments (Cells No. 21, 22, and 24) were performed to test the effect of LiF-LiCl-LiI and LiBr-RbBr eutectic electrolytes on selenium transport rates. The experimental design and loading procedures were the same as those used in Cell No. 20. Cell No. 21, which employed the LiF-LiCl-LiI electrolyte at 375°C, experienced rapid decrease of cell performance during the seventh cycle. A sample of the upper portion of the viscous electrolyte was found to contain 4.4 wt % selenium. It was concluded that the LiF-LiCl-LiI electrolyte was not effective in reducing the rate of selenium transport. Cells No. 22 and 24 used the LiBr-RbBr electrolyte. Although this electrolyte resulted in improved cell lifetimes, it was found that the selenium transfer rate was still too high.

c. Selenium Transport Reversal Test

An experiment was performed to determine whether selenium transferred to the anode may be returned to the cathode electrochemically during the charging cycle. In this test, two identical small alumina crucibles with current collectors, one serving as a selenium-deposition electrode and the other serving as an analytical blank, were both immersed in an electrolyte at 325°C. A stainless steel Feltmetal, containing lithium, was coated with a layer of Li_2Se and introduced into the salt bath, and a voltage was impressed across the electrodes as in a normal charge. The blank crucible was positioned next to the cathode but was not introduced into the circuit. After 18 hr of charging, it was found that 4 mg of selenium had been transported to the positive electrode despite an unfavorable geometry and an interelectrode distance of more than 5 cm. An analysis of the blank electrode showed no selenium; thus it was concluded that the selenium had transported electrochemically. This result is considered to be important relative to the development of long-lived cells since it indicates that a small but significant rate of selenium transport to the lithium electrode can be tolerated because this selenium can be returned to the selenium electrode during recharge.

d. Thallium Additive Experiments

An experiment (Cell No. 26) testing the effect of thallium as an additive to the selenium electrode was performed using a viscous LiBr-RbBr electrolyte. Previous work at Argonne (see Section VI.B.1) indicated that the addition of about 40 at. % thallium to the selenium had greatly reduced the rate of selenium transport in a paste-electrolyte cell. An experiment was performed in order to test the effect of a Se-10 at. % Tl cathode on cell lifetime using the same procedures employed in Cells No. 20, 21, 22, and 24. The presence of 10 at. % thallium in the selenium electrode was found to significantly reduce the rate of selenium transport and allowed

the attainment of "steady-state" cell operation with acceptable electrical performance. Cell No. 26 achieved 532 hr and 74 cycles of operation at a capacity density of 0.41 A-hr/cm^2 at 0.061 A/cm^2.

A series of three experiments was performed using cathode alloy compositions of pure selenium, Se-2 at. % Tl, and Se-10 at. % Tl in an attempt to determine the minimum concentration of thallium necessary to reduce the rate of selenium transport and allow steady-state cell operation with high performance. The experimental design and procedure were the same as those used for Cell No. 26 except that the electrolyte consisted of the LiF-LiCl-KCl eutectic with no filler added.

The results of these tests are as follows: (a) the use of 10 at. % Tl resulted in satisfactory cell performance with the selenium well contained in the cathode cup; (b) the use of 2 at. % Tl resulted in long-term cell operation, but resulted in poor selenium utilization owing to inadequate containment of selenium within the cathode cup; and (c) the cell with pure selenium experienced a selenium-utilization level lower than that found for 2 at. % thallium.

It is concluded that thallium addition to the selenium cathode provides an acceptable solution to the solubility-transport lifetime problem. It should be possible to operate high-performance lithium/selenium cells with long lifetimes using a thallium concentration of less than 10 at. % but somewhat more than 2 at. %.

2. Studies of Full-Sized Cells

The objective of this effort was to develop and demonstrate a full-scale cell (7.5-cm-diameter) that had a long cycle life at a power density of 0.2 W/cm^2 and an energy density of about 0.76 W-hr/cm^2. Most of the cell tests in this program have been conducted with 7.5-cm-dia cells with a lithium anode, a selenium cathode, and a molten-salt electrolyte. To assure no mixing of reactants, either the electrolyte or the reactants must be immobilized. In the early cell work, the electrolyte was immobilized by combining it with a finely divided inert ceramic filler such as lithium aluminate to form a paste that remained rigid (because of surface forces) above the melting point of the salt. Subsequent studies have involved cells containing liquid electrolytes and immobilized anode and cathode phases.

a. Paste Electrolyte Cells

A total of 32 full-scale paste-electrolyte cells were built and tested in the NHLI program. These cells generally exhibited excellent performance during the first discharge but experienced rapid loss of performance (which prevented the attainment of a second cycle). A program

to develop improved paste electrolytes was conducted over a period of about two years. Significant progress was made in improving the physical properties of the pastes as evidenced by greatly reduced gas permeabilities at room temperature. Paste electrolyte fabrication using the infiltration technique was particularly effective in this regard. The use of the improved paste electrolytes in cell experiments did not result in improved cell lifetimes; consequently an effort to develop a liquid-electrolyte cell was initiated.

b. Liquid Electrolyte Cells

The advances made in related programs with high-power-density and high-capacity-density cells using liquid electrolytes provided the motivation for an examination of the use of a liquid electrolyte in cells designed to meet the NHLI performance goals.

The first NHLI liquid electrolyte cell design involved an immobilized cathode alloy, an electrolyte of molten LiF-LiCl-KCl eutectic, and a solid anode consisting of a 45 at. % Li-Al alloy. A Li-Al alloy[13] was proposed for the anode because the reduced lithium activity in the molten salt would result in lower self-discharge rates and corrosion rates and superior lithium collection during the charging portion of the cycle. Four full-scale cell experiments (Cells No. 35-38) were performed to examine the feasibility of the design in meeting the NHLI goals.

Each of the four cells yielded promising results with an improvement in performance from cell to cell. The best performance was achieved in the last cell (Cell No. 38) in which a lithium-soaked Feltmetal was used to deposit lithium into the cathode during the first discharge, and an aluminum disk was substituted for the lithium anode for the remainder of the cell test. The Li-Al alloy was formed by slow charge-discharge cycling. The cathode used was $S_6Se_7Tl_3$ (atom ratio) developed in the U.S. Army program (Section VI.B). Cell No. 38 achieved 169 hr of operation and 19 cycles. This cell showed excellent performance capabilities, reaching a peak cathode performance during the 14th discharge when 0.25 A-hr/cm^2 was achieved at an average current density of 0.061 A/cm^2 and an average voltage (IR-included) of 1.48 V. This corresponds to a specific energy of 111 W-hr/kg. The cathode-alloy utilization was 79%.

These early liquid-electrolyte cells have demonstrated the capability of achieving multiple cycles with high performance. The full-scale paste-electrolyte cells tested previously in the NHLI program tended to deteriorate in performance within a few cycles. In addition, the liquid-electrolyte cell has met or exceeded the capacity, power, and weight specifications for a 30-W battery.

[13] J. L. Benak, Method of Treating Lithium-Aluminum Electrode, U. S. Patent 3,501, 349, assigned to Standard Oil of Ohio (1970).

VII. FLUIDIZED-BED COMBUSTION OF FOSSIL FUELS

The Office of Air Programs of the Environmental Protection Agency is funding an investigation at Argonne National Laboratory of the effects of variables on the removal of atmospheric pollutants (oxides of sulfur and nitrogen) generated during the combustion of fossil fuels in a fluidized bed. The concept involves burning fuel (coal, oil, or natural gas) in a fluidized bed of particulate solids (usually limestone) that react with gaseous sulfur compounds (and possibly nitrogen compounds) released during combustion. Subsequently, the sulfur-containing additive can be regenerated to CaO for reuse and the sulfur can be recovered. A fluidized bed is a highly efficient contacting medium for carrying out gas-solid reactions and for removing or adding heat.

A. Bench-Scale Combustion Experiments

The fluidized-bed combustion equipment at Argonne consists of a 6-in.-dia, 6-ft-long bench-scale combustor operated in series with a 3-in.-dia, 7-ft-long preheater for the fluidizing gas. Ancillary equipment for operation of the combustor includes mechanical powder feeders for introducing coal and additive into the combustor, a gas manifold for the air supply to the combustor, two cyclone separators and a final filter for removing particulates from the flue gas, and a flue gas sampling and analytical system.

Experiments to investigate the effects of operating variables on SO_2 and NO levels in the flue gas have been continued. Variables affecting the chemical composition and physical properties of the bed and elutriated particles have been studied, and material balances have been obtained for some experiments. Except in a few runs in which the fluidized bed was particulate alumina or coal ash, the fluidized bed consisted of partially reacted limestone. The combustor was operated in the single-stage and two-stage modes with coal as the fuel.

In single- or one-stage combustion, a quantity of oxygen (as air) in excess of the stoichiometric quantity is added to the fluidized-bed combustion zone to burn the coal to CO_2 and water. Typically, the flue gas from the bed contains ~3% oxygen. In two-stage combustion, less than the stoichiometric volume of air is added to the fluidized-bed combustion zone, which comprises the first stage. The oxygen concentration of the gas leaving this stage is approximately zero or near zero, and because relatively large amounts of CO and hydrocarbons are produced, the atmosphere in the bed is highly reducing. The CO and hydrocarbons from this stage are oxidized in a second stage. The second stage could be physically separate from the first stage, but in the ANL combustor it consists of the freeboard volume above the fluidized bed. Enough air is injected into the second stage so that in most runs, the oxygen concentration in the flue gas is above zero percent.

1. Results of Single-Stage Combustion Runs

Major findings during the past year in the one-stage combustion experiments were that over the ranges tested, retention of sulfur in the bed is strongly influenced by operating variables, as described below.

Fluidized-Bed Temperature. For a given coal, limestone, and set of operating conditions, sulfur retention is at a maximum at a particular temperature, decreasing at higher and lower temperatures. For example, with Illinois coal at a Ca/S ratio of 2.5, maximum sulfur retention occurs at 1550°F; with Pittsburgh coal at a Ca/S ratio of 4.0, maximum sulfur retention occurs at 1450°F.

Ca/S Mole Ratio (ratio of moles of calcium in the additive to moles of sulfur in the coal). Sulfur retention increases rapidly as the Ca/S ratio is increased to 3 and then increases less rapidly as the Ca/S ratio is further increased.

Superficial Gas Velocity. Sulfur retention decreases as the gas velocity is increased. At a Ca/S ratio of ~4, sulfur retention decreases approximately 5% for each 1 ft/sec increase in gas velocity in the range from 2.0 to 7.6 ft/sec. At lower Ca/S ratios, the sulfur retention decrease is greater than 5% for each 1 ft/sec increase in gas velocity; at higher ratios, sulfur retention may be essentially independent of gas velocity.

Variables that have a lesser effect on sulfur retention over the ranges studied include (1) type of coal, (2) coal particle size, (3) limestone type, (4) limestone particle size, (5) fluidized-bed height, (6) moisture concentration, (7) solids feeding method, and (8) temperature of the upper stage of the combustor.

Levels of NO in these coal combustion runs ranged from ~250 to ~550 ppm. No satisfactory correlations with operating conditions were found except for the case of water addition. When water was injected into the base of the bed at rates representing a range of moisture contents of different coals, the NO concentration in the flue gas decreased from 530 ppm, with no water addition, to 380 ppm, with water added at a rate corresponding to a coal moisture content of 51%.

2. Results of Two-Stage Combustion Runs

Two-stage experiments were conducted to determine whether the two-step procedure might have benefits over the single-stage fluidized-bed combustion concept, particularly with respect to decreased nitrogen oxide emissions. To simulate the conditions of combustion in the first stage only, some of the experiments were carried out with a substoichiometric addition of air to the first stage and no introduction of air to the second stage. In other experiments, secondary air was introduced above the fluidized bed.

The experimental results included information on the concentrations of H_2S, CO, and NO in the off-gases and on the chemical compositions of bed materials and elutriated solids. Correlation of the effects of operating variables on the emission of sulfur and nitrogen compounds was attempted, and the following preliminary observations were made.

1) In experiments in which a substoichiometric quantity of air was fed to the first stage only, the percent of sulfur in the flue gas as H_2S as compared with the percent present as SO_2 was sensitive to the amount of air introduced into the fluidized bed, the H_2S increasing drastically when the air feed rate was reduced below a value corresponding to ~70% of the calculated stoichiometric quantity of air necessary to react with the coal being fed.[1] At an air feed rate equivalent to ~50% of the stoichiometric quantity, the concentration of H_2S (611 ppm) was nearly equivalent to the concentration of SO_2 (660 ppm). At air inputs of 70 to 80% of the stoichiometric quantity, the relative amount of H_2S fell to about 2% of the total sulfur contained in the gas. (These values refer to the sulfur compounds that were not removed from the flue gas by the lime bed.)

In those experiments where secondary air was introduced above the fluidized bed, the H_2S level in the off-gas was low--corresponding to less than 1% of the total sulfur in the gas. This suggests that any H_2S in the gas leaving the first stage is oxidized to SO_2 by air fed to the second stage.

2) For experiments in which air was added only to the first stage, the effect of air feed rate on CO concentration in the off-gas was similar to that on H_2S behavior, the CO level decreasing from 13,000 ppm to 6000 ppm as the air rate to the fluidized bed was increased from 50% to 80% of stoichiometric. The CO level in the flue gas was, in general, significantly lower (<2000 ppm) for experiments in which secondary air was introduced above the bed.

3) The NO concentrations observed in the flue gas when air was added only to the first stage were generally <250 ppm, with an apparent dependence on the temperature of the fluidized bed--i.e., at equivalent air feed rates, higher NO levels were observed at lower bed temperatures. This could mean that NO is chemically reduced by CO, with the rate of reaction increasing with temperature. The NO levels in two-stage combustion were substantially lower than those observed in one-stage combustions.

Introduction of secondary air above the fluidized bed caused somewhat erratic behavior of NO levels, but in general, NO levels were increased. Plausible explanations for this behavior include the following:

---

[1]The calculated stoichiometric quantity assumes that all of the carbon and hydrogen in the coal is oxidized completely to $CO_2 + H_2O$. Although the parameter, air feed rate as a percent of the stoichiometric quantity, was based on feed rates of coal and air, it is recognized that the quantity of coal actually oxidized varies with other parameters (i.e., temperature, etc.). The stoichiometric air feed rate based on the coal actually oxidized may well be more suitable for certain correlations.

(1) introduction of secondary air would suppress any reduction of NO by CO in the zone above the bed or (2) a nitrogen compound such as ammonia might be present in the gas, and this compound might be oxidized to NO by the secondary air. Further experimental work will be needed to resolve the cause of varying NO levels.

4) The data on sulfur retention with air added only to the first stage exhibit a large amount of scatter, but better sulfur retention appears to have occurred at 1450°F than at 1550°F or 1650°F. The sulfur retentions at 1450°F, in general, are better than those achieved during earlier experiments conducted under one-stage oxidizing conditions at the same Ca/S mole ratio.

5) No simple relationship between the amount of air introduced into the bed and sulfur retention was evident. At an air rate of 100% of the calculated stoichiometric requirement, sulfur retention was about 65%, decreasing as the air flow rate was decreased to 75% of the calculated stoichiometric requirement, and then increasing very rapidly as the air flow rate was further decreased. This suggests that removal by lime of sulfur in the form of SO_2 is poor in an oxygen-deficient region (75-95% of the calculated stoichiometric requirement), but that sulfur in the form of H_2S is removed efficiently. This would be expected because retention of SO_2 by lime requires oxidizing conditions to convert the calcium sulfite intermediate to $CaSO_4$, whereas retention of H_2S by lime requires reducing conditions.

6) The carbon content (unburned coal) of samples of the fluidized bed ranged from 7.1 to 0.41 wt %. No relationship between the carbon content and either the bed temperature or the air feed rate could be found. The lack of correlation may be due to the short durations of the runs. Long-duration runs will be needed to establish the steady-state carbon content of the bed.

The carbon content of samples of the elutriated solids collected in the primary cyclone ranged from 43.9 to 20.0 wt % and apparently decreased as bed temperature increased.

7) The bed material (partially reacted lime) contained sulfur in three forms, sulfate, sulfite, and sulfide. The sulfide content of bed material decreased as air flow was increased to near-stoichiometric feed rates. At air inputs corresponding to 50% of the stoichiometric quantity, up to 100% of the bed sulfur was detected as sulfide. In most cases, the sulfide content dropped off rapidly to less than 1% when the air feed rate exceeded 65% of the stoichiometric quantity.

The sulfite content of bed samples was erratic and ranged between 6.2 and <0.1 wt %. No correlation could be found with either bed temperature or air feed rate.

The results of bench-scale combustion experiments have thus far led to the following conclusions:

1) The two-stage combustion concept appears to have good prospects for low sulfur emissions if the first-stage fluidized bed is operated under conditions that favor H_2S formation (i.e., highly substoichiometric air feed rates).

2) To avoid SO_2 production in the second stage, it may be desirable to carry out second-stage combustion after particulate matter has been removed from the flue gas by cyclones. This is necessary to avoid combustion of unburned, fine coal particles in the second stage.

3) Prospects for reduced emissions of NO seem good, but tests are needed to determine whether a nitrogen compound is contained in the gas leaving the first stage and whether such a compound is oxidized to NO in the second stage.

4) Measurements and calculations of combustion efficiency have not been completed. However, it has been observed that a large quantity of carbon is contained in the solids elutriated from the first stage, indicating that combustion efficiency may be lower than required. To achieve the required overall combustion efficiency, the use of a separate carbon burnup cell operating under oxidizing conditions will probably be necessary. Further evaluation of the overall potential advantages of the two-stage combustion scheme is needed.

B. Mechanism of Lime Sulfation Reaction

Studies have been made on the mechanism of the lime-SO_2 reaction, specifically on the mode of SO_2 penetration into lime particles in fluidized beds. In this laboratory, it is believed that the mechanism is essentially the shell-formation model enhanced by localized reducing conditions in the dense phase[2] of the fluid bed. Because of a large demand for oxygen by the carbon combustion reaction near the bottom of the combustor, the dense phase of the fludized bed in this location is depleted in oxygen in comparison to the bubble phase. As a result, at some locations in the dense phase where the SO_2-lime reaction takes place, the CO concentration is relatively high.

Recent ANL work on the mechanism of the lime-SO_2 reaction comprises (1) electron-microprobe examination of sulfated lime particles taken from elutriated solids and from combustor beds and (2) laboratory-scale experiments with sulfated lime to measure SO_2 evolution under reducing conditions.

---

[2]The dense or emulsion phase is the portion of the bed where gas flows in intimate contact with the solids. The remainder of the gas passes through the bed in the form of bubbles. As a bubble rises through the bed, gas circulates from the bubble into the emulsion phase and back into the bubble. The gas in a bubble is available for reaction only as rapidly as it circulates into the emulsion phase.

Microprobe examination of particles sampled during an experiment in which calcined limestone was exposed to an SO_2-air mixture with no combustion occurring showed that their sulfur profile was radically different from the sulfur profile of particles from an experiment conducted under similar operating conditions except that combustion of coal was occurring. Sulfur formed a very thin shell on the surface of the particles from the former experiment. Furthermore, the thickness of this layer did not change appreciably with increasing reaction time and was considerably thinner than in lime particles from the coal-combustion experiment.

The conclusion from these microprobe examinations is that sulfation reactions during the combustion of carbon differ from sulfation reactions in the absence of combustion. Although it cannot be said that the mechanisms of the reactions are different, the extent of the sulfation reaction is considerably greater for the combustion case. This lends support to the hypothesis that local reducing conditions existing during combustion produce greater mobility of the SO_2 for penetration into the lime particles.

Laboratory-scale experiments to determine the effect of CO on the sulfation reaction showed that SO_2 can be released readily from sulfated lime at about 1750°F, when CO is used as the reductant. Hence, it is possible for SO_2 to be released from $CaSO_4$ in the reducing phase of the fluidized bed; the released SO_2 could then penetrate deeper into the lime particle or it could escape into the gas phase. At lower temperatures (~1650°F), the reduction reaction apparently produces CaS rather than CaO and SO_2 since it has been demonstrated that when air is passed through a bed that has been treated with CO at the lower temperature, SO_2 is released in high concentrations. In experiments in which the temperature of reaction was 1500°F, the rate of reaction to form CaS was nearly zero. Hence, it is believed that at some combustion temperatures cyclic reduction and reoxidation of the sulfated lime occurs during combustion.

C. Regeneration of Calcium Sulfate with Carbon Monoxide/Carbon Dioxide Mixtures

It is economically and ecologically desirable to regenerate used additive from fluidized-bed combustion to mitigate the problem of lime disposal. Several processes to regenerate the additive for reuse and to recover its sulfur content in a marketable or storable form are under study.

Equilibrium calculations have been made for the purpose of evaluating several schemes for the regeneration of spent additive, which is considered to be present as $CaSO_4$ when coal is burned with excess oxygen present. In one scheme, $CaSO_4$ would be converted directly to SO_2 and CaO with a CO/CO_2 mixture. In another scheme, $CaSO_4$ would be reduced to CaS, and CaS would be either (1) converted to H_2S and $CaCO_3$ with H_2O/CO_2 mixtures or (2) roasted in air or oxygen to give SO_2 and CaO. SO_2 or H_2S would

be converted to elemental sulfur in a Claus plant (a commercially available process for production of sulfur from H_2S). When coal is burned in deficient oxygen, the spent additive contains CaS, which can be regenerated by either scheme described above.

Equilibrium calculations have been performed for reduction of $CaSO_4$ with CO/CO_2 mixtures to determine the maximum amounts of gaseous sulfur species that can be formed as a function of temperature and equilibrium CO/CO_2 ratio. They also show the conditions under which various sulfur-bearing solids can exist. Calculations were made for temperatures of 1700 to 2300°F and CO/CO_2 ratios of 0.005 to 0.040 to determine the amount of SO_2 in equilibrium with a solid phase of $CaSO_4$ (or its reduction products) as a function of temperature and equilibrium CO/CO_2 ratio. The SO_2 concentrations and solid phases present at equilibrium as a function of temperature and CO/CO_2 ratios are shown in Fig. VII-1. The calculations indicate that at 1900°F, for example, the maximum attainable pressure of SO_2 is 0.25 atm and that the SO_2 pressure increases with temperature. An SO_2 pressure of 0.6 atm can be attained at 2025°F and a CO/CO_2 ratio of 0.021. Similar calculations show that only small amounts (typically, 10^{-3} atm) of COS and S_2 vapor are formed in this system. The S_2 and COS concentrations at equilibrium are shown in Fig. VII-2.

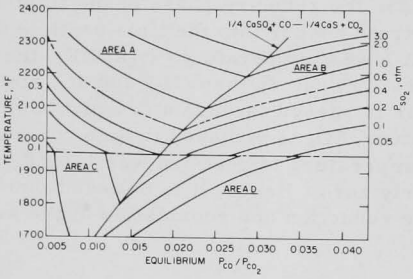

Fig. VII-1. Solid Phases and SO_2 Concentrations at Equilibrium as a Function of Temperature and CO/CO_2 Ratio

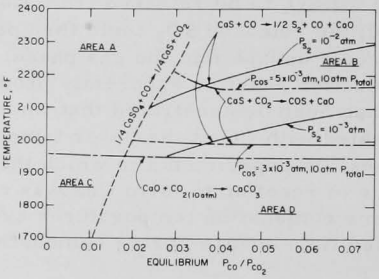

Fig. VII-2. S_2 and COS Concentrations at Equilibrium as a Function of Temperature and CO/CO_2 Ratio

An experimental program is under way to determine the accuracy of the equilibrium calculations. $CaSO_4$ is being reduced in a static reactor, and the gases are being analyzed for CO, CO_2, and SO_2. In another test program, $CaSO_4$ has been reduced to CaS in a 2-in.-dia fluidized-bed reactor. The CaS will be treated with H_2O/CO_2 mixtures to evaluate the formation of H_2S and $CaCO_3$ as a regeneration scheme.

D. Modelling Studies

Equations can be derived to predict SO_2 removal by lime in a fluidized bed. Numerical study of these equations showed that the effects of gas

bubbles bypassing the fluidized bed could be omitted. The equation[3] for SO_2 removal, R, is reproduced here for the case of no bubble flow.

$$R = 1 - \frac{\alpha[e^{-\alpha} - e^{-H(1-R/r)}]}{(1 - e^{-\alpha})[H(1 - R/r) - \alpha]} \tag{1}$$

If all SO_2 is generated at the entrance to the bed, $\alpha \rightarrow \infty$ and Eq. 1 reduces to

$$R = 1 - e^{-H(1-R/r)} \tag{2}$$

And if the SO_2 is generated uniformly throughout the bed, $\alpha = 0$ and Eq. 1 reduces to

$$R = 1 - \frac{1 - e^{-H(1-R/r)}}{H(1 - R/r)} \tag{3}$$

TABLE VII-1. Definitions of Symbols

b_1, b_2, b_3, b_4, b_5	=	model fitting constants
c	=	exit concentration of SO_2, mol/volume
F	=	total gas flow, volume/time
f	=	ratio of actual to ideal absorption capacity, y_e/y_s
H	=	bed inventory parameter
K	=	value of reaction velocity constant for fresh additive, volume/(time)(weight of additive)
M	=	Ca/S mole ratio in feed to fluidized bed
R	=	fractional removal of SO_2, $1-Fc/S$
r	=	effective feed ratio of additive to SO_2, wy_e/S
S	=	total rate of generation of SO_2, mol/time
T	=	operating temperature of fluidized bed, °F
W	=	total weight of reacted and unreacted additive in fluidized bed
w	=	feed rate of fresh additive, mass/time; also equals removal rate of exhausted additive
y_e	=	ultimate SO_2 absorption capability of additive particles
y_s	=	stoichiometric SO_2 absorption capability of additive particles
α	=	shape parameter describing SO_2 generation pattern; higher values of α correspond to relatively more SO_2 generation near the bed entrance

The parameters H and r are related to the physical parameters by

$$H = \frac{KW}{F} \tag{4}$$

[3]See Table VII-1 for definitions of symbols used in this discussion.

$$r = \frac{wy_e}{S} \tag{5}$$

However, if M is the Ca/S mole ratio in the feed to the column, r can also be expressed as

$$r = Mf \tag{6}$$

where the fraction f is defined by

$$f = \frac{y_e}{y_s} \tag{7}$$

and is the ultimate SO_2 absorption capability of additive particles relative to the ideal stoichiometric absorption capability of the SO_2 particles.

The reaction velocity constant K and the fraction f may depend on the reactor operating temperature T. Two forms of this dependence were chosen for investigation:

$$\begin{aligned} K &= b_1 + b_2(T+460) + b_3(T+460)^2 \\ f &= b_4 \end{aligned} \tag{8}$$

and

$$\begin{aligned} K &= b_1 + b_2(T+460) \\ f &= b_4 + b_5(T+460) \end{aligned} \tag{9}$$

Four models were investigated for fitting the experimental data:

$$\left.\begin{array}{l}\text{Model 1--Eqs. 2 and 8}\\ \text{Model 2--Eqs. 2 and 9}\end{array}\right\}\text{All } SO_2 \text{ generated at bed entrance}$$

$$\left.\begin{array}{l}\text{Model 3--Eqs. 3 and 8}\\ \text{Model 4--Eqs. 3 and 9}\end{array}\right\}SO_2 \text{ generated uniformly throughout the bed}$$

A computer program was devised to find values of the fitted constants b_1, b_2, b_3, b_4, and b_5, such that best agreement (in the least-squares sense) was obtained between values of R calculated from the model and those observed experimentally. Data from a total of 45 runs were fitted to the models. The ranges of experimental values covered were:

T	1325 to 1800°F
W	18 lb
F	458 to 1412 cfh
M	1.0 to 5.5

The results show that the standard error for each model is similar and is in the range 10-11%. Thus, the results of the fitting calculations do not indicate which SO_2 generation pattern is more realistic; nevertheless, the agreement between calculated and experimental results is reasonably good.

VIII. NUCLEAR SAFEGUARDS STUDY

To assure a capability for the deterrence and the prompt detection of theft or diversion of special nuclear material (SNM), safeguards-related criteria are needed for those nuclear facilities using significant quantities of SNM. At the request of the AEC's Office of Safeguards and Materials Management (now Office of Safeguards--OSG), a program study was initiated in June 1970 directed at developing general design criteria important to safeguarding SNM in certain nuclear facilities. Argonne's initial efforts were directed toward future, privately owned facilities engaged in nuclear fuel conversion, preparation, and fabrication operations. To provide graduated safeguards--that is, an intensity of safeguards dependent upon the relative strategic value of SNM involved--primary concern was directed toward facilities using plutonium, ^{233}U, and high-enriched uranium, with secondary concern toward low-enriched uranium facilities.

The three techniques generally conceded to be applicable to safeguards are material accountability, physical protection (containment), and surveillance. All of these techniques were considered in evolving the suggested comprehensive safeguards-related general design criteria for fuel-manufacturing facilities. These criteria have been submitted to OSG. They will be used by OSG and the AEC's Division of Nuclear Material Safeguards (DNMS) in developing overall criteria and performance requirements in applications for construction and operating licenses for fuel manufacturing facilities in the U. S. They will also be used by OSG in international safeguards considerations and discussion.

Recently, following submission of the criteria for fuel manufacturing facilities, Argonne was requested to undertake the responsibility of completing safeguards-related general design criteria for spent fuel chemical processing facilities and then similar criteria covering nuclear power reactors. Previously, the responsibility for preparation of such criteria for chemical processing and nuclear power plants had been assigned to other contractor groups.

Discussions are now under way with both the OSG and DNMS for continued and expanded studies related to the implementation and enhancement of nuclear safeguards.

IX. ADDENDUM

CHEMICAL ENGINEERING DIVISION PUBLICATIONS 1971

A. Open-Literature Publications

M. D. Adams
Ultramicrosampling with a Laser Microscope
Microscope 19, 157-169 (April 1971)

L. J. Anastasia, P. G. Alfredson, and M. J. Steindler
Reaction Model for the Fluorination of Uranium and Plutonium Compounds in Fluidized-Bed Reactors
Ind. Eng. Chem. Process Des. Develop. 10, 150 (April 1971)

P. E. Blackburn, A. E. Martin, J. E. Battles, P. A. G. O'Hare, and W. N. Hubbard
Sodium-Fuel Interactions
Trans. Amer. Nucl. Soc. 14(Suppl. 1), 20 (1971) Abstract

F. A. Cafasso, R. J. Meyer, and L. Burris
The Analytical Standards Program for Sodium Technology
Trans. Amer. Nucl. Soc. 14(2), 616 (1971) Abstract

E. J. Cairns, J. P. Ackerman, P. D. Hunt, and B. S. Tani
The Thermodynamics and Electrochemistry of the Lithium/Sulfur Cell by EMF and Phase Equilibration Methods
Electrochem. Soc. Extended Abstracts, Fall Mtg., Cleveland, October 3-7, 1971, Electrochem. Soc., Princeton, N. J., pp. 118-120 (1971)

E. J. Cairns
Research and Development on a Lithium/Sulfur Battery
Technical Report of the Conference on Low-Pollution Power Systems Development, NATO Committee on the Challenges of Modern Society, Eindhoven, Netherlands, February 1971, Air Pollution Technical Report No. 4, Environmental Protection Agency, Rockville, Md. (1971)

E. J. Cairns
Remarks on Secondary Alkali-Metal Chalcogen Batteries in Urban Transportation
Power Sources 3, p. 281, D. H. Collins, ed., Oriel Press, Newcastle-Upon-Tyne (1971)

N. R. Chellew, R. W. Kessie, and W. E. Miller
Gas Stripping of Xenon from Sodium for Fuel-Failure Characterization
Trans. Amer. Nucl. Soc. 14(2), 626 (1971) Abstract

L. F. Coleman
Shielding for a Pyrometallurgical Fuel Processing Plant
Engineering Compendium on Radiation Shielding, Vol. III, Eds. R. G. Jaeger, M. Grotenhuis, et al., Springer-Verlag, Heidelberg, pp. 181-188 (1970)

P. T. Cunningham, S. A. Johnson, and E. J. Cairns
Phase Equilibria in Lithium-Chalcogen Systems
J. Electrochem. Soc. 118, 1941 (1971)

J. E. Draley, B. R. T. Frost, D. M. Gruen, M. Kaminsky, and V. A. Maroni
An Assessment of Some Materials Problems for Fusion Reactors
Proc. 1971 Intersociety Energy Conversion Engineering Conf., AIChE, New York, pp. 1065-1075 (1971)

N. D. Dudey, R. R. Heinrich, and J. Williams
Integral Alpha Measurements for U and Pu Isotopes in EBR-II
Trans. Amer. Nucl. Soc. 14(2), 817 (1971) Abstract

J. G. Eberhart
Evidence for Long-Range Repulsive Atomic Interactions in Metals from Bond Energy Calculations
Met. Trans. 2, 3007-3010 (November 1971)

T. W. Eckels
Shielding Windows for Pyrometallurgical Fuel Processing Plant
Engineering Compendium on Radiation Shielding, Vol. III, Eds. R. G. Jaeger, M. Grotenhuis, et al., Springer-Verlag, Heidelberg, pp. 188-193 (1970)

D. E. Ferguson, C. R. Cooley, E. B. Sheldon, and D. S. Webster
Recovery of LMFBR Fuels--Development of Techniques
Proc. 4th Int. Conf. on Peaceful Uses of Atomic Energy, Geneva, Sept. 6-16, 1971, Vol. 1, paper No. 64 (1971)

A. K. Fischer
Secondary Power Producing Cell
U.S. Patent No. 3,615,828 (October 1971)

A. K. Fischer and F. A. Cafasso
Observations on the System Na-N_2-Ca-Type 304 Stainless Steel
Trans. Amer. Nucl. Soc. 14(2), 624 (1971) Abstract

H. E. Flotow, W. N. Hubbard, P. A. G. O'Hare, D. W. Osborne, and J. L. Settle
Heat Capacity from 1 to 350 K and Enthalpy of Formation at 298.15 K of Uranium Diboride
Proc. 1st Int. Conf. on Calorimetry and Thermodynamics, Warsaw, Aug. 31-Sept. 4, 1969, pp. 197-202, Polish Science Publrs. (1971)

M. J. Fluss and N. D. Dudey
Tritium and Helium Yields in Fast Fission of ^{235}U
Trans. Amer. Nucl. Soc. 14(2), 809 (1971) Abstract

D. R. Fredrickson and M. G. Chasanov
The Enthalpy of Molybdenum Disulfide to 1200 K by Drop Calorimetry
J. Chem. Thermodynam. 3, 693-696 (September 1971)

J. D. Gabor
Boundary Effects on a Bubble Rising in a Finite Two-Dimensional Fluidized Bed
Chem. Eng. Sci. 26, 1247-1257 (August 1971)

E. Greenberg, H. M. Feder, and W. N. Hubbard
The Thermochemistry of HF: The Enthalpy of Formation of Liquid HF
Proc. 1st Int. Conf. on Calorimetry and Thermodynamics, Warsaw, Aug. 31-Sept. 4, 1969, pp. 275-277, Polish Science Publrs. (1971)

J. R. Humphreys, E. C. Filewicz, S. Greenberg, S. B. Skladzien, and P. Vilinskas
Behavior and Calibration of Devices for Monitoring Impurities in Sodium
Trans. Amer. Nucl. Soc. 14(2), 614 (1971) Abstract

C. E. Johnson, D. V. Steidl, and C. E. Crouthamel
Distributions of Gaseous Fission Products in Irradiated Mixed-Oxide Fuels
Trans. Amer. Nucl. Soc. 14(Suppl. 1), 27 (1971) Abstract

C. E. Johnson and C. E. Crouthamel
Fuel-Clad Reactions in Irradiated Mixed-Oxide Fuels
Trans. Amer. Nucl. Soc. 14(Suppl. 1), 17 (1971) Abstract

C. E. Johnson and E. J. Hathaway
Solid-Liquid Phase Equilibria for the Ternary Systems Li(F,Cl,I) and Na(F,Cl,I)
J. Electrochem. Soc. 118, 631-634 (April 1971)

C. E. Johnson and C. E. Crouthamel
Fuel-Clad Interactions in Mixed-Oxide UO_2-PuO_2 Fuel
Trans. Amer. Nucl. Soc. 14(1), 173 (June 1971) Abstract

I. Johnson, C. E. Johnson, and C. E. Crouthamel
Fission Product Element Distribution in Irradiated Oxide Fuels
162nd Amer. Chem. Soc. Nat. Mtg., Washington, D.C., September 13-17, 1971, Abstracts of Papers, NUCL-45

T. R. Johnson, R. D. Pierce, F. G. Teats, and E. F. Johnston
Behavior of Countercurrent Liquid-Liquid Columns with a Liquid Metal
A.I.Ch.E. Journal 17, 14-18 (January 1971)

A. A. Jonke, E. L. Carls, G. J. Vogel, L. J. Anastasia, R. L. Jarry, and M. Haas
Reducing Pollution from Fossil Fuel Combustion
Instruments and Control Systems 44, 95-98 (July 1971)

W. Y. Kato, R. J. Armani, R. P. Larsen, P. E. Moreland, L. A. Mountford, J. M. Gasidlo, R. J. Popek, and C. D. Swanson
An Integral Measurement of Plutonium-239 and Uranium-233 Alpha
Nucl. Sci. Eng. 45, 37-46 (July 1971)

V. M. Kolba, M. A. Slawecki, E. C. Filewicz, and J. T. Holmes
Design and Performance of an Oxygen-Hydrogen Meter Module for On-Line Sodium Analysis at FFTF
Trans. Amer. Nucl. Soc. 14(2), 608 (1971) Abstract

M. L. Kyle, H. Shimotake, R. K. Steunenberg, F. J. Martino, R. Rubischko, and E. J. Cairns
Lithium/Sulfur Batteries for Electric Vehicle Propulsion
Proc. 1971 Intersociety Energy Conversion Engineering Conf., Soc. Automotive Engineers, Inc., pp. 80-95, New York (1971)

R. P. Larsen, R. R. Heinrich, N. D. Dudey, R. D. Oldham, and R. J. Popek
^{235}U and ^{239}Pu Fast Fission Yields as a Function of Neutron Energy
Trans. Amer. Nucl. Soc. 14(1), 370 (1971) Abstract

L. Leibowitz, M. G. Chasanov, and R. A. Blomquist
Speed of Sound in Liquid Sodium to 1000°C
J. Appl. Phys. 42, 2135-2137 (April 1971)

L. Leibowitz, M. G. Chasanov, L. W. Mishler, and D. F. Fischer
Enthalpy of Liquid Uranium Dioxide to 3500 K
J. Nucl. Mater. 39, 115-116 (1971) Letter

C. Luner, J. T. Holmes, and P. A. Nelson
Evaluation of an On-Line Carbon Meter for Use in LMFBR Sodium
Trans. Amer. Nucl. Soc. 14(2), 610 (1971) Abstract

V. A. Maroni, E. J. Hathaway, and E. J. Cairns
Structural Studies of Magnesium Halide-Potassium Halide Melts by Raman Spectroscopy
J. Phys. Chem. 75, 155-159 (January 7, 1971)

V. A. Maroni
Laser Raman Spectra of PbX_2-KX Melts (X=Cl and Br)
J. Chem. Phys. 54, 4126-4127 (May 1, 1971)

V. A. Maroni and R. V. Schablaske
Characterization of P_4Se_3 by X-Ray Powder Diffraction and Raman Spectroscopy
J. Inorg. Nucl. Chem. 33, 3182-3184 (1971)

V. A. Maroni
Vibrational Frequencies and Force Constants for Tetrahedral MgX_4^{-2} (X=Cl, Br, and I) in MgX_2-KX Melts
J. Chem. Phys. 55, 4789-4792 (November 15, 1971)

C. C. McPheeters, D. R. Vissers, M. A. Slawecki, and P. A. Nelson
Design and Performance of Hydrogen Meters for Detecting Water-to-Sodium Leaks in LMFBR Steam Generators
Trans. Amer. Nucl. Soc. 14(2), 614 (1971) Abstract

J. M. McKee, V. M. Kolba, E. C. Filewicz, and J. T. Holmes
Design and Testing of a Standard Device for Determining Oxygen Activity in Sodium by Vanadium Wire Equilibration
Trans. Amer. Nucl. Soc. 14(2), 609 (1971) Abstract

P. A. G. O'Hare
Hartree-Fock Calculations for the Ground States of CF and CF^+
Abstracts of Papers, 161st Nat. Amer. Chem. Soc. Mtg., Los Angeles, March 28-April 2, 1971, PHYS-087

P. A. G. O'Hare and A. C. Wahl
Dissociation Energy, Ionization Potential, Electron Affinity, Dipole and Quadrupole Moments of Chlorine Monoxide (ClO, $^2\Pi$) from Ab Initio Molecular Orbital Calculations
J. Chem. Phys. 54, 3770-3776 (May 1, 1971)

P. A. G. O'Hare
Electron Affinity of NS, and the Dipole and Quadrupole Moments of NS^-
J. Chem. Phys. 54, 4124-4126 (May 1, 1971) Letter

P. A. G. O'Hare and A. C. Wahl
Quantum-Chemical Study of Some Pnicogen Monofluorides
J. Chem. Phys. 54, 4563-4577 (June 1, 1971)

P. A. G. O'Hare and A. C. Wahl
Molecular Orbital Investigation of CF and SiF and Their Positive and Negative Ions
J. Chem. Phys. 55, 666-676 (July 15, 1971)

P. A. G. O'Hare and A. C. Wahl
The Dissociation Energies of NaO and Its Ions from Thermochemical and Molecular Orbital Studies
Abstracts of Papers, 162nd Amer. Chem. Soc. Mtg., Washington, D.C., September 12-17, 1971, PHYS-096

M. F. Roche, L. E. Ross, and R. J. Meyer
Determination of Oxygen in Liquid Sodium by Proton Activation Analysis
Trans. Amer. Nucl. Soc. 14(2), 617 (1971) Abstract

S. Rosen, J. M. Simmons, E. A. Aitken, B. R. T. Frost, A. D. Tevebaugh, and W. F. Sheely
Fundamental Properties and Behavior of Fuel Materials in Fast Reactor Environments
Nuclear USA, Proc. 4th Int. Conf. on the Peaceful Uses of Atomic Energy, Geneva, September 6-16, 1971, Vol. 1, pp. 2.6-1 to 2.6-17 (1971)

R. R. Schlueter and W. E. Ruther
An Inexpensive Pump for Liquid Sodium
Nucl. Technol. 11, 266-267 (June 1971)

B. Singer and L. Burris
Continuous On-Line Monitoring of Oxygen, Carbon, and Hydrogen in Sodium
Trans. Amer. Nucl. Soc. 14(2), 608 (1971) Abstract

G. P. Stavropoulos and F. A. Cafasso
Oxygen in Liquid Sodium: Thermodynamics and Electrochemical Determination
Trans. Amer. Nucl. Soc. 14(2), 621 (1971) Abstract

M. Tetenbaum and P. D. Hunt
High-Temperature Thermodynamic Properties of Hypo- and Hyper-stoichiometric Uranium Carbides
J. Nucl. Mater. 40(1), 104-112 (1971)

L. E. Trevorrow, J. G. Riha, and M. J. Steindler
The Formation and Fluorination of Lithium Fluoroplutonate(IV) Compounds
J. Inorg. Nucl. Chem. 33, 2875-2882 (1971)

E. Veleckis, S. K. Dhar, F. A. Cafasso, and H. M. Feder
Solubility of Helium and Argon in Liquid Sodium
J. Phys. Chem. 75, 2832-2838 (September 2, 1971)

D. R. Vissers, J. T. Holmes, P. A. Nelson, and L. G. Bartholme
A Hydrogen Monitor for Detection of Leaks in LMFBR Steam Generators
Nucl. Technol. 12, 218-225 (October 1971)

D. R. Vissers, J. T. Holmes, and P. A. Nelson
A Hydrogen Activity Meter for LMFBR's
Trans. Amer. Nucl. Soc. 14(2), 610 (1971) Abstract

I. O. Winsch, R. D. Pierce, and T. R. Johnson
Melt Decladding of Fast Reactor Fuels
Trans. Amer. Nucl. Soc. 14(1), 78 (1971) Abstract

B. Papers Accepted for Publication in the Open Literature

J. E. Battles, W. A. Shinn, and P. E. Blackburn
Thermodynamic Investigation of Trisodium Uranium(V) Oxide (Na_3UO_4). Part IV. Mass Spectrometric Study of the Na-U-O System
Accepted for publication in J. Chem. Thermodyn.

E. J. Cairns, R. K. Steunenberg, and H. Shimotake
Cells--High Temperature
Accepted for publication in Kirk-Othmer Encyclopedia of Chemical Technology

M. G. Chasanov, L. Leibowitz, D. F. Fischer, and R. A. Blomquist
Speed of Sound in Liquid Sodium from 1000 to 1500°C
Accepted for publication in J. Appl. Phys.

D. R. Fredrickson and M. G. Chasanov
Thermodynamic Investigation of Trisodium Uranium(V) Oxide (Na_3UO_4). Part III. Enthalpy to 1200°K by Drop Calorimetry
Accepted for publication in J. Chem. Thermodyn.

B. D. Holt, A. G. Engelkemier, and A. Venters
Variations of Sulfur Isotope Ratios in Samples of Water and Air Near Chicago
Accepted for publication in Environ. Sci. Technol.

G. K. Johnson, P. A. G. O'Hare, and E. H. Appelman
Thermodynamic Properties of Perbromyl Fluoride (BrO_3F)
Accepted for publication in Inorg. Chem.

L. Leibowitz, D. F. Fischer, and M. G. Chasanov
Enthalpy of Uranium-Plutonium Oxides: ($U_{.8}Pu_{.2}O_{1.97}$) from 2350 to 3000°K
Accepted for publication in J. Nucl. Mater. (letter)

P. A. G. O'Hare, W. A. Shinn, F. C. Mrazek, and A. E. Martin
Thermodynamic Investigations of Trisodium Uranium(V) Oxide (Na_3UO_4). Part I. Preparation and Enthalpy of Formation
Accepted for publication in J. Chem. Thermodyn.

G. T. Reedy and M. G. Chasanov
Total Pressure of Uranium-Bearing Species over Molten Urania
Accepted for publication in J. Nucl. Mater.

D. J. Rokop, D. N. Metta, and C. M. Stevens
$^{236}U/^{238}U$ Measurements in Three Terrestrial Minerals and One Processed Ore
Accepted for publication in Int. J. Mass Spectrometry and Ion Physics

C. ANL Reports

G. J. Bernstein, D. E. Grosvenor, J. F. Lenc, W. E. Miller, I. O. Winsch, J. Wolkoff, and R. C. Paul
The EBR-II Skull Reclamation Process. Part V. Design and Development of Plant-Scale Equipment
ANL-7772

P. E. Blackburn, C. E. Johnson, J. E. Battles, I. Johnson, A. E. Martin, M. Tetenbaum, C. E. Crouthamel, A. D. Tevebaugh, and R. C. Vogel
Chemical Engineering Division Fuels and Materials Semiannual Report, January-June 1971
ANL-7822

L. Burris, J. E. Draley, P. A. Nelson, F. A. Cafasso, T. F. Kassner, J. T. Holmes, W. E. Miller, R. J. Meyer, M. H. Barsky, and J. G. Eberhart
Sodium Technology Quarterly Report, July-September 1970
ANL/ST-4

L. Burris, J. E. Draley, P. A. Nelson, F. A. Cafasso, T. F. Kassner, J. T. Holmes, W. E. Miller, and R. J. Meyer
Sodium Technology Quarterly Report, October-December 1970
ANL/ST-8

L. Burris, F. A. Cafasso, R. J. Meyer, M. H. Barsky, and H. S. Edwards
Interim Methods for the Analysis of Sodium and Cover Gas
ANL/ST-6

L. Burris, J. E. Draley, P. A. Nelson, F. A. Cafasso, T. F. Kassner, J. T. Holmes, W. E. Miller, R. J. Meyer, and M. H. Barsky
Sodium Technology Quarterly Report, January-March 1971
ANL-7817

E. J. Cairns, E. C. Gay, V. M. Kolba, M. L. Kyle, A. D. Tevebaugh, and L. E. Trevorrow
Lithium/Selenium Secondary Cells for Components in Electric Vehicular-Propulsion Generating Systems. First Semiannual Technical Summary Report for May 23, 1969 to November 22, 1969
ANL-7663

E. J. Cairns, E. C. Gay, V. M. Kolba, M. L. Kyle, A. D. Tevebaugh, and L. E. Trevorrow
Lithium/Selenium Secondary Cells for Components in Electric Vehicular-Propulsion Generating Systems. Interim Technical Summary Report No. 2 for November 23, 1969 to May 22, 1970
ANL-7745

E. J. Cairns, M. L. Kyle, V. A. Maroni, H. Shimotake, R. K. Steunenberg, and A. D. Tevebaugh
Development of High-Energy Batteries for Electric Vehicles, Progress Report for February 1969 through June 1970
ANL-7756

E. J. Cairns, E. C. Gay, M. L. Kyle, A. D. Tevebaugh, L. E. Trevorrow, W. J. Walsh, and D. S. Webster
Lithium/Chalcogen Secondary Cells for Components in Electric Vehicular-Propulsion Generating Systems. Interim Technical Summary Report No. 3 for May 23, 1970 to November 22, 1970
ANL-7777

E. J. Cairns, F. A. Cafasso, P. T. Cunningham, J. G. Eberhart, H. M. Feder, V. A. Maroni, H. C. Schnyders, E. Veleckis, A. D. Tevebaugh, and R. C. Vogel
Chemical Engineering Division Physical Chemistry of Liquid Metals and Molten Salts Semiannual Report, January-June 1971
ANL-7823

E. J. Cairns, A. A. Chilenskas, H. Shimotake, R. K. Steunenberg, A. D. Tevebaugh, and W. J. Walsh
Lithium/Selenium Secondary Battery for Implantation
U.S. Dept. Health, Education, and Welfare, National Institutes of Health Report
ANL-MDAP-70

M. G. Chasanov, J. Fischer, D. R. Fredrickson, S. D. Gabelnick, L. Leibowitz, A. D. Tevebaugh, and R. C. Vogel
Chemical Engineering Division Reactor Safety and Physical Property Studies Semiannual Report, January-June 1971
ANL-7820

M. G. Chasanov and D. F. Fischer
Out-of-Pile Study of the Effects of Thermal Gradients on the Distribution of Plutonium in Fast-Reactor Fuel Materials
ANL-7703

N. D. Dudey, R. R. Heinrich, R. J. Popek, R. P. Larsen, and R. D. Oldham
Activation-Rate Measurements in the ZPR-3 Mockup Critical Experiments. Part I. Measurements of Foil-Activation Rates and Fission Yields in Assembly 60 of ZPR-3 - Mockup of EBR-II with a Uranium Blanket
ANL-7781

R. R. Heinrich, J. Williams, A. A. Madson, and N. D. Dudey
Integral Measurements in EBR-II of Capture Rates, Fission Rates, and Alpha for ^{233}U, ^{235}U, ^{238}U, ^{239}Pu, ^{240}Pu, and ^{242}Pu
ANL-7791

W. N. Hubbard, P. A. G. O'Hare, G. K. Johnson, M. Ader, J. L. Settle, A. D. Tevebaugh, and R. C. Vogel
Chemical Engineering Division Thermochemical Studies Semiannual Report, January-June 1971
ANL-7821

A. A. Jonke, E. L. Carls, R. L. Jarry, L. J. Anastasia, M. Haas, J. R. Pavlik, W. A. Murphy, C. B. Schoffstoll, and G. N. Vargo
Reduction of Atmospheric Pollution by the Application of Fluidized-Bed Combustion, Annual Report July 1969-June 1970
ANL/ES-CEN-1002

A. A. Jonke, G. J. Vogel, L. J. Anastasia, and R. L. Jarry
Work Plan for Continuation of the Project "Reduction of Atmospheric Pollution by the Application of Fluidized-Bed Combustion"
ANL/ES-CEN-1003

R. A. Juvinall, R. W. Kessie, and M. J. Steindler
Sand-Bed Filtration of Aerosols: A Review of Published Information on Their Use in Industrial and Atomic Energy Facilities
ANL-7683

J. B. Knighton, G. J. Bernstein, G. N. Vargo, and R. D. Pierce
Development of a Mixer-Settler for Liquid Metal-Salt Systems
ANL-7810

R. P. Larsen, N. D. Dudey, M. J. Fluss, R. R. Heinrich, R. L. Malewicki, R. D. Oldham, R. J. Popek, J. Williams, C. E. Crouthamel, and R. C. Vogel
Cross Sections and Burnup Semiannual Report, January-June 1971
ANL-7824

R. J. Meyer, C. E. Johnson, and L. E. Ross
A Feasibility Study of the Identification of Fuel-Cladding Failures Using Sodium-Soluble Isotopic Tags
ANL-7785

P. A. Nelson, J. Fischer, J. F. Lenc, J. R. Haley, and J. D. Schilb
Pyrochemical Processing of Fuel Materials and Scrap Containing Plutonium-238
ANL-7709

P. A. G. O'Hare and A. C. Wahl
Complete Hartree-Fock Wavefunctions and One-Electron Properties for $CF(^2\Pi)$, $CF^+(^1\Sigma)$, and $CF^-(^3\Sigma)$, and Charge-Density Diagrams for CF and Its Component Orbitals
ANL-7806

D. Ramaswami, J. R. Pavlik, and A. A. Jonke
Conversion of Uranium Dioxide to Uranium Carbide in an Induction Plasma Torch Reactor
ANL-7671

K. A. Varteressian and L. Burris
Fission-Product Spectra from Fast and Thermal Fission of ^{235}U and ^{239}Pu
ANL-7678

E. Veleckis, S. K. Dhar, F. A. Cafasso, and H. M. Feder
Solubility of Helium and Argon in Liquid Sodium
ANL-7802

D. S. Webster, A. A. Jonke, G. J. Bernstein, N. M. Levitz, R. D. Pierce, M. J. Steindler, and R. C. Vogel
Chemical Engineering Division Fuel Cycle Technology Quarterly Report, July, August, September 1970
ANL-7755

D. S. Webster, A. A. Jonke, G. J. Bernstein, N. M. Levitz, R. D. Pierce, M. J. Steindler, and R. C. Vogel
Chemical Engineering Division Fuel Cycle Technology Quarterly Report, October, November, December 1970
ANL-7767

D. S. Webster, A. A. Jonke, G. J. Bernstein, N. M. Levitz, R. D. Pierce, M. J. Steindler, and R. C. Vogel
Chemical Engineering Division Fuel Cycle Technology Quarterly Report, January, February, March 1971
ANL-7799

D. S. Webster, A. A. Jonke, G. J. Bernstein, N. M. Levitz, R. D. Pierce, M. J. Steindler, and R. C. Vogel
Chemical Engineering Division Fuel Cycle Technology Quarterly Report, April, May, June 1971
ANL-7841

R. C. Vogel, L. Burris, A. D. Tevebaugh, D. S. Webster, E. R. Proud, and J. Royal
Chemical Engineering Division Research Highlights--January-December 1970
ANL-7750

D. Papers Presented at Scientific Meetings

L. J. Anastasia, E. L. Carls, R. L. Jarry, A. A. Jonke, and G. J. Vogel
Pollution Control Capabilities of Fluidized Bed Combustion
Presented at 69th National Meeting, AIChE, Cincinnati, May 16-19, 1971

E. J. Cairns
Batteries for Electric Automobiles
Presented at University of California Radiation Laboratory, Berkeley, Calif., Apr. 21, 1971

E. J. Cairns
High-Temperature Electrochemical Cells
Presented at Electrochemical Society Meeting, San Francisco Section, Palo Alto, Calif., Apr. 21, 1971

E. J. Cairns
Recent Advances in High-Temperature Cells for Electric Automobiles
Presented at University of California, Berkeley, Apr. 22, 1971

E. J. Cairns, P. T. Cunningham, and V. A. Maroni
Phase Diagram and EMF Investigations of the Pseudo-Ternary Li_2Se-Se-(LiX-MX) and Li_2S-S-(LiX-MX) Systems
Presented at Chemistry of Molten Salts Gordon Conference, Meriden, N.H., Aug. 29-Sept. 3, 1971

E. J. Cairns
Lithium/Sulfur Cells for Electric Automobiles
Presented at The University of Wisconsin, Oct. 20, 1971

P. T. Cunningham and E. J. Cairns
The ANL Electrochemical Energy Conversion Program
Presented at Power Information Center Meeting, NASA Goddard, Greenbelt, Md., Mar. 24, 1971

J. E. Draley
Nonmetallic Impurities in Liquid Sodium and Their Electrochemical Determination
Presented at Iowa State University, Feb. 12, 1971

J. G. Eberhart
A Groovy Way to Study Surface and Volume Diffusion--Grain Boundary Groove Growth
Presented at Chemical Engineering Division, The Pennsylvania State University, Nov. 2, 1971

J. G. Eberhart
A Groovy Way to Study Surface Tension and Surface Diffusion--Grain Boundary Groove Growth
Presented at Chemistry Department, The University of Wisconsin, Milwaukee, Oct. 25, 1971

J. Faris
Ion Exchange Methods in Trace Analysis
Presented at 15th Conf. on Analytical Chemistry in Nuclear Technology, Oak Ridge, Tenn., Oct. 12-14, 1971

H. M. Feder and H. C. Schnyders
Solubility of Noble Gases in Liquid Metals
Presented at University of Notre Dame, April 29, 1971

S. D. Gabelnick and G. T. Reedy
Vacuum System for Matrix Isolation Studies
Presented at Annual Symposium of the Great Lakes Regional Administrative Group, American Vacuum Society, Batavia, Ill., May 7, 1971

S. D. Gabelnick
Infrared Fourier Transform Spectroscopy
Presented at Physics Colloquium, Northern Illinois University, Mar. 5, 1971

E. C. Gay, L. E. Trevorrow, W. J. Walsh, E. J. Cairns, J. D. Arntzen, and J. G. Riha
Lithium/Selenium Secondary Cells for High-Power Applications
Presented at 64th Annual AIChE Meeting, San Francisco, Nov. 28-Dec. 3, 1971

E. C. Gay
Lithium/Selenium Secondary Cells with Paste Electrolytes
Presented at The University of Michigan, Feb. 11, 1971

G. K. Johnson, J. G. Malm, and W. N. Hubbard
The Enthalpy of Formation of Xenon Hexafluoride
Presented at The Second International Conference on Calorimetry and Thermodynamics, Orono, Maine, July 12-14, 1971

A. A. Jonke, E. L. Carls, R. L. Jarry, and L. J. Anastasia
Anti-Pollution Aspects of Fluidized-Bed Combustion
Presented at Economic Commission for Europe Seminar on Desulphurization of Fuels and Combustion Gases, Geneva, Nov. 16-20, 1970

A. A. Jonke
Pollution Control Aspects of Fluidized-Bed Combustion
Presented at University of Kentucky, Nov. 18, 1971

A. A. Jonke
Problems of Our Air Environment
Presented to Joliet Branch of the Illinois Society of Professional Engineers, Joliet, Ill., Dec. 1, 1971

A. A. Jonke
Potential for Pollution Control by Fluidized-Bed Combustion
Presented at Wayne State University, Oct. 13, 1971

M. L. Kyle
Lithium/Sulfur Cells and Their Potential for Electric Automobile Propulsion
Presented at Dupage County Naval Reserve Officers Association Meeting, Argonne, Ill., June 30, 1971

S. Lawroski
Safety Problems in Nuclear Fuel Reprocessing Plants
Presented at The University of Arizona, Mar. 31, 1971

S. Lawroski
Some Thoughts on the Need for an Improved Fuel Cycle for LMFBR's
Presented at 64th Annual Meeting, AIChE, San Francisco, Nov. 28-Dec. 2, 1971

P. A. G. O'Hare
Some Recent Thermochemical and Molecular Orbital Results for the Sodium-Oxygen System
Presented at National Bureau of Standards, Washington, D.C., Dec. 16, 1971

P. A. G. O'Hare, F. C. Mrazek, and W. A. Shinn
A Calorimetric Study of Trisodium Uranium(V) Oxide (Na_3UO_4)
Presented at The Second International Conference on Calorimetry and Thermodynamics, Orono, Maine, July 12-14, 1971

P. A. G. O'Hare
Some Recent Thermochemical and Molecular Orbital Results for the Sodium-Oxygen System
Presented at Scarborough College, University of Toronto, June 29, 1971

R. K. Steunenberg, C. A. Trapp, R. M. Yonco, and E. J. Cairns
Electrical Conductivity of Liquid Sulfur and Sulfur-Phosphorus Mixtures
Presented at 3rd Annual Mardi Gras Symposium on Sulfur Chemistry and Theoretical Chemistry, New Orleans, Feb. 18-19, 1971

M. Tetenbaum and P. D. Hunt
Phase Transformations in the U-C and U-C-O Systems via Controlled Oxygen and Carbon Potentials
Presented at International Colloquium on the Study of Crystalline Transformations at High Temperature, Odeillo, France, Sept. 27-Oct. 1, 1971

M. Tetenbaum
High Temperature Behavior and Characteristics of Uranium Carbide Fuels
Presented at Idaho Facilities, Argonne-West, Mar. 16, 1971

D. R. Vissers and L. G. Bartholme
A Hydrogen Activity Meter for Liquid Metal Fast Breeder Reactor Systems
Presented at Annual Symposium of the Great Lakes Regional Administration Group, American Vacuum Society, Batavia, Ill., May 6-7, 1971

G. J. Vogel
Fluidized-Bed Combustion of Coal
Presented at Dupage County Naval Reserve Officers Association Meeting, Argonne, Ill., Apr. 28, 1971

G. J. Vogel, D. Ramaswami, R. L. Jarry, L. J. Anastasia, E. L. Carls, and A. A. Jonke

Variables Affecting Retention of Sulfur by Calcined Limestone or Dolomite in the Fluidized-Bed Combustion of Fossil Fuels

Presented at 64th Annual Meeting, AIChE, San Francisco, Nov. 28-Dec. 2, 1971

D. S. Webster

Nuclear Power Fuel Cycles

Presented at Kansas State University, Feb. 8, 1971

ARGONNE NATIONAL LAB WEST
3 4444 00010993 4

B